Medical Research Council
London Institute of Medical Sciences
Imperial College London

AMPK and hypoxia: crosstalk in the endothelium

Lida Kabir
BHF PhD Studentship

Professor David Carling, Dr Graeme Birdsey and Dr Charis Pericleous

Thesis submitted to Imperial College London for the degree of Doctor of Philosophy

January 2024

Statement of Originality

I, Lida Kabir, declare that this thesis was written by myself, and the work contained herein is my own. Information derived from published sources or by the work of others been explicitly acknowledged both in the text and in the list of references. This work has not been previously submitted at any other university or tertiary education institution in any form.

Copyright Declaration

The copyright of this thesis rests with the author. Unless otherwise indicated, its contents are licensed under a Creative Commons Attribution-Non-Commercial 4.0 International Licence (CC BY-NC). Under this licence, you may copy and redistribute the material in any medium or format. You may also create and distribute modified versions of the work. This is on the condition that: you credit the author and do not use it, or any derivative works, for a commercial purpose. When reusing or sharing this work, ensure you make the licence terms clear to others by naming the licence and linking to the licence text. Where a work has been adapted, you should indicate that the work has been changed and describe those changes. Please seek permission from the copyright holder for uses of this work that are not included in this licence or permitted under UK Copyright Law.

Abstract

ECs are highly reliant on metabolic stimuli, integrating nutrient and oxygen (O_2) availability to alter vascular function under physiological and pathological conditions. This remarkable metabolic plasticity is evident during angiogenesis, where metabolic changes promote the emergence of distinct EC subtypes. Hypoxia is a major stimulator of angiogenesis, a phenomenon frequently dysregulated in pathologies such as cancer and cardiovascular diseases. AMP-activated protein kinase (AMPK) is a master regulator of energy metabolism, restoring ATP levels during metabolic stress. Endothelial dysfunction and capillary rarefaction are hallmark features of cardiometabolic diseases; therefore, therapeutic targeting of AMPK holds promise in the treatment of these disorders. Despite extensive research having established the link between hypoxia signalling, and endothelial metabolism, the role of AMPK remains largely unexplored.

Examination of AMPK activity across different O_2 tensions shows that short-term hypoxia does not appear to profoundly impact AMPK activity in HUVECs. There was no significant effect of 991 and/or BI-9774, a novel small molecule activator of AMPK, on HIF-1α stabilisation, although an increase in HIF-1α protein was noted. BI-9774 increased HRE-dependent transcription and enrichment in HIF-1α signalling based on luciferase reporter assays and transcriptomics. *In vitro* kinase assays and phospho-proteomics show that AMPK is capable of phosphorylating HIF-1α with putative phosphorylation sites identified by LC/MS^2. Proximity ligation assays confirmed that AMPK and HIF-1α may directly interact *in vitro*. Despite suppressing endothelial proliferation, BI-9774 treatment still promoted Matrigel tube formation *in vitro*, with enhanced vascularisation observed in the global AMPK activating (γ_1D316A-Tg) model. Endothelial-specific AMPK activation (EC-γ_1D316A-Tg) promoted resistance against HFD-induced weight gain and hepatic steatosis. Further validation is required to determine (1) if HIF-1α is a target of AMPK *in vivo*; (2) whether the observed vascular and angiogenic phenotypes are dependent on HIF-1α activity; and (3) the possibility of AMPK rewiring the HIF-1α transcriptional response.

Acknowledgements

I would first like to sincerely thank my supervisors for their support throughout the course of this PhD. I would like to express my sincere gratitude to Professor David Carling for his generosity, scientific discussions and encouragement throughout the years. I would also like to thank Dr Graeme Birdsey for his patience and encouragement, particularly with the post-natal angiogenesis assays. I am also incredibly grateful to Dr Charis Pericleous for her mentorship and scientific discussion, which has helped me greatly as a scientist. I would like to dedicate this thesis to Professor Justin Mason, who sadly passed away in May 2022, for it was his enthusiasm for hypoxia-related work that made the findings presented in this thesis possible. I would like to credit Justin and his former group members, Dr Robert Maughan and Andrew Porter, for inspiring me to always look for a translational approach to my work. Finally, I would also like to thank the British Heart Foundation for providing the funding to carry out this work.

I am indebted to several people who have provided a great deal of assistance throughout the project. I would like to thank Dr Angela Woods for her patience, particularly with performing kinase assays. I would also like to thank Dr Nav Navaratnam for his helpful comments regarding experimental ideas, protocols and constructive discussions regarding this work. I would also like to thank Dr Alice Pollard for her enthusiasm and support with my high fat diet study, who I have learnt a lot from with regards to *in vivo* work. I would like to thank other members of the Cellular Stress group for their ideas, constructive criticism and entertaining discussions. I would like to thank Dr Alex Sardini for his assistance and technical expertise with CLAMS. I would like to thank Dr Yi-Fang Wang and Dr Jesus Urtasun from the LMS Bioinformatics facility for the extensive RNA-seq analysis they performed on my dataset. I would also like to thank Dr Pavel Shliaha for the mass spectrometry studies and Dr Alex Montoya for the proteomics analysis. I am grateful to Dr Daniela Pirri who assisted me in optimising the luciferase assays, for being a listening ear with regards to HIF and for the consolatory late work evening dinners.

Throughout the course of my PhD, I feel privileged to have met such wonderful people and create such wonderful friendships both in ICTEM and MRC. To Marie Lang, thank you for being such an inspiration, I am so grateful for your support and engaging scientific and non-scientific discussions throughout the years. To Kelly De Coteau, a fellow BHF student, thank you for all the laughs and the gossip – your friendship is invaluable to me! I would also like to thank Jane Bennett and Rupali Dabas, thank you both for making the MRC such a wonderful

place to work, I truly do not know what I'd do without you both. I would like to thank Daisy Jones, Daisy Gresham and Andrew Porter for all the gossip, the pop culture discussions and making tissue culture an entertaining place to be.

Finally, I would like to thank my parents and my friends. I am incredibly fortunate to have such a wonderful group of people for there are not enough words to show how truly thankful I am. To my mother, for her unwavering support and encouragement, for always believing in me and providing me reassurance during difficult times, I do not think I would have done this without you.

Table of Contents

ABSTRACT **3**
ACKNOWLEDGEMENTS **4**
TABLE OF CONTENTS **6**
LIST OF FIGURES **9**
LIST OF TABLES **12**
ABBREVIATIONS **13**
1. CHAPTER 1 – INTRODUCTION **15**
1.1 Development of the Vascular System 15
1.2 Structure and Heterogeneity of the Endothelium 16
1.3 Endothelial Metabolism 17
1.4 Mechanosensing, Shear Stress and Regulation of Vascular Tone 20
1.5 Modulation of Inflammation and Haemostasis 22
1.6 Angiogenesis 24
1.6.1 Sprouting Angiogenesis *24*
1.6.2 Vasculogenesis beyond Sprouting Angiogenesis *30*
1.7 AMP-activated Protein Kinase 32
1.7.1 Structure, Function and Evolution of AMPK *32*
1.7.2 Metabolic Functions of AMPK *35*
1.7.3 First- and Second-Generation AMPK activators *38*
1.7.4 AMPK in the Endothelium and the Vasculature *41*
1.8 Oxygen Sensing, Homeostasis and Hypoxia Inducible Factors 49
1.8.1 Oxygen and Oxygen Sensing Mechanisms in Metazoans *49*
1.8.2 Hypoxia Inducible Factors *49*
1.8.3 Hypoxia-dependent and -independent Regulation of HIFα *51*
1.8.4 HIFα in the Vasculature *57*
1.9 Project Scope and Aims 62
2. CHAPTER 2 – MATERIALS AND METHODS **63**
2.1 Reagents 63
2.1.2 Buffers and Solutions *63*
2.1.2 Primers *64*
2.1.3 Antibodies *65*
2.1.4 Pharmacological agents *66*
2.1.5 Plasmids *66*
2.1.6 Transfection Reagents *67*
2.2 Tissue Culture 67
2.2.1 HUVECs *67*
2.2.2 HEK293Ts *68*
2.3 *In vitro* Hypoxia Studies 69
2.4 Glucose Deprivation Studies 69
2.5 Cell Viability and Death Assays 69
2.5.1 CyQUANT™ LDH Cytotoxicity Assay *69*
2.5.2 CyQUANT™ Cell Proliferation Assay *70*
2.5.3 RealTime-Glo™ Annexin V Apoptosis and Necrosis Assay *70*
2.6 RT-qPCR 70
2.7 Immunoblotting (IB) 71
2.8 Multiple Sequence Alignment 72
2.9 Immunofluorescence (IF) 72
2.10 Proximity Ligation Assay (PLA) 73
2.11 Bulk RNA-seq 73
2.11.1 RNA Extraction and Quality Control *73*
2.11.2 RNA-seq Analysis *74*
2.11.3 Pathway Enrichment Analysis *74*

2.12 Plasmid DNA Preparation 74
2.12.1 Bacterial Transformation and Culture *74*
2.12.2 Plasmid DNA Purification *75*
2.13 DNA Transfection 75
2.13.1 Plasmid Transfection (HEK293Ts) *75*
2.13.2 Plasmid Transfection (HUVECs) *75*
2.14 HRE Luciferase Reporter Assays 76
2.15 SAMS Peptide AMPK Kinase Activity Assays 77
2.16 Radiolabelled-ATP *In Vitro* Phosphorylation Assays 77
2.17 Phosphoproteomics 78
2.17.1 Sample Preparation *78*
2.17.2 Liquid chromatography mass spectrometry (LC/MS^2) analysis *78*
2.17.3 Raw Data Processing *79*
2.17.4 Results Processing *80*
2.18 *In vitro* Seahorse (XFe96) Flux Analyzer Metabolic Phenotyping 80
2.19 mtDNA Measurements 81
2.20 Flow cytometry (FACS) 82
2.20.1 Mitochondrial membrane potential ($\Delta\Psi_m$) and mass measurements *82*
2.20.2 EdU incorporation and Propidium Iodide Cell Cycle Analysis *82*
2.21 Matrigel Tube Formation Assay *In Vitro* 84
2.22 Recombinant HEK293T Protein Expression and Myc-Trap® Immunoprecipitation 85
2.23 Immunohistochemistry (IHC) 85
2.24 *In vivo* Vascular and Metabolic Phenotyping of Global and EC-specific AMPK activation mouse models 86
2.24.1 Animal Husbandry *86*
2.24.2 Genotyping *87*
2.24.3 Ex vivo retina angiogenesis *88*
2.24.4 Diet-induced obesity studies *89*
2.24.5 CLAMS *89*
2.25 Statistics 89

3. CHAPTER 3 – REGULATION OF AMPK UNDER HYPOXIA 91

3.1 Introduction 91
3.2 Hypotheses and Aims 93
3.3 Results 95
3.3.1 Transcript expression of AMPK subunits in endothelial subtypes and optimisation of the AMPK activator BI-9774 ..... *95*
3.3.2 The effect of hypoxia on AMPK activity in ECs *100*
3.3.3 The effect of AMPK activation on HIF-1α stability *113*
3.4 Discussion and Limitations 117

4. CHAPTER 4 – CROSSTALK BETWEEN AMPK AND HYPOXIA SIGNALLING IN THE ENDOTHELIUM 123

4.1 Introduction 123
4.2 Hypothesis and Aims 125
4.3 Results 126
4.3.1 The effect of BI-9774 and/or hypoxia on the endothelial transcriptome *126*
4.3.2 Common pathways based on shared DEGs between hypoxia and BI-9774 treatment *136*
4.3.3 Effect of AMPK-mediated phosphorylation on HIF-1α function *141*
4.4 Discussion and Limitations 153

5. CHAPTER 5 – FUNCTIONAL CHARACTERISATION OF AMPK ACTIVATION IN THE ENDOTHELIUM 160

5.1 Introduction 160
5.2 Hypothesis and Aims 161
5.3 Results 162
5.3.1 The impact of BI-9774-mediated AMPK activation on endothelial glycolytic and mitochondrial metabolism in vitro *162*
5.3.2 The effects of AMPK activation on endothelial proliferation and angiogenesis in vitro and in vivo. *169*

5.3.4 Characterising the metabolic phenotype of the EC-specific AMPK gain-of-function (γ_1D316A-Tg) mouse model in vivo *177*
5.4 Discussion and Limitations 184
6. SUMMARY AND PERSPECTIVES 193
6.1 The role of AMPK in the hypoxia response 193
6.2 AMPK and HIFa signalling crosstalk and potential physiological relevance 194
6.3 The metabolic effects of endothelial AMPK 197
7. BIBLIOGRAPHY 199
8. APPENDICES 221

List of Figures

FIGURE 1.1 – SUMMARY OF THE MAIN METABOLIC PATHWAYS REQUIRED FOR ENERGY PRODUCTION IN ECS. 19
FIGURE 1.2 – A SCHEMATIC PROVIDING AN OVERVIEW OF THE KEY STEPS IN SPROUTING ANGIOGENESIS. 26
FIGURE 1.3 – SCHEMATIC ILLUSTRATING THE FEATURES AND SIGNALLING UNDERLYING THE DISTINCT ENDOTHELIAL PHENOTYPES THAT ARISE DURING SPROUTING ANGIOGENESIS. 29
FIGURE 1.4 – A SCHEMATIC ILLUSTRATING THE COMPOSITION, UPSTREAM REGULATION AND FUNCTIONS OF AMPK. 34
FIGURE 1.5 – A SCHEMATIC REPRESENTING THE DOWNSTREAM METABOLIC FUNCTIONS OF AMPK. 38
FIGURE 1.6 – GENERAL PROTEIN STRUCTURE OF HIFA TRANSCRIPTION FACTORS. 50
FIGURE 1.7 – OXYGEN-DEPENDENT REGULATION OF HIFA TRANSCRIPTION FACTORS BY PROLYL AND ASPARAGINYL HYDROXYLASES. 54
FIGURE 2.1 – A SCHEMATIC REPRESENTING CALCULATION OF MITOCHONDRIAL PARAMETERS BASED ON THE AGILENT SEAHORSE XF MITOSTRESS ASSAY. 81
FIGURE 2.2 – DEFINITIONS OF THE PARAMETERS MEASURED USING ANGIOGENESIS ANALYZER ON FIJI. 84
FIGURE 2.3 – A SCHEMATIC ILLUSTRATING THE BREEDING SCHEME USED FOR THE GENERATION OF THE AMPK Γ_1 EC-SPECIFIC WT AND D316A-TG. 87
FIGURE 3.1 – A SIMPLIFIED OVERVIEW OF HIF-INDEPENDENT RESPONSES TO HYPOXIA. ..93
FIGURE 3.2 – TPM EXPRESSION OF AMPK SUBUNIT ISOFORMS IN HUVECS, HAECS AND ADULT ECFCS. 96
FIGURE 3.3 – THE EFFECT OF INCREASING BI-9774 CONCENTRATION ON ACC^{S79} PHOSPHORYLATION IN HUVECS. 97
FIGURE 3.4 – THE EFFECT OF BI-9774 ON ENDOTHELIAL VIABILITY AND CYTOTOXICITY. 98
FIGURE 3.5 – BI-9774 TREATMENT TIME COURSE IN HUVECS. 99
FIGURE 3.6 – THE EFFECT OF ACUTE EXPOSURE TO DIFFERING O_2 TENSIONS ON AMPK ACTIVITY. 103
FIGURE 3.7 – THE EFFECT OF CHRONIC EXPOSURE TO DIFFERING O_2 TENSIONS ON AMPK ACTIVITY. 104
FIGURE 3.8 – THE EFFECT OF MODERATE AND SEVERE HYPOXIA, IN COMBINATION WITH BI-9774 TREATMENT ON CELL VIABILITY IN HUVECS. 106
FIGURE 3.9 – TIME COURSE EXPERIMENT EXAMINING THE EFFECT OF NORMOXIA AND HYPOXIA ON $AMPK^{T172}$ PHOSPHORYLATION STATUS AND KINASE ACTIVITY. 108
FIGURE 3.10 – THE EFFECT OF NORMOXIA, HYPOXIA AND HYPOXIA/REOXYGENATION ON $AMPKA^{T172}$ PHOSPHORYLATION STATUS. 109
FIGURE 3.11 – THE EFFECT OF PAN-PHD INHIBITOR FG-4592 ON $AMPKA^{T172}$ PHOSPHORYLATION. 110
FIGURE 3.12 – THE EFFECT OF HYPOXIA ON $EEF2^{T56}$ PHOSPHORYLATION. 111
FIGURE 3.13 – THE EFFECT OF SODIUM FLUORIDE ON $AMPKA^{T172}$ PHOSPHORYLATION STATUS UNDER HYPOXIA. 112
FIGURE 3.14 – THE EFFECT OF 991 ON HIF-1A STABILITY ACROSS DIFFERENT O_2 TENSIONS. 113
FIGURE 3.15 – THE EFFECT OF ACUTE BI-9774 TREATMENT ON HIF-1A STABILITY. 114
FIGURE 3.16 – THE EFFECT OF BI-9774 TREATMENT ON HIF-DEPENDENT TRANSCRIPTION AND TARGET EXPRESSION IN HUVECS. 115
FIGURE 3.17 – THE EFFECTS OF GLUCOSE DEPRIVATION ON HIF-1A STABILITY IN HUVECS. 116
FIGURE 4.1 – A SCHEMATIC REPRESENTING PHOSPHORYLATION SITES REPORTED IN THE LITERATURE FOR HIF-1A. 125
FIGURE 4.2 – SCHEMATIC DESCRIBING THE EXPERIMENTAL DESIGN FOR RNA-SEQUENCING. 126
FIGURE 4.3 – CLUSTER ANALYSIS OF RNA-SEQ GENE EXPRESSION DATA. 128
FIGURE 4.4 – VOLCANO PLOTS DISPLAYING DEG ANALYSIS ACROSS ALL PAIRWISE COMPARISONS. 129

FIGURE 4.5 – CANONICAL PATHWAYS ANALYSIS (CPA) FOR 3% O_2 (HYPOXIA) VERSUS 21% O_2 (NORMOXIA).....131
FIGURE 4.6 – CANONICAL PATHWAYS RESULTS FOR BI-9774 TREATMENT VERSUS UNTREATED AT 21% O_2.....132
FIGURE 4.7 – CANONICAL PATHWAYS RESULTS FOR BI-9774 TREATMENT VERSUS UNTREATED AT 3% O_2.....134
FIGURE 4.8 – IPA UPSTREAM REGULATOR ANALYSIS OF HIFA ISOFORMS ACROSS ALL PAIRWISE COMPARISONS.....135
FIGURE 4.9 – PAIRWISE COMPARISON OF DEGS BETWEEN 21% O_2 BI-9774 TREATED VERSUS 3% O_2 UT.....136
FIGURE 4.10 – IPA CANONICAL PATHWAYS RESULTS WITH COMMON DEGS SHARED BETWEEN 3% O_2 UT AND 21% O_2 BI-9774.....138
FIGURE 4.11 – IPA FUNCTIONS ANNOTATIONS WITH COMMON UPREGULATED DEGS SHARED BETWEEN 3% O_2 UT AND 21% O_2 BI-9774.....139
FIGURE 4.12 – IPA DISEASES ANNOTATIONS ON COMMON UPREGULATED DEGS SHARED BETWEEN 3% O_2 UT AND 21% O_2 BI-9774.....140
FIGURE 4.13 – PROXIMITY LIGATION ASSAY OF PHOSPHO-AMPKA^{T172} AND HIF-1A IN HUVECS UNDER 21% O_2.....141
FIGURE 4.14 – PHOSPHORYLATION OF PURIFIED HIF-1A BY PURIFIED ACTIVE AMPK$A_2B_1\Gamma_1$ COMPLEX IN VITRO.....143
FIGURE 4.15 – IDENTIFICATION OF AMPK-MEDIATED HIF-1A PHOSPHORYLATION SITES BY LC/MS^2.....143
FIGURE 4.16 – MASS SPECTROMETRY ANALYSIS OF S65, T652 AND S727.....145
FIGURE 4.17 – EVOLUTIONARY MULTIPLE SEQUENCE ALIGNMENT (MSA) ANALYSIS OF PUTATIVE AMPK PHOSPHORYLATION SITES IN HIF-1A.....146
FIGURE 4.18 – DENDROGRAM ILLUSTRATING THE PHYLOGENETIC RELATIONSHIP OF THE T652/S563 FLANKING PEPTIDE SEQUENCE ACROSS SEVERAL MAMMALIAN SPECIES.147
FIGURE 4.19 – AMINO ACID SEQUENCE COMPARISON OF PHOSPHO-SITES BETWEEN HIF-1A AND HIF-2A.....147
FIGURE 4.20 – A SCHEMATIC MAPPING THE S65, T652 AND S727 SITES WITH THE SEQUENCE OF HIF-1A.....148
FIGURE 4.21 – IN VITRO PHOSPHORYLATION OF IMMUNOPRECIPITATED WT AND MUTANT HIF-1A.....149
FIGURE 4.22 – TRANSIENT EXPRESSION OF HIF-1A CONSTRUCTS IN HUVECS.....150
FIGURE 4.23 – TRANSCRIPTIONAL ACTIVITY OF HIF-1A PHOSPHO-MUTANTS USING AN HRE-DEPENDENT LUCIFERASE ASSAY.....152
FIGURE 5.1 – REPRESENTATIVE TRACES DERIVED FROM AGILENT SEAHORSE XF MITOSTRESS ASSAY UNDER 3% AND 21% O_2.....162
FIGURE 5.2 – COMPARISON OF TREATMENTS ON MITOCHONDRIAL METABOLIC PARAMETERS AS DETERMINED BY THE AGILENT SEAHORSE XF MITOSTRESS ASSAY. 164
FIGURE 5.3 – THE EFFECT OF TREATMENT RESPONSES ON OXPHOS PARAMETERS UNDER DIFFERENT O_2 TENSIONS IN HUVECS.....165
FIGURE 5.4 – COMPARISON OF TREATMENTS ON BASAL GLYCOLYSIS BETWEEN TREATMENT GROUPS AND O_2 TENSION AS DETERMINED BY AGILENT SEAHORSE XF MITOSTRESS ASSAY.....165
FIGURE 5.5 – THE EFFECT OF ACUTE BI-9774 TREATMENT ON MITOCHONDRIAL MEMBRANE POTENTIAL AND MITOCHONDRIAL MASS.....166
FIGURE 5.6 – THE EFFECT OF CHRONIC BI-9774 TREATMENT ON MITOCHONDRIAL MEMBRANE POTENTIAL, MTDNA CONTENT AND MITOCHONDRIAL MASS.....168
FIGURE 5.7 – EDU INCORPORATION AS A MEASUREMENT OF DNA SYNTHESIS.....169
FIGURE 5.8 – PROPIDIUM IODIDE (PI) CELL CYCLE ANALYSIS OF HUVECS.....171
FIGURE 5.9 – MORPHOLOGICAL CHANGES OCCURRING IN HUVEC IN RESPONSE TO BI-9774 TREATMENT.....172
FIGURE 5.10 – THE EFFECT OF AMPK ACTIVATION AND INHIBITION BY BI-9774 AND BAY-3827 ON MATRIGEL TUBE FORMATION IN VITRO.....174
FIGURE 5.11 – WHOLEMOUNT IMMUNOSTAINING OF NEONATAL RETINAS FROM GLOBAL Γ_1WT-TG AND Γ_1D316A-TG MICE.....176
FIGURE 5.12 – INITIAL BODY WEIGHTS OF EC-Γ_1WT-TG AND EC-Γ_1D316A-TG MICE PRIOR TO DIO.....177

FIGURE 5.13 – BODY WEIGHT THROUGHOUT THE DURATION OF HFD-INDUCED DIO STUDY. 179
FIGURE 5.14 – METABOLIC PARAMETERS MEASURED BY CLAMS OF EC-Γ$_1$WT-TG AND EC-Γ$_1$D316A-TG MICE AT 12 WEEKS OF HFD. 180
FIGURE 5.15 – QUANTIFICATION OF RER AND HEAT PRODUCTION DURING THE LIGHT AND DARK PERIODS. 180
FIGURE 5.16 – WET WEIGHTS OF LIVER AND ADIPOSE DEPOTS FROM 16-WEEK HFD-FED MALE MICE. 181
FIGURE 5.17 – WET WEIGHTS OF HEART, BRAIN AND SPLEEN FROM 16-WEEK HFD-FED MALE MICE. 181
FIGURE 5.18 – HISTOLOGICAL ANALYSIS OF HAEMATOXYLIN-STAINED IWAT SECTIONS FROM 16-WEEK HFD-FED MALE MICE. 182
FIGURE 5.19 – HISTOLOGICAL ANALYSIS OF HAEMATOXYLIN AND EOSIN (H&E)-STAINED LIVER SECTIONS FROM 16-WEEK HFD-FED MALE MICE. 183
FIGURE 5.20 – MAGNIFICATION 100X OF LIVERS FROM 16-WEEK HFD-FED EC-Γ$_1$WT-TG AND EC-Γ$_1$D316A-TG MALE MICE. 183
FIGURE 5.21 – COMPARISON OF BODY WEIGHTS FOR THE C57BL/6J STRAIN ON CHOW VERSUS TIE2-CRE ECΓ$_1$WT-TG AND D316A-TG FEMALES ON HFD. 191
FIGURE 8.1 – IMAGES OF ORGANS FROM EC-Γ$_1$WT-TG AND EC-Γ$_1$D316A-TG 3-MONTH-OLD MALE MICE. 225
FIGURE 8.2 - O_2 DOSE RESPONSE (1 HOUR) WITH BI-9774 RAW IMAGES 226
FIGURE 8.3 – TIME COURSE (21% VERSUS 3% O_2) RAW IMAGES WITH PHOSPHO-AMPKA^{T172}, AMPKA AND A-TUBULIN. 227
FIGURE 8.4 – TIME COURSE (21% VERSUS 3% O_2) RAW IMAGES WITH PHOSPHO-ACCS^{79} AND ACC. 228
FIGURE 8.5 – HYPOXIA/REOXYGENATION EXPERIMENT RAW IMAGES 229
FIGURE 8.6 – NAF AND BI-9774 TREATMENT UNDER NORMOXIA (21% O_2) AND HYPOXIA (3% O_2) RAW IMAGES. 230
FIGURE 8.7 – NAF AND BI-9774 TREATMENT UNDER NORMOXIA (21% O_2) AND HYPOXIA (3% O_2) RAW IMAGES. 231

List of Tables

TABLE 1.1 – SUMMARY OF KEY STUDIES ON THE EFFECT OF AMPK ON THE VASCULAR ENDOTHELIUM. 48
TABLE 1.2 – K_M VALUES OF O_2 PROVIDED FOR PHD AND FIH1 IN VITRO. 52
TABLE 1.3 – SUMMARY OF ALL PROCESSES AND TARGETS REGULATED BY HIFA ISOFORMS. 56
TABLE 2.1 – LIST OF RT-QPCR PRIMERS. 64
TABLE 2.2 – LIST OF ANTIBODIES USED IN THIS STUDY. 65
TABLE 2.3 – LIST OF PLASMIDS USED. 66
TABLE 2.4 – LIST OF GENSCRIPT PLASMIDS USED FOR HIF-1A MUTAGENESIS STUDIES. 67
TABLE 2.5 – DETAILS OF MEDIA CONDITIONS USED FOR EXPERIMENTS. 68
TABLE 2.6 – LIST OF PROTEIN SEQUENCES USED FOR MSA ACCORDING TO THEIR NCBI REFSEQ ACCESSION IDS. 72
TABLE 2.7 – IN VITRO KINASE PREPARATIONS FOR LC/MS^2. 78
TABLE 2.8 – LIST OF MOUSE STRAINS USED IN THIS STUDY. 86
TABLE 2.9 – PRIMER SEQUENCES USED FOR GENOTYPING. 88
TABLE 8.1 – IPA FUNCTIONS ANNOTATIONS FOR COMMON DOWNREGULATED DEGS. 221
TABLE 8.2 – IPA DISEASE FUNCTIONS FOR COMMON DOWNREGULATED DEGS. 222
TABLE 8.3 – SPECTRONAUT ANALYSIS ON PUTATIVE KINASES FOR THE IDENTIFIED HIF-1A PHOSPHOSITES. 224

Abbreviations

A list of commonly used abbreviations within this thesis has been outlined below.

ACh	Acetylcholine
ADaM	Allosteric drug and metabolite binding (ADaM) site
ADP	Adenosine diphosphate
ADSC	Adipose-derived stem cells
AICAR	5-aminoimidazole-4-carboxamide ribonucleoside
AMP	Adenosine monophosphate
AMPK	AMP-activated protein kinase
Ang-II	Angiotensin II
ANOVA	Analysis of variance
ATP	Adenosine triphosphate
BAT	Brown adipose tissue
bHLH	Basic helix-loop-helix domain
BM	Basement membrane
Ca^{2+}	Calcium (II) ions
CAD	Coronary artery disease
CAMKK2	Ca^{2+}/calmodulin-dependent protein kinase kinase 2 (CAMKK2)
CI	Complex I, type I NADH dehydrogenase
CII	Complex II, succinate dehydrogenase
CIII	Complex III, coenzyme Q:cytochrome c – oxidoreductase
CIV	Complex IV, cytochrome c oxidase
CLAMS	Comprehensive Lab Animal Monitoring System
CPT1a	Carnitine palmitoyl-transferase 1
CV	Complex V, ATP synthase
CVD	Cardiovascular disease
DIO	Diet-induced obesity
DLL4	Delta-like canonical NOTCH ligand 4
ECAR	Extracellular acidification rate
ECFCs	Endothelial colony forming cells
ECM	Extracellular matrix
ECs	Endothelial cells
eEF2	Eukaryotic elongation factor-2
eEF2K	Eukaryotic elongation factor-2 kinase
eNOS	Endothelial nitric oxide synthase
EPO	Erythropoietin
FAO	Fatty acid oxidation
FBS	Foetal bovine serum
FCCP	Carbonyl cyanide-p-trifluoromethoxyphenylhydrazone
Fe^{2+}	Iron (II) ion
FIH1	Factor-inhibiting HIF-1α 1
GO	Gene Ontology
HAECs	Human aortic endothelial cells
HBSS	Hanks Buffered Saline Solution
HEK293T	Human embryonic kidney 293 T
HFD	High fat diet
HIF-1α	Hypoxia inducible factor 1 alpha
HIF-1β	Hypoxia inducible factor 1 beta

HIF-2α	Hypoxia inducible factor 2 alpha
HIF-3α	Hypoxia inducible factor 3 alpha
HRE	Hypoxia response element
HUVECs	Human umbilical vein endothelial cells
IPA	Ingenuity Pathway Analysis
IRE	Iron response element
KLF2	Krüppel-like factor 2
KLF4	Krüppel-like factor 4
LKB1	Liver kinase B1
LSEC	Liver sinusoidal endothelial cells
LSS	Laminar shear stress
MEFs	Mouse embryonic fibroblasts
Mg^{2+}	Magnesium (II) ion
MI	Myocardial Infarction
mTOR	Mechanistic target of rapamycin
NAFLD	Non-alcoholic fatty liver disease
NASH	Non-alcoholic steatohepatitis
NO	Nitric oxide
NRP	Neuropilin
OCR	Oxygen consumption rate
OSS	Oscillatory shear stress
OXPHOS	Oxidative Phosphorylation
PAD	Peripheral artery disease
PAH	Pulmonary arterial hypertension
PAS	Per-Arnt-Sim domain
PBS	Phosphate Buffered Saline
PCA	Principal Component Analysis
PHD	Prolyl hydroxylases
PKA	Protein kinase A
PKC	Protein kinase C
PLA	Proximity ligation assay
RER	Respiratory exchange ratio
ROS	Reactive oxygen species
SERCA1	Sarcoplasmic/endoplasmic reticulum calcium ATPase 1
SMART	Skeletal muscle-like AMPK reprogrammed thermogenic (SMART) adipocytes
T2DM	Diabetes mellitus, type 2
TCA	Tricarboxylic acid (TCA cycle)
TMRM	Tetramethylrhodamine methyl ester
VEGF	Vascular endothelial growth factor
VEGFR	VEGF receptor
VSMCs	Vascular smooth muscle cells
WAT	White adipose tissue

1. Chapter 1 – Introduction

The endothelium constitutes a monolayer of endothelial cells (ECs) that line the inner lumen of the blood vessels, covering a surface area of approximately ~7000 m^2 in humans [1]. Originally assumed to be a metabolically inert cellular barrier, formative studies by Furchgott and Zawadzki in 1980 demonstrated the role of ECs in the regulation of arterial smooth muscle vasorelaxation in response to acetylcholine [2]. The diverse niches occupied by ECs differ in terms of haemodynamic forces, oxygen tension, metabolites, paracrine factors and the surrounding glycocalyx means that ECs retain a great degree of phenotypic plasticity [3]. As a result, ECs constitute a highly heterogeneous and dynamic population of cells depending on organotypic and angiogenic origins. Owing to their remarkable heterogeneity, ECs are paramount to vascular homeostasis, regulating physiological processes both on a local and systemic level. The function of the endothelium spans from facilitating delivery of oxygen and nutrients, regulation of vascular tone, mechanosensing, lipid and cholesterol metabolism, production of paracrine signals, inflammation, immunity and haemostasis, which will be discussed in depth later [1]. Disturbances in endothelial function exert profound systemic effects, being implicated in the pathophysiology of atherosclerosis, pulmonary disorders, ischaemic heart disease (IHD), obesity, diabetes, non-alcoholic fatty liver disease (NAFLD) and autoimmune diseases.

1.1 Development of the Vascular System

The vascular system is amongst the first to emerge during development, a critical event in facilitating the subsequent development of other organ systems. ECs arise from a mesodermal progenitor population known as haemangioblasts, that form aggregates in the early embryo known as ‘blood islands’. Haemangioblasts give rise to two population of cells: haematopoietic stem cells (HSCs) and ECs. ECs rapidly proliferate and expand, coalescing to form the primitive vascular plexus. Once formed, remodelling and specialization of the vascular plexus occurs in a process known as vasculogenesis, involving coordination of endothelial proliferation, migration and recruitment of vascular smooth muscle cells (VSMCs) and pericytes. As the vascular plexus matures, ECs undergo arterial-venous specification to form the arterial and venous circulation. Several signal transduction pathways are implicated in this process including vascular endothelial growth factor (VEGF), Hedgehog, Wnt/β-catenin and Notch pathways [4-6]. Active VEGF and Notch signalling upregulates expression of the arterial specific genes, to promote arterial identity whilst suppressing venous specification [6]. Venous identity is induced upon expression of chicken ovalbumin upstream promoter-transcription

factor 2 (COUP-TF II) [7]. A subset of cells from the cardinal vein, adopt a lymphatic identity due to co-expression of COUP-TF II, SRY-Box Transcription Factor 18 (SOX18) and Prospero homeobox 1 (PROX1) expression and initiating lymphangiogenesis [8-10]. Once the vasculature is established, ECs undergo specialisation whereby their phenotype is altered in terms of their structure and metabolism, allowing specialisation to accommodate the vascularisation needs of tissues and organs.

1.2 Structure and Heterogeneity of the Endothelium

Morphology of ECs varies depending on their location in the vasculature. Venous ECs are typically shorter and polygonal in appearance whereas arterial ECs are narrow, elongated and oriented in the direction of blood flow [11]. ECs are typically flat with varying cell thickness ranging from less than 0.1 μm in capillary and venous ECs increasing to 1 μm in arterial ECs [11]. Quiescent by nature, ECs undergo contact-inhibition and do not actively proliferate their cellular turnover is estimated to be between 1-3 years, except for uterine and corpus luteum ECs which maintain a proliferative phenotype [11, 12].

As ECs occupy distinct vascular niches depending on the organ and/or tissue, they adapt their morphology to suit the needs of the organ. A variation in capillary ECs are the characteristics of their intracellular junctions e.g., continuous, discontinuous and fenestrated. Continuous ECs are connected by tight junctions, with the monolayer possessing an uninterrupted basal lamina. This type of endothelium is found in large blood vessels and in the capillary beds of the brain, lungs, intestines, adipose depots and the heart. The blood-brain barrier (BBB) endothelium is tightly regulated by high expression of transcytosis receptors, tight junction proteins and efflux transporters, preventing the passage of pathogens and drugs [13]. Fenestrated ECs possess pores that span the apical-basal axis of the ECs, known as fenestrae, but still possess an intact basal lamina, allowing water and solutes without active transport but limiting transport of plasma proteins. Fenestrated endothelium line the glomeruli of the renal cortex and tubuli of the medulla, permitting ultrafiltration of blood plasma and solute exchange and/or water resorption, respectively [13]. Discontinuous endothelium is characterised by large intracellular gaps along with a disjointed basement membrane known as sieve plates, rendering them highly permeable to plasma components. Discontinuous ECs are found in the bone marrow, spleen and the liver and contain clathrin-coated pits and scavenger receptors important for transluminal delivery and waste clearance of blood-borne products [14].

1.3 Endothelial Metabolism

The prevailing dogma in the endothelial biology field is that ECs are hypometabolic, i.e., they have low O_2 consumption and mitochondrial content (~3-5% of cell volume versus ~30% in cardiomyocytes). Despite oxidative phosphorylation (OXPHOS) yielding ~36 molecules of ATP and the proximity of ECs to oxygenated blood, up to 85% of endothelial ATP is derived from glycolysis, the process by which glucose is converted to pyruvate/lactate [15]. The glycolytic rate and glucose consumption of ECs have been reported to lie within the range observed in cancer cells [15]. Reliance on anaerobic glycolysis maybe due to protection against the formation of reactive oxygen species (ROS) whilst maximising oxygen delivery to perivascular cells [15, 16]. Endothelial glycolytic flux is controlled by two key enzymes: hexokinase 2 (HK2) and phosphofructokinase-1 (PFK1), regulating the rate-limiting steps of glycolysis. Fructose-2,6-bisphosphatase 3 (PFKFB3) converts F6P to fructose-2,6-bisphosphate (F2,6P), a potent allosteric activator of PFK1, thereby further increasing glycolytic flux (Figure 1.1). Glycolysis confers the rapid ability to generate ATP with faster kinetics, therefore increased glycolytic flux enhances EC metabolic fitness during angiogenesis. This will be discussed in depth in Section 1.6 Angiogenesis.

Recent studies in the past decade cast doubt on the dispensability of endothelial mitochondria. ECs in fact possess an extensive mitochondrial network and emerging evidence implicates mitochondrial metabolism, quality control and dynamics in dictating vascular tone, angiogenesis and permeability. Proliferating ECs are highly dependent on OXPHOS, consuming ~3 times more oxygen than quiescent, contact inhibited ECs [17]. Treatment with the benzoquinone embelin impaired neo-angiogenesis during wound healing and tumour growth. Moreover, Coutelle *et al.* (2014) revealed that Matrigel plugs injected into mitochondrial DNA (mtDNA) mutator mice had reduced vascularisation, showing that mitochondrial targeting of ECs could prove clinically useful in treating cancers [17]. Endothelia-specific ablation of specific OXPHOS components such as protoheme IX farnesyltransferase (*Cox10*) and complex III (CIII) subunit ubiquinol-cytochrome c reductase (*Qpc*) hindered retinal and tumour angiogenesis in mouse models [18, 19]. Mitochondrial metabolism confers flexibility during angiogenesis to allow them to seamlessly switch between tip and stalks cells phenotypes (See 1.6 Angiogenesis). Moreover, OXPHOS-dependent ATP production supports endothelial fatty acid uptake and transport across the vascular wall, a process potentially dysregulated in conditions like obesity and metabolic syndrome [20, 21].

The mitochondria are biosynthetic hubs in endothelial cells, producing intermediates from the tricarboxylic acid (TCA) cycle that feed into critical biosynthetic pathways e.g., *de novo*

nucleotide, lipid and amino acid synthesis [22, 23]. Despite the relatively low basal mitochondrial respiration reported in ECs, nutrients such as glucose, glutamine and other amino acids are used to replenish the TCA cycle intermediates in a process known as anaplerosis. ECs utilise the fatty acid (FA)- and anaplerotic-derived carbons from fatty acid β-oxidation (FAO) for deoxynucleotide triphosphate (dNTP) synthesis, with the highest oxidation rates observed for glutamine, glutamate and aspartate in cultured ECs [22, 24]. Carnitine palmitoyltransferase 1a (CPT1a) facilitates the transfer of long chain fatty acids (LCFAs) for FAO in the mitochondria and silencing of CPT1a reduces dNTP pools, EC proliferation and sprouting *in vivo* (Figure 1.1) [22]. It is presumed that the metabolism of quiescent (i.e., non-proliferating) ECs are hypometabolic compared to proliferating ECs yet interestingly, FAO is upregulated in quiescent ECs (>3-fold higher versus proliferating ECs) [25]. In the context of quiescent EC, TCA intermediates are diverted towards pathways supporting NADPH production and glutathione metabolism in contrast to supporting biosynthesis in proliferating ECs (Figure 1.1) [25]. Mice with deletion of endothelial CPT1a mice have increased oxidative stress, leukocyte infiltration, endothelial permeability and susceptibility in a model of dextran sodium sulphate (DSS)-induced colitis inflammatory bowel disease, demonstrating the importance of FAO in endothelial homeostasis [25]. It is clear that the role of mitochondria in endothelial function is versatile, underappreciated and increasingly highlighted by emerging studies.

It is important to underscore that both glycolysis and mitochondrial metabolism become more predominant in certain contexts, but both are critical for vascular function. The prevailing viewpoint that glycolysis is the primary bioenergetic pathway in ECs can at times be reductionist. This viewpoint is based off *in vitro* metabolic data, assumptions that low mitochondrial content equates low activity, inferences made from transcriptomics data about enzyme expression without taking into consideration of metabolic flux and enzyme activity.

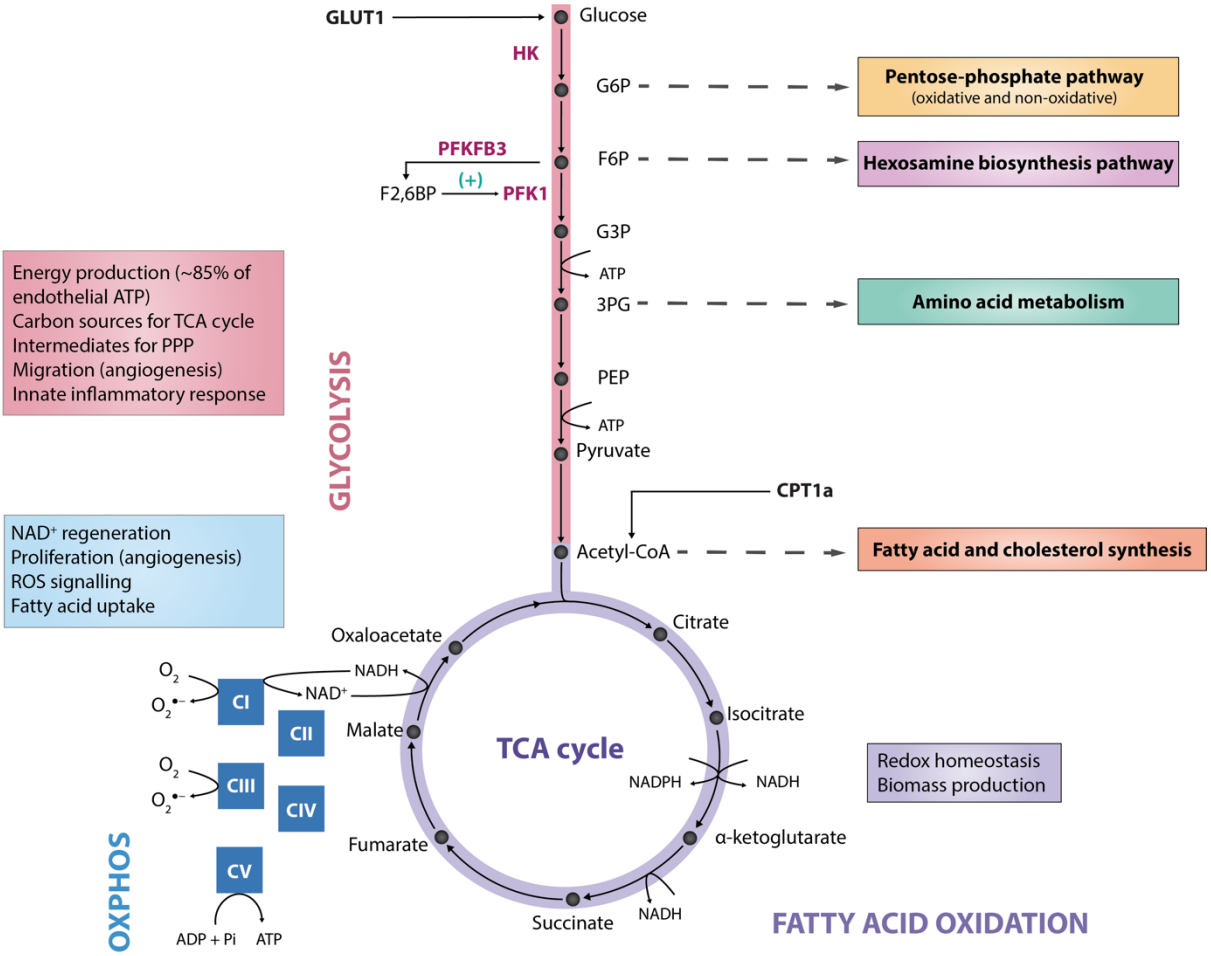


Figure 1.1 *– Summary of the main metabolic pathways required for energy production in ECs.*

ECs rely on glycolysis for basal energy production (~85% ATP production) but also to provide intermediates for other pathways such as pentose-phosphate pathway and hexosamine biosynthesis. Glycolysis is also crucial during angiogenesis, providing ATP in conditions where O_2 and/or nutrient availability is greatly reduced. The TCA cycle also provides intermediates for biomass production (e.g. nucleotide synthesis) whilst generating NADH/NADPH for redox homeostasis. Although OXPHOS activity is low in ECs, the electron transport chain is a source of ROS, which at low levels contributes to signalling processes downstream. Moreover, OXPHOS activity has been shown to be important for proliferating ECs during angiogenesis whilst mitochondrial ATP production has been implicated in fatty acid uptake in quiescent ECs. The following abbreviations are used: - 3PG: 3-phosphoglycerate, CI: complex I (type I NADH dehydrogenase), CII: complex II, (succinate dehydrogenase), CIII: complex III (coenzyme Q:cytochrome c – oxidoreductase), CIV: complex IV (cytochrome c oxidase), CPT1a: carnitine palmitoyltransferase 1A, CV: complex V (ATP synthase), F2,6BP: fructose 2,6-bisphosphate, F6P: fructose 6-phosphate, G3P: glycerol-3-phosphate, G6P: glucose 6-phosphate,HK: hexokinase, NAD(H): nicotinamide adenine dinucleotide, NADP(H): nicotinamide adenine dinucleotide phosphate, PEP: phosphoenolpyruvate, PFK1: phosphofructokinase-1, PFKFB3: fructose-2,6-biphosphatase 3, Pi: inorganic phosphate, PPP: pentose-phosphate pathway.

1.4 Mechanosensing, Shear Stress and Regulation of Vascular Tone

The primary function of blood vessels is to facilitate oxygen and nutrient exchange; therefore, mechanisms exist to adjust blood flow and vascular tone according to the needs of the local environment. Delivery of oxygenated-/nutrient-rich and -poor blood is carried out by arteries and veins, respectively; however, the exchange of oxygen, nutrients and waste metabolites is primary carried out in the microcirculation. The vessels comprising the microcirculation are: (i) capillaries forming the site of metabolite exchange; (ii) arterioles that act as resistance vessels to distribute and maintain blood flow; and (iii) venules as collection vessels to transfer blood back into the venous circulation. ECs regulate vascular tone systemically by either releasing paracrine factors or in response to exogenous vasoactive mediators that ultimately alter the contractile ability of VSMCs. The categories of vasoactive signals encompass neurotransmitters (e.g., acetylcholine, ACh; serotonin), peptides (e.g., adrenomedullin, ADM), adenosine and autacoids (e.g., nitric oxide, NO; angiotensin, Ang II and eicosapentaenoic acid, EPA). The regulation of vascular tone leads to either vasodilation or vasoconstriction of blood vessels. Vasoconstrictors released by the endothelium include the prostanoid thromboxane (TXA_2) and endothelin-1 (ET-1). TXA_2 and ET-1 possess a similar mechanism of action and act on VSMCs via their cognate receptors: thromboxane receptor (TP) and ET type A (ET_A) receptor, respectively. As a result, VSMC calcium (Ca^{2+}) channels open to allow extracellular Ca^{2+} to enter cells and induce muscle contraction. ET-1 and thromboxane release are induced by factors released by activated platelets, liposaccharide (LPS), thrombin, oscillatory shear stress and hypoxia [26]. Vasodilators released by the endothelium include another prostanoid, prostacyclin (PGI_2), produced from the same precursor as TXA_2 and the elusive endothelium-derived hyperpolarising factor (EDHF), both of which lie beyond the scope of this thesis [27].

One of the most important vasodilators produced by ECs is NO, produced from $_L$-arginine by the enzyme endothelial nitric oxide synthase (eNOS). The enzyme belongs to the family haem-containing oxidoreductases and exists in a ‘coupled’ homodimeric state. NO synthesis is initiated when $_L$-arginine is converted to N-hydroxy-l-arginine (NOHA), which is subsequently metabolised to form $_L$-citrulline and NO by eNOS [28]. This reaction requires tetrahydrobiopterin (BH4) and NADPH as cofactors for enzymatic activity [28]. In the endothelium, eNOS is bound to the protein caveolin and maintained in an inactive state in plasma membrane invaginations known as caveolae [27]. Intracellular Ca^{2+} mobilisation from the endoplasmic reticulum causes eNOS to dissociate from caveolin-1. Ca^{2+} also binds to calmodulin, inducing a conformational change that facilitates binding to eNOS to enhance its enzymatic activity [26, 28]. NO production by eNOS is also regulated by phosphorylation.

Stimulatory phosphorylation sites include Y81, S615, S633 and S1177 whereas phosphorylation on residues S114, T495 and Y657 inhibit enzyme activity based on *in vitro* studies [27]. Upstream kinases that have been implicated in stimulating eNOS activity include Akt, protein kinase A (PKA) and AMP-activated protein kinase (AMPK) [27, 29]. Despite the evidence for eNOS regulation by phosphorylation, the only phosphorylation site validated *in vivo* is the S1177 murine analogue S1176. In a mouse model of atherosclerosis, apolipoprotein E (ApoE)- and Akt1-deficient $eNOS^{S1176A}$ knock in mice reportedly displayed exacerbated aortic lesions, increased monocyte infiltration and lipid deposition in the aortic root (pre-print) [30]. Uncoupling eNOS to its constituent monomers and impaired NO production are hallmark features of endothelial dysfunction, a phenomenon observed in numerous inflammatory and cardiometabolic diseases [29].

ECs are exposed to a complex mechanical environment *in situ*, dependent on frictional forces exerted on the luminal surface by the flow of blood. The difference in the forces of the moving blood and the inert vessel wall leads to a stress induced in parallel to the endothelial surface, a phenomenon known as shear stress. The vessel wall also experiences circumferential tensile stress due to blood pressure, causing circumferential stretching of the vessel wall [31]. Endothelial mechanotransduction employs a diverse classes of cell surface molecules such as vascular endothelial growth factor receptor 2 (VEGFR2), adhesion molecules e.g., platelet endothelial cell adhesion molecule 1 (PECAM-1/CD31) and VE-cadherin (CD144) and tight junction proteins e.g., connexins and zonula occludens [32]. Plasma membrane microdomains and extensions, such as caveolae and cilia, can sense and transmit mechanical cues to the actin cytoskeleton, glycocalyx and extracellular matrix (ECM) [33]. Tzima *et al* demonstrated the role for a multimeric mechanosensory complex comprised of PECAM-1, which transmits mechanical force via VE-cadherin, functioning as an adaptor protein, to VEGFR2 to initiate the PI3K/Akt signalling pathway [34].

Laminar shear stress (LSS) occurs due to pulsatile changes in the cardiac cycle i.e., when blood is ejected into the aorta and pulmonary artery from the ventricles. LSS is critical in conferring an atheroprotective, anticoagulant and anti-inflammatory endothelial phenotype [35]. LSS tends to occur in the laminar regions of the aorta (e.g., thoracic aorta, TA) and most blood vessels greater than >0.5 mm in diameter in humans [31]. Certain capillary beds, however, divert away from this phenomenon e.g., glomerular capillaries. Shear stress enhances endothelial function by increasing NO production and upregulating expression of genes involved in inflammation resolution, cell cycle arrest and antioxidant systems to maintain arterial homeostasis [35]. A body of evidence implicates key transcription factors

including Krüppel-like factor 2 (KLF2), Krüppel-like factor 4 (KLF4) and nuclear factor erythroid 2–related factor 2 (NRF2) in maintaining EC quiescence [36].

LSS is also an important initiator stimulus in vascular remodelling, particularly during angiogenesis and arteriogenesis in the developing vasculature [35]. Arteriogenesis can occur in the adult, for example the occlusion of major arteries results in a steep gradient between the high-pressure pre-occlusion and the low-pressure areas post-occlusion areas, to trigger formation of natural bypass vessels known as collaterals [37-40]. Angiogenesis and arteriogenesis will be discussed in Section 1.6 Angiogenesis. In areas of low LSS or oscillatory shear stress (OSS), ECs are primed towards an atheroprone, pro-inflammatory and pro-thrombotic phenotype [41, 42]. Exposure to disturbed flow increases EC proliferation and enhanced pro-inflammatory nuclear factor kappa-light-chain-enhancer of activated B cells (NFκB), unfolded protein response (UPR) signalling and increased ROS production [41, 43, 44]. OSS tends to occur at bifurcations (e.g., carotid arteries) and high curvature regions of the vascular tree (e.g., the aortic arch), hence why these regions are susceptible to plaque formation and atherosclerosis [35].

1.5 Modulation of Inflammation and Haemostasis

At the interface between the vessel wall, ECs are perpetually in contact with circulating blood cells participating in immune and thrombotic responses. Despite this interaction, intrinsic mechanisms within the endothelium protect the vascular wall from untimely immune cell activation, infiltration and extravasation into the underlying tissue parenchyma, thereby preventing blood vessel lesions and atherosclerosis development [45]. There is increasing appreciation for the role of ECs in immune cell mobilisation, immune tolerance, autoimmunity and vascular inflammation [46]. During inflammation, ECs shift towards a pro-inflammatory, pro-thrombotic phenotype in a phenomenon known as endothelial activation. EC activation occurs as part of the innate immune response, as a result of exposure to pro-inflammatory cytokines [e.g., tumour necrosis factor alpha (TNFα) and interleukin 1-beta (IL-1β) and 6 (IL-6)], pathogen-associated molecular patterns, PAMPs (e.g., liposaccharide) and damage-associated molecular patterns, DAMPs (e.g., extracellular nuclear and/or mitochondrial DNA) [45, 47]. Critical signalling pathways in ECs that participate in the innate immune response include: (i) NF-κB; (ii) triggering receptor expressed on myeloid cells-1 (TREM1); (iii) high-mobility group protein 1 (HMGB1) and (iv) interferon (IFN α/β/γ) pathways [48]. NF-κB is the canonical innate immunity pathway, activated by cytokines, PAMPs and DAMPs. TREM1 and HMGB1 contribute to the amplification of toll-like receptor (TLR) signalling with HMGB1 itself

behaving as a DAMP [49]. Release of HMGB1 from immune cells and TLR engagement on ECs initiates the innate immune response.

Activated ECs increase their affinity for immune cells to facilitate their recruitment. Leukocyte activation and mobilisation at sites of injury perturbs the endothelial barrier [45]. In response to inflammatory cytokines, activated ECs subsequently upregulate expression of adhesion molecules like selectins (E- and P-), intercellular adhesion molecule 1 (ICAM-1) and vascular cell adhesion molecule 1 (VCAM-1) and chemokines [(e.g., monocyte chemoattractant protein-1 (MCP-1)] [45, 50]. Carbohydrate ligands on circulating leukocytes form transitory bonds with adhesion molecules, causing them to slow down and roll on the endothelial surface [51]. Chemokine release from rolling leukocytes induces integrin receptors to shift from a low-affinity to a high-affinity state, binding their cognate ligands present on ECs to immobilise leukocytes [51]. Evolutionary studies suggest that ECs and immune cells shared a common lineage in invertebrates (haemocytes) which expanded and diverged in vertebrates [52]. Subpopulations of ECs [e.g., liver sinusoidal endothelial cells (LSECs)] still possess the ability to scavenge and phagocytose, complementing the functions of macrophages [53, 54]. ECs can also participate in the adaptive immune response, interacting with lymphocytes via expression of co-stimulatory and co-inhibitory receptors and inducing apoptosis through the FasR death receptor ligand: FASL. Endothelial regulation of adaptive immunity lies beyond the scope of this thesis but has been reviewed elsewhere extensively [46].

ECs synthesise and express a wide repertoire of molecules to regulate platelet aggregation, the coagulation system and fibrinolysis. Maintenance of the anti-thrombotic surface is conferred by the expression of heparin sulphate (HS), an anti-coagulant proteoglycan, and tissue factor pathway inhibitor (TFPI) , a key regulator of coagulation. TFPI complexes with and inhibits coagulation Factor Xa factor. The TFPI/Factor Xa complex subsequently inhibits factor VIIa/tissue factor (TF) complex [55, 56]. Laminar shear stress induces expression of thrombomodulin, a membrane protein that enhances the anticoagulant protein C pathway to maintain blood fluidity [57]. Upon injury, ECs will express von Willebrand factor (vWF) on exposed collagen fibrils in the underlying extracellular matrix (ECM) [56, 58]. vWF facilitates adhesion of circulating platelets by binding to the glycoprotein Ib-IX-V receptor expressed on the platelet membrane. The binding of vWF to the glycoprotein Ib-IX-V receptor leading to platelet activation [56]. Platelets subsequently release α-granules containing cytokines, growth factors, fibrinogen, and coagulation factors to promote clot formation at the site of injury and facilitate blood vessel repair [56].

1.6 Angiogenesis

1.6.1 Sprouting Angiogenesis

During mammalian development, simple diffusion of oxygen and nutrients can no longer serve the exponential growth and bioenergetic demands of the embryo, necessitating the need for a circulatory system. A sequence of events encompassing tight spatiotemporal regulation of angioblast and endothelial proliferation, differentiation, migration, matrix adhesion and juxtracrine signalling underlies vasculogenesis [59]. Vessel outgrowth and expansion by sprouting angiogenesis (SA) is a pivotal event during development and in regenerative responses in adulthood (e.g. wound healing). However, SA can also be dysregulated in pathological conditions, for example during chronic inflammation (e.g. in the rheumatoid joint) or in cancer metastasis. Angiogenesis proceeds through the following steps (i) degradation of the basement membrane and sprouting formation (ii) sprout elongation (iii) sprout anastomosis (v) vessel remodelling and restoration of endothelial quiescence (Figure 1.2) [60].

ECs are held in a monolayer through a combination of mural cells (e.g. VSMCs in large vessels and pericytes in capillaries) and the ECM, comprised of the basement membrane and the interstitial matrix. Nutrient- and/or O_2-deprived tissues release mitogenic growth factors e.g. VEGF. Release of mitogenic factors also occurs during wound healing responses, where infiltrating immune cells at the lesion site secrete VEGF to initiate endothelial repair processes. The proangiogenic milieu establishes a VEGF gradient, triggering quiescent ECs to become activated and adopt an invasive phenotype. ECs begin to release tissue proteases such as matrix metalloproteases (MMPs) and plasminogen activator inhibitor 1 (PAI-1) into the local environment, resulting in detachment of the mural cells and degradation of the basement membrane (Figure 1.2A) [60]. Proteolytic breakdown of the ECM by plasmin and MMPs liberates the bioactive forms of angiogenic factors from their anchorage sites in the basement membrane and the interstitial matrix [61]. Antiangiogenic ‘matrikines’ are generated from ECM components, such as collagen and fibronectin, to regulate branching whilst suppressing inappropriate sprouting [62, 63]. Proteolysis also exposes cryptic peptides buried within ECM components, known as ‘matricryptic sites’, that interact with surface receptors on ECs, exerting huge influence on endothelial behaviour and cell-cell interactions [63-66].

The binding of VEGF to its cognate receptor VEGFR2 on the EC plasma membrane, activates a myriad of signalling cascades to promote (i) proliferation (RAF/MEK/ERK pathway); (ii)

survival (PI3K/AKT pathway); and (iii) actin remodelling and migration [focal adhesion kinase (FAK)/paxillin and p38 MAPK pathways] [67]. Tip cells are highly polarised, possessing both lamellipodia and multiple filopodia that dynamically extend and retract into the environment to regulate vessel guidance and branching through attractive and repulsive cues (Figure 1.2B & Figure 1.3) [68]. The protrusions of tip cells can sense VEGF, nutrient and O_2 availability, enabling them to extend into hypoxic tissues for revascularisation [69, 70]. It is often incorrectly presumed that ECs participating in angiogenesis are all actively undergoing proliferation; in fact, tip cells reside in the resting phase of the cell cycle (G_0) as it enhances their motility based on *in vitro* observations (Figure 1.3) [71, 72]. In stark contrast to tip cells, stalk cells do not possess many filopodia and are highly proliferative, to support lumen expansion and sprout outgrowth. Stalk cells ensure: (i) alignment and elongation of the vessel lumen (ii) deposition of the basement membrane and (iii) expression of tight and adherens junctions to stabilise the nascent vessel (Figure 1.2D) [70].

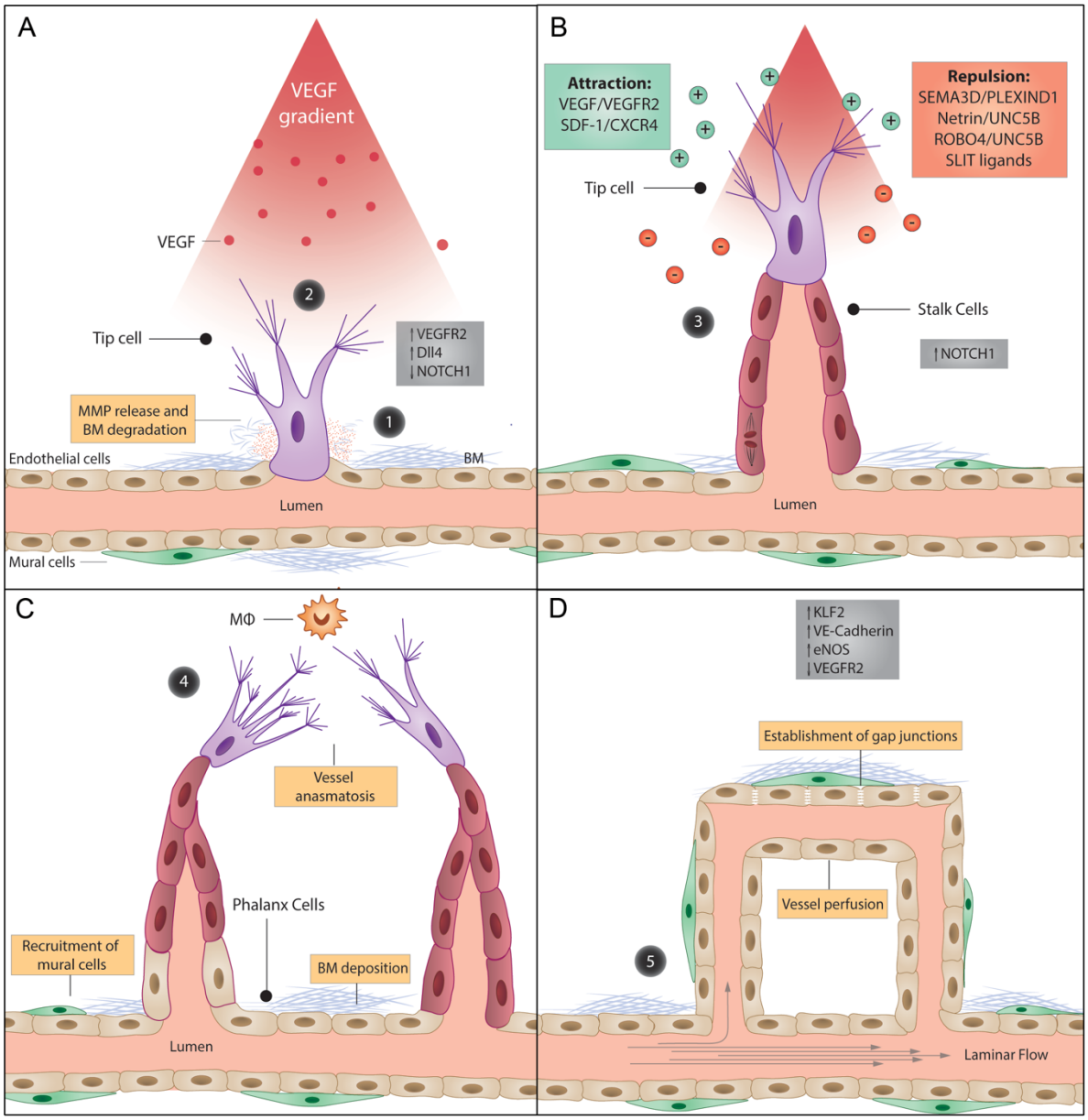


Figure 1.2 *– A schematic providing an overview of the key steps in sprouting angiogenesis.*

Sprouting angiogenesis occurs in the following steps: (A) Degradation of the basement membrane (1) and activation of ECs by VEGF, which is released by hypoxic and ischaemic tissues. VEGF induces the expression of VEGFR2 and Dll4 in ECs to initiate sprout formation (2). (B) The nascent sprout is led by tip cells, characterised by their high motility and the presence of numerous filopodia, enabling them to be highly responsive to environmental cues. Filopodia play a critical role in facilitating the sprout towards the VEGF source as determined by a repertoire of attractive and repulsive guidance (3). Tip cells orchestrate quiescent ECs to transform into stalk cells, highly proliferative ECs that form the lumen of the nascent blood vessel. (C) Eventually two sprouts are guided towards one another, fusing the sprouts in a process known as vessel anastomoses (4). Stalk cells also deposit basement membrane and recruit mural cells (e.g. pericytes and/or vascular smooth muscle cells) to stabilising the vessel. The nascent blood vessel is lined by phalanx cells, quiescent ECs that mechanically strengthen the blood vessel through expression of gap junction proteins in response to laminar shear stress, aiding in the remodelling and normalization of the nascent blood vessel. Figure generated using Adobe Illustrator.

Reciprocal crosstalk between NOTCH and VEGFR signalling in ECs specifies which phenotype adopted by angiogenic cells. [68]. Tip cells are dependent on the VEGF gradient for orientation whereas the proliferative capacity of stalk cells depend on VEGF concentration. ECs with the highest VEGFR2 signalling upregulate expression of the NOTCH ligand delta-like notch ligand 4 (Dll4), enabling them to transform into tip cells [70]. The Dll4 on the surface of tip cells activates NOTCH1 receptor, inducing neighbouring cells to transform into stalk cells through suppression of VEGFR2. NOTCH1 also induces expression of VEGFR1, a VEGF trap, to facilitate vessel guidance as the lumen elongates and to limit inappropriate induction of tip cells [73]. The intricate negative feedback loop generated by NOTCH and VEGFR signalling pathways ensures a stable arrangement of tip and stalk cells in the developing vasculature (Figure 1.3) [74]. It should be noted that tip and stalk cells are phenotypically plastic as opposed to a fixed identity, enabling them to interchange between both identities, depending on local NOTCH and VEGFR signalling. Exposure to VEGF at the angiogenic front alters Dll4 expression, thus influencing phenotype. ECs with either accelerated or persistently high levels of Dll4 have a selective advantage to differentiate into tip cells, as they robustly suppress VEGF sensitivity in neighbouring cells through activation of NOTCH1 and VEGFR1 signalling. The levels of Dll4, VEGFRs and NOTCH1 change as the sprout grows, thus ECs continuously oscillate between stalk and tip cell phenotypes as they compete for the lead position [70, 73]. Although the tip cell phenotype relies on Dll4 and VEGFR2 expression, it is also determined by metabolic and cellular fitness, particularly in avascular environments [73].

Patterning of the vasculature for optimal tissue perfusion is under precise control of tip cells, analogous to the role of axonal growth cones in neurogenesis, seeing as they both use similar attractive and repulsive molecular cues for guidance [75]. The molecules include the slit/roundabout (SLIT/ROBO), netrins/uncoordinated protein 5B (UNC5B), neuropilin (NRP), the semaphorin-plexin and ephrin-Eph family of ligands and receptors (Figure 1.2B) [75]. UNC5B receptor is highly enriched in tip cells and signalling activated in the presence of Netrin-1 to mediate endothelial repulsion through filopodial retraction of tip cells [76]. Repulsive cues like SLIT and semaphorins bind to ROBO receptors and NRP and/or NRP-plexin receptor complexes on ECs, triggering cytoskeletal rearrangements and subsequent repulsion away from the source (Figure 1.2B) [77-79]. Ephrins and Eph receptor tyrosine kinases are unique in the sense that they can simultaneously act as ligands and receptors, enabling bidirectional signalling resulting in repulsion or adhesion (Figure 1.2B). The ECs of the primitive dorsal aorta during the 6-12-somite stage in mice, either express EphrinB2 (arterial) or EphB4 (venous) [80, 81]. The interaction between EphrinB2 and EphB4 induces repulsion in the venous-fated cells, causing them to split away and coalesce to form the cardinal vein [81]. Collectively, these guidance signalling pathways exist as negative feedback

mechanism to avoid aberrant sprouting, ensure appropriate vessel patterning and even determine endothelial identity [76].

Activation of NOTCH1 in stalk cells results in proteolytic cleavage of the notch intracellular domain (NICD), where it forms a transcription factor complex with recombination signal binding protein for immunoglobulin kappa J region (RBPJ). The NICD/RBPJ along with mastermind-like transcriptional coactivator 1 (MAML1) drive expression of genes including cell survival/proliferation (e.g. Bcl2, c-Myc) and gap junction proteins (e.g. VE-cadherin, connexin 37) [82-85]. NICD also promotes the expression of NOTCH regulated ankyrin repeat protein (NRARP), to limit NOTCH1 signalling by enhancing degradation of NICD. NRARP subsequently upregulates Wnt/β-catenin pathway by suppressing the ubiquitination of lymphoid enhancer-binding factor 1 (LEF1). LEF1 promotes expression of target cell cycle progression (e.g. cyclin D1), increasing the proliferation rate of stalk cells. Tip cells interact with the filopodia of other tip cells and fuse in a process known as anastomosis. Anastomosis is supported by macrophages that facilitate the fusion event, establishing cell-cell junctions (e.g. VE-cadherin), recruitment of mural cells and deposition of basement membrane to stabilise the vessel (Figure 1.2C). The onset of blood flow exposes the vessel to haemodynamic forces, thereby activating flow-responsive pathways (e.g., KLF2) that are critical for vessel maintenance, particularly in large arteries and collateral vessels. Perfusion of the lumen introduces O_2 and nutrients, suppressing VEGF and other proangiogenic signalling. A third distinct endothelial phenotype emerges, termed phalanx cells due to their resemblance of Spartan military formation. Phalanx cells possess the distinct cobblestone appearance of ECs, have increased expression of gap junctions and redox proteins, which are critical to maintain appropriate barrier function and redox homeostasis (Figure 1.2D & Figure 1.3).

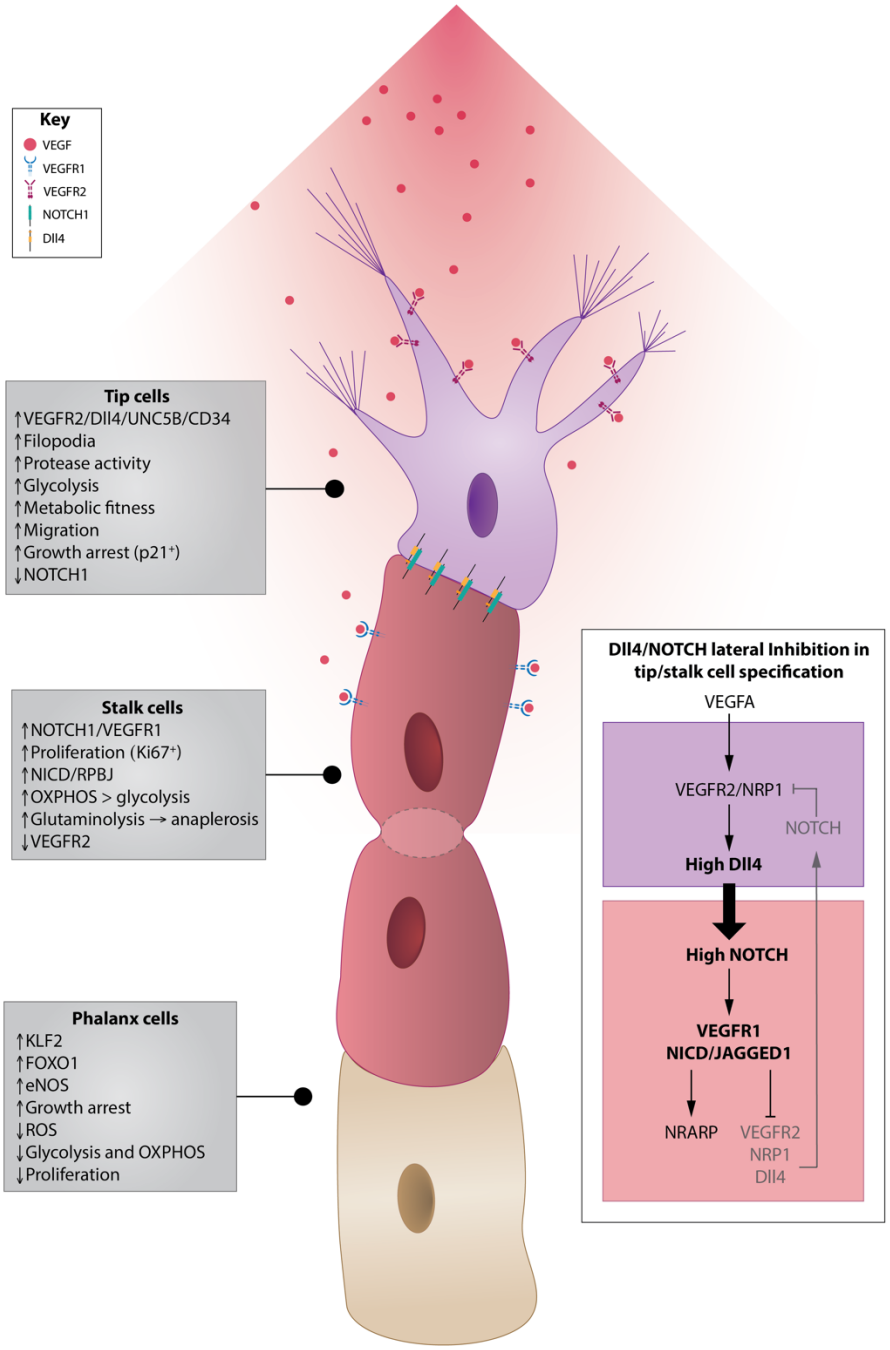


Figure 1.3 *– Schematic illustrating the features and signalling underlying the distinct endothelial phenotypes that arise during sprouting angiogenesis.*

A summary of the characteristic features of tip, stalk and phalanx cells during angiogenesis and Dll4/NOTCH1 lateral inhibition. Figure generated using Adobe Illustrator.

1.6.2 Vasculogenesis beyond Sprouting Angiogenesis

Intussusceptive angiogenesis

Intussusceptive angiogenesis (IA) refers to the remodelling of existing capillaries, characterised by transluminal pillars caused by the capillaries invaginating into the lumen and anastomose, splitting the vessel into two. The theory of intussusceptive vessel growth was first put forward by Caduff and colleagues where they discovered holes in the cast of the developing postnatal lung microvasculature by scanning electron microscopy [86]. The authors hypothesised that holes are points where the microvasculature must expand to form new capillary meshes, due to lack of capillary networks that they were not able to coalesce with in the non-parenchyma. IA plays a critical role in vascular remodelling, pruning the vasculature established by SA. In SA, distinct angiogenic phenotypes exist such as tip cells, which extend outwards into the ECM in response to growth factors and are flanked by the stalk cells. However, there is no evidence to suggest that transluminal ECs in IA exhibit either tip or stalk cell phenotypes, nor do they require a mitogenic gradient for guidance [87, 88]. Computational models suggest that the intraluminal pillars form in areas of low LSS and/or OSS [89]. In terms of kinetics, IA outpaces SA and is far more metabolically favourable as it doesn't require high rates of endothelial proliferation. Unfortunately, the current researching regarding IA is limited due to difficulties in capturing intravascular events [88].

Arteriogenesis

Collateral arteriogenesis is a process by which bypass vessels, termed collaterals, link conductance arteries after vascular occlusion [90]. Following an ischaemic or thrombotic event, collaterals arise as an adaptational response to bypass the site of occlusion and redirect blood towards the peripheral tissues. The collateral circulation is distinct from the arterial-venous and lymphatic circulation, possessing unique endothelial and smooth muscle phenotypes [90, 91]. Collateral vessels are relatively uncommon; however, anastomoses of arterial trees do occur in the human body such as: (i) the recurrent radial artery connecting the brachial and radial arteries and (ii) interconnected arteries that form the circle of Willis in the brain [90]. The underlying mechanisms of collaterogenesis are poorly understood, but it appears to parallel the mechanisms of SA. Arteriogenesis is stimulated by shear stress and requires pro-inflammatory and immune components, in stark contrast to SA, which is dependent on pro-angiogenic factors and hypoxia [92]. Nonetheless, *in vivo* studies have underscored the importance of both hypoxia inducible factors and VEGF/VEGFR signalling in

arteriogenesis, possibly requiring induction of hypoxia inducible factors in the absence of hypoxia [93, 94]. The exposure to extremely low LSS in the collateral circulation leads to endothelial activation through upregulation of MCP-1, ICAM-1 and VCAM-1. Infiltration of pro-inflammatory innate and adaptive immune cells is critical in facilitating collateral remodelling [95]. Several *in vivo* studies based on occlusion mouse models have now demonstrated that genes involved in shear stress mechanotransduction (e.g. PECAM-1, integrins and VEGFR2) and arterial specification (e.g. EphrinB2, DLL1 and NOTCH) are necessary for collateral formation [95, 96]. The presence of established coronary collaterals vessels can determine recovery after a cardiovascular event, as illustrated by a longitudinal study 10-year study conducted by Meier and colleagues. Using quantitative methods based on angiography, the authors found that patients with stable coronary artery disease (CAD) with high collateral flow index (CFI) had improved prognostic outcomes in comparison to the low CFI groups [97].

1.7 AMP-activated Protein Kinase

1.7.1 Structure, Function and Evolution of AMPK

ATP is the principal energy carrier molecule in eukaryotes, storing and releasing energy in its 'high energy' phosphoanhydride bonds which link the three phosphate groups. Removal of the terminal phosphate group forms ADP and inorganic phosphate (P_i), releasing free energy to drive other biochemical reactions. Moreover, energy can also be released through further hydrolysis of ADP, producing AMP and P_i. Energy transformations driving core cellular processes require large amounts of ATP, necessitating a cellular energy sensor to integrate and respond to changes in adenine nucleotide levels. As the master regulator of energy metabolism, AMPK is activated by AMP and/or ADP during states of energy depletion, where the cellular ATP:ADP/AMP ratio falls. AMPK preserves energy homeostasis by suppressing anabolic, ATP-consuming pathways and promoting catabolic processes to replenish ATP levels. Mounting evidence implicates AMPK far beyond its direct role in energy metabolism, including regulation of ferroptosis, DNA damage and repair, mitochondrial and lysosomal homeostasis, angiogenesis and stem cell fate [98].

AMPK is a serine/threonine kinase, existing as a heterotrimeric complex comprised of a catalytic α subunit and two regulatory subunits, β and γ. Multiple isoforms of the α (α_1/α_2), β (β_1/β_2) and γ ($\gamma_1/\gamma_2/\gamma_3$) subunits exist, encoded by *PRKAA1*/*PRKAA2*, *PRKAB1*/*PRKAB2* and *PRKAG1*/*PRKAG2*/*PRKAG3* genes, respectively. As a result, all potential combinations of subunits give rise to 12 distinct complexes *in vivo*, with the existence of alternatively spliced isoforms adding another layer of complexity [99]. The alpha subunits have a kinase domain (α-KD) comprised of two lobes, α-N- and α-C-lobes near the N-terminus. The cleft between the two lobes creates a binding site for substrates along with Mg^{2+} and ATP. Adjacent to the kinase domain lies the auto-inhibitory domain (α-AID), connected to the α-C-terminal domain (α-CTD) by an α-linker region [99]. The α-AID interacts with the α-N- and α-C-lobes, preventing phosphoryl transfer to its substrate (Figure 1.4).

A carbohydrate binding module (CBM) lies within the β subunit, suggesting a putative interaction of AMPK with glycogen granules, although there is insufficient evidence to suggest this occurs *in vivo*. The interface between the α-N-lobe and the β-CBM forms a pocket known as the allosteric drug and metabolite binding (ADaM) site, important for regulation by pharmacological agents and potentially, by a yet unknown endogenous metabolite(s) (Figure 1.4) [99-101]. Interactions between the β-C-terminal region (β-CTR) and the α and γ subunits

create a scaffold to tightly link the subunits and form the functional holoenzyme. The γ domain contains four highly conserved cystathionine-β-synthase (CBS) domains in tandem (Figure 1.4). The CBS domains form pseudo-dimeric pairs known as Bateman domains, which then associate with other CBS pairs in a head-to-head manner and produce four putative adenine nucleotide binding sites [99, 100]. A molecule of AMP is constitutively bound to CBS4 whereas CBS2 remains unoccupied. The remaining domains, CBS1 and CBS3, bind adenine nucleotides in an exchangeable manner thereby conferring the ability to sense changes in AMP levels (Figure 1.4). A fall in ATP:ADP/AMP ratio, with a concomitant increase in AMP, can arise due to nutrient deprivation, hypoxia, and mitochondrial electron transport chain (ETC) inhibitors, resulting in AMPK activation [98]. *In vivo*, AMPK activation can occur as a result of exercise, cold exposure, caloric restriction, ischaemia or drugs that inhibit mitochondrial respiration and ATP production (e.g., metformin) (Figure 1.4) [99-101].

Allosteric activation by AMP induces conformational changes throughout the structure of the AMPK holoenzyme, relieving α-AID inhibition of the kinase domain. A conserved regulatory threonine (T) residue, T172, resides within the activation loop of the α-KD and is amenable to phosphorylation by two upstream kinases: liver kinase B1 (LKB1) and Ca^{2+}/calmodulin-dependent protein kinase kinase 2 (CAMKK2) (Figure 1.4) [98]. LKB1 phosphorylates AMPK in response to energy stress, whereas CAMKK2 phosphorylates AMPK in a nucleotide-independent manner, in response to increased intracellular Ca^{2+}. AMP binding not only allosterically activates AMPK, but it also enhances LKB1-mediated T172 phosphorylation whilst suppressing T172 dephosphorylation by phosphatases, such as protein phosphatases 2Cα and 2A (PP2Cα and PP2A, respectively) [99]. Once activated, AMPK can phosphorylate a distinct subset of proteins involved in cellular metabolism, achieved through phosphorylation of proteins containing an AMPK consensus motif [102]. The optimal consensus motif comprises of hydrophobic residues (Φ) at P−5 and P+4 relative to the serine/threonine (S/T) site (P_0) with basic residues (β) at P−4 to P−3 and X denoting any residue. Motif affinity and mass spectrometry proteomic approaches have revealed that AMPK motifs contain a variation of ΦββXX(S/T)XXXΦ [100, 102]. It should be noted that consensus motifs only provide a guide owing to steric hindrance arising from the 3D structure and localisation of the substrate protein.

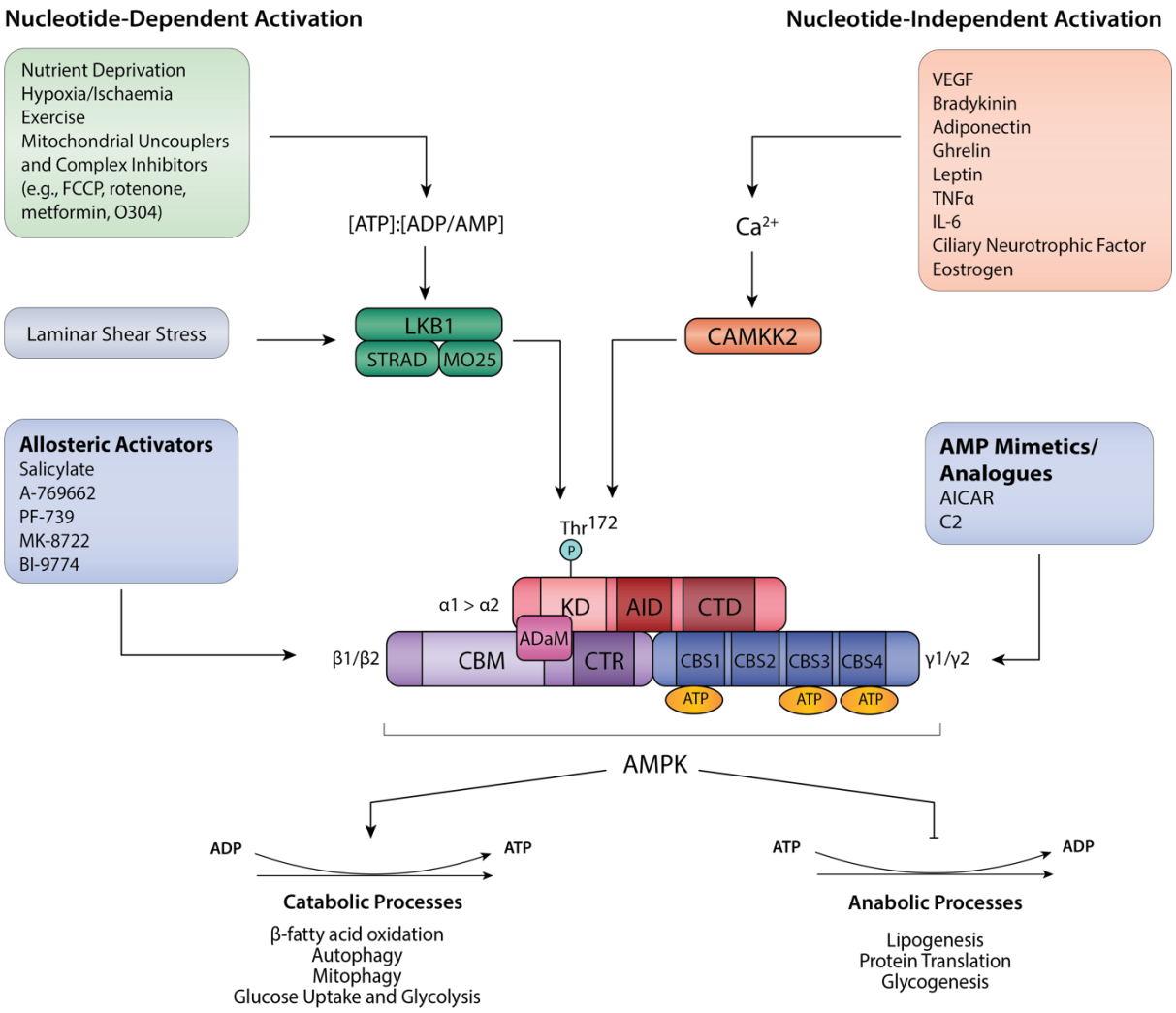


Figure 1.4 *– A schematic illustrating the composition, upstream regulation and functions of AMPK.*

The structural composition of the AMPK holoenzyme along with its known regulators including upstream kinases, physiological and pathophysiological stimuli, pharmacological agents, mitochondrial toxins and cytokines. Figure created by Adobe Illustrator. The following abbreviations are used in this figure: − ADaM: allosteric drug and metabolic binding site; AID: autoinhibitory domain; CBS: cystathionine-beta-synthase (CBS) domain; CBM: carbohydrate binding module, CTD: C-terminal domain (α subunit); CTR: C-terminal region (β subunit) and KD: kinase domain. Adapted from Herzig and Shaw, *Nature Reviews Molecular Cell Biology* (2018) [98].

AMPK is conserved amongst eukaryotes with paralogues identified in budding yeast (SNF1) and in plants (SNF1-related kinase 1) [103]. The question of whether AMPK was present in the last eukaryotic common ancestor remains to be answered. Phylogenetic data reveals that predecessors of the common kinases, including AMPK, are the oldest amongst eukaryotes with the α subunit orthologues in prokaryotes still possessing the ATP-binding motif, essential catalytic residues and the regulatory T172 residue [104]. Fungi and invertebrates have only one functional copy of the α subunit, with duplications (*PRKAA1* and *PRKAA2*) occurring in the vertebrate lineage [104]. Duplications of the β and γ subunits also occur in vertebrates, although the presence of the β subunit is restricted to eukaryotes [104]. A functional γ orthologue, MJ1225, has been identified in the archaeon *Methanocaldococcus jannaschii.*

MJ1225 possesses four CBS domains that gives rise to a similar structure to its eukaryotic counterpart based on crystallography studies [105].

1.7.2 Metabolic Functions of AMPK

AMPK activation leads to phosphorylation of over 100 proteins, exerting profound effects on glycolysis, glucose uptake, lipid metabolism, autophagy, cell growth, proliferation and mitochondrial function. Metabolic activity is reprogrammed towards increasing availability and utilisation of nutrients (e.g., glucose and lipids) to restore bioenergetic homeostasis. Acetyl-CoA is the principal intermediate metabolite in carbohydrate metabolism, lipogenesis and β-oxidation of fatty acids (FAs). Acetyl-CoA is converted into malonyl-CoA by acetyl-CoA carboxylases (ACC1/2) [106]. Acetyl-CoA can also be converted to 3-hydroxy-3-methyl-glutaryl-coenzyme A (HMG-CoA) which is itself converted to mevalonic acid by 3-hydroxy-3-methyl-glutaryl-coenzyme A reductase (HMGR). Malonyl-CoA is a key intermediate in fatty acid synthesis and mevalonic acid in cholesterol production [106]. AMPK phosphorylates both ACC1 and ACC2 at S79 and S212, respectively, and HMGR on S872 to suppress *de novo* lipogenesis and cholesterol biosynthesis (Figure 1.5) [107, 108]. The inhibitory effects of AMPK on fatty acid biosynthesis requires ACC phosphorylation, as mutations of those phosphorylation sites *in vivo* results in elevated ACC activity and hepatic lipogenesis [108]. Mice harbouring such mutations are also insensitive to the lipid lowering and insulin-sensitising effects of metformin [108].

AMPK also promotes uptake of non-esterified FAs, released from lipolysis occurring in adipose depots, by increasing expression of fatty acid translocase, CD36, at the plasma membrane of skeletal myocytes in response to pharmacological and hormonal stimuli [109, 110]. FAs are then conjugated to coenzyme A (CoA) to form palmitoyl-CoA and subsequently transported into the mitochondria by carnitine palmitoyl-transferase 1a (CPT1a) for FAO. Malonyl-CoA is a competitive inhibitor of CPT1, therefore inhibition of ACC by AMPK indirectly promotes FAO (Figure 1.5) [111]. However, evidence in contracting skeletal myotubes or cardiomyocytes and cold-activated brown adipose tissue (BAT) where FAO occurs independently of ACC phosphorylation, suggests AMPK enhances FAO through alternative mechanisms [112-114].

AMPK directly regulates carbohydrate metabolism at multiple levels from glucose uptake to glycolysis. Activation of AMPK increases glucose uptake by increasing translocation and expression of glucose transporters type 1 and/or 4 (GLUT1/4) as the latter is only expressed in skeletal muscle and adipose tissue [115]. Phosphorylation of thioredoxin interacting protein

TXNIP and RAB GTPase-activating protein (GAP) TBC1 domain family member 1 (TBC1D1), enhances translocation of GLUT1 and GLUT4 to the plasma membrane [115, 116]. AMPK activation has been shown to induce expression of HK2 in rat skeletal myocytes [117]. Glycolytic flux is enhanced by AMPK phosphorylation resulting in activation of PFKFB3, to increase levels of fructose 2,6-bisphosphate which consequently allosterically activates the rate-limiting enzyme in glycolysis 6-phosphofructokinase-1 (PFK1) [118, 119]. Glycogen production and storage is simultaneously inhibited by AMPK, through phosphorylation of glycogen synthases 1 and 2 (GYS1 and GYS2) (Figure 1.5) [120, 121].

The mechanistic target of rapamycin (mTOR) kinase lies at the crux of the intracellular signalling network coupling nutrient availability and bioenergetic status to cell growth, proliferation and survival. mTOR exists in two multiprotein complexes, mTORC1 and mTORC2, comprised of distinct subunits and regulator proteins. Activation of mTOR enhances ribosomal biogenesis, mRNA translation, lipid and nucleotide synthesis whilst suppressing autophagy. Therefore, AMPK and mTOR are interconnected in an antagonistic but complementary manner to regulate cellular energy balance. AMPK suppresses mTOR activity through phosphorylation and activation of tuberin sclerosis complex 2 (TSC2), a negative regulator of mTOR on S1387. AMPK also promotes inactivation of the mTORC1 subunit, regulatory-associated protein of mTOR (Raptor) at S792 (Figure 1.5). Eukaryotic elongation factor-2 kinase (eEF2K) inhibits protein translation by phosphorylating eukaryotic elongation factor-2 (eEF2) on T56. Phosphorylation of eEF2K by mTORC1 inhibits its activity leading to decreased phosphorylation of eEF2 and subsequent increase in protein translation. However, AMPK phosphorylation of eEF2K increases its activity leading to suppression of eEF2 to halt protein synthesis, thereby limiting ATP consumption under energy stress (Figure 1.5) [122].

Interestingly, AMPK activates mTORC2 signalling in response to acute bioenergetic stress, subsequently enhancing cell survival. The work of Kazyken *et al* demonstrate that AMPK phosphorylates mTORC2 on $mTOR^{S1261}$ both *in vitro* and *in vivo* (Figure 1.5) [123]. In contrast to mTORC1, the regulation and downstream effects of mTORC2 are not as well elucidated. In the presence of growth factors, upstream activation of mTORC2 by PI3K results in the phosphorylation of Akt on S473 [124, 125]. Substrates of mTORC2 include AGC kinases such as serum/glucocorticoid regulated kinase 1 (SGK1), protein kinase C α (PKCα) with the most defined one being Akt [126]. mTORC2-mediated activation of Akt promotes selective phosphorylation and subsequent inhibition of FOXO transcription factors to promote cell survival [124]. In addition, mTORC2 signalling also regulates metabolic homeostasis by increasing glucose uptake in brown adipose tissue (BAT) and subcutaneous adipose tissue

(scWAT), decreasing hepatic glucose production [127-129]. The regulation of mTORC2 by AMPK may in part explain the glucose-sensitising effects of AMPK activation.

Autophagy is the process whereby defunct macromolecules, components and organelles are degraded in lysosomes to their constituents e.g., lipids, amino acids and glucose. This process, regulated by mTOR signalling as discussed above, enables cells to replenish ATP levels by reutilising their constituents in other catabolic pathways. Unc-51-like autophagy activating kinase (ULK1) orchestrates the autophagy response through recruitment of autophagy-related proteins (ATGs) for phagophore maturation, autophagosome formation and subsequent fusion with lysosomes for degradation [98]. AMPK has been shown to directly phosphorylate ULK1 on S467/S555/T574/S637 to induce autophagy during nutrient starvation and metabolic stress [130] [101]. AMPK has also been shown to phosphorylate other ATG proteins such as S91/S94 on Beclin1, S791 on ATG9 and S135 on VPS34 to activate the ULK1 initiation complex and nucleation and elongation of the phagophore [131] [98].

The mitochondrial population within cells is dynamic, adjusting their structure, morphology and bioenergetics in response to environmental changes. AMPK preserves mitochondrial homeostasis by altering organelle dynamics and promoting mitochondrial turnover. Mitochondrial fission induced by nutrient starvation, involves AMPK-dependent phosphorylation of mitochondrial fission factor (MFF) and ARMC10 at S129 and S45, respectively [132]. Mitochondrial fission leading to fragmentation is required to isolate dysfunctional, damaged mitochondria from the rest of the mitochondrial network. Aided by mitochondrial dynamics proteins 49 and 51 (MID49/51) and fission mitochondrial 1 (FIS1), phosphorylated MFF recruits DRP1 to the mitochondrial surface for membrane scission. Once fission occurs, AMPK promotes degradation of defunct mitochondria by targeting it for lysosomal degradation in an ULK1-dependent manner [133, 134]. Across all studies examining genetic to pharmacological activation of AMPK, a consistent observation is increased mitochondrial content [135]. AMPK enhances mitochondrial biogenesis by upregulating expression of transcriptional co-activator and master regulator of mitochondrial biogenesis: peroxisome proliferator-activated receptor-γ co-activator 1α (PGC-1α). The issue of whether AMPK directly phosphorylates PGC-1α remains to be explored, barring one study by Jäger *et al* (2007), however evidence for direct phosphorylation is lacking [136]. Enhancing mitochondrial biogenesis serves as an important adaptation to increase the cell's capacity and resilience to cope with potential energetic stressors that it may face in the future.

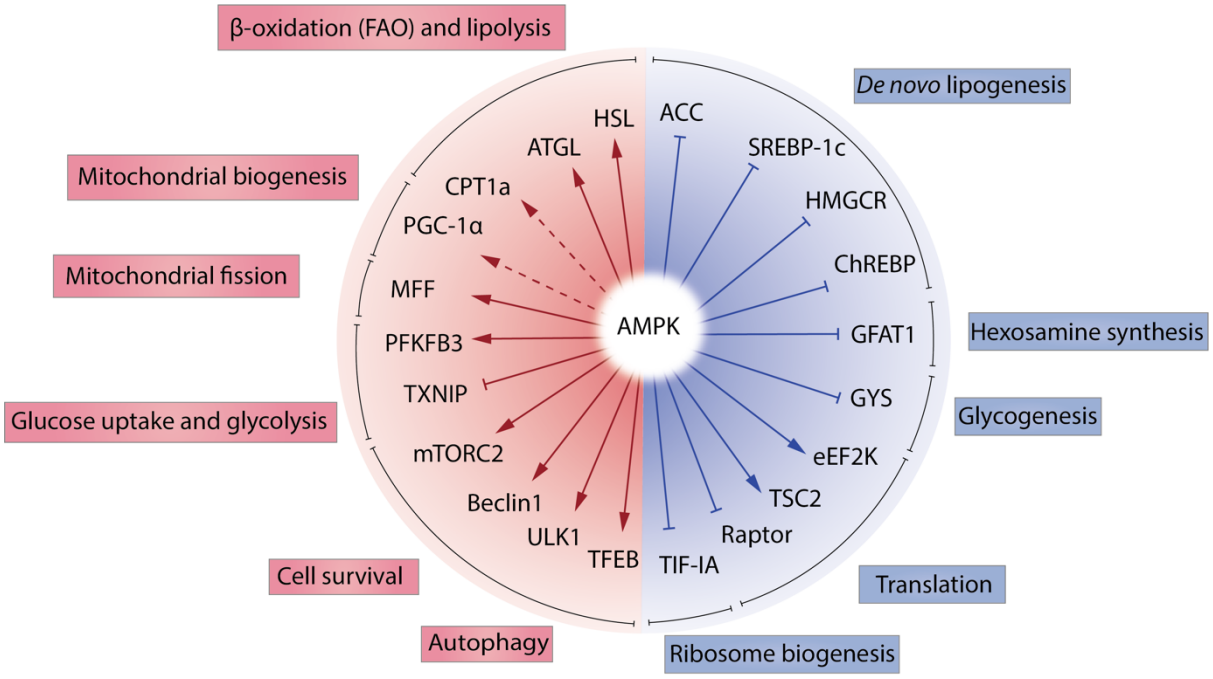


Figure 1.5 *– A schematic representing the downstream metabolic functions of AMPK.*

A summary of all the metabolic processes regulated by AMPK. Processes in red are enhanced by AMPK activation whereas those in blue are suppressed in order to restore metabolic homeostasis. Solid lines represent direct phosphorylation targets whereas dashed lines represent indirect promotion and/or suppression upon AMPK activation. Figure created in Adobe Illustrator.

1.7.3 First- and Second-Generation AMPK activators

In the Western world, the prevalence of obesity has progressively increased in the past few decades with approximately 25% of adults being obese (i.e., a body mass index (BMI) ≥30 kg/m^2). In simplistic terms, obesity results from overconsumption of calorific foods in combination with a sedentary lifestyle leading to increased fat deposition [137]. Obesity predisposes an individual to multiple comorbidities, such as T2DM, non-alcoholic fatty liver disease (NALFD), cardiovascular disease and cancer. As AMPK exerts profound effects on energy metabolism (see Figure 1.5), activation of the kinase represents a promising therapeutic strategy in the treatment of obesity.

Formative studies investigating the cellular functions of AMPK used the as a first-generation AMPK activator 5-aminoimidazole-4-carboxamide ribonucleoside (AICAR). AICAR enters cells through adenosine transporters where it is phosphorylated by adenosine kinase to generate the AICAR monophosphate (ZMP), an AMP analogue [138]. ZMP is a natural metabolite, formed during *de novo* synthesis of inosine 5′-monophosphate (IMP) by AICAR transformylase (ATIC) [139]. Treating cells with AICAR can cause ZMP to accumulate to millimolar concentrations. It is postulated that ZMP binds at CBS3 on the γ subunit to

allosterically activate AMPK in a similar fashion to AMP. AICAR has been shown to exert beneficial effects by sensitising the effects of anticancer agents like methotrexate and other anti-folate drugs [140, 141]. AICAR has been shown to increase skeletal muscle and hepatic insulin sensitivity in patients with type 2 diabetes mellitus (T2DM), providing protection against myocardial ischaemia-reperfusion injury through improving cardiac bioenergetics and regulation of the inflammatory response [142-145]. Nonetheless, AICAR has shown both poor potency and bioavailability through oral administration (< 5-10 % in plasma) as determined by comparing plasma concentrations to renal clearance levels in clinical trials [146]. Benefits of AICAR were only observed when administered intravenously, rendering it unsuitable for T2DM patients where regular injections are necessary [146]. Moreover, AICAR (ZMP) alters the activity of other AMP-dependent enzymes, for example it activates fructose-1,6-bisphosphatase and inhibits adenosine deaminase, thus raising intracellular adenosine levels [147]. Earlier observations seen with AICAR could occur independently of AMPK due to the adenosine-like effects of the drug. Further validation is also required, either by siRNA knockdown or expression of the dominant negative kinase, to confirm dependency on AMPK.

Another drug used in earlier studies to examine the biological effects of AMPK is metformin, a commonly prescribed medication for the treatment of T2DM. Metformin belongs to a class of antihyperglycemic agents known as biguanides, that were synthetically derived from the active ingredient isoamylene guanidine, found in French lilac (*Galega officinalis*) [148]. Biguanide derivatives increase insulin sensitivity and reduce hepatic glucose production, with some studies demonstrating that these effects are, at least in part, dependent on AMPK activation [148-152]. Metformin indirectly activates AMPK by inhibiting complex I of the mitochondrial ETC, thereby blocking mitochondrial ATP production and raising intracellular AMP/ADP levels which are thought to induce effects summarised in Figure 1.5. [148]. The AMPK-independent effects of metformin are thought to be mediated through inhibition of mitochondrial glycerol-3-phosphate dehydrogenase (mGPDH), increasing the cellular NADH:NAD^+ ratio. Metformin also increases the ratio of glutathione (GSH) to oxidized glutathione ratio (GSSG), to inhibit genes that encode enzymes involved in gluconeogenesis through a Let7-tet methylcytosine dioxygenase 3 (TET3)-hepatocyte nuclear factor 4α (HNF4α) pathway [153]. Indeed, Hawley *et al* demonstrated that expression of the AMP-insensitive AMPKγ2^{R531G} subunit *in vitro* renders the complexes insensitive to metformin-induced activation [154]. It should be noted that metformin can confer beneficial effects independently of AMPK as shown by studies in liver-specific AMPKα^{DKO} and LKB1^{KO} mice where metformin is still capable of inhibiting hepatic gluconeogenesis [155].

The emergence of a direct small molecule activator of AMPK, the thienopyridone A-769662, developed by Abbott Laboratories. Administration of A-769662 resulted in reduced body weight, glucose intolerance and plasma/liver triglycerides (TG) in obese rats, as expected with AMPK activation [156, 157]. Remarkably, A-769662 exhibited high specificity towards AMPK, without the need for AMPKα^{T172} phosphorylation, although it is worth noting that T172 phosphorylation is required in cells and *in vivo* [158, 159]. Another AMPK activator was identified soon afterwards, known as compound 991, being 5-10-fold more potent than A-769662 [160]. Notably, A-769662 and 991 prefer complexes where AMPKβ_1^{S108} is phosphorylated, although both can still activate AMPK at high concentrations, suggesting a shared mechanism of activation [160]. Structural resolution of the AMPK$\alpha_2\beta_1\gamma_1$ complex in the presence A-769662 and 991 show the agonists bound to a pocket formed between the α-KD and β-CBM known as the ADaM site as opposed to the CBS domains in the γ subunit [160]. Studies have also revealed that A-769662 and 991 prefer complexes containing β_1 over β_2, suggesting the possibility of isoform- and/or complex-selective drugs [159]. As a result, there have been significant advances in the development of second-generation AMPK activators with improved selectivity and bioavailability.

Currently, there are several promising candidates in the drug landscape for pan-AMPK activators with the following available at the pre-clinical or stage I clinical trials: (i) MK-8722 developed by Merck; (ii) PF-739 by Pfizer; (iii) PXL-770 by Poxel and (iv) BI-9774 by Boehringer Ingelheim [161-163]. The compounds bind to the ADaM site, to promote allosteric activation of AMPK and protect against phosphatase-mediated dephosphorylation, like its predecessors A-769662 and 991. MK-8722 has been shown to improve glucose tolerance in diet-induced obesity murine and diabetic rhesus monkey models but induced reversible cardiac glycogen accumulation and hypertrophy [164]. Regardless, the increased glycogen accumulation and hypertrophy did not appear to be causative, nor did the phenotype result in ECG abnormalities that are typically characteristic of pathological AMPKγ_2 (*PRKAG2*) gain of function mutations in Wolff-Parkinson-White (WPW) syndrome. The authors concluded that the phenotype is reminiscent of physiological cardiac hypertrophy that occur in response to endurance training [164, 165]. The Pfizer AMPK activators and their derivative, PF-739, have been shown to improve skeletal muscle-mediated glucose sensitivity in a diabetic mouse model. Another AMPK activator, PXL-770, has already debuted in Stage I clinical trials for treatment of NALFD with promising results [162]. Therefore, PXL-770 possesses great potential as a treatment for patients with T2DM, NAFLD and its advancement into non-alcoholic steatohepatitis (NASH). The latest activator, BI-9774, has already been shown to mediate glucose lowering effects in rats with T2D and hinders prostate cancer metastasis through inhibition of epithelial-to-mesenchymal transition (EMT) in a PGC-1α-dependent

manner [163, 166]. The heavy focus on these new generation activators on either primarily cardiometabolic disorders has been well characterised, although no study to date examines cardiovascular function or vascular-related disorders.

1.7.4 AMPK in the Endothelium and the Vasculature

Activation of AMPK occurs not only in response to nutrient deprivation but several extraneous signals such as LSS, exercise, ischaemia, adipokines (e.g., adiponectin and leptin), and angiogenic factors (e.g., VEGF). AMPK regulates endothelial mechanosensing, angiogenesis, resolution of inflammation, redox homeostasis, and metabolism. This section will underscore how endothelial functions are heavily dependent on metabolic reprogramming which may explain the pleiotropic effects of AMPK, given its role as a master regulator of energy metabolism. Table 1.1 summarises key studies that examine the role of AMPK in an endothelial and/or vascular context, but the general findings are summarised below.

AMPK promotes vasodilation by phosphorylation of eNOS on S1177, increasing its activity thus augmenting NO production in response to shear stress and VEGF. LSS-induced AMPK activation also upregulates the expression of KLF4. Transcriptional activation of KLF4 induces the inhibitor of cyclin-dependent kinase 1 (CDK1) inhibitor, $p21^{CIP1/WAF1}$ (*CDKN1A)* whilst simultaneously suppressing expression of cyclins D1 and B, both of which promote G_1/S and G_2/S progression, respectively. AMPK and KLF4 also act in tandem to suppress glycolysis and inflammatory pathways in response to LSS in ECs. AMPK phosphorylates glucokinase regulatory protein (GCKR) on S481, which acts to sequester hexokinase 1 (HK1) to inhibit glycolytic flux in endothelial cells. KLF4 concomitantly epigenetically modifies the promoter region of *GCKR*, resulting increased gene transactivation. *KLF4* knockdown by siRNA potentiated TNFα-induced VCAM-1 expression and glycolysis in a PFKFB3-dependent manner in human aortic endothelial cells [167].

AMPK also reprogrammes endothelial metabolism, by phosphorylating three nucleosome remodellers: DNA methyltransferase 1 (DNMT1), retinoblastoma binding protein 7 (RBBP7), and histone acetyltransferase 1 (HAT1). RBBP7 inhibits DNMT1-mediated DNA methylation, alleviating epigenetic silencing, whereas HAT1 ‘opens’ chromatin regions to facilitate gene transactivation by transcription factors. Inhibitory phosphorylation of DNMT1 on S730 by AMPK increased mRNA expression of genes involved in mitochondrial biogenesis or function such as PGC-1α (*PPARGC1A*), nuclear respiratory factors 1 and 2 (*NRF1*/*NRF2*), uncoupled protein 2 (*UCP2*) and mitochondrial transcription factor A (*TFAM)*. The increase in expression

was abrogated upon transduction with the phospho-null mutant DNMT1^{S730A}. Moreover, pharmacological or LSS-mediated AMPK activation promoted mitochondrial membrane potential ($\Delta\Psi_m$), mitochondrial biogenesis and ATP content whilst decreasing ROS production in ECs. These findings may be linked to another study by Dunn *et al* (2014) examining the epigenetic alterations occurring in response to flow, where they demonstrated that DNA hypermethylation promoted endothelial senescence. Furthermore, DNMT1 inhibition significantly improved endothelial inflammation whilst reducing the formation of atherosclerotic lesions *in vivo* [168]. The processes of inflammation, senescence and epigenetic changes converge upon metabolism, primarily the balance between OXPHOS and glycolysis, but the complexities of their cross-regulation and the involvement of AMPK remains unclear.

AMPK moderates inflammatory processes through (i) NFκB; (ii) Janus kinase (JAK) and signal transducer and activator of transcription proteins (STAT); and (iii) NLR family pyrin domain containing 3 (NLRP3) inflammasome signalling pathways [169]. Overexpression of dominant negative AMPKα_2 in TNFα-treated HUVECs resulted in increased NFκB transcriptional activity followed by E-selectin expression and monocyte adhesion. AMPKα_2 phosphorylates IkB kinase on residues S177 and S181 *in vitro*, resulting in its inactivation and of its target, NFκB [170]. Increased eNOS activity resulting from S1177 phosphorylation by AMPK suppresses NFκB signalling in cultured ECs [171]. Vascular inflammation was aggravated in cells deficient in either AMPKα_1 or α_2, with enhanced STAT1 activation in cultured human aortic VSMCs [172]. In line with this, AMPK suppresses IL-6- and IFNα-induced JAK/STAT signalling in ECs, through direct phosphorylation of JAK1 at S515/S518 *in vitro* [173]. NLRP3 inflammasome is a multi-protein complex that triggers the innate immune response, caspase-1 activation and IL-1β secretion. Thioredoxin-interacting protein (TXNIP), an α-arrestin [174]. AICAR and salicylate reduced NLRP3 and caspase-1 expression, thus reducing IL-1β secretion and restoring insulin sensitivity in palmitate-treated HUVECs to simulate Lipotoxicity [175]. AMPK exerts protective effects on the mitochondria by inhibiting ROS-induced mitochondrial fission, thereby suppressing activation of the master ER stress regulators: inositol-requiring enzyme 1α (IRE1α) and PKR-like ER kinase (PERK) [176]. Thus, AMPK may preserve endothelial function by attenuating multiple pro-inflammatory signalling in conditions characterised by overnutrition e.g., in obesity and metabolic syndrome.

Initiation of sprouting angiogenesis (SA) requires changes in metabolic state, which is facilitated by AMPK. AMPK can promote angiogenesis and/or vasculogenesis as an adaptational response to physiological metabolic stress (e.g., exercise and/or ischaemia) or pharmacological activation (e.g., metformin) [177-180]. Hypoxia, VEGF, calcitonin and adiponectin promote cell migration in an AMPK-dependent manner [181-183]. A reciprocal

relationship has been demonstrated between VEGF and AMPK, with VEGF treatment resulting in $AMPK^{T172}$ phosphorylation and AMPK upregulating VEGF expression [184, 185]. Inhibition or deficiency in AMPK activity impairs EC migration in Matrigel tube formation and plug assays [183]. Moreover, AMPK promotes the expansion of differentiation of endothelial progenitor cells (EPCs) or colony forming cells (ECFCs) mature ECs [186, 187]. Loss of AMPK in EPCs leads to a reduction of *bona fide* endothelial markers such as ICAM-1, VE-cadherin and vWF expression [186, 188]. VEGF enhances autophagy through the AMPKα/transcription factor EB (TFEB) axis [189]. Translocation of TFEB into the nucleus results in upregulation of genes involved in lysosomal biogenesis and responses to amino acid starvation [190]. TFEB is upregulated in ischaemic skeletal muscle, particularly enriching in $CD31^{+}$ cells *in vivo* whereas $TFEB^{KO}$ mice are embryonic lethal, due to impairments in placental vascularisation [191]. Moreover, blood flow perfusion is hindered in EC-$TFEB^{KO}$ mice indicating AMPK-induced activation of autophagy may be a time-restricted event to trigger angiogenesis [192]. AMPK plays a pivotal role in the formation of natural bypass vessels known as collaterals (Section 1.6 Angiogenesis). In a murine model of hind limb ischaemia (HLI), Zhu *et al* (2016) demonstrated that loss of AMPK in macrophages resulted in impaired hypoxia and inflammatory signalling corresponding to collateral formation [193]. The extent to which AMPK contributes to collateral formation in ECs requires further investigation.

Decades of work have provided understanding of the endothelial specific effects of AMPK activation (summarised in Table 1.1), however there are several limitations that should be taken into consideration. The data is often based on treatment with non-specific AMPK activators and/or on whole tissue e.g., aorta, which is composed of multiple cell types. Moreover, AMPK specificity is predominantly investigated with global knockout (KO) of either α_1 or α_2, not pan-AMPKα deficiency. This is because $\alpha_{1/2}$ double knockout mice (DKO) are embryonic lethal, although to date no one has utilised a tamoxifen-inducible model of $AMPK\alpha_{1/2}^{fl/fl}$ model. Only a handful of studies utilise endothelial-specific Cre model (e.g., Tie2-Cre and Cdh5-Cre) or the use of 2nd generation AMPK activators, therefore it is difficult to define a clear set of endothelial-specific targets and what functions they may participate in.

Author	Ref	Model System	Findings	Limitations
Response to shear stress				
Chen *et al* (2010)	[194]	LSS-/OSS-exposed human umbilical vein endothelial cells (HUVECs) Aortic regions from AMPKα$_2^{KO}$ C57BL/6† (♂) mice	Pulsatile LSS-exposed HUVECs and TA: ↑ AMPKα^{T172} phosphorylation. ↑ SIRT1 activity. ↑ eNOS^{S1177} phosphorylation. ↑ PGC-1α and Nrf2 mRNA. ↑ Mitochondrial content. Effect abolished in TAs of AMPKα$_2^{KO}$ mice. OSS-exposed HUVECs and AA lesser curvature regions: ↓ eNOS^{S1177} phosphorylation and SIRT1 expression	Whole aorta, not necessarily specific to aortic ECs. Lack of endothelial-specific knockout models employed in the study (e.g., EC-specific Cre/Flox system). AMPKα$_2$ is not the predominant isoform in ECs. Dependency on AMPKα1 not determined in study.
Han *et al* (2021)	[186]	LSS-exposed HUVECs AMPKα$_2^{KO}$ MEFs AMPKα$_2^{KO}$ C57BL/6† (♂) mice High-runner (HR) and non-selected control (NSC) C57BL/6† (♂) mice	↑ GCKR^{S481} phosphorylation by AMPK in TA compared to AA mice. ↑ KLF4-dependent GCKR expression in both LSS-exposed HUVECs and HR mice. ↓ GCKR phosphorylation in AMPKα2^{KO} MEFs. ↓ Chromatin accessibility in promoter regions of glycolytic enzymes. ↓ Glycolytic enzymes mRNA expression. ↓ HK1 enzyme activity determined by extracellular acidification rate.	AMPKα$_2$ is not the predominant isoform in ECs. Dependency on AMPKα$_1$ not determined in study. Differences in AMPKα$_1$ and α$_2$ signalling not determined in endothelial cells.
eNOS Activity and NO Production				
Davis *et al* (2006)	[195]	AICAR- or metformin-treated WT and AMPKα$_1^{KO}$ C57BL/6† (♂) mice	↑ NO bioactivity. ↑ AMPK activity under hyperglycaemic conditions *in vitro*. ↑ eNOS^{S1177} phosphorylation with metformin (50-500 μM). ↓ Responsiveness to treatment in AMPKα1^{KO} mice.	Metformin/AICAR have AMPK-independent effects.

Inflammation				
Rodriguez *et al* (2020)	[196]	Wildtype Wistar Rats Healthy segments from renal tumour patient tissues	↑ ACh-dependent vasodilation with A769662. treatment, in Wistar rats and renal tumour patients. ↑ NO production. ↓ NADPH oxidase 2 and 4 (Nox2/4)-derived ROS production.	Whole aorta, not necessarily specific to aortic ECs.
Wang *et al* (2010)	[197]	siAMPKα_2 HUVEC AMPKα_2^{KO} mouse aortic endothelial cells (MAECs**)** AMPKα_1^{KO}, LDLR^{KO}, and AMPKα_2^{KO}/LDLR^{KO} double knockout (DKO) C57BL/6† (♂) mice	↑ ROS and Nox4 activity. = No differences in body weight, serum lipids or blood glucose in AMPKα_2^{KO} mice. ↑ 26S proteasome activity. ↑ NFκB stability and nuclear RelA/p65 levels.	Lack of endothelial-specific knockout models employed in the study (e.g., EC-specific Cre/Flox system). Atherosclerosis development was not examined under obesogenic conditions in AMPKα_2^{KO}/LDLR^{KO} DKO mice (e.g., high fat/cholesterol studies).
Kroller-Schon *et al* (2019)	[198]	Angiotensin II (AngII)-treated EC AMPKα_1^{KO} C57BL/6† (♂) mice and Tie2- and Cdh5-Cre (EC)	↑ ROS production. ↑ Nox2 expression. ↑ MCP-1 mRNA expression. ↑ Leukocyte rolling and adhesion in carotid arteries. ↑ Infiltration of leukocytes, T-cells, macrophages and monocytes in aortic tissue = No effect on systolic blood pressure. ↓ NO production and ACh-induced relaxation. ↓ Induction of HO-1.	The potential effect of AMPKα_2 compensation was not investigated.
Rutherford *et al* (2016)	[173]	Cytokine-treated HUVECs treated with AICAR, A769662 or metformin/salicylate	↑ JAK1$^{S515/S518}$ inhibitory phosphorylation by AMPK. ↓ STAT3^{Tyr705} phosphorylation by JAK1. ↓ STAT1 and STAT3 activation in response to IFNα. ↓ IL-6 signalling in response to pro-inflammatory cytokines HyIL-6, LIF and OSM.	Not validated *in vivo*.

Angiogenesis and vasculogenesis				
Zibrova *et al* (2017)	[199]	HUVECs	↑ $GFAT1^{S243}$ phosphorylation with AICAR and VEGF treatment in an AMPK-dependent manner. ↑ Endothelial sprouting in GFAT-deficient cells under hyperglycaemic conditions. ↓ GFAT1 activity upon AICAR treatment. ↓ Protein *O*-GlcNAcylation in AICAR-treated HUVEC, reversed upon siAMPK$\alpha_{1/2}$ knockdown. ↓ Sprouting in $GFAT^{S243A}$ mutant HUVECs.	AICAR is a non-specific AMPK activator. Not validated *in vivo*.
Venna *et al* (2014)	[177]	Metformin-treated (50 mg/kg/day) C57BL/6N (♂) mice subjected to middle cerebral artery occlusion (MCAO)	↑ Blood vessel density in mice administered metformin 30-days post stroke. ↑ VEGF expression. ↑ Sensorimotor recovery. ↓ Glial scarring. Effect lost on AMPKα_2 KO mice	Metformin has AMPK-independent effects. AMPKα_1 KO would have been more relevant.
Stahmann *et al* (2010)	[183]	HUVECs WT and $AMPK\alpha_1^{KO}$ C57BL/6† (♂) mice	↑ ACC^{S79} phosphorylation in response to VEGF in an AMPKα_1- and AMPKα_2-dependent manner. ↑ Sprout formation (AMPKα_1 only), phenotype reversible in $AMPK\alpha_1^{KO}$ MLECs and Matrigel plugs in $AMPK\alpha_1^{KO}$ mice.	–
Wang *et al* (2017)	[187]	Human cord-blood ECFCs treated with EPO	↑ $AMPK\alpha^{T172}$ phosphorylation and AMPK-dependent KLF2 expression with EPO treatment. ↑ Matrigel tube formation in EPO-treated ECFCs, reversed with DN-AMPK.	Dependency of AMPK in determining the angiogenic capacity of ECFCs either with shRNA or CRISPR-mediated KO of AMPK subunits. AMPK function in adult peripheral blood ECFCs was not examined.

Zhu *et al* (2016)	[193]	Global and LysM-Cre (MC) $AMPK\alpha_1^{KO}$ $C57BL/6^{\dagger}$ (♂) mice	↓ Blood flow recovery in HLI model. ↓ Arteriolar remodelling. ↓ Collateral vessels. ↓ HIF-1α, VEGF, FGF2, PDGFB and TGFβ protein. ↓ NFκB-driven expression of arteriogenic factors.	Observations only in myeloid/macrophage specific KO model. Authors did not investigate the role of $AMPK\alpha_1$ in endothelium, particularly in determining arterial EC identity during collaterogenesis.
Abdel Malk *et al* (2017)	[178]	*siPRKAA2* HEK293 cells Global, Cdh5-Cre (EC), Tie2-Cre (EC) and LysM-Cre (MC) $AMPK\alpha_2^{KO}$ C57BL/6J	↑ HIF-1α hydroxylation. ↓ HIF-1α protein stability. ↓ Blood flow recovery in HLI model. ↓ Capillarisation ($CD31^+$ immunostaining) in ischemic gastrocnemius muscles (global/LysM-Cre).	Tie2-Cre and VE-Cadherin-Cre showed no differences in recovery post-HLI, but the endothelial predominant $AMPK\alpha_1$ compensation and loss was not investigated.
Yu *et al* (2016)	[200]	Streptozotocin (STZ)-induced diabetic $C57BL/6^{\dagger}$ (♂) mice: vehicle or metformin (250 mg/kg/d)	↑ Wound healing and angiogenesis in metformin-treated mice. ↑ Circulation of BM-EPCs. ↑ Tube formation and migration of BM-EPCs. ↑ $eNOS^{S1177}$ phosphorylation. ↓ Time for wound closure in response to ear punch biopsy.	BM-EPCs were not characterised in terms of surface markers ($CD31^+/CD144^+$) to ensure endothelial and not haematopoietic origin.
Metabolism and Whole-Body Energy Balance				
Cayatte *et al* (2001) Li *et al* (2011)	[201, 202]	S17834-treated HUVECs or $LDLR^{KO}$ C57BL/6J (♂) mice on HFHS	↓ Hyperlipidaemia and hepatic steatosis. ↓ Atherosclerotic lesions. ↓ SREBP-1 activity. ↓ *De novo* lipogenesis. ↓ ICAM1 and VCAM1 expression.	*In vivo* work examined systemic effects of S17834. Beneficial effects of polyphenol may extend beyond AMPK.
Steneberg *et al* (2018)	[203]	O304-treated WT C57BL/6 (♂) mice Beagle Dogs T2D Patients	↑ Peripheral microvascular perfusion. ↑ Cardiac stroke volume. ↓ Systolic and diastolic arterial blood pressure.	–

Ericsson *et al* (2021)	[204]	Age mice (18-month-old) B6CBAF1/J (♂) mice: administered vehicle or O304 (0.25-0.5 mg/g)	↑ Stroke volume and cardiac output. ↑ Capillary density in cardiac tissue. = Cardiac fibrosis or glycogen accumulation. ↓ Insulin resistance. ↓ Age-related capillary rarefaction.	*In vivo* work examined systemic effects of O304, not restricted to the endothelium despite vascular phenotype. Mechanism of AMPK activation and potential off-target effects not known with O304.
Yang *et al* (2018)	[205]	si*PRKAA1* knockdown HUVECs and MAECs Cdh5-Cre AMPKα_1^{KO} ApoE^{KO} VE-Cadherin-Cre AMPKα_1^{KO} C57BL/6J (♀and ♂)	↑ EC apoptosis. ↑ Ly6C^{hi} monocyte infiltration. ↑ Atherosclerotic lesions. ↓ Glucose uptake and glycolytic rate. ↓ HIF-1α, GLUT1 and PFKFB3 mRNA (HUVECs/MAECs). ↓ EC proliferation.	Effects of AMPK deficiency on plasma cholesterol/triglycerides and circulating monocytes were not fully examined. The interaction between AMPK and HIF-1α was not investigated.
Marin *et al* (2017)	[178]	AICAR and metformin treated HUVECs AICAR (200 mg/kg) and metformin (200 mg/kg) administered- WT and AMPKα_1^{KO} C57BL/6† mice (♀and ♂)	↑ DNMT1^{S730}, RBBP7^{S314} and HAT1^{S190} phosphorylation by AMPK. ↑ HAT1-mediated histone acetylation in promoters of *PPARGC1A, TFAM, UCP2 and UCP3* (HUVECs/MEFs) ↑ Mitochondrial content, $\Delta\Psi_m$ and cellular ATP content ↓ Promoter methylation of *PPARGC1A, TFAM, UCP2 and UCP3* (HUVECs/MEFs) ↓ Mitochondrial ROS	Mitochondrial functional parameters were not measured in ECs isolated from treated WT and AMPKα_1^{KO} mice. The impact of DNMT1, RBBP7 and HAT1 on endothelial targets beyond mitochondrial function was not examined.

Table 1.1 *– Summary of key studies on the effect of AMPK on the vascular endothelium.*

The following abbreviations were used in this table: AA: aortic arch; ACh: acetylcholine; AICAR:5-aminoimidazole-4-carboxamide ribonucleoside; ApoE: apolipoprotein E; BM-EPCs: bone marrow endothelial progenitor cells; Cdh5: VE-Cadherin (CD144); DKO: double knockout; DN-AMPK: dominant negative AMPK; DNMT1: DNA-methyltransferase 1; ECFCs: endothelial colony forming cells; eNOS: endothelial nitric oxide synthase; EPO: erythropoietin; GFAT1: glutamine fructose-6-phosphate aminotransferase 1; HAT1: histone acetyltransferase 1; HFHS: high fat/high sucrose; HIF-1α: hypoxia inducible factor 1 alpha; HK1:hexokinase 1; HO-1: haem oxygenase 1; HR: high runner mice; HUVECs: human umbilical vein endothelial cells; HyIL-6: hyper inteleukin-6; ICAM-1: intercellular adhesion molecule 1; IFNα: interferon alpha; IL-6: interleukin-6; JAK1:janus kinase 1; KO: knockout; LDLR: low-density lipoprotein receptor; LIF: leukaemia inhibitory factor; LSS: laminar shear stress; MAECs: mouse aortic endothelial cells; MCAO: middle cerebral artery occlusion; MCP: macrophage chemoattractant protein; MEFs: mouse embryonic fibroblasts; MC: myeloid cell; NO: nitric oxide; NSC: non-selected control mice; OSM: oncostatin M; OSS: oscillatory shear stress; RBBP7: histone-binding protein retinoblastoma binding protein 7; ROS: reactive oxygen species; SIRT1:sirtuin 1; STAT1/3: signal transducer and activator of transcription 1 & 3; STZ: streptozotocin (a toxin that targets insulin-producing pancreatic β-cells); TA: thoracic artery; Tie2: angiopoietin-1 receptor (CD202B); VCAM-1: vascular cell adhesion protein 1 and VEGF: vascular endothelial growth factor.

† C57BL/6J or C57BL/6N sub strain was not specified in studies.

1.8 Oxygen Sensing, Homeostasis and Hypoxia Inducible Factors

1.8.1 Oxygen and Oxygen Sensing Mechanisms in Metazoans

The levels of molecular oxygen (O_2) in the atmosphere have changed dramatically throughout the Earth's history. The earliest life forms on Earth (i.e., primitive prokaryotes) existed in near anoxic conditions. The first great oxidation event (GOE) (approximately 2.4 billion years ago) saw a sharp accumulation in atmospheric O_2 as a by-product of cyanobacterial photosynthesis. This was followed by another surge in atmospheric O_2 during the Neoproterozoic Oxygenation Event (NOE) (~500 million years ago), marking a pivotal point in diversification of multicellular life [206]. O_2 is now an essential metabolic substrate for cellular respiration in metazoans. Arising from a fateful endosymbiotic event into a prokaryote host, mitochondria are the primary site for energy production in cells in a process known as OXPHOS.

Mitochondrial OXPHOS utilises O_2 as the terminal electron acceptor in the mitochondrial ETC to transform the energy derived from the breakdown of glucose for ATP production. OXPHOS significantly increases ATP production, producing 36 molecules of ATP per glucose molecule, in contrast to 2 ATP molecules per glucose molecule produced by glycolysis [207]. The remarkable energetic capacity offered by mitochondria may have potentially paved for the genomic and cellular complexity observed in metazoans [208, 209]. Hence, metazoans rely on a continuous supply of O_2 to sustain basic bioenergetic needs required for survival. Hypoxia occurs when O_2 levels fall, either physiologically due to transient mismatches in O_2 and increased metabolic demands (e.g., high altitude or exercise) or in pathological states (e.g., ischaemia, capillary rarefaction or inflammation) due to poor vascular perfusion. To avert the deleterious effects of hypoxia, metazoans have developed sophisticated mechanisms to sense and respond to fluctuating oxygen availability [210]. The prevailing oxygen sensing system identified across examinable animal taxa involves the hypoxia inducible factors alpha (HIFα) and their regulators: prolyl hydroxylases (PHD) and the von Hippel Landau (pVHL) protein [210].

1.8.2 Hypoxia Inducible Factors

The transcriptional response to low oxygen is orchestrated by HIFα oxygen-sensitive transcription factors belonging to the basic helix–loop–helix/Per-ARNT-SIM (bHLH-PAS)

family, dimerising with the constitutively expressed bHLH-PAS member: HIFβ [211]. The resultant active heterodimer initiates the transcriptional response to low oxygen levels by binding to a regulatory sequence known as a hypoxia responsive element (HRE). HREs are *cis*-regulatory elements comprised of the core sequence: 5′-A/GCGTG-3′. Numerous HREs are found in promoters and distal enhancers of target genes spanning across processes such as angiogenesis, erythropoiesis, metabolic reprogramming, cell cycle regulation and stem cell fate [212-216].

Three HIFα isoforms exist: HIF-1α, HIF-2α and HIF-3α, encoded by the *HIF1A*, *EPAS1* and *HIF3A* genes, respectively, whereas HIFβ exists in two isoforms: HIF-1β (*ARNT1*) and HIF-2β (*ARNT2*). Structurally, HIF-1α and HIF-2α share three essential functional domains: (i) the bHLH and PAS domains; (ii) the N-terminal and C-terminal transactivation domains (N-TAD and C-TAD); (iii) the oxygen-dependent degradation domain (ODDD) in the C-terminus (Figure 1.6). The interaction between the bHLH and the PAS domains forms a functional interface for heterodimerisation with HIF-1β and DNA binding to HRE elements. The N-TAD and C-TAD domains interacts with the constituents of the transcription initiation complex, promoting transcription initiation sites binding and gene transactivation. The inhibitory domain (ID), interceding between the N-TAD and C-TAD domains, supresses transactivation (Figure 1.6). Unfortunately, the suppressive effects of inhibitory domain and its derepression under hypoxia are not well elucidated. It has been shown, however, that HIFα possesses a classical monopartite nuclear localisation sequence (NLS) motif in the bHLH domain, a bipartite NLS, a string of basic arginine/lysine residues separated by a linker sequence, is located within the inhibitory domain.

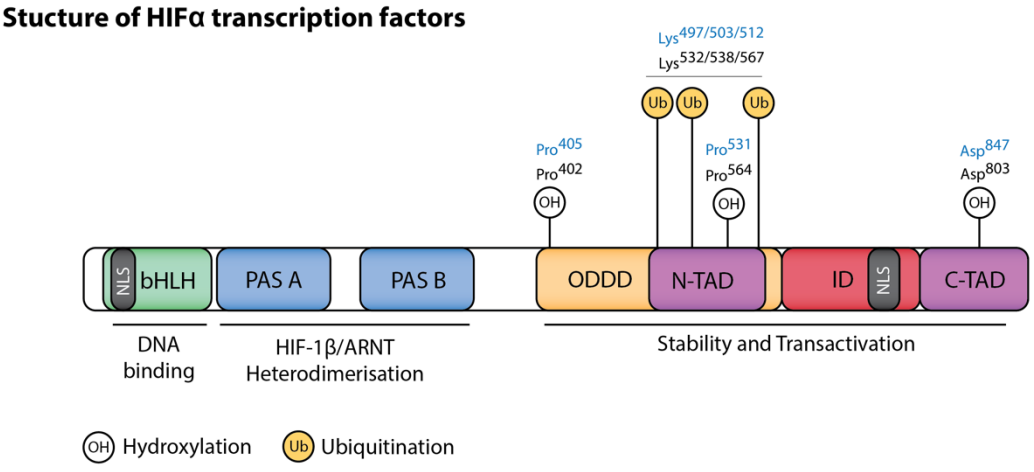


Figure 1.6 *– General protein structure of HIFα transcription factors.*

HIF-1α and HIF-2α share basic helix-loop-helix (bHLH) and Per-Arnt-SIM (PAS) domains DNA binding and heterodimerisation domains as well as inhibitory (ID), N- and C-terminal transactivation domains (N-TAD/C-TAD) and oxygen-dependent degradation domain (ODDD) which dictate in stability and degradation of HIFα. NLS motifs are located in the bHLH and ID regions. Critical regulatory proline, lysine and asparagine residues are highlighted in black for HIF-1α and blue for HIF-2α. Figure generated by Adobe Illustrator.

Phylogenetic data reveal that HIF-1α is evolutionary conserved from nematodes to humans, whereas HIF-2α and HIF-3α may have emerged later in evolution in higher vertebrates such as birds and mammals [217, 218]. HIF-1α and HIF-2α share similarities in their amino acid sequences (~48%), predominantly in their DNA binding and heterodimerisation regions [217, 219]. The structure and function of HIF-3α remains elusive due its low sequence similarity with its counterparts. The existence of differing HIF-3α mRNA splice variants complicates investigations due to tissue specific expression patterns, numerous distinctive and even opposing functions to other variants. Expression patterns of the HIFα isoforms vary *in vivo*. HIF-1α is ubiquitously expressed while HIF-2α and HIF-3α display restricted cell type/tissue expression. Post-transcriptional regulation of HIFα can be regulated in numerous ways like mRNA binding proteins (e.g., HuR for *HIF1A* mRNA) or sequence elements in the 3'-/5'- UTR (e.g., iron responsive element IRE in the 5'-UTR of *EPAS1* mRNA) [220-222]. Nevertheless, HIFα mRNA is always constitutively expressed and translated into a mature polypeptide in oxygenated cells as regulation of HIFα is exerted primarily post-translationally, through modification of key residues that govern its stability in oxygen-dependent manner.

1.8.3 Hypoxia-dependent and -independent Regulation of HIFα

The ability of HIFα to 'sense' oxygen is due to the activities of HIFα prolyl 4-hydroxylases (PHDs 1-3) and the asparaginyl beta-hydroxylase factor-inhibiting HIF 1 (FIH1). The PHD family (also referred to as EGLNs) belong to Fe^{2+}/αKG-dependent family of hydroxylases. All PHD isoforms are encoded by *EGLN1-3* genes due to shared homology with the oxygen sensor *Egl-9* in *C. elegans.* On the other hand, FIH1, encoded by the *HIF1AN* gene*,* was identified through a yeast two-hybrid screen [223, 224]. The evolutionary origins of oxygen sensing by PHDs are unknown however comparative genomic analysis by Loenarz *et al* (2011) reveal that homologues of HIFα are only present in metazoans whereas PHD homologues were identified in eukaryotes [225, 226]. The placozoan *Trichoplax adhaerens,* is the simplest known animal*,* possesses a conserved HIF/PHD signalling system, but FIH is absent. However, a functional FIH homologue was found in the starlet sea anemone (*Nematostella vectensis),* therefore it was present in the last common ancestor of both bilateria and cnidaria. A PHD orthologue, Ofd1, identified in fission yeast (*Schizosaccharomyces pombe*), was found to regulate the transcription factor sterol regulatory element binding protein (Sre1) in an oxygen-dependent manner. However, oxygen availability in budding yeast (*Saccharomyces cerevisiae*) is sensed through haem and sterol levels [227, 228].

HIFα hydroxylases are ubiquitously expressed, although PHD2 is the predominant isoform in almost all cells, with PHD1 and 3 displaying considerable variation between cell types and tissues. PHDs also exhibit differences in subcellular localisation with PHD1 being predominantly retained in the nucleus whereas PHD2 and FIH1 are localised to the cytoplasm and PHD3 distributed throughout the cytoplasmic and nuclear compartments [229]. PHD isozymes also possess differential substrate preferences, with PHD2 being selective for HIF-1α whereas PHD1 and PHD3 preferentially target HIF-2α [230, 231]. PHDs require O_2 as a substrate along with Fe^{2+}, α-ketoglutarate (αKG) and ascorbate as cofactors to allow hydroxylation of proline (PHD 1-3) and asparagine (FIH1) residues (Figure 1.7) [223, 232, 233]. In the presence of O_2 and αKG from the TCA cycle, proline residues within the ODDD (Pro402/Pro564 in HIF-1α, Pro-405/Pro-531 in HIF-2α) are hydroxylated by PHDs (Figure 1.7). Hydroxylation by Fe^{2+}/αKG-dependent hydroxylases begins with αKG and O_2 binding to Fe^{2+}, displacing a constitutively bound water (H_2O) molecule. αKG is decarboxylated, forming succinate along with a ferryl-oxo species that hydroxylates a proline residue. The Fe^{3+} ion is oxidised back to Fe^{2+} by ascorbate for the next round of catalysis (Figure 1.7). Concurrently, FIH1 asparaginyl β hydroxylase also interacts with HIFα through a conserved asparagine (N) residue (Asp803 in HIF-1α, Asp847 in HIF-2α) within the ODDD (Figure 1.7). O_2 affinities (K_m) were initially determined by *in vitro* kinetic assays, where recombinant PHD/FIH1 and HIF-1α substrate were incubated in the presence of isotope-labelled αKG and O_2 affinity was deduced from $^{14}CO_2$ production (Table 1.2) [212, 234, 235]. FIH1 possesses a higher affinity for O_2 and has been shown hydroxylate HIF-1α even under hypoxic conditions both *in vitro* and *in vivo* [224, 234, 236, 237]. The instantaneous accumulation (~4-8 minutes at < 6% O_2) and degradation (< 5 minutes) of HIFα upon reoxygenation demonstrates the rapid nature by which hydroxylases regulate its activity across the physiological range of O_2 [238-240].

HIFα Hydroxylase	**Michaelis Menten, K_m values for O_2 [μM, (% O_2)]**
PHD 1	~230 μM (23%)
PHD 2	~250 μM (25%)
PHD 3	~230 μM (23%)
FIH1	~70 - 110 μM (7-11%)

Table 1.2 *– K_m values of O_2 provided for PHD and FIH1 in vitro.*

Derived from Hirsilä *et al*. (2003) and Koivunen *et al*. (2004) [212, 234].

Under normoxia, hydroxylation of prolyl and asparagine residues in the ODDD creates a high affinity binding site for von-Hippel-Lindau tumour suppressor protein (pVHL), leading to HIFα degradation in the presence of oxygen. Von-Hippel-Lindau tumour suppressor protein, pVHL, encoded by the *VHL* gene, exists as two proteins: the full-length form (24-30 kDa) and the predominant protein in cells, the short form (18-20 kDa), arising out of an alternative translation initiation codon at a methionine residue at position 54 in the full-length form [241]. pVHL is found in a pentameric VCB-CUL2 complex, along with elongin B, elongin C, cullin-2 (CUL2) and RING-box protein 1 (Rbx1) proteins [242]. The VCB-CUL2 complex possesses intrinsic E3 ligase activity, polyubiquitinating lysine (K) residues in HIFα (K532/538/567 in HIF-1α, K497/503/512 in HIF-2α) targeting it for proteolytic degradation by the 26S proteasome (Figure 1.7) [243-246]. pVHL dynamically shuttles between the cytoplasm and nucleus ubiquitinating HIFα in both compartments under steady-state conditions, although its dynamics can be impacted by changes in transcription and cell cycle states [247, 248]. As oxygen tensions fall under hypoxia, HIFα evades pVHL-mediated degradation and dimerises with HIF-1β. Upon translocation into the nucleus, HIFα/HIFβ dimers binds HRE-elements and recruiting transcriptional coactivators, p300/CREB-binding protein (CBP) and histone deacetylases to target genes (Figure 1.7) [211, 216, 249] involved in cell survival, autophagy, glucose metabolism, iron homeostasis, inflammation, angiogenesis and vascular remodelling. The functions of HIFα activation are described in Table 1.3 below.

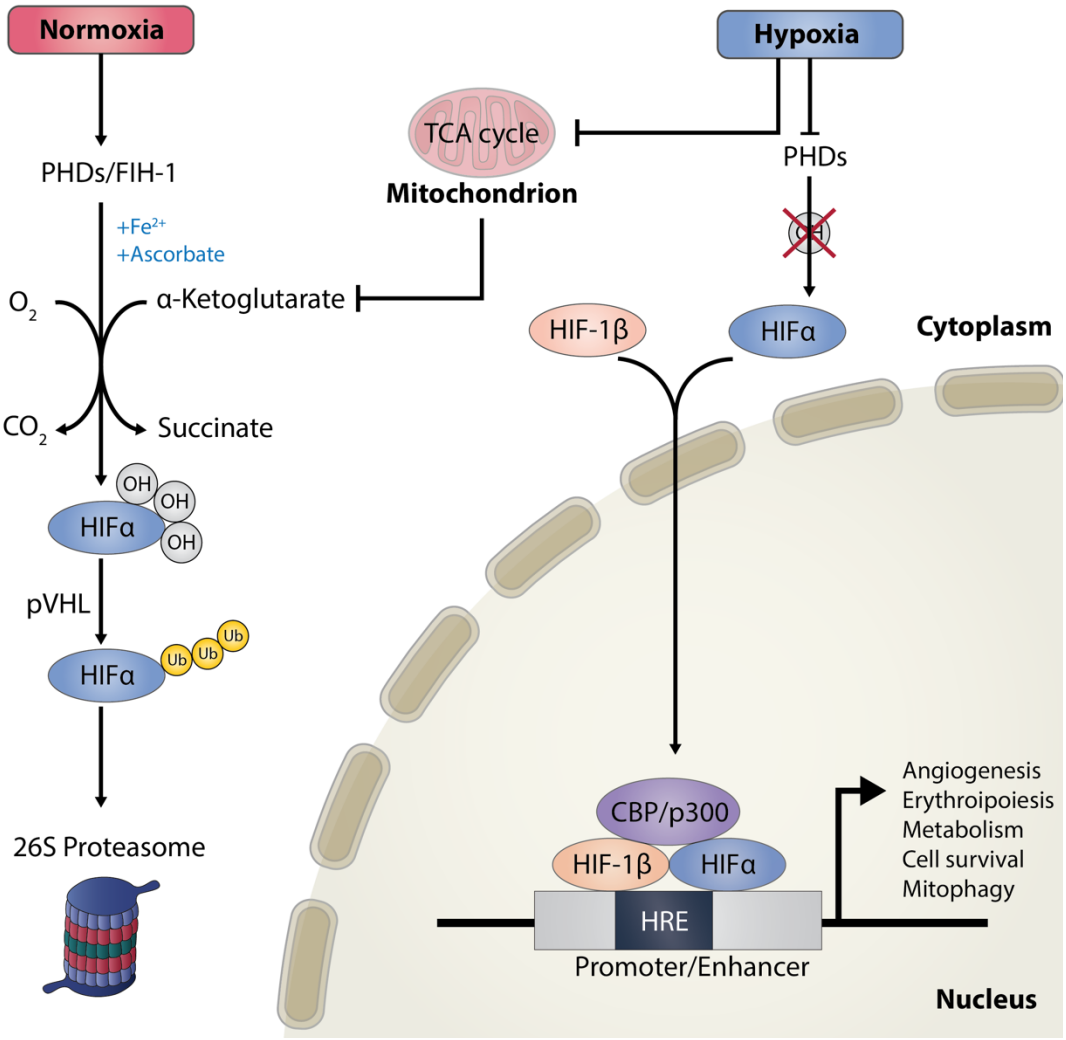


Figure 1.7 *– Oxygen-dependent regulation of HIFα transcription factors by prolyl and asparaginyl hydroxylases.*

HIFα isoforms are constitutively transcribed and translated. In the presence of O_2, HIFα is hydroxylated on proline and asparagine residues by PHDs and FIH-1 respectively. The activities of PHDs and FIH-1 require O_2 and α-ketoglutarate derived from the TCA cycle, using iron (II) ions (Fe^{2+}) ascorbate as co-factors, producing CO_2 and succinate as by-products. The hydroxylation events increase the proteins affinity for pVHL binding for ubiquitination at several lysine residues. Ubiquitination serves as a signal for targeted degradation by the 26S proteasome, prevent stabilisation and accumulation of HIFα. A fall in O_2 results in the inhibition of mitochondrial respiration and TCA cycle, thereby inhibiting the activities of PHDs/FIH-1 leading to stabilisation and accumulation of HIFα. HIFα subsequently dimerises with HIF-1β and translocates into the nucleus. The HIFα/HIF-1β heterodimer binds to HRE-elements in the promoter and enhancer regions of genes involved in processes such as angiogenesis, erythropoiesis, metabolism, cell survival and mitophagy. The transcriptional programmes activated by HIFα elicit systemic effects, facilitating the individual to adapt under lower O_2 tensions. Adapted from Pearl, Chandel and Celeste Simon, *Nature Reviews Molecular Cell Biology* (2020). Figure generated by Adobe Illustrator.

Function	Target	Effect	Isoform	Ref
Cell survival, growth, cell cycle progression and proliferation	REDD1	⊣ mTOR	HIF-1α	[250]
	BCL-xL	⊣ Apoptosis	Both	[251]
	Cyclin D1	→ CDK4 ⊣ Rb ⊣ G1/S transition	HIF-2α	[252]
	TGFα	↑ Cell proliferation	HIF-2α	[253]
Redox Homeostasis	MnSOD	↓ Superoxide ($O_2^{\bullet-}$)	HIF-2α	[254]
	Catalase	↓ H_2O_2	HIF-2α	[255]
Erythropoiesis	Erythropoietin (EPO)	↑ Haemotocrit (kidney and liver)	HIF-2α	[256]
Angiogenesis and vascular remodelling	VEGF	↑ Proliferation and migration (ECs)	Both	[257]
	DLL4	⊣ NOTCH ↑ Tip cell formation (ECs)	HIF-2α	[257]
	PAI-1	↑ Invasion (ECs)	Both	[257]
	Tie2	↑ Angiogenesis	HIF-2α	[257]
Cell migration	SDF1/CXCR4	↑ Migration	HIF-1α	[258]
Invasion	MMP13	↑ Invasiveness	HIF-2α	[259]
	MMP2	↑ Invasiveness	HIF-2α	[259]
Glucose and fructose metabolism	GLUT1	↑ Glucose uptake	Both	[260]
	LDHA, HK2, PDK1, PGK1	↑ Glycolytic flux	HIF-1α	
	IRS2	↑ Insulin sensitivity	HIF-2α	[261]
	SF3B1	→ KHK ↑ Fructolysis(CMCs)	HIF-1α	[262]
Inflammation	IL-1β	↑ Inflammation (M1 Mφ)	HIF-1α	[263]
	RORγt	↑ IL-17 production ↑ Inflammation ↑ Th17 development ($CD4^+$ T-cells)	HIF-1α	[264]
	Adenosine receptors (ADORAs)	↑ Extracellular adenosine ↓ Inflammation	Both	[265]
	iNOS	↑ NO production ↑ Inflammation (M1 Mφ and ACs)	HIF-1α	[266]
	Arginase-1	↓ NO production ↓ Inflammation (M2 Mφ)	HIF-2α	[267]
Lipid storage	Perilipin-2	↑ Lipid droplet formation	Both	[268]
Mitophagy	BNIP3 NIX	↑ Mitophagy ↓ Mitochondrial content	HIF-1α	[269]

Pluripotency	OCT4	= Stemness	HIF-2α	[270]
	Wnt	= Stemness	HIF-1α	[271]

Table 1.3 *– Summary of all processes and targets regulated by HIFα isoforms.*

The following abbreviations are used: − ACs: adipocytes; ADORAs: adenosine receptors; BCL-xL: B-cell lymphoma-extra-large; BNIP3: BCL2 interacting protein 3; CDK4: cyclin-dependent kinase 4; CXCR4: C-X-C chemokine receptor type 4; EPO: erythropoietin; GLUT1: glucose transporter 1; HK2: hexokinase 2; IL-1β: interleukin-1β; iNOS: inducible nitric oxide synthase; IRS2: insulin receptor substrate 2; KHK: ketohexokinase; LDHA: lactate dehydrogenase A; Mφ: macrophages; M1 Mφ: alternatively activated macrophages; M2 Mφ: classically activated macrophages; MMP13: matrix metalloprotease 13; MMP2: matrix metalloprotease 2; MnSOD: manganese superoxide dismutase; OCT4: octamer-binding transcription factor 4; PDK1: pyruvate dehydrogenase kinase 1; PGK1: phosphoglycerate kinase 1; REDD1: regulated in development and DNA damage response 1; RORγt: RAR-related orphan receptor γt; SDF1: stromal derived factor 1; SF3B1: splicing factor 3B subunit 1; TGFα: transforming growth factor α; Th17: T helper 17.

HIF-1α and HIF-2α exhibit differential activation and temporal patterns in response to hypoxia, with HIF-1α mediating the acute response and HIF-2α mediating the chronic, long-term adaptive response. Advances in next-generation sequencing, e.g., ATAC-seq and ChIP-seq, have facilitated our understanding of the HIFα epigenomic landscape. Interestingly, differences in HIF-1α and HIF-2α-mediated transcription are not thought to be due to competition of binding to HREs but (i) location and number of HREs and (ii) innate spatial preferences e.g., HIF-1α binds proximal-promoter HREs whereas HIF-2α binds HREs in distal enhancers. Regardless of O_2 tension, duration of hypoxia and cell type, these distinctions between HIF-1α and HIF-2α transcriptional and chromatin signatures persist. Overexpression of HIF-1α and -2α in HUVECs reveal divergence in isoform-specific responses e.g., HIF-1α targets processes in energy metabolism, whereas HIF-2α is implicated in a wider repertoire of processes. The number of biological functions modulated by HIF-2α suggests that it's *cis*-regulatory functions are not determined by HRE binding alone. The differential functions and what biological processes are regulated by each HIFα isoform is summarised in Table 1.3. How the concerted actions of HIF-1α and HIF-2α along with their interactions with transcription cofactors and chromatin modelers in driving spatiotemporal and/or cell-specific hypoxic responses remains elusive.

Activity of PHDs is not only dependent on the presence of oxygen, but also iron and αKG, an intermediate in the TCA cycle. Therefore, it is not implausible to assume that HIFα is responsive to iron redox states, ferritin stores and metabolic stimuli [272, 273]. Control of HIFα extend beyond intracellular metabolites, with reports of induction by growth factors, pH and OSS [273]. Significant progress in the study of HIFα regulatory mechanisms have shown oxygen-independent regulation of the transcription factor. Transition metals such as cobalt (Co^{2+}) and nickel (Ni^{2+}) stabilise HIFα and induce target gene transcription under normoxic

conditions. The mechanisms by which Co^{2+}/Ni^{2+} behave as hypoxia mimetics remains unknown. ROS production under hypoxia primarily occurs at the mitochondrial ETC. Impaired electron flow through the respiratory complexes, causes electrons to accumulate and monovalently reduces residual O_2 to $O_2^{\bullet-}$ [274]. The theory of mitochondrial ROS (mtROS)-mediated HIFα expression is a subject of controversy. First postulated by Chandel *et al*, they observed mitochondria can sense O_2 by increasing mtROS production during hypoxia [275]. Several studies have shown mitochondrial ROS production augments or is a prerequisite for HIF-1α induction, with mitochondria-deficient cells failing to stabilise HIF under hypoxia [275-278]. Evidence from other groups however contest this theory, showing oxidant-independent HIFα stabilisation [279]. Pharmacological inhibition of each individual respiratory complex altered HIFα accumulation but had no effect on ROS production [280]. Further studies are required to fully understand the mechanism by ROS-mediated regulation of HIFα.

Recent developments reveal another paradigm of regulation of HIFα regulation by metabolites, stemming from studies involving inherited and acquired mutations in genes encoding TCA enzymes that predisposes individuals to tumorigenesis. Elevated levels of succinate and fumarate, caused by defects in succinate dehydrogenase (SDH) subunits and fumarate hydratase, respectively, promotes a pseudo-hypoxic phenotype through stabilisation of HIFα [281]. Fumarate and succinate act as competitive inhibitors of PHDs to stabilise HIFα, resulting in increased expression of genes that ultimately promote angiogenesis, epithelial-to-mesenchymal transition and metastasis [282]. Under physiological circumstances, succinate-/fumarate-dependent upregulation of HIFα protein has also been noted under in response to increased glucose in POMC neurons of mice, to link appetite control with whole-body energy balance [283].

1.8.4 HIFα in the Vasculature

HIFα isoforms greatly influence endothelial metabolism, vascular tone, vasculogenesis and vascular remodelling. The following sections will highlight both the overlapping and distinct roles of HIF-1α and HIF-2α in various aspects of endothelial and vascular-related functions along with some discussion of their role in disease.

1.8.4.1 Lessons from HIFα knockout models

The phenotype of *Hif1a* and *Epas1* mouse KO models, regardless of strain, exhibit vascular abnormalities. *Hif1a*$^{-/-}$ mouse embryos are embryonic lethal at E11, having cardiac malformations, vascular regression, and impairments in haematopoiesis. *Hif1a*$^{+/-}$ mice are

viable but exhibit blunted physiological responses to hypoxia and ischaemia [215, 284]. Unexpectedly, *Vegf* mRNA was increased in *Hif1a*$^{-/-}$ embryos, perhaps as a compensatory mechanism due to nutrient deprivation. EC-specific conditional knockout (CKO) of HIF-1α exhibited defective angiogenesis, delayed wound healing and tumour vascularisation. The phenotype of *Epas1*$^{-/-}$ mice vary depending on the genetic background of mice strains, however the overarching features are cardiovascular and pulmonary defects. In the model developed by Peng *et al.* (2000), *Epas1*$^{-/-}$ mice failed to assemble large vessels from smaller ones, exhibiting improper yolk sac vascular remodelling and haemorrhagic vessels [285].

Another model developed by Scortegagna *et al* (2003), *Epas1*$^{-/-}$ mouse embryos present with multi-organ pathologies including hepatic steatosis, cardiac hypertrophy, skeletal myopathy, bone marrow hypocellularity and retinopathy [255, 286]. Metabolic disturbances were also reported such as hypoglycaemia, lactic acidosis, ketone accumulation and alterations in TCA metabolites based on urine and serum analysis [255]. The observations paralleled the hallmarks of mitochondrial diseases such as presence of ragged red fibres in skeletal and cardiac muscle, increased ROS production, and enlarged degenerating mitochondria. This indicates HIF-2α may participate in the regulation of mitochondrial homeostasis, with previous studies observing reduced manganese-dependent superoxide dismutase MnSOD (SOD2) expression and frataxin (FXN) in *Epas1*$^{-/-}$ mice. Further studies show that haematopoiesis was impaired in *Epas1*$^{-/-}$ mice [286]. HIF-2α CKO studies demonstrate the importance for vessel maturation, as EC-specific *Hif-2*α$^{fl/\Delta}$ exhibit pulmonary hypertension, lung lymphocyte infiltration and vascular leakage in the lungs and adipose tissue [287, 288].

1.8.4.2 The role of HIFα in angiogenesis and endothelial fate

During developmental angiogenesis, angioblasts respond to their hypoxic microenvironment to initiate vascular development through HIFα stabilisation. Mobilised angioblasts activate HIFα transcriptional programmes to drive expression of downstream genes that co-ordinate branching, vascular morphogenesis and endothelial differentiation. Upon establishing the primary vascular plexus, HIFα isoforms participate at every phase of SA (see Section 1.6.1 Sprouting Angiogenesis) through upregulation of MMPs (e.g. MMP-2) to degrade the ECM [289]. HIF-1α is also necessary to establish the hypoxia-induced autocrine loop of VEGF/VEGFR2 signalling [289-292]. Activation of the HIFα transcriptional network promotes expression of other pro-angiogenic genes like angiopoietin 1 *(*Ang-1), angiopoietin 2 (Ang-2), the angiopoietin receptor (Tie2), stem cell factor (SCF) and its cognate receptor c-KIT [293]. Guidance and patterning of blood vessels are also regulated by HIFα, by modulating NOTCH signalling through upregulating Dll4 expression and directly associating with NICD to enhance

its transcriptional activity [287, 294]. HIF-2α participates in vessel remodelling through deposition of fibronectin to form the basement membrane [287]. Moreover, HIF-2α-mediated upregulation of Ang-1 and Ang-2 facilitates lumen formation, attachment of pericytes and pruning of blood vessels in the absence of growth factors. HIFα factors also determine the endothelial fate of these progenitors as HIF-1α-mediated upregulation NOTCH target gene is critical for arterial specification. Upregulation of Dll4 and HEY2 suppresses the venous-specific Coup-TF II transcription factor [295, 296]. The complementary roles of endothelial HIF-1α and HIF-2α in vessel outgrowth and maturation, respectively, is best illustrated in tumour xenograft studies where HIF-1α^{ECKO} reduces tumour angiogenesis whereas HIF-2α^{ECKO} exhibit defects in lumen acquisition [287]. HIF prolyl hydroxylase inhibitors such the anti-anaemia drug FG-4592 (roxadustat), have been shown to accelerate wound healing in cutaneous diabetic lesions in rats by enhancing the HIF-1α/VEGF/VEGFR2 pathway [297]. Therefore, HIFα targeting presents an attractive target in pathologies where angiogenesis is dysregulated such as cancer, peripheral artery disease (PAD) and diabetes, perhaps through mobilisation of EC progenitors.

1.8.4.3 HIFα and endothelial haemodynamics

Across numerous cell types, HIFα isoforms exert profound effects on local blood flow (i.e. autoregulation) and systemic blood pressure. HIF-1α and HIF-2α co-operate antagonistically to control NO homeostasis in macrophages by modulating the expression of inducible nitric oxide synthase (iNOS) and arginase 1 [298]. L-arginine is the common substrate for iNOS and arginase1, metabolising the amino acid into NO and ornithine/urea, respectively, therefore relative levels of both enzymes dictate NO bioavailability. The authors noted that HIF-1α and HIF-2α expression change depending on the polarity of macrophages: HIF-1α is predominant in the classically activated M1 macrophages in response to T helper (Th) 1 cytokines (e.g., IFNγ, TNFα) whereas HIF-2α is upregulated by Th2 cytokines (e.g., IL-4). The balance between HIF-1α and HIF-2α in keratinocytes also appears to control systemic blood pressure, where HIF-1α deficiency augments systolic and diastolic blood pressure whereas HIF-2α deficiency protects against Ang-II-induced hypertension [299]. HIF-1α exerts profound effects on systemic blood pressure with endothelial deficiency of HIF-1α leading to the development of hypertension, diminished vasodilatory responses to ACh and increased metabolic rate [300].

Anaemia is a condition described by a reduction circulating red blood cells (RBCs), with a broad range of aetiologies including iron deficiency, nutritional deficiencies (e.g. vitamin B12), schistosomiasis, malaria or chronic kidney disease (CKD) [301]. Treatment of renal anaemia

in CKD requires administration of recombinant human EPO (rhEPO) to normalise their haematocrit, but there are several adverse effects of treatment including increased risk of blood clots and development of hypertension due to increased blood viscosity [302, 303]. Patients on rhEPO require close monitoring by clinicians, particularly patients whose anaemia is attributed to CKD or cancer treatment. Preclinical studies using a rat model of renal anaemia and a novel HIF prolyl hydroxylase inhibitor, BAY-85-3934 (molidustat), showed enhanced EPO production and haematocrit to levels greater than rhEPO, without inducing hypertension [304]. Assuming that BAY-85-3934 is not associated with an elevated risk of thrombosis, it may serve as a promising alternative for patients who develop resistance to rhEPO.

Elevated endothelial HIFα expression can be a key driver in the development of hypertension under specific pathological contexts. The deleterious effects of Ang-II-induced CKD is exerted through HIF-1α. In a mouse model of CKD, EC-specific HIF-1α ablation alleviated the hypertensive phenotype through the reduction of circulating endothelin-1, a bona fide HIF-1α target [305]. In a similar vein, HIF-2α is heavily implicated in the pathogenesis of pulmonary hypertension (PH), with elevated levels of HIF-2α in the pulmonary arterial ECs of pulmonary arterial hypertension (PAH) and idiopathic pulmonary fibrosis (IPF) patients [306, 307]. Tang and colleagues demonstrated that lung ECs underwent endothelial-to-mesenchymal transition leading to increased thickening of the arterial intima and occlusive lesions [308]. *Epas1*-deficient mice exhibited resistance against hypoxia-induced PH. HIFα isoforms can exert pleiotropic effects, further complicated by co-operative or antagonistic actions of HIF-1α and HIF-2α, disease-specific contexts and discrepancies due to method of HIFα modulation (e.g. genetic or pharmacological). Additional studies are required to further delineate the roles of HIFα isoforms, particularly in disease-specific contexts.

1.8.5.4 HIFα and endothelial dysfunction

Endothelial dysfunction encompasses a series of changes including loss of vasodilatory responses and endothelial activation, predisposing ECs to a prothrombotic, pro-inflammatory state. The balance between OXPHOS and glycolysis is a key determinant in the immunometabolic phenotype of ECs in the aetiologies of conditions characterised by systemic inflammation [309]. Interestingly, emerging evidence suggests that endothelial immunometabolism may be determined by the antagonistic actions of HIF-1α and HIF-2α. Haemodynamic forces modulate HIF-1α stability in the endothelium, with disturbed flow increasing HIF-1α expression. Exposure to disturbed flow (i.e., OSS) shifts the metabolism of ECs towards a more glycolytic, pro-inflammatory state, leading to the development of endothelial dysfunction. OSS was shown to stabilise HIF-1α expression in arterial ECs,

through increased NADPH oxidase 4 (NOX4) expression and ROS production. OSS-mediated stabilisation of HIF-1α inhibits mitochondrial OXPHOS whilst concomitantly stimulating glycolysis, in addition to driving pro-inflammatory gene expression in the bifurcations of the aorta. Knockdown of HIF-1α or its metabolic targets GLUT1 and HK2 normalised prevented the OSS-induced pro-inflammatory phenotype [310].

1.8.5.5 HIFα and endothelial metabolism

HIFα transcription factors alter cellular metabolism to facilitate adaptation under low oxygen, by reducing energy-consuming pathways (e.g., protein translation) and shifting towards anaerobic metabolism. HIF-1α regulates almost 80% of glycolysis-related genes according to RNA-sequencing data from HUVECs overexpressing HIFα isoforms [311]. HIF-1α promotes expression of glycolytic enzymes such as *HK2*, enolase 1 (*ENO1*), aldolase A (*ALDOA*) [312]. Moreover, both HIFα isoforms regulate expression of several glucose transporters (*GLUT1/3*). HIF-1α upregulates pyruvate dehydrogenase kinase (*PDK*), an enzyme which redirects pyruvate towards anaerobic glycolysis rather than the TCA cycle [311]. Pyruvate is subsequently reduced to lactate, catalysed by HIF-1α target lactate dehydrogenase A (*LDHA*), to regenerate $NADP^+$. To avert intracellular acidification from lactate accumulation, HIF-1α increases levels of lactate and proton symporter (*SLC16A3)* and carbonic anhydrase 9 (*CA9*) [311]. A phenomenon observed under hypoxia is a reduction in mitochondrial mass, as an adaptive mechanism to prevent cell death and maintain ATP levels [312, 313]. HIF-1α promotes mitochondrial degradation through upregulation of target genes such as mitophagy-related proteins BCL2 interacting protein 3 (*BNIP3*) and NIX (*BNIP3L*) [311, 313].

Although metabolic reprogramming is primarily mediated by HIF-1α, HIF-2α also alters lipoprotein uptake, cholesterol processing and lipid metabolism. HIF-2α induces expression of transcription factors peroxisome proliferator-activated receptor alpha (PPARα) and gamma (PPARγ). PPARα promotes catabolism of lipids through (i) peroxisomal and mitochondrial fatty acid FAO and (ii) ketogenesis, whereas PPARγ regulates lipid uptake [314-317]. PPARα also regulates pyruvate dehydrogenase kinase 4 (PDK4), which acts to inhibit the pyruvate dehydrogenase complex thereby limiting mitochondrial glucose oxidation [318]. Other genes implicated in lipid metabolism such as lysosomal acid lipase A (*LIPA*), sialidase-3 (*NEU3*), very low-density lipoprotein receptor (*VLDLR*) and perilipin-2 (*PLIN2*) are increased by HIF-2α [268, 311].

1.9 Project Scope and Aims

The evidence here establishes the importance of AMPK as a cellular metabolic gauge, exerting pleiotropic effects on aspects of cellular metabolism and vascular function. It is clear based on the studies summarised in Table 1.1 that AMPK is critical for angiogenesis following ischaemic insults and endothelial metabolism through (i) regulation of glucose metabolism and (ii) mitochondrial quality control and biogenesis. Despite this, the vascular functions attributed to AMPK have heavily relied on knockout studies rather activation using novel small molecule activators that have emerged over the past decade (e.g., BI-9774). Another caveat is that these effects have largely been derived from other cell types without thorough examination in endothelial cells. Therefore, the scope of this project will cover two areas: (i) establish the physiological regulation of AMPK by hypoxia and crosstalk with HIF-1α signalling, followed by (i) characterisation of the endothelial phenotype following BI-9774 treatment *in vitro* using HUVECs and endothelial-specific activation of AMPK *in vivo* using transgenic mouse models. This will provide a foundation for future studies for in-depth characterisation between AMPK and HIFα-related signalling pathways.

Hypothesis: AMPK activation exerts profound systemic effects on endothelial metabolism and angiogenesis, which may act partly through hypoxia and/or HIF-related pathways.

This will be achieved by the following aims:

Aim 1: To examine how hypoxia impacts AMPK activity in HUVECs (Chapter 3).

Aim 2: Assess whether pharmacological agonists and bioenergetic stressors that induce AMPK activity also alter HIF-1α expression in ECs (Chapter 3).

Aim 3: To characterise the effects of the pan-AMPK activator, BI-9774, on the transcriptome of endothelial cells (Chapter 4).

Aim 4: To investigate crosstalk between AMPK and HIFα signalling pathways and delineate a potential mechanism by which AMPK regulates HIFα stability (Chapter 4).

Aim 5: To validate the functional and metabolic effects of AMPK activation on the endothelium as predicted from RNA-seq data both *in vivo* and *in vitro* (Chapter 5).

Aim 6: To generate and initially characterise the vascular phenotype of global (β-actin-cre) AMPK activating (γ_1D316A-Tg) mouse model with further studies on the metabolic effects of the endothelial specific model (Chapter 5).

2. Chapter 2 – Materials and Methods

2.1 Reagents

2.1.2 Buffers and Solutions

Buffer formulations are described below.

DPBS: 137.9 mM NaCl, 1.47 mM KH_2PO_4, 2.67 mM KCl, 8.09 mM Na_2HPO_4.
FACS Permeabilization Buffer: 1× DPBS, 0.2% BSA , 25 mM HEPES, 1 mM EDTA, 0.1 % Triton X-100.
HBSS: 5.33 mM KCl, 0.44 mM KH_2PO_4, 138 mM NaCl, 4 mM $NaHCO_3$, 0.30 Na_2HPO_4, 5.55 mM glucose.
HEPES Buffer A: 50 mM HEPES, pH 7.4, 50 mM NaF, 5 mM $Na_4P_2O_7$, 1 mM EDTA, 10% (v/v) glycerol, 1 mM DTT, 4 µg/mL soybean trypsin inhibitor, 0.1 mM PMSF and 157 µg/ml benzamidine.
HEPES Lysis Buffer: HEPES Buffer A with 1% Triton X-100. Used for AMPK kinases assays.
HGE Buffer: 50 mM HEPES pH 7.4, 10% (v/v) glycerol and 1 mM EDTA.
PBLEC Solution: 1 mM $MgCl_2$, 1 mM $CaCl_2$, 1 mM $MnCl_2$ and 1% (v/v) Triton X-100 in PBS.
PBS: 137 mM NaCl, 2.7 mM KCl, 10 mM Na_2HPO_4, and 1.8 mM KH_2PO_4, pH 7.4.
Propidium Iodide Staining Solution: 0.1% (v/v) Triton X-100, 50 mM EDTA, 50 µg/ml propidium iodide and 400 µg/ml RNase A in PBS.
Retina Blocking Buffer (RBB): 1% (w/v) BSA and 1% (v/v) Triton X-100 in PBS.
Retina Wash Buffer: RBB and DPBS (1:1).
TBS: 150 mM NaCl, 50 mM Tris HCl, pH 7.4
TBS-T: TBS with 0.1% (v/v) Tween-20.

2.1.2 Primers

All primers were purchased from ThermoFisher and Merck and reconstituted in molecular grade ddH_2O at a stock concentration of 50 µM. The primer sequences are detailed in Table 2.1.

Gene	Forward Sequence	Reverse Sequence
TBP	TTTGCAGTGACCCAGCATCA	CCAGCACACTCTTCTCAGCA
GLUT1/SLC2A1	GGCCAAGAGTGTGCTAAAGAA	ACAGCGTTGATGCCAGACAG
PLAU	GGGAATGGTCACTTTTACCGAG	GGGCATGGTACGTTTGCTG
VEGFA	AGGGCAGAATCATCACGAAGT	AGGGTCTCGATTGGATGGCA
B2M	GAGGCTATCCAGCGTGAGTC	GAAGTCACGGAGCGAGAGAG
MT-ND1	ATGGCCAACCTCCTACTCCT	AGATGTGGCGGGTTTTAGGG
MT-CO1	CCAATACCAAACGCCCCTCT	AGAATGGGGTCTCCTCCTCC

Table 2.1 *– List of RT-qPCR primers.*

2.1.3 Antibodies

All antibodies used throughout the project have been detailed in Table 2.2 along with dilutions for each technique in question.

Primary antibodies				
Antibody	**Species**	**Catalogue Number**	**Source**	**Dilution Factor (Method)**
Phospho-AMPKα^{T172}	Rabbit mAb	2535	Cell Signalling	1:1,000 (IB) 1:100 (PLA)
AMPKα	Rabbit mAb Mouse mAb	5831 2793	Cell Signalling	1:1,000 (IB)
Phospho-ACC^{S79}	Rabbit mAb	3661	Cell Signalling	1:1,000 (IB)
ACC	Rabbit mAb	3676	Cell Signalling	1:1,000 (IB)
Phospho-Raptor^{S729}	Rabbit mAb	2083	Cell Signalling	1:1,000 (IB)
Raptor	Rabbit mAB	2280	Cell Signalling	1:1,000 (IB)
Phospho-ULK1^{S555}	Rabbit mAb	5869	Cell Signalling	1:1,000 (IB)
ULK1	Rabbit mAb	8054	Cell Signalling	1:1,000 (IB)
Phospho-eEF2^{T56}	Rabbit mAb	2331	Cell Signalling	1:1,000 (IB)
eEF2	Mouse mAb	67550-1-Ig	Proteintech	1:1,000 (IB)
HIF-1α	Mouse mAb	610958	BD Pharmingen	1:750 (IB) 1:200 (PLA)
Cytochrome c	Mouse mAb	556432	BD Pharmingen	1:200 (IF)
α-Tubulin	Mouse mAb	3873	Cell Signalling	1:3,000 (IB)
Fluorescent and/or HRP-conjugated antibodies and fluorescent probes				
Hoechst	-	17533-AAT	Stratech	1:2,000 (IF) [10 mg/mL stock]
TRITC-Phalloidin	-	5783/12U	Bio-techne	1:40 (IF)
α-Mouse IgG (H+L) AlexaFluor 568	Goat	A-11031	Invitrogen	1:500 (IF)
Polyclonal Goat Anti-Mouse Immunoglobulins/HRP	Goat	P0447	Agilent	1:3,000 (IB – HIF-1α only)
α-Mouse IgG (H+L) AlexaFluor 680	Goat	A-21057	Invitrogen	1:5,000 (IB)
α-Rabbit IgG (H+L) DyLight 800 4×PEG	Goat	10733944	Invitrogen	1:5,000 (IB)

Table 2.2 *– List of antibodies used in this study.*

2.1.4 Pharmacological agents

991 AND BI-9774, 2nd generation pan-AMPK activators used in this project, were produced by AstraZeneca (AstraZeneca R&D, Cambridge, UK). BAY-3827, an AMPK selective inhibitor, was purchased from Selleck Chemicals supplied by Stratech (Stratech Scientific Ltd, Ely, UK). FG-4592, a pan HIFα prolyl hydroxylase inhibitor, was purchased from Tocris (Bio-Techne, Abingdon, UK). Puromycin, FCCP and rotenone was purchased from Merck (Merck, Dorset, UK). Oligomycin and antimycin A were purchased ChemCruz. (R)-MG-132 was purchased from MedChem Express. VEGF-A_{165} was purchased from Proteintech (Proteintech Europe Ltd, Manchester, UK).

2.1.5 Plasmids

All plasmids were purchased from AddGene (Watertown, MA, USA) or Promega (Promega, Southampton, UK) details of which are outlined in the table below.

Plasmid ID	Catalogue Number	Supplier	Expression Vector Type
pGL4.42[luc2P/HRE /Hygro]	E4001	Promega	Mammalian
pGL4.75[*hRluc*/CMV]	E6931	Promega	Mammalian

Table 2.3 *– List of plasmids used.*

Dash '–' indicates information is not applicable.

HIF-1α WT and mutant plasmids were generated by GenScript. Briefly, HIF1A GenEZ ORF Clone (RefSeq ID: NM_001530) was subcloned into pcDNA3.1(+)-myc-His A backbone vector, under a CMV promoter and a C-terminal Myc tag. The 6xHis tag was removed by mutagenesis from the parent plasmid, to generate the parent WT HIF-1α-C-Myc plasmid. Candidate serine (S) or threonine (T) phosphorylation sites that closely matched the AMPK consensus motif based on phospho-proteomics data (See Chapter 4) were mutated to alanine (A). Plasmids were sequenced by Sanger sequencing as a QC measure to verify that the desired residues were mutated.

Plasmid ID	Abbreviation	Epitope Tags
WT HIF-1α-C-Myc	WT-HIF-1α	C-Myc tag
HIF-1α-C-Myc S65A	S65A-HIF-1α	C-Myc tag
HIF-1α-C-Myc T652A	T652A-HIF-1α	C-Myc tag
HIF-1α-C-Myc S727A	S727A-HIF-1α	C-Myc tag
HIF-1α-C-Myc T652A and S727A	DM-HIF-1α	C-Myc tag
HIF-1α-C-Myc S65A, T652A and S727A	TM-HIF-1α	C-Myc tag

Table 2.4 *– List of GenScript plasmids used for HIF-1α mutagenesis studies.*

Abbreviations: DM, double mutant; TM, triple mutant.

2.1.6 Transfection Reagents

PEI stock solution (1 mg/ml) was prepared by dissolving linear PEI (PolySciences Europe, Hirschberg an der Bergstraße, Germany) in ddH_2O and adding 6 M HCl dropwise until the pH fell below 2.0. Once the PEI was dissolved, the pH was then readjusted to 7.0 using 10 M NaOH and subsequently sterile filtered by vacuum filtration using a 0.22 µm Steriflip (Merck). PEI aliquots were stored at −80 ºC until use. Plasmid transfection into HUVECs were performed using LipoJet (SignaJen, Frederick, Maryland, USA), except for luc2P/HRE/Hygro and *hRluc*/CMV plasmids which were performed using GeneJuice (Merck) for luciferase reporter assays.

2.2 Tissue Culture

All cells were maintained in a humidified incubator at 37 ºC, 5% CO_2 with media changes occurring every two days, under normoxia (21% O_2) unless stated otherwise. Specific culturing conditions for each cell type are described below.

2.2.1 HUVECs

Human umbilical cord vein endothelial cells (HUVECs) were used in this study. Several batches of pooled HUVECs were purchased from PromoCell (PromoCell GmbH, Heidelberg, Germany), therefore experiments were performed on different HUVEC pools simultaneously (i.e. biological replicate) unless stated otherwise. HUVECs were expanded in T75 flasks coated with 1% (v/v) gelatin (Merck, Gillingham, UK) and cultured in growth medium

comprised of EGM2 (PromoCell GmbH, Heidelberg, Germany) supplemented with growth factors, penicillin/streptomycin (penicillin (100 U/ml) and streptomycin (100 µg/ml) (Merck) and 10-20% (v/v) heat inactivated FBS (Cytiva, Little Chalfont, United Kingdom). The EGM2 SupplementMix contained the following: recombinant human epidermal growth factor (EGF, 5 ng/ml), basic fibroblast growth factor (bFGF, 10 ng/ml), long R^3 insulin-like growth factor (IGF, 20 ng/ml), vascular endothelial growth factor A 165 ($VEGFA_{165}$, 0.5 ng/ml), ascorbic acid (1 µg/ml), heparin (22.5 µg/ml) and hydrocortisone (0.2 µg/ml). Growth factor concentrations in EGM-MV2 SupplementMix were identical to EGM2 apart from heparin being omitted from the media. Unless stated otherwise, ECs were cultured in low-serum EGM2 with 2% (v/v) FBS conditions for all experimental conditions. Cells were seeded at ~2.1×10^4 cells/cm^2 until they reached 85-90% confluency prior to stimulation or treatment with pharmacological agents. For all experiments, ECs were used at P4-5.

Media	Supplements
Growth Medium	EGM2 with SupplementMix + 10% (v/v) FBS
Treatment Medium	EGM2 with SupplementMix + 2% (v/v) FBS
Transfection/Transduction Medium	Serum Free EGM-MV2 with SupplementMix

Table 2.5 *– Details of media conditions used for experiments.*

2.2.2 HEK293Ts

HEK293T were cultured and treated in DMEM GlutaMAX (ThermoFisher Scientific, Loughborough, United Kingdom) containing penicillin (100 U/ml) and streptomycin (100 µg/ml) and 10% (v/v) FBS. For subculturing or seeding, all cells were detached using 0.025% (w/v) trypsin and reseeded into the appropriate culture vessel for expansion or assays. HEK293Ts were used below passage 10 for lentivirus generation and below passage 30 for all other assays.

2.3 *In vitro* Hypoxia Studies

All experiments were carried out within the H35 Hypoxystation (Don Whitley Scientific, Bingley, UK) in a humidified atmosphere composed of 3% O_2/5% CO_2/92% N_2 gas mixture at 37ºC. The workstation sustains a controlled environment where factors such as oxygen, humidity and temperature can be specifically determined and maintained throughout. Replicate plates were set up at 21% O_2 as normoxia controls in standard tissue culture incubators. Reagents and plastics including media, pipette tips, buffers and fixatives were equilibrated in the workstation for at least 3-4 hours at the stated O_2 tension prior to use to purge oxygen dissolved in solution. Cells were lysed and harvested at the stated points *in situ* to prevent reoxygenation of samples.

2.4 Glucose Deprivation Studies

For all glucose/pyruvate deprivation (GPD) studies, HUVECs were seeded in M199 media (Sigma) containing 10% (v/v) FBS, 2 mM glutamine (Sigma), penicillin/streptomycin and heparinised ECGS (Merck). This was done to reduce the metabolic effect of various growth factors in EGM2 and allow them to be more responsive to changes in carbon substrates. Media was replenished two hours prior to the removal of glucose to prevent any inadvertent starvation-induced activation of AMPK. After two hours, media was switched over to glucose/pyruvate/glutamine-free DMEM supplemented with varying levels of glucose (0-1 g/L), 2mM glutamine, 1 mM pyruvate and 2% (v/v) FBS and heparinised ECGS for 6 hours until harvesting.

2.5 Cell Viability and Death Assays

2.5.1 CyQUANT™ LDH Cytotoxicity Assay

The CyQUANT LDH Cytotoxicity Assay (Invitrogen) were performed according to manufacturer's instructions. Cytotoxicity was measured as release of extracellular lactate dehydrogenase (LDH) that catalyses the production of formazan as a readout of enzyme activity. HUVECs were seeded at 10,000 cells per well in a Nunc™ 96-well plate (ThermoFisher Scientific) overnight and were subsequently treated with varying concentrations of BI-9774 for 24 hours. The following day, 50 µL of culturing media was transferred to a new plate, mixed with 50 µL pre-prepared Reaction Mixture, and incubated at RT for 30 minutes prior to adding 50 µL Stop Solution. Absorbance measurements were read

at optical density (OD) of 490 and 680 nm (as a reference wavelength) on the BMG Labtech CLARIOstar Plus plate reader. OD680 values were subtracted from OD490 values to account for background. Values from untreated wells were subtracted from treated wells to account for spontaneous LDH activity present in the serum-containing media.

2.5.2 CyQUANT™ Cell Proliferation Assay

The CyQUANT Cell Proliferation Assay (Invitrogen) were performed according to manufacturer's instructions. Briefly, media was aspirated from microplates and cells were washed twice with PBS and frozen at −20 ºC for later batch processing. Microplates were thawed and allowed to equilibrate to RT. Meanwhile the CyQUANT® GR dye/cell-lysis buffer solution was prepared by diluting CyQUANT® GR dye (1:400) in 1× Cell Lysis Buffer and 200 µL was added to each well. Microplates were incubated at RT for 5 minutes protected from light. Fluorescence readings were measured using BMG Labtech CLARIOstar Plus plate reader at λex/λem 488/525 settings. A cell titration was performed ranging from 0-50,000 cells/well in serum-free media overnight along with media only wells to account for background signal.

2.5.3 RealTime-Glo™ Annexin V Apoptosis and Necrosis Assay

RealTime-Glo™ Annexin V Apoptosis and Necrosis Assay were performed conducted according to manufacturer's instructions. The level of Annexin V binding to phosphatidylserine (PtS) and DNA release from loss of membrane integrity provided a readout apoptosis and necrosis, respectively. Briefly, HUVECs, cord blood ECFCs and adult ECFCs were seeded at a density of 10,000 cells/well in a white 96-well plate (Greiner Bio-One, Kremsmünster, Austria) until they reached ~80% confluency. After stated pre-treatments, 2× Detection Reagent was added to each well and incubated for 10 minutes at 37 ºC in a tissue culture incubator. Luminescence (apoptosis) and fluorescence (necrosis) λex/λem 488/525 nm readings were measured at stated timepoints on the BMG Labtech CLARIOstar Plus plate reader.

2.6 RT-qPCR

Total RNA was harvested from cells using RLT with 1% βME (v/v), DNase (I) treated to remove genomic DNA and purified using the RNeasy Mini Kit (QIAGEN, Hilden, Germany) according to manufacturer's instructions. RNA (1 µg) was reverse transcribed using qScript SuperMix

cDNA synthesis kit and further diluted in RNase free water. For each reaction, 10 ng of cDNA was amplified in a 10 µL reaction mixture containing SYBR Green (Bio-Rad, Hercules CA, USA), 600 nM forward and reverse primers (ThermoScientific, Cheshire, UK) and nuclease-free water (QIAGEN, Hilden, Germany). Primers were designed using NCBI primer BLAST tool and verified for primer specificity using the UCSC In-Silico PCR tool (http://genome.ucsc.edu/cgi-bin/hgPcr). TATA-binding protein (*TBP*) was used as the housekeeping gene as its values were unaltered by both hypoxia and BI-9774 treatment unlike β-actin (*ACTB*) and glyceraldehyde 3-phosphate dehydrogenase (*GAPDH*). All reactions were performed in triplicate, ran on QuantStudio 6 PCR system. CT values within 0.5 range were analysed using the $2^{-\Delta CT}$ ($\Delta CT = CT_{\text{gene of interest}} - CT_{\text{housekeeping gene}}$)method to provide arbitrary values for each biological/experimental replicate and expressed as such.

2.7 Immunoblotting (IB)

Cells were first washed once with HBSS/PBS and then subsequently lysed using Whole Cell Lysis Buffer or HEPES Lysis Buffer (AMPK kinase assays) supplemented with Roche PhosSTOP phosphatase inhibitor (Merck) and cOmplete mini EDTA-free protease inhibitor cocktails (Merck) on ice. Harvested lysates were centrifuged at 18,000 *g* at 4ºC for 15 minutes to obtain the supernatant. Protein concentration was determined using Pierce™ Coomassie (Bradford) Protein Assay Kit (ThermoFisher, Dartford, UK). Varying amounts of protein (5-30 µg) was prepared using 4× Bolt™ LDS buffer (Invitrogen) and 0.1 mM β-mercaptoethanol and boiled at 100 ºC for 5 minutes. Gel electrophoresis was carried out using 4-12% or 8% Bolt™ Bis-Tris Plus gels at 165 V (Invitrogen). Protein transfer was performed with Mini Blot Module with gels submerged in 1× Bolt™ Transfer Buffer with 10% MeOH (v/v) and transferred onto Immobilon PVDF-FL membranes for 1 h at 20 V. PVDF membranes were stained with Ponceau Red to confirm transfer of proteins and blocked in 5% skimmed milk/TBS for 1 hour rotating at RT.

Membranes were incubated with primary antibodies diluted in 5% BSA (w/v)/TBS-T overnight at 4 ºC. The following day, membranes were extensively washed with TBS-T and incubated with secondary fluorophore-conjugated antibodies (680- or 800-) in 5% milk/TBS-T for 1 hour at RT. Blots were scanned using LI-COR Odyssey CLx (LI-COR Biosciences UK Ltd., Cambridge, UK) and quantified using Image Studio Software. Chemiluminescence detection was used instead for membranes probed for HIF-1α/HIF-2α primary antibodies by incubation with HRP-conjugated secondary antibodies (DAKO Agilent, Santa Clara CA, USA) for 1 hour at RT. Signals were developed using Amersham ECL Select Western Blotting Detection

Reagent (Cytiva, Little Chalfont, UK) and imaged by radiography using the Xograph Compact X4 developer (Xograph Healthcare, UK). Band densitometry was carried out using LI-COR Image Studio Lite (version 5.2.5) for blots developed by near-infrared antibodies or Fiji Is Just Image J (FIJI) software for chemiluminescence blots developed by film.

2.8 Multiple Sequence Alignment

The following FASTA files were downloaded from NCBI according to the following NCBI RefSeq Accession IDs (Table 2.6) and aligned using EMBL-EBI Clustal Omega Multiple Sequence Alignment (https://www.ebi.ac.uk/Tools/msa/clustalo/). Figures were generated using RStudio.

Protein	Species	NCBI RefSeq Accession ID
HIF-1α	*H. Sapiens*	NP_001521.1
	M. musculus	NP_032247.1
	R. novergicus	NP_036730.2
	B. taurus	NP_001069013.1
	M. mulatta	NP_001039398.1
	C. elegans	NP_001023891.2
HIF-2α	*H. Sapiens*	NP_001421.2

***Table 2.6** – List of protein sequences used for MSA according to their NCBI RefSeq Accession IDs.*

2.9 Immunofluorescence (IF)

Cells were seeded onto coverslips and/or Ibidi µ-Slide 18 Well Glass Bottom (Thistle Scientific, Glasgow, UK). At treatment endpoints, cells were washed once with PBS and fixed using 4% (w/v) PFA for 15 minutes at RT. After the end of the fixation period, cells were washed twice with PBS and permeabilised with PBS 0.2% (v/v) Triton X-100 for 5 minutes. Cells were then incubated with primary antibodies diluted in 3% (w/v) BSA/PBS 0.2% (v/v) Triton X-100 overnight at 4 ºC on a rocking platform. After incubation with the primary antibodies, the coverslips/slides were washed three times with PBS 0.2% (v/v) Triton X-100 and then incubated with the appropriate fluorophore-conjugated secondary antibodies diluted in 3% (w/v) BSA/PBS 0.2% (v/v) Triton X-100 at RT in the dark. Following three PBS washes, cells were incubated with TRITC-Phalloidin for 20 minutes at RT in the dark and/or proceeded straight to Hoechst (1 µg/ml) staining for 5 minutes at RT. Cells were washed once more with PBS 0.2% (v/v) Triton X-100 prior to mounting. Fluoromount-G (ThermoFisher Scientific) was

used as the mounting medium and the coverslips were sealed with nail varnish and stored at 4 ºC prior to confocal imaging.

2.10 Proximity Ligation Assay (PLA)

HUVECs were seeded (5,000 cells/well) in an Ibidi 18-well glass bottom dish coated with 0.1% (v/v) gelatin. The following day, cells were subjected to 21% or 3% O_2 with/without BI-9774. To stabilise HIF-1α under 21% O_2, HUVECs were treated with MG-132 (10 μM) for 1 hour prior to treatment endpoint prior to fixation and permeabilization as described for immunofluorescence. Samples were blocked with Duolink® Blocking Solution for 1 hour in a humidified 37 ºC incubator. Samples were incubated with rabbit anti-phospho-AMPKα^{T172} (1:100) and mouse anti-HIF-1α (1:200) diluted in Duolink® Antibody Diluent in a humidified incubator overnight, rocking at 4 ºC. Negative controls contained no antibodies, only incubated with diluent solution overnight. Samples were processed as per manufacturer's protocols using In Situ Detection Reagents Green (λex/λem 495/527 nm) and mounted using the Duolink® In Situ Mounting Medium with DAPI. Images were acquired on a Leica TCS SP5 confocal laser scanning microscope with z-stacks collected at 20× magnification with an oil immersion objective. Total number PLA signals were quantified per cell across all samples and normalised to untreated control.

2.11 Bulk RNA-seq

2.11.1 RNA Extraction and Quality Control

RNA was extracted from 4 different pools of HUVECs treated with BI-9774 and subjected to 21% or 3% O_2 for 24 hours, cleaned up with RNA Clean & Concentrator (Zymo Research, Freiburg im Breisgau, Germany) and quantified by NanoDrop 2000 spectrophotometer. A total of 2 μg of RNA was diluted in nuclease-free 20 μL H_2O analysed by Bioanalyzer 2100 (Agilent, Santa Clara CA, USA) to determine RNA integrity number (RIN). All samples had RIN values greater than > 9. Single-end (100 bp) sequencing was performed by Mr Ivan Andrew on the Illumina NextSeq2000 (Illumina, San Diego CA, USA) at the MRC LMS Genomics Facility.

RNA-sequencing data derived from HUVECs, human aortic endothelial cells (HAECs) and healthy control ECFCs were generated by Dr Charis Pericleous and Dr Robert Maughan based in Vascular Sciences, National Heart and Lung Institute (NHLI), who kindly shared the dataset for AMPK subunit analysis.

2.11.2 RNA-seq Analysis

The RNA-seq workflow was conducted by Dr Yi-Fang Wang and Dr Jesus Urtasun at the MRC LMS Bioinformatics and Computing Facility. FASTQ files were processed using FastQC to assess quality of sequencing reads including sequence counts, % GC content and % duplicate reads. Reads were aligned to human genome assembly GRCh37/Hg19 using the STAR tool (v2.7.9a). Binary alignment map (BAM) output files from STAR alignment were converted into bigWig files and imported into Integrative Genome Viewer (Broad Institute, Cambridge, MA, USA) to visualise alignment. DESeq2 was used to calculate transcripts per million (TPM) from raw counts, which were then log transformed to produce log_2FC values along with adjusted p-values for differentially expressed genes (DEG). DEG analysis was performed for the following pairwise comparisons of interest: 3% UT over 21% UT, 21% BI-9774 over 21% UT and 3% BI-9774 over 3% UT. A significance threshold of FC > 1.5 and adjusted p-value < 0.05 applied as a cut off. Principal component analysis (PCA) and hierarchal clustering on principal components (HCPC) demonstrated that all replicates clustered based on treatment and/or oxygen tension.

2.11.3 Pathway Enrichment Analysis

Tables for each pairwise comparison containing list of DEGs along with log_2FC and adjusted p-values were uploaded onto QIAGEN Ingenuity Pathway Analysis (QIAGEN, Hilden, Germany) with cut-off thresholds of log_2FC +/− 0.58 and adjusted p-value < 0.05. Analyses were then exported into Microsoft Excel and filtered depending on z-activation score 1 > or < −1 (i.e., two standard deviations from the mean) and adjusted p-value < 0.05. Results were visualised on GraphPad Prism 9 software (GraphPad, San Diego, CA, USA).

2.12 Plasmid DNA Preparation

2.12.1 Bacterial Transformation and Culture

A total of 100 ng of plasmid DNA was mixed with 50 µL competent DH5α *E. Coli* cells or NEB® Stable (NEB, Hitchin, UK) on ice for 30 minutes. The mixture was then subjected to heat shock at 42 ºC for 30 seconds before being placed back on ice for 5 minutes. For bacterial outgrowth, SOC medium was added to the bacteria/DNA mixture and the tube was transferred to an

orbital shaker, rotating at 250 rpm, 37 ºC for 1 hour. Several dilutions of transformed bacteria were streaked onto LB agar plates supplemented either with ampicillin (100 µg/ml) or kanamycin (50 µg/ml) and incubated overnight at 37 ºC. Isolated colonies were inoculated in antibiotic-treated LB Broth overnight rotating at 250 rpm, 37 ºC.

2.12.2 Plasmid DNA Purification

Overnight bacterial culture was spun down at 4,000 *g* at 4 ºC for 15 minutes using Sorvall LYNX 4000 ultracentrifuge (ThermoFisher Scientific) to pellet bacteria. Plasmid DNA was extracted from the pellets using Plasmid Maxi Kit (QIAGEN, Hilden, Germany) according to manufacturer's instructions. DNA concentration was quantified on the NanoDrop 2000 spectrophotometer.

2.13 DNA Transfection

2.13.1 Plasmid Transfection (HEK293Ts)

HEK293Ts were seeded at 5×10^4 cells/cm^2 in a 6 cm dish plate and allowed to reach approximately 50% confluency for maximum transfection efficiency. The transfection solution for ECs was prepared by first diluting 2 µg of plasmid DNA (pDNA) in 150 mM NaCl. PEI was also diluted in 150 mM NaCl prior to being added to the pDNA/NaCl mixture with the final ratio of pDNA:PEI is 1:2.5. The resultant plasmid/transfection solutions were gently vortexed and incubated at RT for at least 30 minutes to allow for the formation of transfection complexes. Media was switched to OptiMEM to enhance transfection and the pDNA:PEI mixture was added drop rise across the dish for 24 hours. After the incubation period, DMEM (10% v/v FBS) was added for recovery. At 24-hours post-transfection, HEK293Ts were examined for GFP expression to examine transfection efficiency and were then either treated with selection antibiotics or with pharmacological treatments for downstream analysis.

2.13.2 Plasmid Transfection (HUVECs)

HUVECs were seeded at 15,789 cells/cm^2 in a 6-well plate containing EGM-MV2 2% (v/v) FBS for 16 hours prior to transfection. For overexpression studies, 1 µg pDNA was diluted in 1× LipoJet Transfection Buffer and LipoJet transfection reagent. HUVECs were transfected using pDNA (µg):LipoJet (µL) ratio of 1:2 for 48 hours in EGM-MV2 2% (v/v). At the 48-hour

time point, media was changed over to EGM2 2% (v/v) FBS with various treatments for up to 24 hours and lysed at the specified time point. For luciferase reporter assays, plasmids (pDNA) were diluted in OptiMEM (ThermoFisher Scientific, Loughborough, United Kingdom). GeneJuice was also diluted separately in OptiMEM prior to being added to the pDNA/OptiMEM mixture with the ratio of pDNA:GeneJuice being 1:3. The resultant plasmid/transfection solutions were gently vortexed and incubated at RT for at least 30 minutes to allow for the formation of transfection complexes.

2.14 HRE Luciferase Reporter Assays

The HRE luciferase plasmid (*luc2P*/HRE/Hygro) plasmid encodes the eastern firefly luciferase under the control of four HRE repeats whereas the h*Rluc*/CMV plasmid encodes the *Renilla* sea pansy luciferase under the control of a CMV promoter and serves as a control for invariant background expression. On the day of transfection, 1 µg HRE luciferase and 100 ng of *Renilla* luciferase (h*Rluc*/CMV) plasmids were diluted in OptiMEM and mixed with GeneJuice/OptiMEM as previously described in Section 2.12.1. Media was changed over to 800 µL serum-free EGM-MV2 and 200 µL of the transfection mixture was added dropwise into each well for 6 hours followed by addition of 1 ml EGM-MV2 (4%) for recovery to prevent cytotoxicity. The following day, media was replenished with fresh EGM2 2% with following drug treatments for 16 hours: DMSO (0.1% v/v), BI-9774 (10 µM) and FG-4592 (10 µM) to serve as a positive control for HIFα transcriptional activity under 21% O_2.

At the treatment endpoint, cells were washed once with PBS, lysed using 1X Passive Lysis Buffer (Promega, Southampton, UK) and placed on an orbital shaker for 15 minutes at RT. After scraping, lysates were transferred to 1.5 ml Eppendorf tubes and centrifuged at 4 ºC for 10 minutes to get rid of cellular debris. The Dual-Luciferase Reporter Assay system (Promega, Southampton, UK) was used to measure HIFα binding to HRE elements as a determination of transcriptional activity according to manufacturer's instructions. Luciferase activity (RLU) was quantified using BMG Labtech CLARIOstar Plus plate reader. Data analysis incorporated background subtraction from non-transfected cells treated with the Dual-Glo® luciferase assay and Stop & Glo® reagents. All replicates were normalised to UT wells (control) for individual biological replicates.

2.15 SAMS Peptide AMPK Kinase Activity Assays

Cells were lysed with HEPES Lysis Buffer and were processed as previously described for immunoblotting. A total of 250 µg of protein was incubated with rabbit anti-AMPKβ1/2 (SIP2), generated in house, and 10 µL of 50% (v/v) Protein A Sepharose bead slurry (Merck) overnight with rotation at 4 ºC. The immunocomplex was twice washed with HGE buffer 1% Triton X-100 and pulse centrifuged at 10,000 *g* for 30 seconds. The beads were resuspended in HGE assay mix, as previously described, and incubated at 37 ºC for 1 hour with vigorous shaking. After briefly centrifuging the beads, 20 µL of the supernatant was spotted onto P81 phosphocellulose paper and washed three times with a 1% (v/v) orthophosphoric acid solution. P81 papers were dried, placed in scintillation tubes with 2 ml of scintillation solution to determine ^{32}P incorporation.

2.16 Radiolabelled-ATP *In Vitro* Phosphorylation Assays

Bacterially produced human recombinant AMPK $\alpha_1\beta_1\gamma_1$ and $\alpha_2\beta_1\gamma_1$ were a gift from Dr Yang Chen. Recombinant AMPK$\alpha_2\beta_1\gamma_1$ and recombinant human HIF-1α (Abcam, Cambridge, UK) were diluted in HGE assay mix containing AMP (112.5 µM), ATP (125 µM) with $MgCl_2$ and 1 mM [γ-^{32}P]-ATP (Perkin Elmer) and incubated at 37 ºC for 1 hour with vigorous shaking. Bolt™ LDS sample buffer was added to the reaction mixture, boiled, and resolved on a 4-12% Bis-Tris gel in MOPS buffer. Gel was stained in InstantBlue (Abcam, Cambridge, UK), destained in 20% EtOH/5% glycerol for 5 minutes and dried for 2 hours at 80 ºC. Gels were imaged on the ChemiDoc Imaging System (Bio-Rad, Hercules CA, USA). The dried gel was placed in a cassette with a film for 1 hr exposure at RT in the darkroom. Phosphorylation signal was developed using Xograph Compact X4.

2.17 Phosphoproteomics

Mass spectrometry experiments were performed by Dr Pavel Shliaha, and phosphoproteomics analysis was conducted by Dr Alex Montoya at the LMS Proteomics and Metabolomics facility.

2.17.1 Sample Preparation

Conditions	ATP/$MgCl_2$
HIF-1α only	Yes
HIF-1α + AMPK$\alpha_1\beta_1\gamma_1$	No
HIF-1α + AMPK$\alpha_2\beta_1\gamma_1$	No
HIF-1α + AMPK$\alpha_1\beta_1\gamma_1$	Yes
HIF-1α + AMPK$\alpha_2\beta_1\gamma_1$	Yes

Table 2.7 *– In vitro kinase preparations for LC/MS^2.*

In vitro phosphorylation assays were performed according to 2.16 Radiolabelled-ATP *In Vitro* Phosphorylation Assays without [γ-^{32}P]-ATP and the following mixtures were sent for analysis (Table 2.7). The reaction was stopped by adding 20 µL of 5% SDS, 100mM chloroacetamide and 50 mM TCEP. 70 µL of sample was subjected to precipitated assisted capture (PAC) by addition of 70 µg of hydroxyl beads (2BScientific) and 100 µL EtOH [319]. The precipitated beads were washed three times with 100 µL 80% EtOH and digested overnight in 50mM ammonium bicarbonate buffer with 20 ng/µL trypsin and 10 ng/µL endopeptidase Lys-C shaking at 1,700 rpm. The digest was transferred to a new plate and the resin was washed with 10 µL of 1% trifluoracetic acid (TFA) followed by combining the washing solution with the digest.

2.17.2 Liquid chromatography mass spectrometry (LC/MS^2) analysis

Chromatographic separation was performed using an UltiMate™ 3000 RSLCnano System (ThermoFisher Scientific) coupled to an Orbitrap Exploris mass spectrometer (ThermoFisher Scientific) via an EASY-Spray source. Electro-spray nebulisation achieved by interfacing to Bruker PepSep emitters (PN: PSFSELJ10, 10µm). Peptide solutions were injected directly onto the analytical column (self-packed column, CSH C18 1.7µm beads, 150 µm × 35 cm) at

working flow rate of 1.25 µL/min for 8 minutes. Peptides were then separated using a 66-minute stepped gradient: 0-45% of buffer B for 66 minutes (75/20/5% MeCN/H_2O/DMSO + 0.1% FA), followed by column conditioning and equilibration. Eluted peptides were analysed by the mass spectrometer in positive polarity using a data-independent acquisition (DIA) mode as follows: an initial MS1 scan was carried out at 120,000 resolution with an AGC target of 3E6 for a maximum IT of 200ms, m/z range: 410-1650. A boxcar MS1 scan was followed using 120,000 resolution and sequential MS2 acquisition and fragmentation of ions at 30,000 resolution over 30 variable windows. AGC target set to 3E6 with maximum IT on auto. Normalised collision energy was set to 30%. Total run acquisition time was 80 minutes.

2.17.3 Raw Data Processing

Data were processed using the Spectronaut software (v18.3.230830.50606, Biognosys, Schlieren, Switzerland) [320]. Analysis was carried out in direct data-independent acquisition (DIA) mode with default settings and the following adjustments as follows:

Pulsar Search: library generation and database search carried out using default settings for a trypsin-specific digest as follows - missed cleavage rate set to 3 and variable modifications allowed for methionine oxidation, protein N-terminal acetylation and serine/threonine/tyrosine phosphorylation. PSM, Peptide and Protein group FDR = 0.01. Searches were carried out against the SwissProt *H. sapiens* (downloaded 20230130, 21,594 entries) and *E. Coli* protein sequence database (downloaded 20230130, 4,403 entries). Additionally, searches were also carried against a universal protein contaminants database (downloaded 20220604, 381 entries) [321].

Direct DIA analysis: a mutated decoy database approach was employed with protein q-value cut-off for the experiment set to 0.01 at the identification level. Quantification set to MS2 (integrated area) with proteotypicity filter set to 'only proteotypic' with imputation strategy disabled. Label-free quantification was performed using a method set to MaxLFQ [322]. PTM workflow option enabled in order to generate site level tables for phospho-sites, with a site localisation probability cut-off set to 0.75. PTM analysis settings as follows: – multiplicity enabled, flanking region = 14 and with PTM consolidation method set to sum all peptide intensities for a given PTM site group.

2.17.4 Results Processing

Exploratory and technical analysis of data carried out using in-house developed python pipeline with various visualisations using both the Plotly and Pandas plotting libraries. Spectronaut protein level output tables were filtered to remove hits to the contaminants database.

2.18 *In vitro* Seahorse (XFe96) Flux Analyzer Metabolic Phenotyping

Seahorse XFe96 Flux Analyzer (Agilent, Santa Clara CA, USA) measures oxygen consumption rate (OCR) and extracellular acidification rate (ECAR), providing a readout for mitochondrial respiration and glycolysis, respectively. HUVECs were seeded at 20,000 cells/well in quadruplicate onto gelatin-coated Seahorse XFe96 plate in EGM2 (2%) and allowed to adhere overnight. The following day, HUVECs were treated with either BI-9774 and/or VEGF-165 (20 ng/ml) for 24 h. On the day of assay, cells were switched over to unbuffered Seahorse XF DMEM supplemented with 5.55 mM glucose, 2 mM glutamine and 1 mM pyruvate (Agilent, Santa Clara CA, USA) with/without treatments in a non-CO_2 chamber at 37 ºC for 1 h. OCR and ECAR were measured according to four consecutive (mix/measure) cycle: 3-minute wait and 3-minute measure for baseline and injection readings. Changes in mitochondrial bioenergetics was determined by initially measuring baseline respiration, followed by injection of oligomycin (2.5 µM), FCCP (4 µM) and rotenone/antimycin A (2 µM). Oligomycin, a CV inhibitory, determines mitochondrial ATP production. Carbonyl cyanide-p-trifluoromethoxyphenylhydrazone (FCCP), a protonophore, permits calculation of maximal O_2 consumption. Injection of rotenone and antimycin A, inhibitors of CI and CIII, respectively, permit calculation of spare respiratory capacity as well as non-mitochondrial O_2 consumption (Figure 2.1).

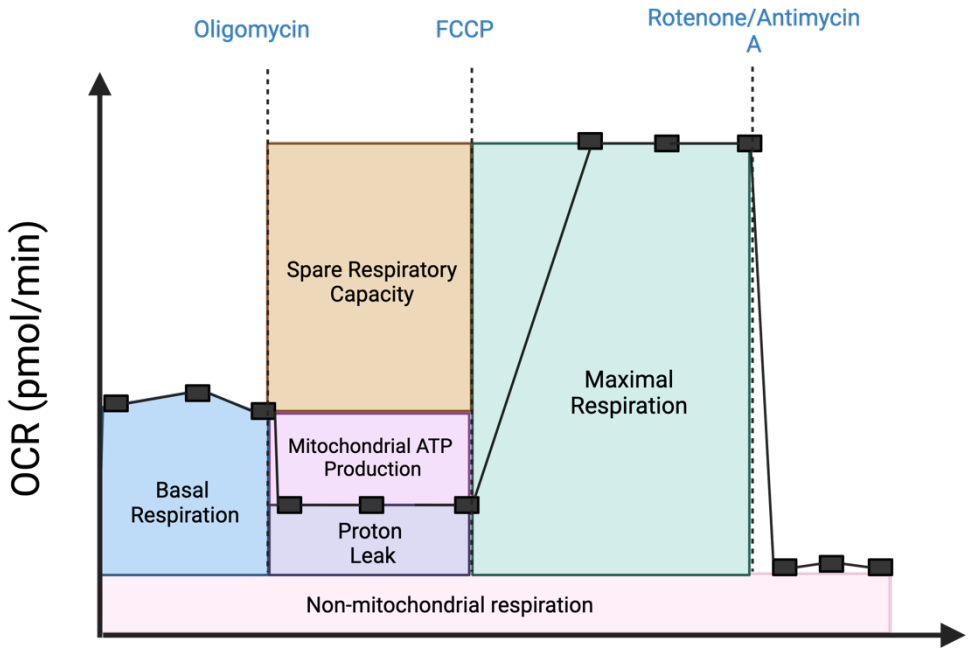


Figure 2.1 *– A schematic representing calculation of mitochondrial parameters based on the Agilent Seahorse XF MitoStress Assay.*

Figure created using BioRender.

Seahorse assays under hypoxia (3% O_2) were done by downloading Hypoxia Mode for Wave software (Agilent) and placing the XFe96 analyser in a Coy O_2 Control InVitro Glove Box (Wolflabs, Pocklington, UK) and left to equilibrate to 3% O_2 overnight. Seahorse XF DMEM, XFe96 sensors cartridges, calibrant solution were also left to hydrate in ddH_2O in the hypoxic chamber overnight. Injection compounds were left in the chamber for at least 1 hour prior to the assay. As a '/0%' O_2 reference, wells in column 12 only had calibrant solution with 100 mM sodium sulphite (Sigma) injections across all injection ports throughout the assay.

2.19 mtDNA Measurements

HUVECs were seeded in a 6-well plate and allowed to reach 80% confluency prior to any treatments. For chronic BI-treatments, HUVECs were initially seeded in a 100 mm dish at a density of 10,000 cells/cm^2 the day prior to treatment initiation with BI-9774 (10 μM) for 10 days. Upon reaching confluency before the endpoint, cells were split and placed into a new dish with treatment media. At day 10, cells were trypsinised and spun down at 300 *g* for 5 minutes. HUVECs were then resuspended in PBS for a wash step and centrifuged again to remove residual trypsin/media. The resultant cell pellet was resuspended in 200 μL PBS and frozen at −20 ºC until processing. Frozen pellets were treated with proteinase K prior to DNA extraction using DNeasy Blood & Tissue Kit (QIAGEN) according to manufacturer's

instructions. DNA was eluted in buffer AE for quantification by NanoDrop 2000 and further diluted down to 1.11 ng/µL in molecular ddH_2O. A total of 5 ng DNA was used per RT-qPCR reaction along with 600 nM DNA primers and SYBR Green diluted in molecular ddH_2O. DNA primers targeted were designed to target mitochondrial DNA regions corresponding to *MT-CO1* and *MT-ND1* (mtDNA) along with the single copy nuclear gene, *B2M*, encoding β_2 macroglobulin (nucDNA). Primers encoding mtDNA regions were aligned to the human genome to ensure that they did not amplify regions corresponding to nuclear mitochondrial pseudogenes. First, ΔC_T was calculated as $CT_{nucDNA} - CT_{mtDNA}$ to normalise against the amount of nuclear DNA present. Relative mtDNA copy numbers were calculated using $2 \times 2^{\Delta CT}$.

2.20 Flow cytometry (FACS)

2.20.1 Mitochondrial membrane potential ($\Delta\Psi_m$) and mass measurements

TMRM is a cationic lipophilic dye used to monitor changes in $\Delta\Psi_m$ as it accumulates in the negatively charged mitochondrial matrix in an inverse proportion to $\Delta\Psi_m$ according to the Nernst equation. Mitochondria with more negative $\Delta\Psi_m$ value will sequester more dye and vice versa [323]. MitoTracker Green also accumulates in mitochondria, independently of $\Delta\Psi_m$, by reacting to thiol residues of cysteine residues in mitochondrial proteins. To assess both short-term and long-term effects of AMPK activation on endothelial mitochondrial function, HUVECs were either treated with: (i) BI-9774 for 24 h or (ii) passaged and cultured in EGM2 2% with BI-9774 in the media for 10 days. HUVECs were incubated with 25 nM TMRM ($\Delta\Psi_m$) and 20 nM MitoTracker Green (mitochondrial mass) for 30 minutes prior to assay endpoint. As controls, oligomycin and FCCP were also used as controls for hyperpolarisation and depolarisation of mitochondrial membrane potential, respectively. Cells were washed three times with PBS, trypsinised and resuspended in phenol-free DMEM supplemented with 5.55 mM glucose, 2 mM glutamine and 1 mM pyruvate and analysed by FACS as soon as possible. Channels used for detection of TMRM and MitoTracker Green fluorescence were Texas Red and FITC on a BD FACSymphony™ A3, respectively.

2.20.2 EdU incorporation and Propidium Iodide Cell Cycle Analysis

HUVECs were seeded at a density of 15,789 cells/cm^2 in EGM2 2% FBS and allowed to settle for a few hours, before switching over to serum-free EGM2 overnight for cell cycle synchronisation. The following day, HUVECs were subjected to various treatments: BI-9774

treatment only, BI-9774 in combination with 21% O_2 versus 3% O_2 or BI-9774 pre-treatment followed by treatment with $VEGFA_{165}$ (20 ng). At stated timepoints, cells were trypsinised, washed twice with PBS and fixed with ice-cold 70% EtOH overnight prior to storage at −20 ºC. Post-fixation, cells were washed twice with PBS and treated with freshly prepared propidium iodide staining solution for 30 minutes at 37 ºC. Cells were subsequently analysed by FACS on a BD FACSymphony™ A3, counting 10,000 events per sample. FACS analysis was performed using FlowJo™ software (Becton Dickinson, Wokingham, UK). For EdU incorporation assays, HUVECs were treated with EdU (5 μM) for 24 hours and subsequently fixed in 4% PFA or 15 minutes at RT and washed three times with TBS. HUVECs were incubated in staining mixture comprised of Tris (pH 8.5, 100 μM), $CuSO_4$ (1 mM), Alexa Fluor 488 Azide (50 μM) and freshly prepared $_L$-ascorbic acid (100 mM) diluted in ddH_2O, which was added last to the mix. After staining, the cells were washed three times with TBS/0.5% Triton X-100 and counterstained with Hoechst before being resuspended in Cell Staining Buffer for FACS analysis.

2.21 Matrigel Tube Formation Assay *In Vitro*

HUVECs were seeded at a density of 21,277 cells/cm^2 in serum-free EGM2 in a 6-well plate overnight for 16 hours before proceeding with DMSO, BI-9774 and BAY-3827 treatment under 21% and 3% O_2 for 24 hours. Matrigel (Corning, Flintshire, UK) was thawed overnight at 4 ºC. Prior to harvesting, a pre-cooled Ibidi µ-Plate 96 Well 3D (Thistle Scientific) was coated with 10 µL Matrigel at a concentration of 10 mg/ml and allowed to polymerise for 2 hours at 37 ºC. HUVECs were trypsinised and were overlaid onto the Matrigel matrix at a concentration of 10,000 cells/well. $VEGFA_{165}$ (20 ng/ml) and suramin (100 µM), was used as a positive and negative control for tube formation, respectively. After 24 hours, brightfield images of the tubular networks were captured using the EVOS M7000 imaging system. After the imaging period, cells were stained with Calcein-AM (10 µM, Biolegend) to check cell viability and for network visualisation by fluorescence. Brightfield images were used for analysis using the Angiogenesis Analyzer plug developed by Carpentier *et al.* for FIJI (Figure 2.2) [324].

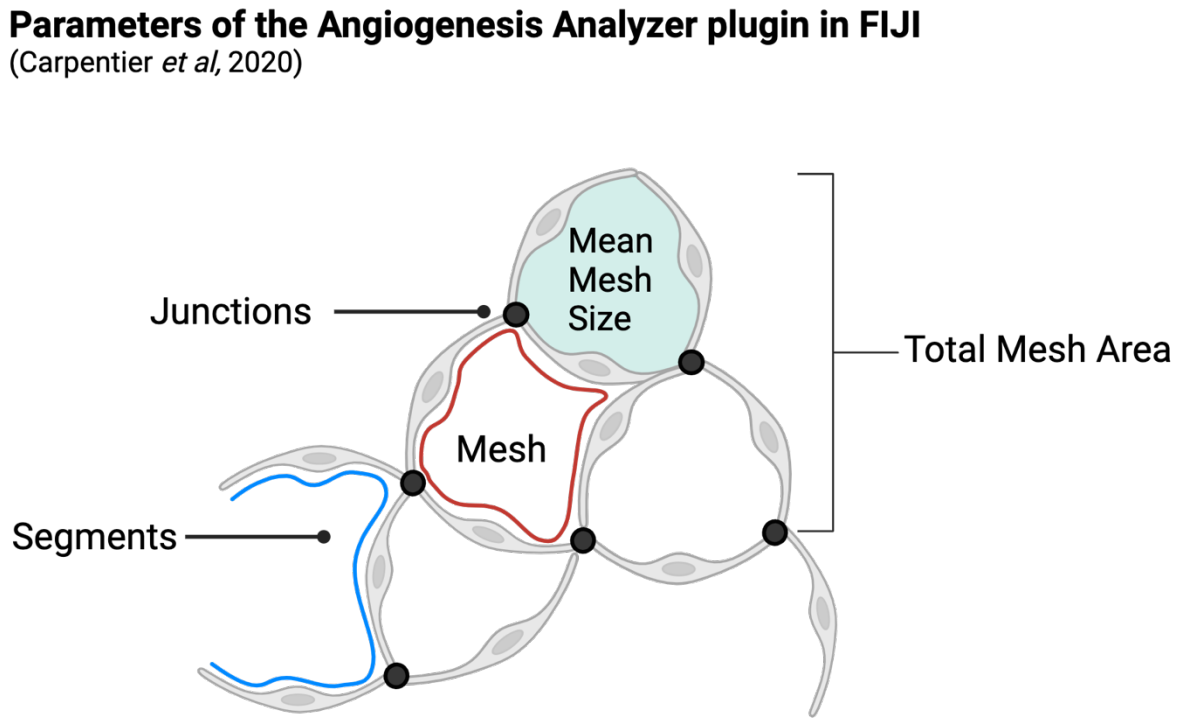


Figure 2.2 *– Definitions of the parameters measured using Angiogenesis Analyzer on FIJI.*

The following features were determined using the Angiogenesis Analyzer: junctions, segments, mean mesh size and total mesh area. Junctions is defined as the convergence of three cells. Segments is characterised by extremities connected by two junctions. Total mesh area is the sum of all the meshes within the image.
Figure created using BioRender.

2.22 Recombinant HEK293T Protein Expression and Myc-Trap® Immunoprecipitation

HEK293T were seeded in a 15 cm dish at 50,000 cells/cm^2 in DMEM GlutaMAX 10% (v/v) FBS and allowed to adhere overnight. The following day, cells were transfected with HIF-1α-c-Myc plasmids (30 µg) using PEI transfection reagent at a pDNA:PEI ratio of 1:2.5 diluted in OptiMEM for 24 hours. Cells were subsequently cultured in DMEM GlutaMAX for a further 24 hours and lysed in HEPES lysis buffer. Lysates were sonicated for 2 minutes for 2 cycles of 30 seconds ON/30 seconds OFF in a sonicating water bath at 4 ºC to release any HIF-1α in the nucleus. To determine if mutants caused impacted protein stability, lysates (30 µg) were analysed by immunoblotting and probed using Myc-Tag antibody and normalised to the mutant with the lowest expression. Lysates (200 µg) were incubated with 10 µL ChromoTek Myc-Trap® Agarose beads with end-over-end rotation at 4 ºC for 2 hours. Beads were spun at 4 ºC for 2 minutes at 4 ºC and the supernatant was transferred into a new tube and resuspended in HGE buffer, AMP (300 µM) and [γ-^{32}P]ATP/$MgCl_2$ *in vitro* kinase assays with rAMPK$\alpha_1\beta_1\gamma_1$ as described in Section 2.16.

2.23 Immunohistochemistry (IHC)

Harvested organs were fixed in 4% PFA with rotation 3-16 hours at RT and transferred to 70% EtOH. Paraffin embedding and haematoxylin and eosin (H&E) staining was kindly performed by Connor Preston at Imperial College Research Histology Facility. Tissue sections were baked for 1 hour at 55 ºC in an oven until the paraffin has melted and subsequently deparaffinized and hydrated according to the following wash sequence: Xylene (2 × 5 minutes), 100% EtOH (2 × 5 minutes), 70% EtOH (2 × 5 minutes) and ddH_2O (2 × 5 minutes) before proceeding to H&E staining. Sections were stained with Mayer's haematoxylin for 1 minute, rinsed in running tap water until it ran clear and rinsed in ddH_2O. Counterstaining was performed using Eosin Y solution for 5 minutes and rinsed using ddH_2O until the Eosin stopped streaking. Slides were dehydrated according to the following protocol: ddH_2O (2 × 5 minutes), 70% EtOH (2 × 5 minutes), 100% EtOH (2 × 5 minutes) and Xylene (2 × 5 minutes). Sections were mounted using Vectamount® mounting medium and left to harden overnight. Brightfield images were captured using 20× objective by the ZEISS Axioscan 7 microscope slide scanner.

2.24 *In vivo* Vascular and Metabolic Phenotyping of Global and EC-specific AMPK activation mouse models

2.24.1 Animal Husbandry

The list of mouse strains used in this study have been detailed in Table 2.7 below. All strains were maintained on a C57BL/6J background and backcrossed every 6-months to WT C57BL/6J to avoid genetic drift. Unless stated otherwise, all mice were maintained on Teklad Global Protein Rodent Diet (Inotiv Co, Blackthorn, UK) with calories (% kJ) from protein (22%), fat (12%) and carbohydrates (66%). Mice were group-housed in individually ventilated cages (IVC) and maintained on a 12-hour light/dark cycle at 22 ºC with *ad libitum* access to food and water, unless stated otherwise. All animal procedures were carried out in accordance with institution and national review committees. EC-D316A-Tg mice were generated according to Figure 2.3.

Strain Nomenclature (Strain ID #)	**Abbreviation**	**Source**
C57BL/6J (632)	B6/WT	Charles River UK
Prkag1 AMPKγ$_1$-WT-FLAG$^{fl/STOP/fl}$	WT-Tg	AstraZeneca, Mölndal, Sweden
Prkag1 AMPKγ$_1$-D316A-FLAG$^{fl/STOP/fl}$	D316A-Tg	AstraZeneca, Mölndal, Sweden
B6.Cg$^{Tg(Tek-cre)12Flv/J}$ (004128)	Tie2-cre	Jackson Laboratory, Farmington, CT, USA
Tmeme163$^{Tg(ACTB-cre)2Mrt}$ (003376)	β-actin-cre	Jackson Laboratory, Farmington CT, USA

Table 2.8 *– List of mouse strains used in this study.*

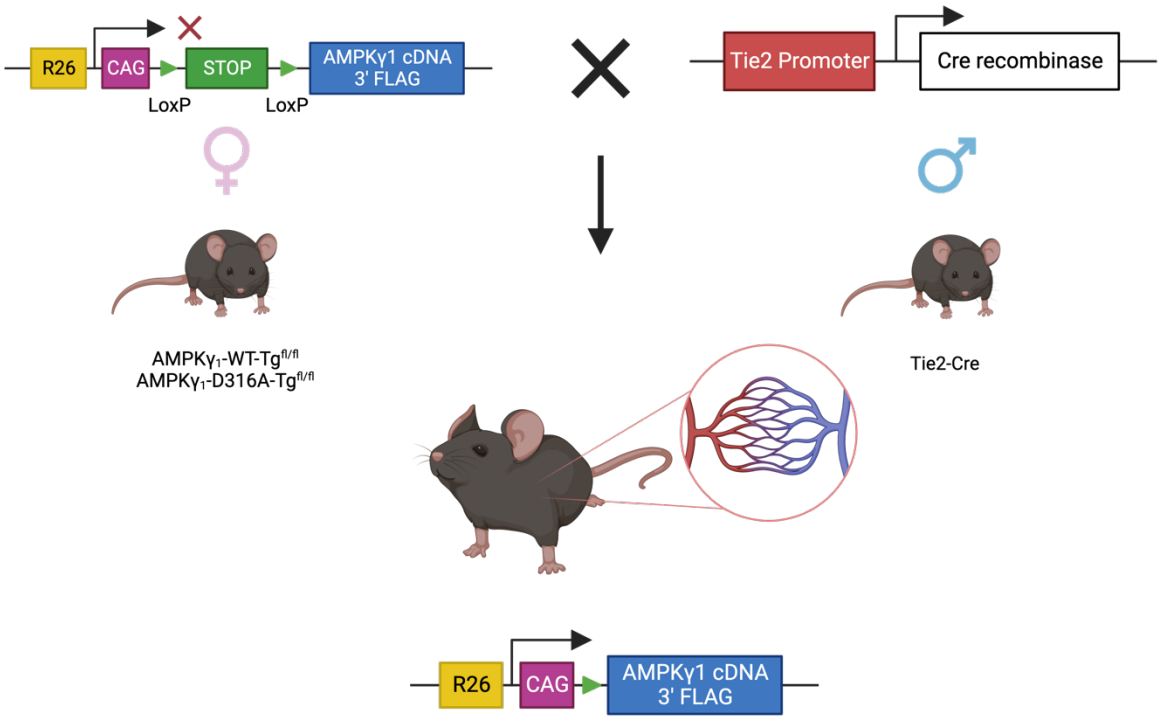


Figure 2.3 *– A schematic illustrating the breeding scheme used for the generation of the AMPK γ_1 EC-specific WT and D316A-Tg.*

Homozygote *Prkag1* AMPKγ_1-WT-FLAG$^{fl/STOP/fl}$ or AMPKγ_1-D316A-FLAG$^{fl/STOP/fl}$ females and heterozygote Tie2-Cre^{+} males were mated to generate F1 endothelial-specific AMPKγ_1 transgenic (Tg) mice. Figure created using BioRender.

2.24.2 Genotyping

Ear punch and tail biopsies were digested in 0.1 M NaOH at 100 ºC for 20 minutes before being neutralised by 1 M Tris HCl (pH 8.0) and stored at -20 ºC until further processing. Two forward primers were used to amplify regions of endogenous *ROSA26^{WT} (Prkag1^{WT})* and ROSA26 *Prkag1^{Flag}*-Tg (γ_1WT-Tg and γ_1D316A) sequences regions to differentiate between WT, heterozygote, and homozygote mice (Table 2.8). DNA from digested biopsies was amplified in a multiplex PCR reaction containing MyTaq™ HS Red Mix (Bioline, London, UK) *Cre* and *Prkag1^{WT}*/*Prkag1^{Flag}* primers. PCR reaction mix were loaded onto a 2 % (w/v) agarose/Tris-acetate-EDTA gel with SYBR Safe (ThermoFisher) to visualise bands. PCR products were resolved by gel electrophoresis at 120 V for 40 minutes and visualised by UV illumination on the GelDoc Go System (Bio-rad).

Primer ID	Sequence (5' → 3')	PCR Product Size
Cre (F)	GCCTGCATTACCGGTCGATGCAACGA	**Cre recombinase**: 800 bp
Cre (R)	GTGGCAGATGGCGCGGCAACACCATT	
Prkag1^{Flag} (F_1) [Across FLAG]	GGACGACGATGACAAGTGAG	**WT:** 365 bp **Heterozygote:** 365 bp and 498 bp **Homozygote**: 498 bp
Prkag1^{WT} (F_2)	CACGTTTCCGACTTGAGTTG	
Prkag1 (Rev)	TAAGCCTGCCCAGAAGACTC	

Table 2.9 *– Primer sequences used for genotyping.*

2.24.3 *Ex vivo* retina angiogenesis

Protocol was performed as outlined in Pitulescu *et al*., with minor modifications [325]. Breeding pairs were set up and monitored for birth of new litters. Between postnatal days 5-6 (P5-6), pups were weighed and then culled by cervical dislocation. Retinas were dissected out and placed in ice-cold PBS on ice until all retinas were. Tail samples were also obtained for genotyping by PCR later. PBS was then aspirated and replaced with 4% (v/v) PFA and incubated at RT for 30 minutes on a rotating wheel. After removal of the fixative solution, retinas were washed 5 times with PBS and stored in PBS at 4 ºC for later processing. Following an incision in the cornea, the outer layer of the eye along with lens and vitreous humour were removed with careful dissection under a stereomicroscope. Hyaloid vessels were also removed from the inner eye and then 4-5 radial incisions were made to divide the retina into quadrants.

Dissected retinas were then transferred into round-bottom Eppendorf tubes where they were blocked with retina blocking buffer (RBB) at 4 ºC overnight with rotation. Retinas were then washed 3 times at 20-minute intervals with PBLEC. Biotinylated *Griffonia Simplicifolia* isolectin B4 (IB4) was diluted in PBLEC solution (1:100). Retinas were incubated with diluted IB4 overnight at 4 ºC with rocking. The following day, retinas were washed 5 times (20 minutes) with wash buffer and stained with Alexa Fluor 546 fluorophore-conjugated streptavidin antibody diluted in RBB (1:400) for 2 hours at RT with rocking. Retinas were subsequently

washed 4 times (20 minutes) with wash buffer and then washed twice with PBS for 5 minutes. Retinas were then mounted onto glass slides and excess PBS solution was carefully removed with a 200 µL pipette tip. Fluoromount-G (~60 µL) was pipetted onto the coverglass and then inverted over the retina and sealed using nail varnish. Slides were stored at 4 ºC, protected from light exposure until imaging.

2.24.4 Diet-induced obesity studies

To examine how mice responded to diet-induced obesity (DIO), high fat diet with lard (HFD) was purchased from Ssniff (Ssniff Spezialdiäten GmbH, Soest, Germany), with calories (% kJ) derived from fat (45%), protein (20%) and carbohydrates (35%). At 8 weeks, mice were placed on HFD for 16 weeks with body weight being monitored and recorded on a weekly basis. At the end of the study, mice were culled by cervical dislocation for weighing of organs which were subsequently either flash-frozen in liquid nitrogen for downstream RNA/protein analysis or fixed in 4% (v/v) PFA for 3 hours to overnight for immunohistochemical analysis.

2.24.5 CLAMS

Energy expenditure was measured using the Columbus Oxymax® Comprehensive Lab Animal Monitoring System (CLAMS) (Columbus Instruments, Columbus, OH, USA), an open flow indirect calorimeter. Mice were individually housed in a sealed metabolic cages for 7 days with *ad libitum* access to food and water at 22 ºC. Body weight was recorded prior to and after being placed in the CLAMS system. O_2 consumption and CO_2 production were measured by a paramagnetic sensor and a nondispersive infrared sensor, respectively. The system was also able to monitor food intake, water intake and locomotor activity levels with all parameters were continuously monitored and recorded by a computer. These measurements were then used to calculate indirect calorimetry parameters such as VO_2, VCO_2 and RER by using the web-based analysis tool CaIR (https://www.calrapp.org/) by Mina *et al* [326].

2.25 Statistics

All HUVEC experiments were performed in parallel using at least 4-6 donor pools so all experiments are with multiple biological replicates, unless stated otherwise. Pairwise comparisons were performed using a one-tailed Student's t-test for HUVECs derived from the same donor, which were expanded and cultured simultaneously. For comparisons of three or more datasets, one-way ANOVA was performed followed by Dunnett's multiple comparisons

test when comparing against a control group. Repeated measures one-way ANOVA was used for the O_2 tensions experiments as the same donor of cells were used throughout the study. Two-way ANOVA was performed when assessing the effects of two independent variables (e.g., the combined effect of drug treatments and O_2 tension on necrosis/apoptosis) followed by Tukey's post hoc analysis to account for interactions between variables in order to compare across all possible comparisons. Two-way ANOVA followed by Bonferroni multiple comparison tests were used for specified comparisons. For experiments involving mice, data was initially analysed by the normality and lognormality test on GraphPad to examine if results were normally distributed for $n \geq 6$ replicates. If normality criteria was met, unpaired t-tests were performed otherwise Mann-Whitney tests were performed for non-normally distributed groups. Kruskal-Wallis non-parametric one-way ANOVA test followed by Dunn's multiple comparisons test post hoc for Matrigel tube formation assays as some of the groups were not normally distributed and the presence of outliers in some samples meant paired analysis could not be performed. All data are presented as mean ± standard error of the mean (SEM). Statistical significance was defined as follows: * p-value < 0.05, ** p-value < 0.01, *** p-value < 0.001 and **** p-value < 0.0001.

3. Chapter 3 – Regulation of AMPK under hypoxia

3.1 Introduction

The most extensively studied hypoxia response mechanism is the PHD/FIH-1/HIFα axis, which orchestrates the transcriptional changes to allow the organism to adapt to low O_2 (Section 1.8 Oxygen Sensing, Homeostasis and Hypoxia Inducible Factors). However, the transcription-independent adaptive responses to hypoxia are poorly understood, but are known to profoundly alter protein translation, ROS signalling, endoplasmic reticulum (ER) stress response and ATP:ADP/AMP ratio. ER stress response and ROS signalling lies beyond the scope of this thesis but is presented in Figure 3.1.

Global suppression of protein translation represents a major adaptive response, mediated in part through mTORC1 inhibition, although the exact mechanisms by which this occurs are not delineated. The tumour suppressor proteins TSC1 (hamartin) and TSC2 (tuberin), forms a complex to suppress mTORC1 signalling under poor growth conditions (e.g. low nutrient and growth factor availability). The binding of TSC1 to TSC2 results enhances the GTPase activating protein (GAPs) of TSC2 for Rheb (Ras homolog enriched in brain), a small GTPase. In its active state, Rheb•GTP stimulates mTORC1 activity leading to downstream phosphorylation of p70 ribosomal protein S6 kinase (S6K1), which phosphorylates ribosomal protein S6 thereby enhancing protein synthesis at the ribosome. mTORC1-mediated inhibitory phosphorylation of eukaryotic translation initiation factor 4E-binding protein 1 (4E-BP1) releases eukaryotic translation initiation factor (eIF4E) from its inhibitory complex with 4E-BP1 to initiate cap-dependent translation. TSC1/2 converts Rheb•GTP to its inactive form Rheb•GDP, effectively inhibiting mTORC1 signalling. Phosphorylation and binding of 14-3-3 adaptor protein is thought to restrain TSC2, preventing complex formation with TSC1.

A fall in O_2 triggers upregulation of regulated in development and DNA damage response 1 (REDD1) which competitively binds to 14-3-3, alleviating its inhibition of TSC2 [327]. Complex formation of TSC1 and TSC2 subsequently downregulates mTORC1 activity. Repression of global protein synthesis can also occur through phosphorylation and inhibition of eukaryotic translation elongation factor 2 (eEF2), a GTP-dependent protein that promotes ribosomal translocation of peptidyl-tRNA during the elongation phase of translation [328]. Phosphorylation of eEF2 at T56 by eEF2K inhibits protein translation by diminishing its affinity for the 80S ribosome and disrupts the translocation of ribosomal tRNA [329]. Accumulation of unfolded peptides in the ER lumen triggers activation of protein kinase R (PKR)-like ER kinase

(PERK), phosphorylating eukaryotic initiation factor 2α eIF2α, inhibiting the binding of the initiator methionyl-tRNA onto the ribosomal subunits.

Hypoxia results in decreased TCA cycle flux and O_2 availability for OXPHOS-dependent ATP production, followed by HIF-1α-mediated upregulation of NADH dehydrogenase:ubiquinone 1α subcomplex, 4-like 2 (NDUFA4L2) and certain microRNAs (e.g. mir120) to suppress complex I and ETC complex assembly, respectively (Figure 3.1) [216, 330]. As a result, the intracellular ATP:ADP/AMP ratio falls leading to nucleotide-dependent activation of AMPK via LKB1-mediated phosphorylation of T172. AMPK suppresses mTOR through phosphorylation of the mTOR-inhibitor Raptor on S792 and activates eEF2K through phosphorylation of S491/S492, effectively halting mRNA translation and other anabolic pathways linked to growth and proliferation. Concomitant activation of autophagy by AMPK leads to enhanced utilisation of recycled constituents in other catabolic processes to increase ATP levels. Therefore, hypoxia-induced activation of AMPK is essential for reducing cellular metabolic demand and diverting ATP for cell survival and adaptational processes. Intriguingly, multiple studies suggest that hypoxia does not in fact alter ATP:ADP/AMP ratio as intracellular O_2 levels only become limiting at 0.3% for cytochrome c oxidase activity [331-334].

AMPK exists in unique complexes depending on the isoform expression of α, β and γ subunits, reflecting the energetic needs in a particular cell type e.g., expression of γ_3 is restricted to skeletal myocytes for glycogen resynthesis following exercise [335]. Expression of γ_2 appears to be highest in the heart and mutations in γ_2 lead to Wolff-Parkinson-White syndrome, a cluster of cardiac phenotypes such as hypertrophy, bradycardia and electrophysiological abnormalities (e.g., ventricular pre-excitation). Despite the appreciation of differential isoform expression in certain tissues (e.g., skeletal and cardiac muscle), the composition of AMPK complexes in the endothelium has not been described extensively. To date, only a handful of studies have examined the effect of hypoxia on AMPK activity in response to hypoxia in ECs. Occurrences of nucleotide-independent activation of AMPK such as elevated Ca^{2+} leading to CAMKK-dependent phosphorylation of AMPKα^{T172} in endothelial cells *in vitro* [333, 336, 337]. Other studies have demonstrated that AMPK is deactivated by hypoxia in O_2 tensions <1.5% in the endothelium, but elevated activity was reported at 3% O_2, however the underlying mechanisms were not investigated [338] [339]. Putative links have also been observed *in vivo* to show there is some degree of interdependence between AMPK and HIFα interactions during ischaemia, where O_2 and nutrient deprivation both occur, but this has not been examined in ECs [178, 193].

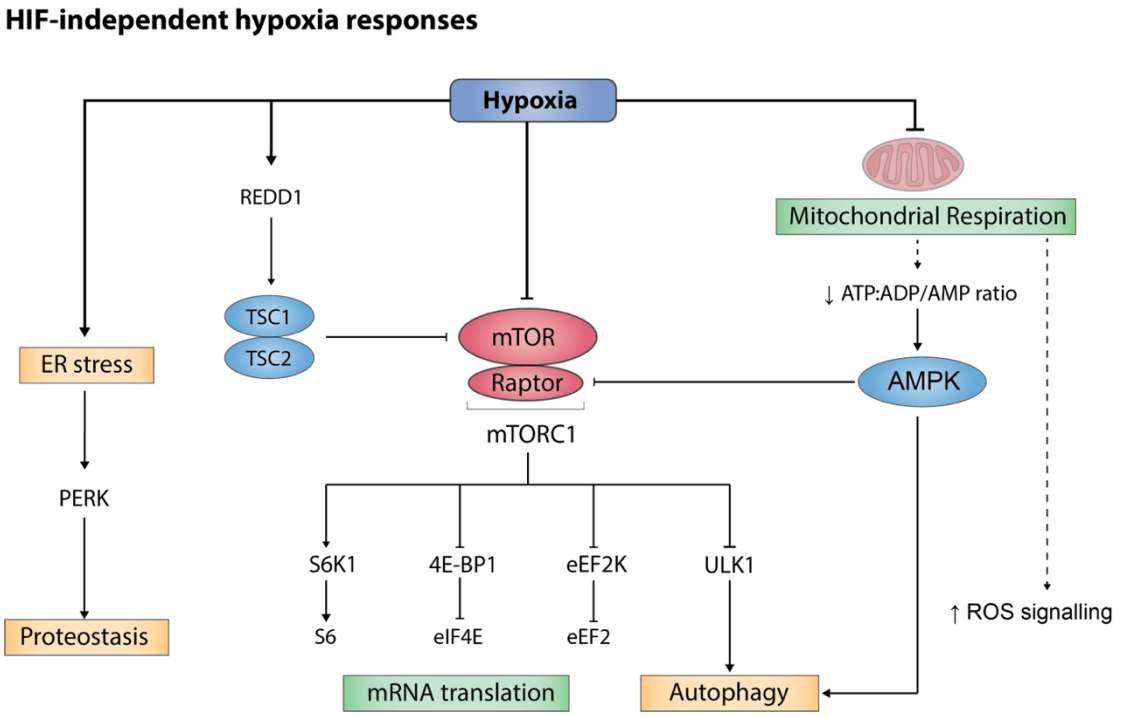


Figure 3.1 – *A simplified overview of HIF-independent responses to hypoxia.*

Low O_2 can elicit profound changes on multiple cellular processes. A marked reduction in global protein translation follows due to (i) inhibition of mTORC1 by REDD1 and TSC1/TSC2, (ii) activation of eEF2K to inhibit translation elongation and (iii) activation of PERK to halt translation initiation at the ribosomes. Decreased flux through the TCA cycle and O_2 availability for mitochondrial ATP production results in a fall in intracellular ATP and concomitant rise in AMP and ADP levels leading to AMPK activation, that provides another negative feedback loop by phosphorylating Raptor on S792 to inhibit mTORC1 whilst phosphorylating and activating eEF2K on S491/S492 to prevent protein translation and activating autophagy to recycle defunct proteins and organelles to generate ATP. The reduction in O_2 induces proteostasis mechanisms due to accumulation of misfolded proteins in the ER and generation of ROS species at the mitochondria which may alter downstream processes and/or compromise cell viability.

3.2 Hypotheses and Aims

There is little evidence towards the role of AMPK in the endothelial response to hypoxia and whether there is potential crosstalk between AMPK and HIF-1α signalling in the adaptive response to low O_2. There are two hypotheses under investigation in this chapter, which are outlined below with their corresponding aims below: -

Hypothesis 1: AMPK is dephosphorylated in response to hypoxia, due to resultant inhibition of protein translation.

Aim 1: Characterise the expression of AMPK subunit isoforms in EC subtypes based on transcript levels

Aim 2: Evaluate the use of the small molecule direct AMPK activator, BI-9774, in ECs

Aim 3: Investigate the effects of hypoxia on AMPK activity.

Aim 4: Initially examine whether changes in $eEF2^{T56}$ phosphorylation occur in hypoxic HUVECs.

Hypothesis 2: Activation of AMPK increases HIF-1α stability resulting in downstream transactivation of target genes.

Aim 5: Determine whether AMPK activation alters HIF-1α stabilisation either using (i) pharmacological activators (e.g., 991 or BI-9774) or (ii) physiological by glucose deprivation.
Aim 6: Assess whether BI-9774 alters HIF-1α-dependent transcription through the use of affects HRE-dependent luciferase activity and RT-qPCR analysis of HIF-1α targets.

3.3 Results

3.3.1 Transcript expression of AMPK subunits in endothelial subtypes and optimisation of the AMPK activator BI-9774

Based on the literature review in Table 1.1, ECs express both isoforms of the catalytic subunit α_1 and α_2 *in vivo* based on previous mouse studies. However, expression of other AMPK subunit isoforms aren't known and may differ in human ECs, particularly depending on their tissue of origin. Some of the novel AMPK activators in development can only target specific AMPK complexes e.g., Pfizer's PF-249 only activates complexes containing β1. Therefore, identifying isoform expression will determine suitability of the novel activator, BI-9774, for ECs.

To examine endothelial expression of AMPK isoforms, I utilised RNA-seq data available in house to obtain transcript per million (TPM) value for AMPK isoforms from healthy donor HUVECs, human aortic endothelial cells (HAECs) and endothelial colony forming cells (ECFCs). ECFCs are derived from circulating endothelial progenitors in the blood and 'grow-out' of long-term PBMC cultures, therefore represent another source of adult-derived ECs [340-342]. Across all EC subtypes, levels of *PRKAA1* transcripts are on average ~78 times higher compared to *PRKAA2*, suggesting preference for α_1 subunit complexes. B-subunit transcripts are the lowest compared to α- and γ-subunits (Figure 3.2A & B). Regardless, HUVECs, HAECs and ECFCs express both β_1 and β_2 isoforms, but β_1 levels are only significantly higher than β_2 in ECFCs (p-value < 0.0001) (Figure 3.2B)**.** As expected, ECs do not express γ_3 given it's a muscle-specific isoform but transcript levels of γ_1 and γ_2 exist across all subtypes. HUVECs and HAECs have ~1.5-fold higher levels of $\gamma_1 > \gamma_2$ (p-value < 0.0001). HAEC express significantly higher expression of γ_2 versus HUVEC (p-value = 0.029), but γ_2 transcripts are still lower than γ_1. ECFCs express both γ_1 and γ_2 at equal levels with expression of γ_2 expression significantly higher than both HUVECs and HAECs (p-value < 0.0001) (Figure 3.2C). Altogether, the data suggests that endothelial AMPK complexes are putatively composed of the catalytic α_1 subunit, associated with either β_1/β_2 and γ_1/γ_2 regulatory subunits. Therefore, pharmacological activation of AMPK requires pan-AMPK activators that are capable of targeting both β_1- and β_2-complexes.

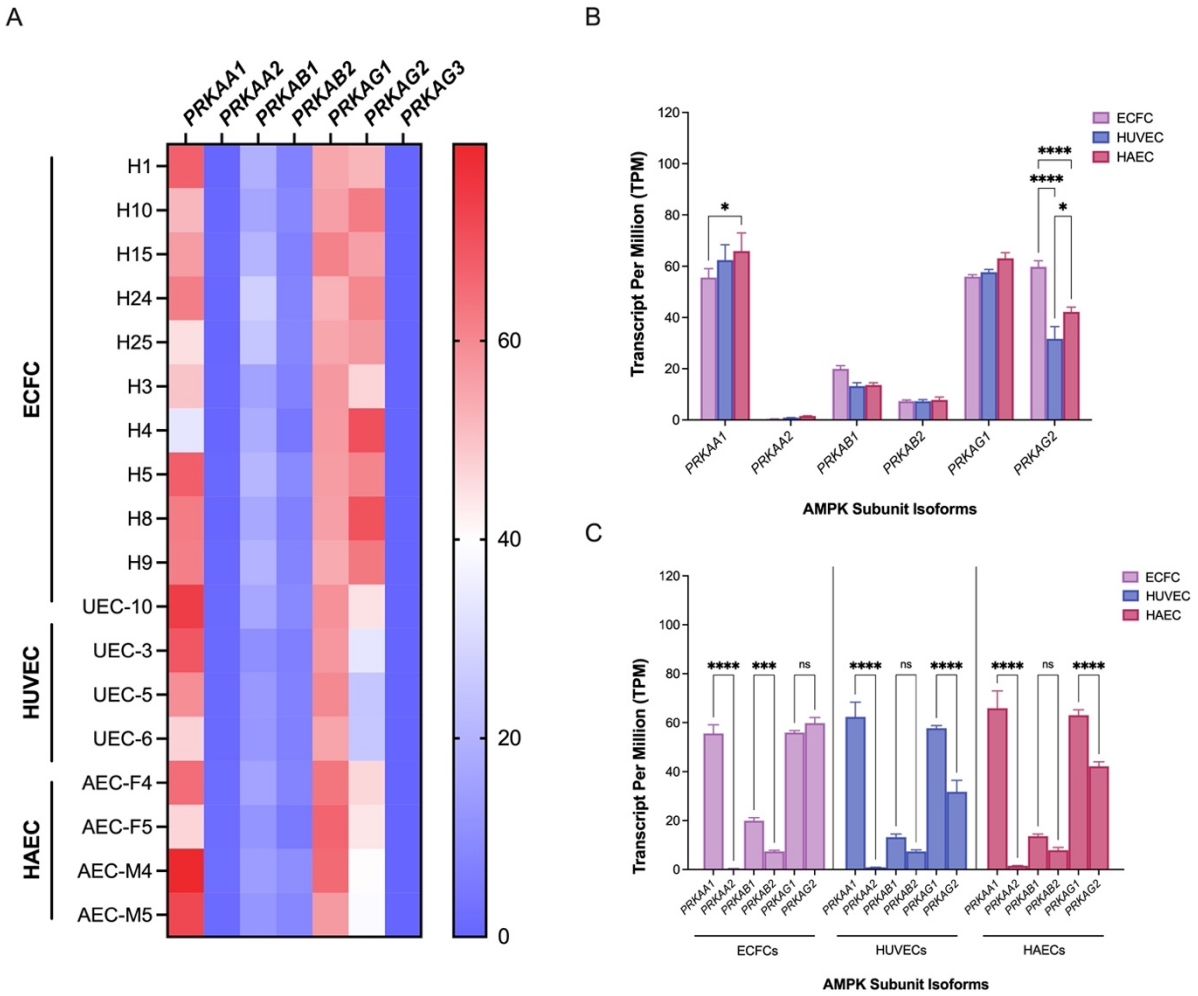


Figure 3.2 *– TPM expression of AMPK subunit isoforms in HUVECs, HAECs and adult ECFCs.*

HUVECs, HAECs and healthy control ECFCs were cultured under basal conditions until confluency. Purified RNA was analysed by RNA-sequencing. TPM values were obtained for the catalytic subunits α_1 (*PRKAA1*) and α_2 (*PRKAA2*); the regulatory scaffolding subunits β_1 (*PRKAB1*) and β_2 (*PRKAB2*); and the regulatory nucleotide-binding subunits γ_1 (*PRKAG1*), γ_2 (*PRKAG2*) and γ_3 (*PRKAG3*).
(A) A heatmap to visualise differences in TPM expression of subunit isoforms across HUVECs (n=4 single donors), HAECs (n=4 single donors) and healthy control ECFCs (n=11 donors). Range across subunit isoforms is 0-80 TPM. (B) A graph showing variability in isoform expression across different EC subtypes.
(C) A graph displaying intra-subunit isoform preferences across all three EC groups. All data is displayed as mean ± SEM. Data analysis was performed using ordinary two-way ANOVA analysis by Tukey's post hoc analysis, ns, not significant; * p-value < 0.05, ** p-value < 0.01, *** p-value < 0.001, **** p value < 0.0001.

BI-9774 is a potent pan-AMPK activator, originally developed by Boehringer-Ingelheim, allosterically activating AMPK by binding to the ADaM site lying between the α- and β-subunits. BI-9774 has previously been used to increase glucose tolerance in a rodent diabetes model and inhibit progression of prostate and radioresistant colon cancer cells as previously mentioned (Section 1.7.3 First- and Second-Generation AMPK activators). BI-9774 has not been used in ECs, therefore I performed a dose-response experiment on HUVECs to identify the optimal drug concentration. AMPK activity was determined by quantification of phospho-ACC^{S79} levels as it provides a sensitive readout of downstream AMPK activation by

immunoblotting following 1 hr treatment. BI-9774 appears to be highly potent, as exhibited by the robust increased ACC^{S79} phosphorylation in HUVECs seen at the lowest dose of 100 nM BI-9774 (p-value < 0.01) and reaching maximal phosphorylation at 25 μM (p-value < 0.0001) (Figure 3.3).

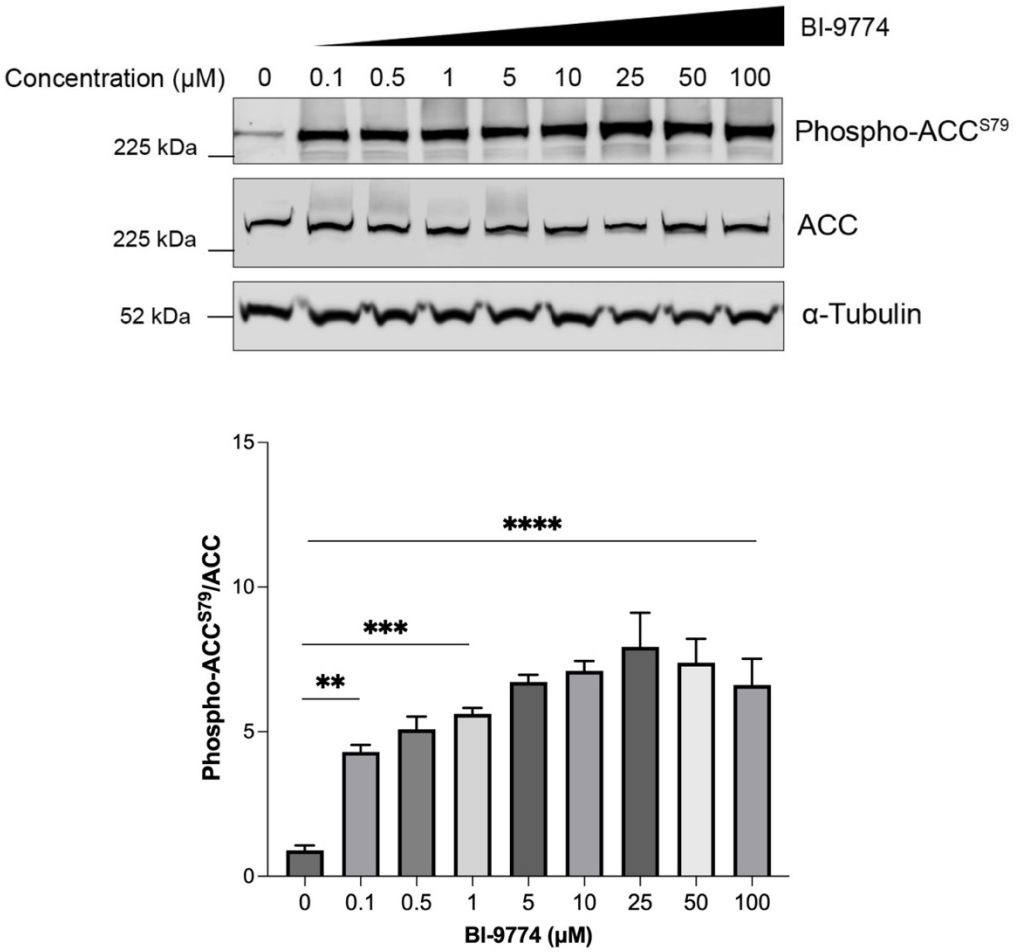


Figure 3.3 *– The effect of increasing BI-9774 concentration on ACC^{S79} phosphorylation in HUVECs.*

HUVEC lysates following treatment either with the vehicle DMSO (0 μM) or with increasing doses of BI-9774 (0.1-100 μM) for 1 h prior to analysis by immunoblotting. The immunoblot (upper panel) demonstrates robust activation of AMPK reflected by phospho-ACC^{S79} levels and quantification of phospho-ACC^{S79} to ACC (bottom panel). Data is presented as mean ± SEM with n = 3 biological replicates. Statistical analysis was performed one-way ANOVA with Dunnett's multiple comparisons test with ns, not significant; ** p-value < 0.01, *** p-value < 0.001 and **** p-value < 0.0001.

The effect of BI-9774 on cell viability and cytotoxicity was assessed by CyQUANT Cell Proliferation and CyQUANT LDH Release Assays, respectively. The former quantified cell number through binding of the CyQUANT® GR dye to nucleic acids whereas the latter measured levels of extracellular LDH, which only occurs during apoptosis, by absorbance at 490 and 680 nm. HUVECs were treated with varying concentrations of BI-9774 for 24 hours and assayed afterwards. BI-9774 0 μM corresponded to vehicle treatment (DMSO) and served as the control (Figure 3.4). Between concentrations of 1-5 μM, BI-9774 had little to no effect

on cell number and extracellular LDH levels. At 10 μM, a significant increase in cell number was observed (p-value = 0.0303) but no change in LDH levels compared to control. At 50-200 μM, there was a considerable reduction in cell number (p-value ≤ 0.0005), particularly at 200 μM, that coincided with significantly increase in LDH levels (p-value < 0.0002). Based on these results, 10 μM BI-9774 was selected as the concentration for future assays, as it provided maximal activation of AMPK and its downstream target ACC without compromising HUVEC viability.

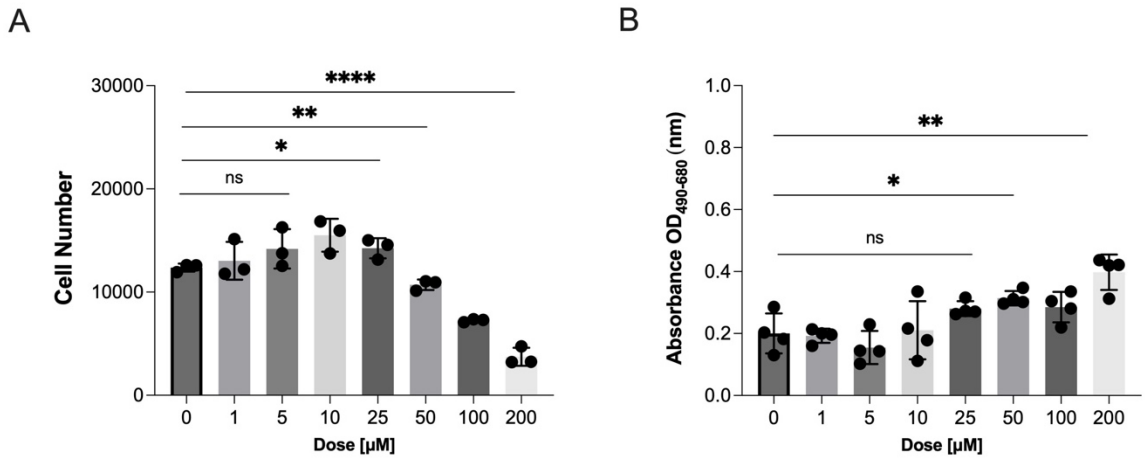


Figure 3.4 *– The effect of BI-9774 on endothelial viability and cytotoxicity.*

HUVECs were treated with either DMSO (0 μM) or increasing concentrations of BI-9774 for 24 h. (A) Cell viability was determined by cell number, quantified using the CyQUANT Proliferation Assay. (B) Drug cytotoxicity was determined using by LDH release into cultured media using CyQUANT LDH Release Assay. All data is displayed as mean ± SEM with n = 3-4 biological replicates. Data analysis was performed using paired t-tests, ns, not significant; * p-value < 0.05, ** p-value < 0.01, *** p-value < 0.001, **** p value < 0.0001.

To assess how long BI-9774-mediated AMPK activation persists in culture, HUVECs were treated with 10 μM BI-9774 for 0-48 hours compared to DMSO (Figure 3.5). Levels of phospho-AMPK^{T172} and phospho-ACC^{S79} were quantified by immunoblotting. No striking differences were observed in phospho-AMPK^{T172} levels, as AMPK appears to be basally phosphorylated in HUVECs, although band densitometry analysis only showed significant increase in phosphorylated AMPK at 6 hours. Downstream analysis of AMPK's substrate, ACC, showed increased phosphorylation starting as early as 0.5 hours (paired t-test, p value= 0.09). Phospho-ACC^{S79} levels were significantly increased between 6 and 24 hours, ~3-4-fold compared to the control and phosphorylation maintained for up to 48 hours without replenishing media (Figure 3.5). There were no significant differences in total AMPK and ACC in response to BI-9774 compared to across all time points examined (Figure 3.5D & E).

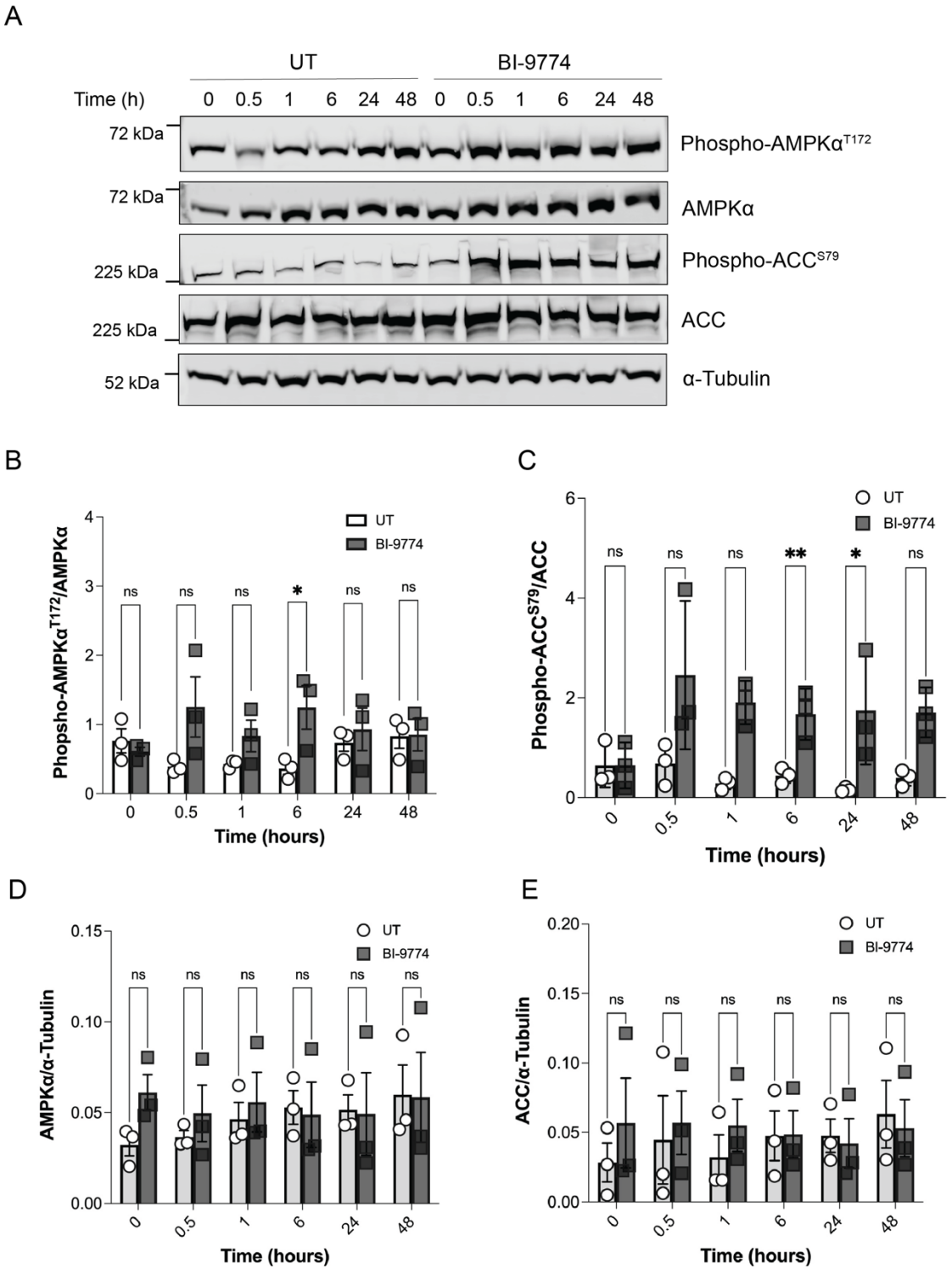


Figure 3.5 *– BI-9774 treatment time course in HUVECs.*

HUVECs were incubated in the presence or absence of BI-9774 (10 μM) for 0-48 h prior to analysis by Western blotting.
(A) Representative immunoblot showing levels of phospho-AMPKα^{T172}, AMPKα, phospho-ACC^{S79}, ACC with α-Tubulin as the loading control. All signals were normalised initially to α-Tubulin prior to ratiometric calculations.
(B) Quantification of phospho-AMPKα^{T172} normalised to total AMPKα.
(C) Quantification of phospho-ACC^{S79} normalised to total ACC.
(D) Quantification of AMPKα normalised to α-Tubulin.
(E) Quantification of ACC normalised to α-Tubulin.
All data is displayed as mean ± SEM with n = 3 biological replicates. Data analysis was performed using paired t-tests, ns, not significant; * p-value < 0.05, ** p-value < 0.01.

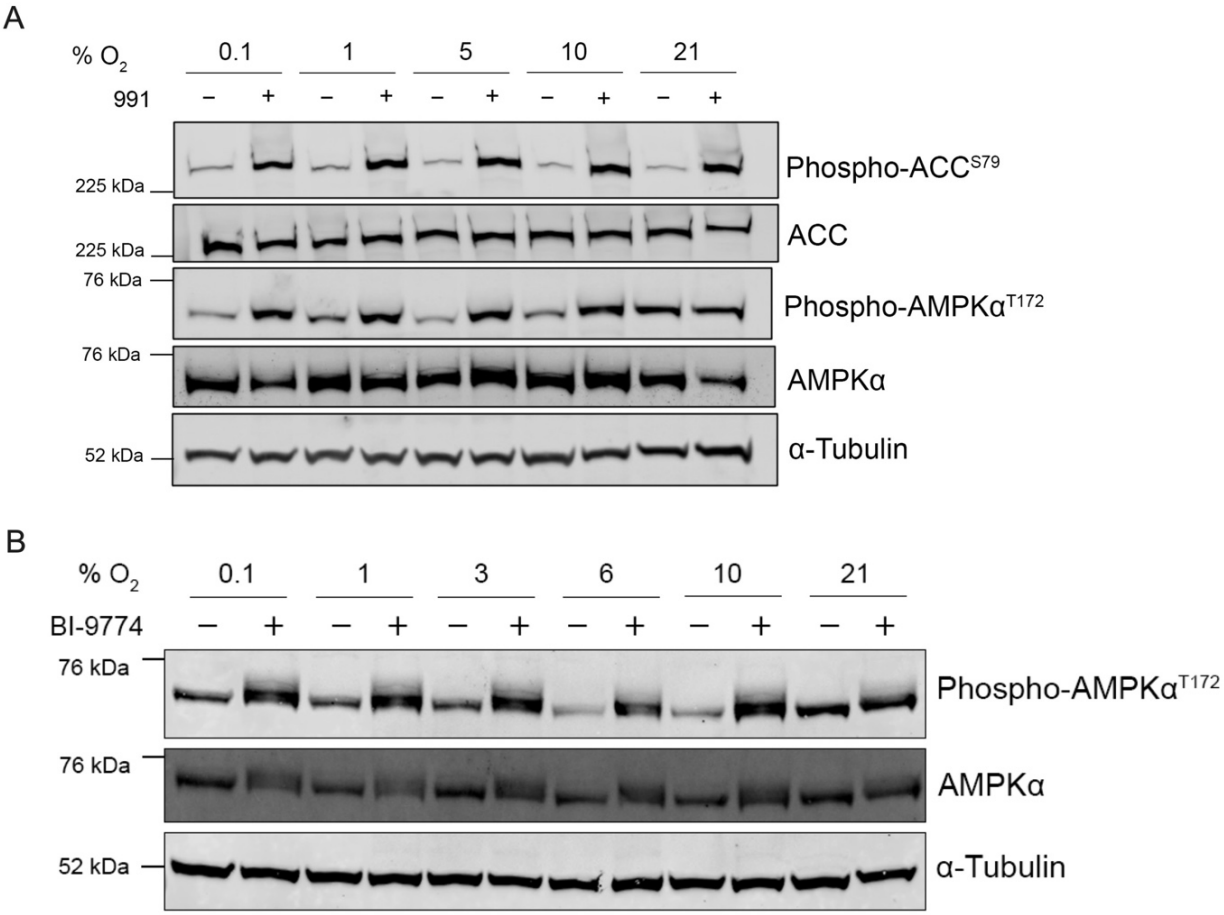
3.3.2 The effect of hypoxia on AMPK activity in ECs

Canonically, AMPK is thought to be activated under hypoxia following inhibition of the mitochondrial respiratory chain, which in turn triggers a rapid decrease in ATP:ADP/AMP ratio. As mentioned previously in Section 1.3 Endothelial Metabolism, ECs are highly dependent on aerobic glycolysis for ATP production therefore suppression of endothelial mitochondrial function under hypoxia may not impact AMPK signalling. Several oxygen tensions were chosen ranging from 0.1% O_2 (near anoxia), 1% O_2 (moderate hypoxia), 3% O_2 (mild hypoxia), 5-10% O_2 (physiological hypoxia, termed 'physioxia') and 21% O_2 (tissue culture normoxia or hyperoxia). HUVECs were placed in the hypoxic workstation for 1 hour or 24 hours following media changes with pre-equilibrated media at the chosen O_2 tension. In the initial studies, the benzimidazole derivative small-molecule 991 (50 μM) was used to activate AMPK (Figure 3.6A). Similar to BI-9774, 991 activates AMPK upon binding to the ADaM site but a caveat is its preference for targeting β_1 containing AMPK complexes although it can activate β_2 complexes at higher concentrations. Given that ECs express both β_1 and β_2, 991 was phased out in favour of BI-9774 as it was more potent, targeted both β_1 and β_2 complexes equally and can also be used *in vivo*, unlike 991.

The experiment was repeated recently with BI-9774 but only examined early response to treatment (1 hour) and expanded to include more physiologically relevant O_2 tensions (3-10% O_2). Phospho-AMPKα^{T172} levels were analysed by immunoblotting, followed by an *in vitro* kinase assay on immunoprecipitated AMPK from the same lysates to provide quantitative data on AMPK activity (Figure 3.6). At 21% O_2, there was no visible differences between control and 991/BI-9774 treatment (Figure 3.6A-B). Densitometry analyses revealed no significant differences between untreated HUVECs compared to those treated with BI-9774 regardless of O_2 tension (Figure 3.6C, top). No significant differences in phospho-AMPKα^{T172} in 21% O_2 untreated HUVECs versus those exposed to O_2 tensions 0.1-10% (Figure 3.6C, bottom).

Further work was done by performing *in vitro* kinase assays, as it provided a far more sensitive readout of AMPK activity. Pairwise comparisons of untreated versus BI-9774 kinase activities showed that BI-9774 significantly increased AMPK activity under hypoxia at all stated O_2 tensions, apart from HUVECs cultured 3% O_2 and 21% O_2 (Figure 3.6D, top). In untreated HUVECs, there was no significant differences in AMPK activity when comparing 21% O_2 to 10% O_2 (Figure 3.6D, lower). However, there was a significant reduction in AMPK kinase activity in HUVECs exposed to 1-6% O_2 (>2-fold reduction, p-value < 0.05) when compared to their normoxic counterparts (Figure 3.6D, lower). Exposure to near-anoxic conditions (0.1%

O_2) can potently trigger a bioenergetic crisis in most cells, falling below the threshold for cytochrome *c* oxidase [COXIV, complex IV (CIV)] activity (~0.3% O_2), the terminal enzyme complex of the electron transport chain (ETC). COXIV facilitates the reduction of O_2 to H_2O, thus it is considered to be a major regulator of mitochondrial ATP production. No significant differences were noted between 0.1% O_2 versus 21% in untreated samples, although it appears to follow the same trend as HUVECs cultured at 1 or 3% O_2 with a 42% reduction in activity (Figure 3.6D, bottom). Kinase activity assays showed no significant difference between untreated and BI-9774 HUVECs at 21% O_2, although BI-9774 appears to elevate AMPK activity (Figure 3.6D, top). Further examination of other validated AMPK substrates in response to chronic exposure at the stated O_2 tensions showed no significant differences in levels of ACC^{S79}, $Raptor^{S792}$ and $ULK1^{S555}$ phosphorylation based on O_2 tension in untreated samples. No significant differences were reported when examining pairwise comparisons between control and 991-treated HUVECs at the states O_2 tensions (Figure 3.7).


A
% O2
0.1
1
5
10
21
991
225 kDa
Phospho-ACCS79
225 kDa
ACC
76 kDa
Phospho-AMPKαT172
76 kDa
AMPKα
52 kDa
α-Tubulin
B
% O2
0.1
1
3
6
10
21
BI-9774
76 kDa
Phospho-AMPKαT172
76 kDa
AMPKα
52 kDa
α-Tubulin

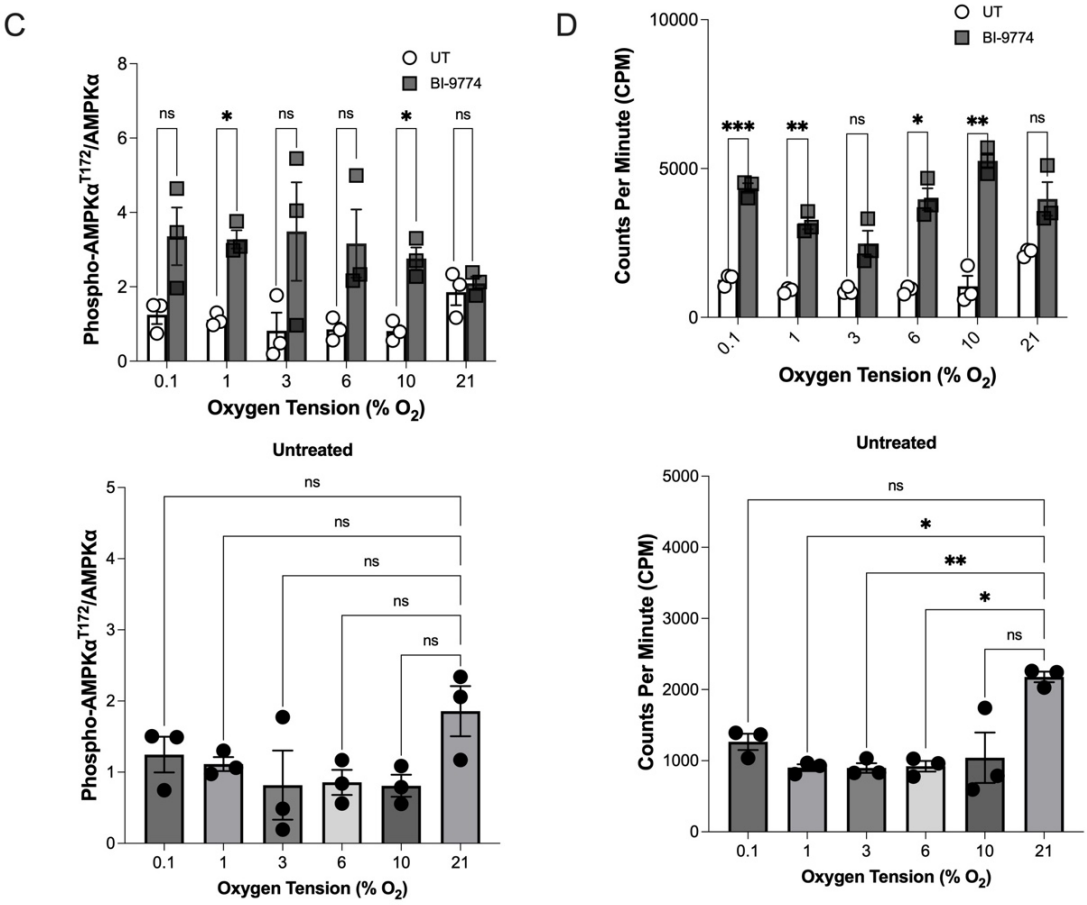

C
UT
BI-9774
Phospho-AMPKαT172/AMPKα
Oxygen Tension (% O2)
D
Counts Per Minute (CPM)
Oxygen Tension (% O2)
Untreated
Phospho-AMPKαT172/AMPKα
Oxygen Tension (% O2)
Untreated
Counts Per Minute (CPM)
Oxygen Tension (% O2)

Figure 3.6 *– The effect of acute exposure to differing O_2 tensions on AMPK activity.*

HUVECs were exposed to different O_2 tensions for 1 hour in the absence or presence of 991 (50 μM) or BI-9774 (10 μM).
(A) Representative immunoblot showing levels of phospho-AMPKα^{T172}, AMPKα, phospho-ACC^{S79}, ACC ± 991 treatment.
(B) Representative immunoblot showing levels of phospho-AMPKα^{T172}, AMPKα, phospho-ACC^{S79}, ACC ± BI-9774 treatment.
(C) Quantification of phospho-AMPKα^{T172} normalised to total AMPKα with pairwise comparisons between UT and BI-9774 treatment (upper) and multiple comparisons between untreated samples across all O_2 tensions (lower)
(D) Incorporation of [γ-^{32}P]-ATP based on *in vitro* AMPK kinase assays using immunoprecipitated AMPK complexes from matched lysates with pairwise comparisons between UT and BI-9774 treatment (upper) and multiple comparisons between untreated samples across all O_2 tensions (lower).
α-Tubulin was used the loading control for the immunoblots in (B) for initial normalisation prior to ratiometric calculations for BI-9774 treatment only. All data is displayed as mean ± SEM with n = 3 biological replicates. Data analysis was performed using paired t-tests for comparisons between UT and BI-9774 at each O_2 tension whereas repeated measures one-way ANOVA followed by Dunnett multiple comparisons test, ns, not significant; * p-value < 0.05.

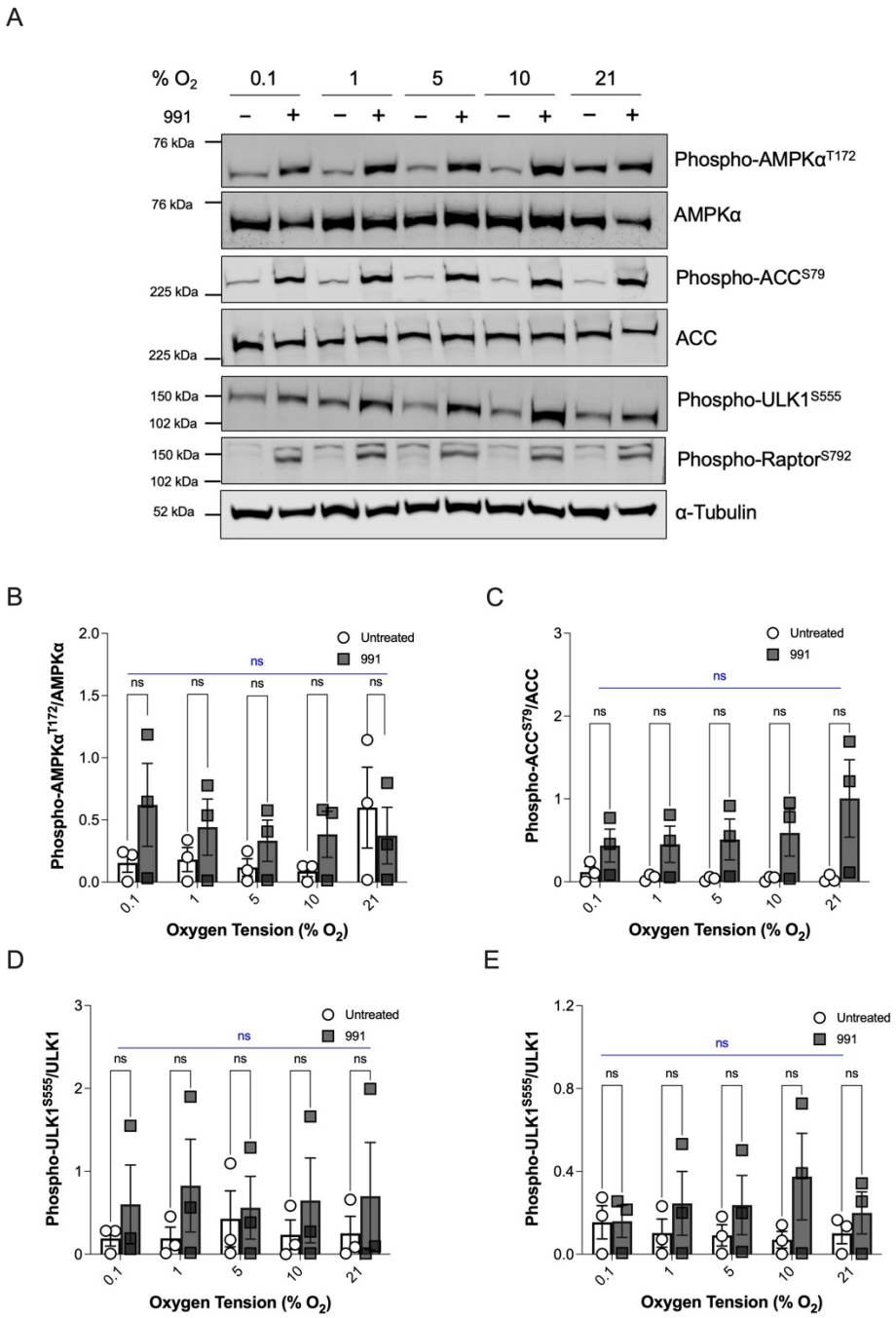


Figure 3.7 *– The effect of chronic exposure to differing O_2 tensions on AMPK activity.*

HUVECs were subjected to O_2 tensions between 0.1-21% in the absence or presence of 991 treatment (50 μM) for 24 hours.
(A) Representative immunoblot showing levels of phospho-AMPKα^{T172}, AMPKα, phospho-ACC^{S79}, ACC, phospho-ULK1^{S555}, ULK1, phospho-Raptor^{S792} and Raptor ± 991 treatment. α-Tubulin was used the loading control for the immunoblots in and for initial normalisation of phosphorylated and total protein prior to ratiometric calculations.
(B) Quantification of phospho-AMPKα^{T172} normalised to total AMPKα.
(C) Quantification of phospho-ACC^{S79} normalised to total ACC.
(D) Quantification of phospho-ULK1^{S555} normalised to total ULK1.
(E) Quantification of phospho-Raptor^{S792} normalised to total Raptor.
All data is displayed as mean ± SEM with n = 3 biological replicates. Data analysis was performed using repeated measures one-way ANOVA with Dunnett's multiple comparisons test (blue) whereas paired t-tests were performed (black). Ns, not significant.

Sub-physiological O_2 tensions (< 3%) can have deleterious effects on cells, depending on acute (< 24 hours) or chronic (> 24 hours) duration. To examine any changes on cell viability in response to both hypoxia and BI-9774, a non-lytic apoptosis and necrosis assay was performed. Apoptosis was determined by the interaction of annexin V with the phospholipid phosphatidylserine, which is normally in the inner leaf of the plasma membrane in healthy, viable cells. During apoptosis, translocation of phosphatidylserine to the outer plasma membrane serves as an 'eat-me' signal for phagocytosis. Loss of membrane integrity, determined by entry of a membrane-impermeant fluorescent DNA dye into the cell, was also measured as a marker of necrosis.

The assay revealed no significant differences in apoptosis and necrosis at 24 hours regardless of O_2 levels or BI-9774 treatment, although there was a noticeable non-significant reduction in apoptosis with BI-9774 (Figure 3.8A & B). Compared to HUVECs under hypoxia, normoxic HUVECs had significantly elevated apoptosis and necrosis at 72 hours, suggestive of cell turnover following contact inhibition upon reaching confluency (Figure 3.8C). BI-9774 significantly reduced the elevated levels of apoptosis and necrosis in normoxic HUVECs (Figure 3.8C & D) and protected HUVECs against apoptosis and necrosis under chronic hypoxia (3% O_2) conditions. Interestingly, BI-9774 had deleterious effects on HUVECs exposed to pathological hypoxia (1% O_2), as displayed by the elevated levels of apoptosis and necrosis (Figure 3.8C & D). Based on the O_2 dose response studies and cell viability studies, 3% was used as the hypoxic O_2 tension going forward as it falls below what HUVECs would experience *in vivo* (~5-6% O_2 is 'physiological normoxia') but did not compromise cell viability long-term compared to O_2 tensions commonly used in hypoxia studies using HUVECs published by other groups (~1% O_2).

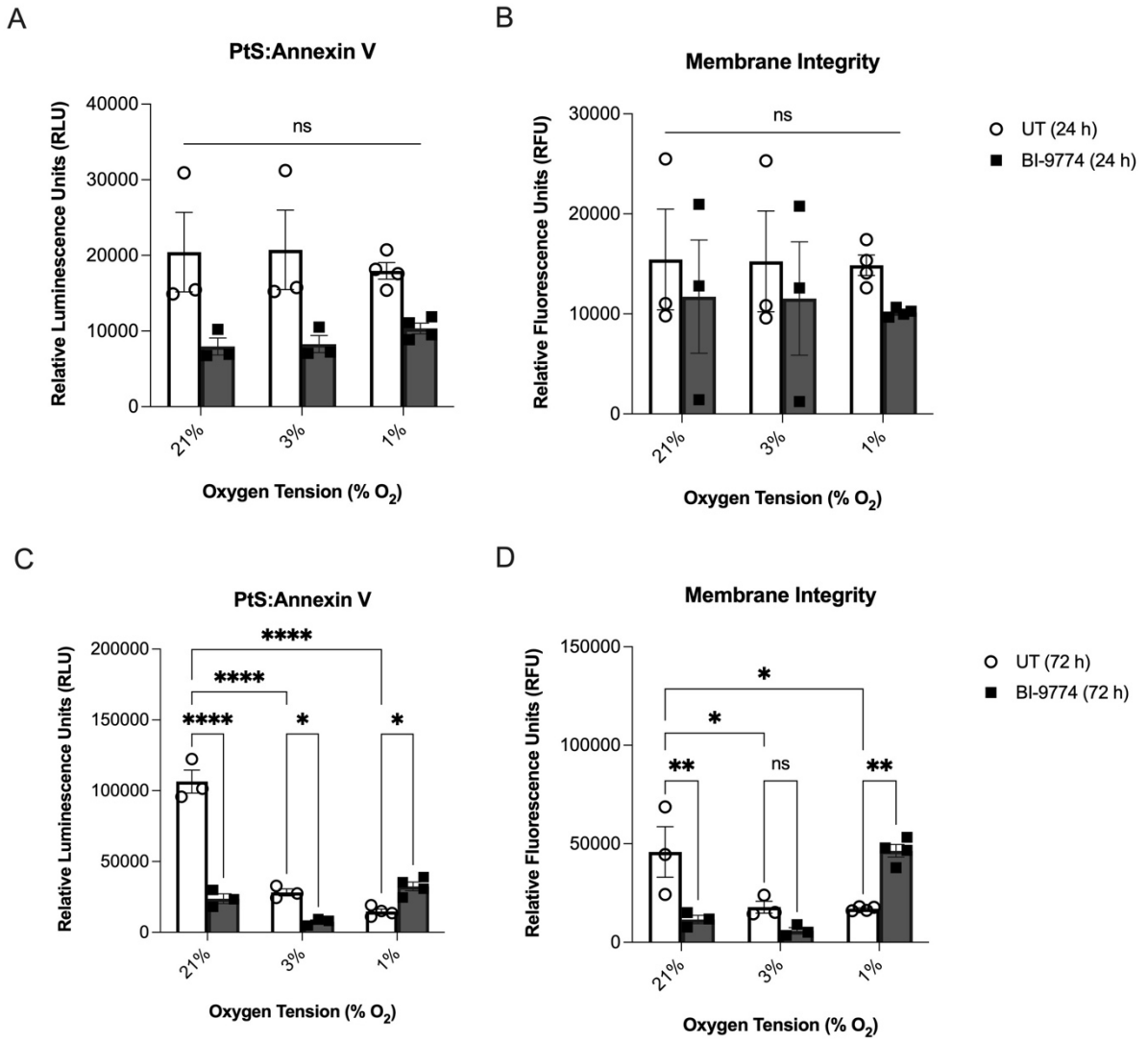


Figure 3.8 *– The effect of moderate and severe hypoxia, in combination with BI-9774 treatment on cell viability in HUVECs.*

HUVECs were cultured under 1, 3 and 21% O_2 for 24 h and 72 h in the absence or presence of BI-9774 (10 μM). Live measurements of apoptosis (defined as the binding of PtS:Annexin V interaction) and/or necrosis (membrane integrity) were measured by luminescence and fluorescence, respectively.
(A) and (B) represent apoptosis and necrosis at 24 h, respectively.
(C) and (D) represent apoptosis and necrosis at 72 h, respectively.
All data is displayed as mean ± SEM with n = 3 biological replicates. Statistical analysis was performed using two-way ANOVA with Tukey's *post hoc* analysis. Ns, not significant, * p-value < 0.05, ** p-value < 0.01, **** p-value < 0.0001.

Next, I performed a time course experiment in untreated HUVECs under these O_2 tensions to examine whether temporal changes in AMPK activity arise. Time indicates exposure to normoxia (21% O_2) or hypoxia (3% O_2) following media change with pre-equilibrated media. Levels of phosphorylated AMPKα^{T172} and ACC^{S79} were analysed as a readout of AMPK activity by immunoblotting (Figure 3.9A). Lysates were also probed with HIF-1α as a positive control to differentiate between normoxic and hypoxic lysates (Figure 3.9A). Hypoxia exposure significantly reduced AMPKα^{T172} phosphorylation between 0.5 and 1 hour of exposure onwards (−64%, p-value = 0.0469) (Figure 3.9A & B), but no significant differences were noted at later time points. Phospho-ACC^{S79} levels were also significantly reduced at 0.5 and 1 hours of hypoxia exposure, but again there was no significant differences at 6 and 24 hours, mirroring the phospho-AMPKα^{T172} densitometry quantification (Figure 3.9A-C). To examine whether the change in phosphorylation status agrees with endogenous AMPK activity, AMPK complexes were immunoprecipitated from HUVECs using a pan-AMPKβ antibody incubated with [γ-^{32}P]-ATP and SAMS peptide, a synthetic AMPK substrate (see 2.15 SAMS Peptide AMPK Kinase Activity Assays). *In vitro* kinase activity assays confirmed high basal activity in the normoxic samples even at 0.5 hours that was significantly increased at the 6- and 24-hour time points (>1.8 fold-change, p-value < 0.001) when compared at 0.5 hours (Figure 3.9D). In contrast, immunoprecipitated AMPK from hypoxic lysates had significantly reduced activity after 1 hour onwards in comparison to their normoxic counterparts (Figure 3.9D). At 24 hours, kinase activity was reduced by 71% compared to normoxic immunoprecipitants at the same time point (p-value < 0.0001). These results suggest that hypoxia exposure may alter AMPKα^{T172} phosphorylation status at earlier time points, but differences in *in vitro* kinase activity are only apparent at later time points between the normoxic and hypoxic samples. The findings also suggest that regardless of phosphorylation status, no effect is seen on phospho-ACC^{S79} levels.

Next, I examined whether levels of AMPKα^{T172} phosphorylation change following hypoxia and reoxygenation in the absence of media changes. HUVECs were initially exposed to 3% O_2 for 1 hour and subsequently exposed to 21% O_2 for 5 minutes or 1 hour. As shown in Figure 3.10A & B, phospho-AMPKα^{T172} levels were significantly decreased at 3% O_2 (−47%, p-value = 0.0286), that subsequently increased significantly upon exposure to 21% O_2 at 5 minutes and 1 hour (~2-fold change, p-value < 0.05). There were no differences were observed in phospho-ACC^{S79} levels, as observed in the time course experiment (Figure 3.10C). The results suggests that phospho-AMPKα^{T172} may change in response to hypoxia, but this occurs independently of any downstream changes in AMPK signalling and bears no effect on substrate phosphorylation.

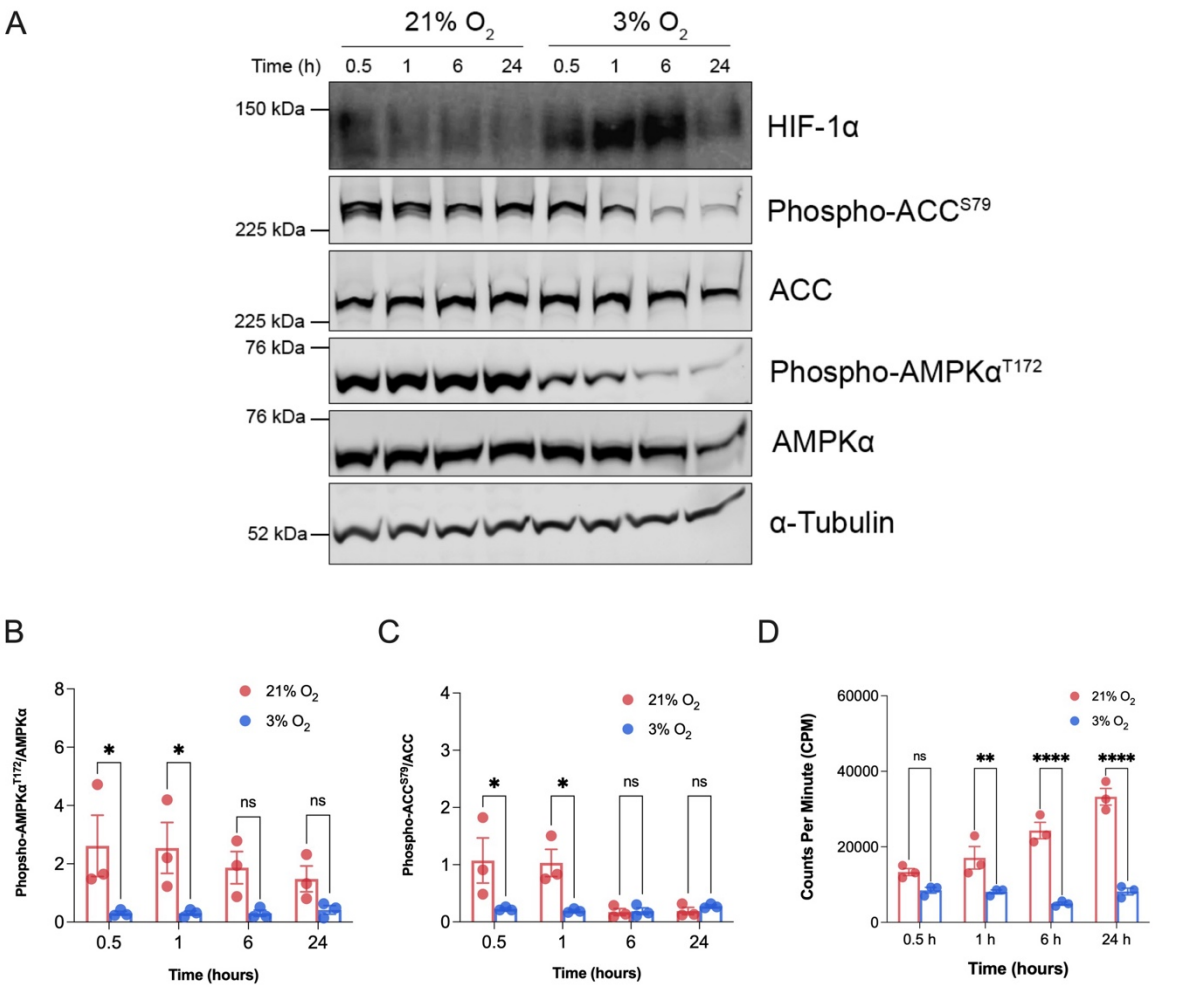


Figure 3.9 *– Time course experiment examining the effect of normoxia and hypoxia on AMPK^{T172} phosphorylation status and kinase activity.*

HUVECs were cultured under normoxia (21% O_2) and hypoxia (3% O_2) for 0.5-24 hours. (A) Representative immunoblot showing HIF-1α, phospho-AMPKα^{T172}, AMPKα, phospho-ACC^{S79}, ACC with α-Tubulin as the loading control. All signals were normalised initially to α-Tubulin prior to ratiometric calculations between phosphorylated and total protein.
(B) Quantification of phospho-AMPKα^{T172} normalised to total AMPKα.
(C) Quantification of phospho-ACC^{S79} normalised to total ACC.
(D-F) Incorporation of [γ-^{32}P]-ATP based on *in vitro* AMPK kinase assays using immunoprecipitated AMPK complexes from matched lysates.
All data is displayed as mean ± SEM with n = 3-4 biological replicates. Statistical significance was determined using paired t-tests for (B)-(D). Ns, not significant, * p-value < 0.05, *** p-value < 0.001, ****, p-value < 0.0001.

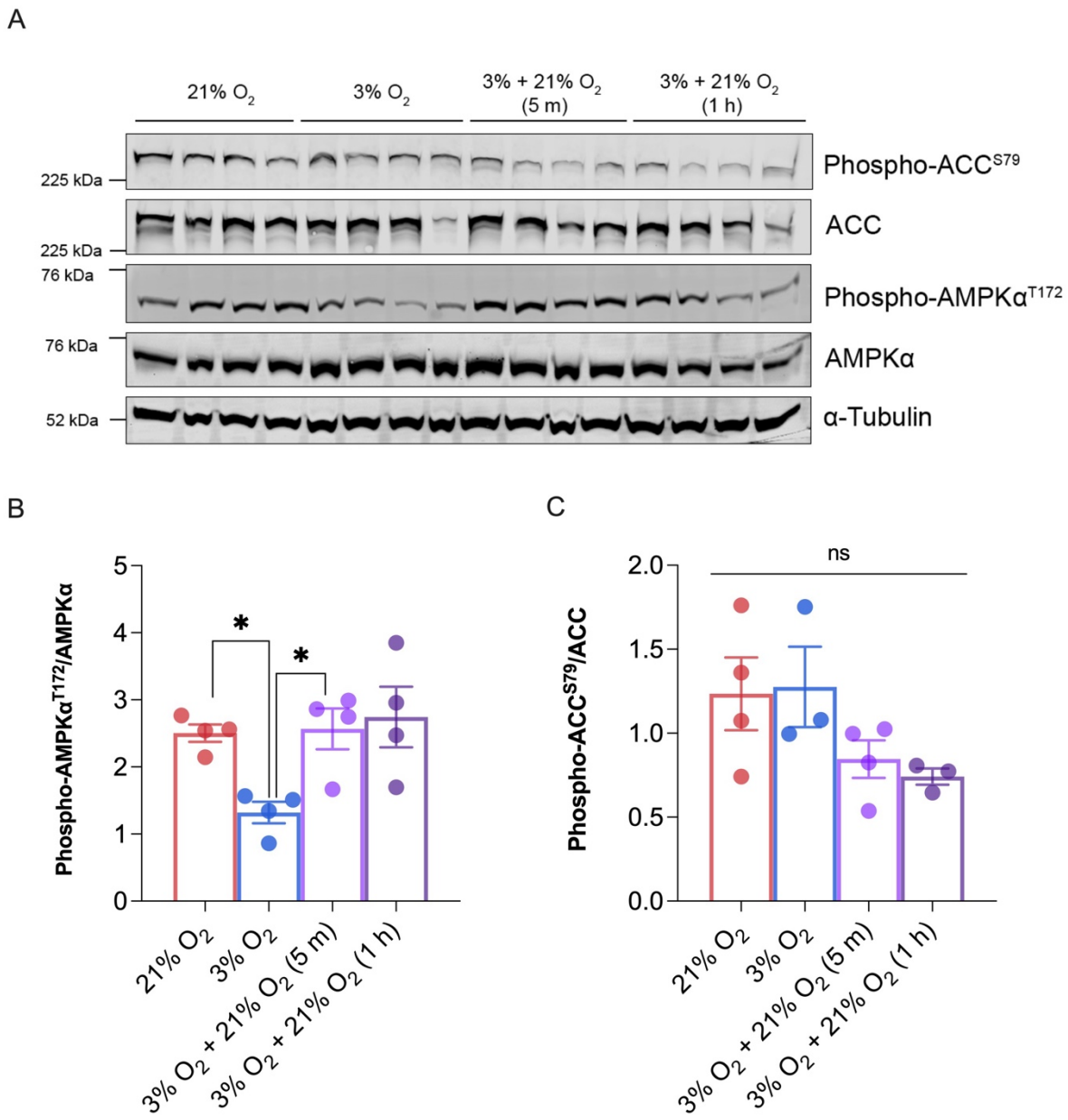


Figure 3.10 *– The effect of normoxia, hypoxia and hypoxia/reoxygenation on AMPKα^{T172} phosphorylation status.*

HUVECs were cultured under normoxia (21% O_2, 1 hour), hypoxia (3% O_2, 1 hour), hypoxia (1 hour) followed by 5 minutes or 1 hour of reoxygenation.
(A) Representative immunoblot showing phospho-AMPKα^{T172}, AMPKα, phospho-ACC^{S79}, ACC with α-Tubulin as the loading control. All signals were normalised initially to α-Tubulin prior to ratiometric calculations between phosphorylated and total protein.
(B) Quantification of phospho-AMPKα^{T172} normalised to total AMPKα.
(C) Quantification of phospho-ACC^{S79} normalised to total ACC.
All data is displayed as mean ± SEM with n = 4 biological replicates. Statistical significance was determined using paired t-tests. Ns, not significant, * p-value < 0.05.

To determine if inhibition of PHD hydroxylase activity alters AMPKα^{T172} phosphorylation, HUVECs were treated with the pan-PHD inhibitor FG-4592 (10 μM) for 3 hours under normoxia prior to downstream analysis by immunoblotting. As shown by Figure 3.11, FG-4592 was able to stabilise HIF-1α confirming that the inhibitor is functional. Regardless, no significant differences was seen in phospho-AMPKα^{T172} levels, despite a minimal increase in elevation in FG-4592-treated HUVECs (1.39-fold change, p-value = 0.200). Therefore, it is unlikely that PHDs have any effect on phosphorylation of AMPKα^{T172} phosphorylation status.

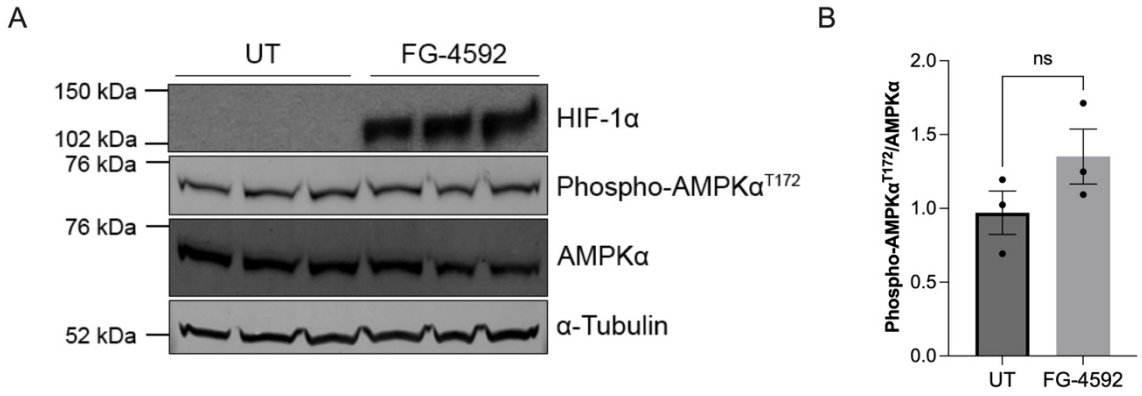


Figure 3.11 *– The effect of pan-PHD inhibitor FG-4592 on AMPKα^{T172} phosphorylation.*

HUVECs were treated with FG-4592 (10 μM) for 3 hours prior to lysis.
(A) Representative immunoblot showing HIF-1α, phospho-AMPKα^{T172}, AMPKα with α-Tubulin as the loading control. All signals were normalised initially to α-Tubulin prior to ratiometric calculations between phosphorylated and total protein.
(B) Quantification of phospho-AMPKα^{T172} normalised to total AMPKα.
All data is displayed as mean ± SEM with n = 3 biological replicates. Statistical significance was determined using paired t-tests. Ns, not significant, * p-value < 0.05.

Hypoxia limits energy-intensive processes such as protein translation, a process heavily regulated by mTORC1, to conserve ATP until mitochondrial respiration is restored upon reoxygenation. As mentioned in 3.1 Introduction, eEF2K phosphorylates eEF2 on T56, halting the elongation phase of protein synthesis at ribosomes, thus effectively inhibiting protein translation. This may explain why AMPKα activity remains unchanged or even decreases under hypoxia [334, 343, 344]. I assessed whether hypoxia affects phosphorylation of phospho-eEF2^{T56} in order to gauge whether protein translation is affected. In control HUVECs, immunoblotting analysis revealed a significant increase in phospho-eEF2^{T56} levels in hypoxic HUVECs versus their normoxic counterparts (Figure 3.12A & B). There was no significant increase in eEF2^{T56} phosphorylation under normoxia nor hypoxia in HUVECs treated with BI-9774 versus control, despite a trend of increased phospho-eEF2^{T56} levels at 21% O_2 (1.42-fold change, p-value = 0.2653) (Figure 3.12C). As mentioned previously, eEF2K is a downstream target of AMPK in order to suppress protein translation under conditions of energy

depletion. Under hypoxia, eEF2K appears to be active as shown by the robust increase in eEF2^{T56} phosphorylation (2.33-fold change, p-value = 0.0154) (Figure 3.12B). Therefore, eEF2K-dependent phosphorylation of eEF2^{T56} occurs independently of AMPK, suggesting other kinases maybe responsible for triggering translational arrest, although further experiments are required to confirm that protein translation is inhibited in HUVECs.

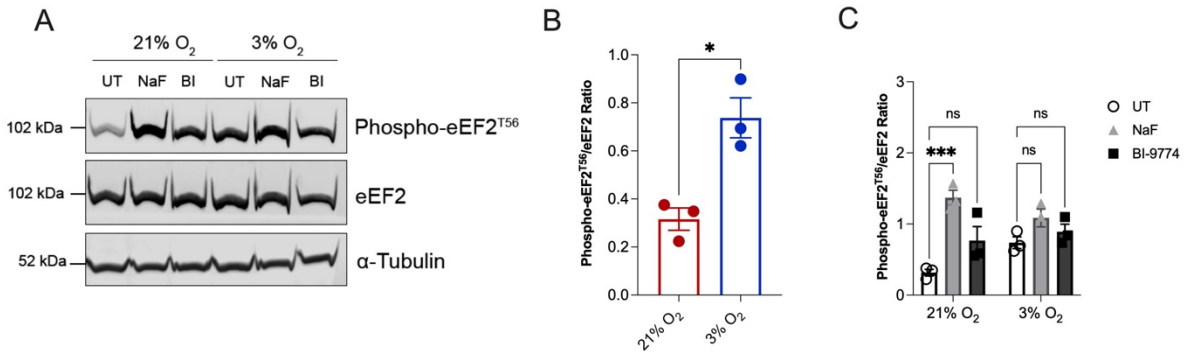


Figure 3.12 *– The effect of hypoxia on eEF2^{T56} phosphorylation.*

HUVECs were treated with NaF (50 mM) or BI-9774 (10 μM) under normoxia (21% O_2) and hypoxia (3% O_2) for 1 hour prior to lysis.
(A) Representative immunoblot showing phospho-eEF2^{T56} and eEF2 with α-Tubulin as the loading control. All signals were normalised initially to α-Tubulin prior to ratiometric calculations between phosphorylated and total protein.
(B) Quantification of phospho-eEF2^{T56} normalised to total eEF2 between baseline untreated normoxia (21% O_2) and hypoxia (3% O_2).
(C) Quantification of phospho-eEF2^{T56} normalised to total eEF2 across all treatments and O_2 tensions.
All data is displayed as mean ± SEM with n = 3 biological replicates. Statistical significance was determined using paired t-tests. Ns, not significant, ** p-value < 0.01.

AMPKα^{T172} dephosphorylation is mediated by (at least) two phosphatases, PP2Cα and PP2A. A study by Romero-Ruiz *et al.* used the pan-phosphatase inhibitor sodium fluoride (NaF) to demonstrate that dephosphorylation AMPKα^{T172} occurs under hypoxia [343]. To assess whether phosphatase activity affects AMPKα^{T172} phosphorylation, HUVECs were treated with vehicle and NaF (50 mM) under normoxia and hypoxia for 1 hour. BI-9774 treatment was also included as a positive control, as binding to the ADaM site protects AMPKα^{T172} from phosphatases. As shown by Figure 3.13, NaF treatment significantly enhanced AMPK phosphorylation by 3.4-fold (p-value = 0.0058) compared to untreated HUVECs under hypoxia. Despite this, there was no significant difference between phospho-AMPKα^{T172} levels under normoxia and hypoxia, despite previous experiments indicating otherwise (Figures 3.9-3.10). Therefore, these findings do not provide sufficient evidence to suggest that NaF protects against AMPKα^{T172} dephosphorylation under hypoxia.

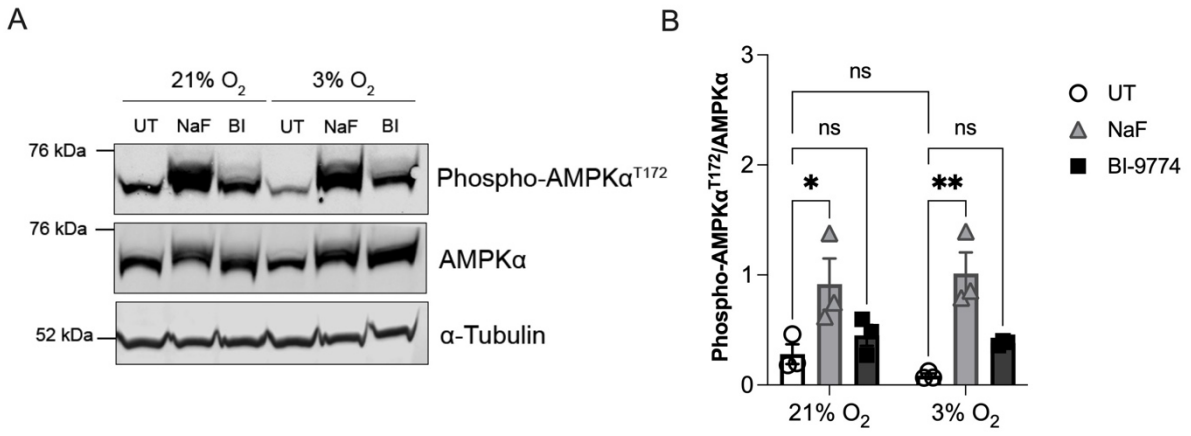


Figure 3.13 *– The effect of sodium fluoride on AMPKα^{T172} phosphorylation status under hypoxia.*

HUVECs were treated with NaF (50 mM) or BI-9774 (10 μM) under normoxia (21% O_2) and hypoxia (3% O_2) for 1 hour prior to lysis.
(A) Representative immunoblot showing phospho-AMPKα^{T172} and AMPKα with α-Tubulin as the loading control. All signals were normalised initially to α-Tubulin prior to ratiometric calculations between phosphorylated and total protein.
(B) Quantification of phospho-AMPKα^{T172} normalised to total AMPKα across all treatments and O_2 tensions.
All data is displayed as mean ± SEM with n = 3 biological replicates. Statistical significance was determined using a paired t-test. Ns, not significant, ** p-value < 0.01.

3.3.3 The effect of AMPK activation on HIF-1α stability

Post-translational modifications of HIF have been shown to alter HIF-1α stability and transcriptional activity independently of hydroxylation and ubiquitination. Onset of hypoxia disturbs kinase signalling networks, particularly those signalling pathways that are implicated in survival and metabolic reprogramming, in turn impacting HIF-1α stability, translocation and transactivation. In HUVECs that were treated with 991 under various O_2 tensions, I examined whether there are changes in HIF-1α. Overall, there were no significant differences in HIF-1α stabilisation with 991 treatment (Figure 3.14B), despite the agonist inducing a noticeable increase in HIF-1α stabilisation at the O_2 tensions examined (Figure 3.14A & C).

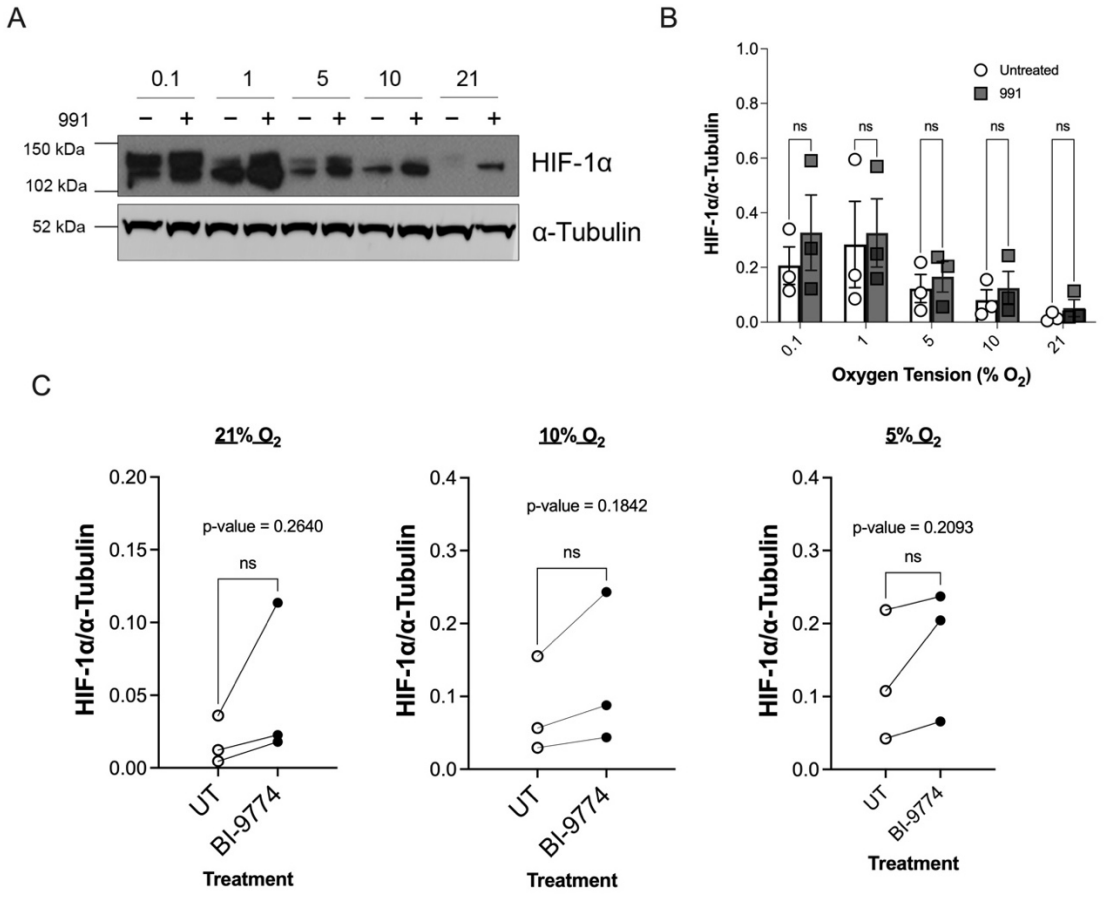


Figure 3.14 *– The effect of 991 on HIF-1α stability across different O_2 tensions.*

HUVECs were treated with 991 (50 μM) for 24 hours under 0.1-21% O_2.
(A) Representative immunoblot showing levels of HIF-1α with α-Tubulin as the loading control.
(B) Quantification of HIF-1α normalised to total α-Tubulin.
(C) Pairwise comparison of HIF-1α levels between UT and 991 at 5,10 and 21% O_2.
All data is displayed as mean ± SEM with n = 3 biological replicates. Statistical significance was determined using paired t-tests across all O_2 tensions in (B) or in the physiologically relevant O_2 tensions in (C), ns, not significant.

Next, I sought to examine whether BI-9774 has any effect on HIF-1α stabilisation, HUVECs were treated with BI-9774 under normoxia and hypoxia (3% O_2) for 1 hour and HIF-1α levels

were analysed by immunoblotting (Figure 3.15A). To focus solely on AMPK, NaF treatment is omitted from discussion. There were no significant differences in HIF-1α levels in BI-9774-treated cells compared to control, although some induction of HIF-1α appeared to occur with BI-9774 treatment but the response to be variable across the HUVEC pools (Figure 3.15B).

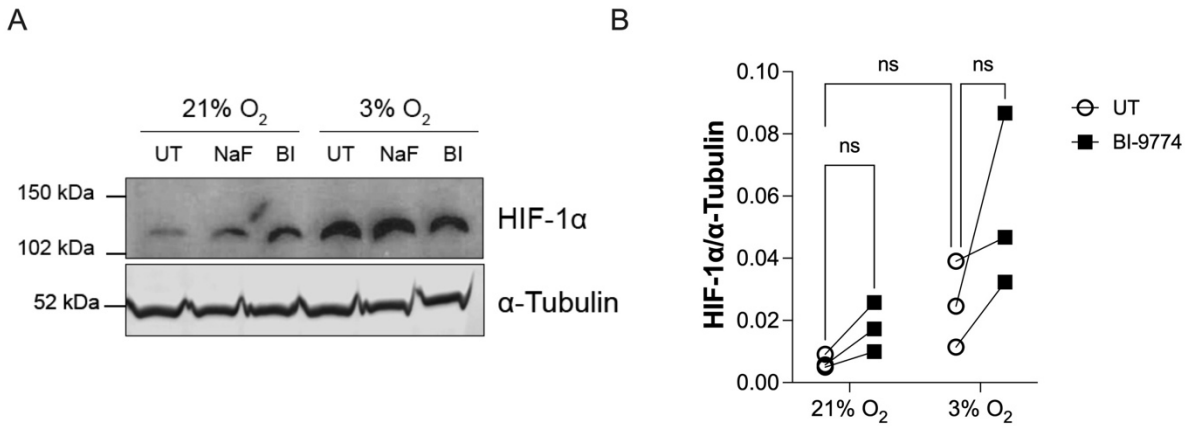


Figure 3.15 *– The effect of acute BI-9774 treatment on HIF-1α stability.*

HUVECs were treated with NaF (50 mM) or BI-9774 (10 μM) under normoxia (21% O_2) and hypoxia (3% O_2) for 1 hour prior to lysis.
(A) Representative immunoblot showing HIF-1α and α-Tubulin as the loading control. All signals were normalised initially to α-Tubulin prior to ratiometric calculations between phosphorylated and total protein.
(B) Quantification of HIF-1α normalised to α-Tubulin across all treatments and O_2 tensions.
All data is displayed as mean ± SEM with n = 3 biological replicates. Statistical significance was determined using a paired t-tests for the pairwise comparisons at each O_2 tension.

Next, I addressed whether BI-9774-induced stability of HIF-1α corresponded to gene transactivation, I carried out an HRE-dependent luciferase assay. HUVECs were treated with BI-9774 for 16 hours to allow sufficient stabilisation of HIF-1α-dependent transcription, especially as the assay was performed under normoxia. Treatment with FG-4592 robustly increased HRE-dependent luciferase activity (1.69-fold-change, p-value = 0.0046). BI-9774 treatment also significantly enhanced HRE-dependent luciferase activity (2.93-fold-change, p-value = 0.0011) (Figure 3.16A). Therefore, it appears that BI-9774 induces HRE-dependent transcription downstream, implying that BI-9774 may alter HIF-1α transcriptional activity. To confirm induction of HIF-dependent transcription, a time course experiment was performed using BI-9774 and mRNA expression of bona fide HIF-1α targets was measured including GLUT1 (*SLC2A1*), VEGF-A (*VEGFA)* and urokinase (*PLAU*) (see Table 1.3). HIF-1α induces expression of glucose transporters to increase glucose intake, thereby promoting a shift towards anaerobic metabolism. BI-9774 significantly increased expression of *SLC2A1* at 6 hours of treatment (1.5-fold, p-value = 0.0355) but there was no significant differences at later time points, perhaps due to the presence of outliers (Figure 3.16B). HIF-1α also controls expression of genes involved in angiogenesis such as VEGF-A and urokinase, both of which are critical for vessel sprouting and proteolytic degradation of the extracellular matrix,

respectively. BI-9774 significantly increased *VEGFA* mRNA expression throughout the 48-hour duration of the experiment (1.38-2.47-fold, p-value < 0.05) (Figure 3.16C). Similarly, expression of PLAU significantly increased with BI-9774 treatment between 6 and 24 hours (1.54-2-fold-change, p-value < 0.05), but no differences were noted at 48 hours (Figure 3.16D).

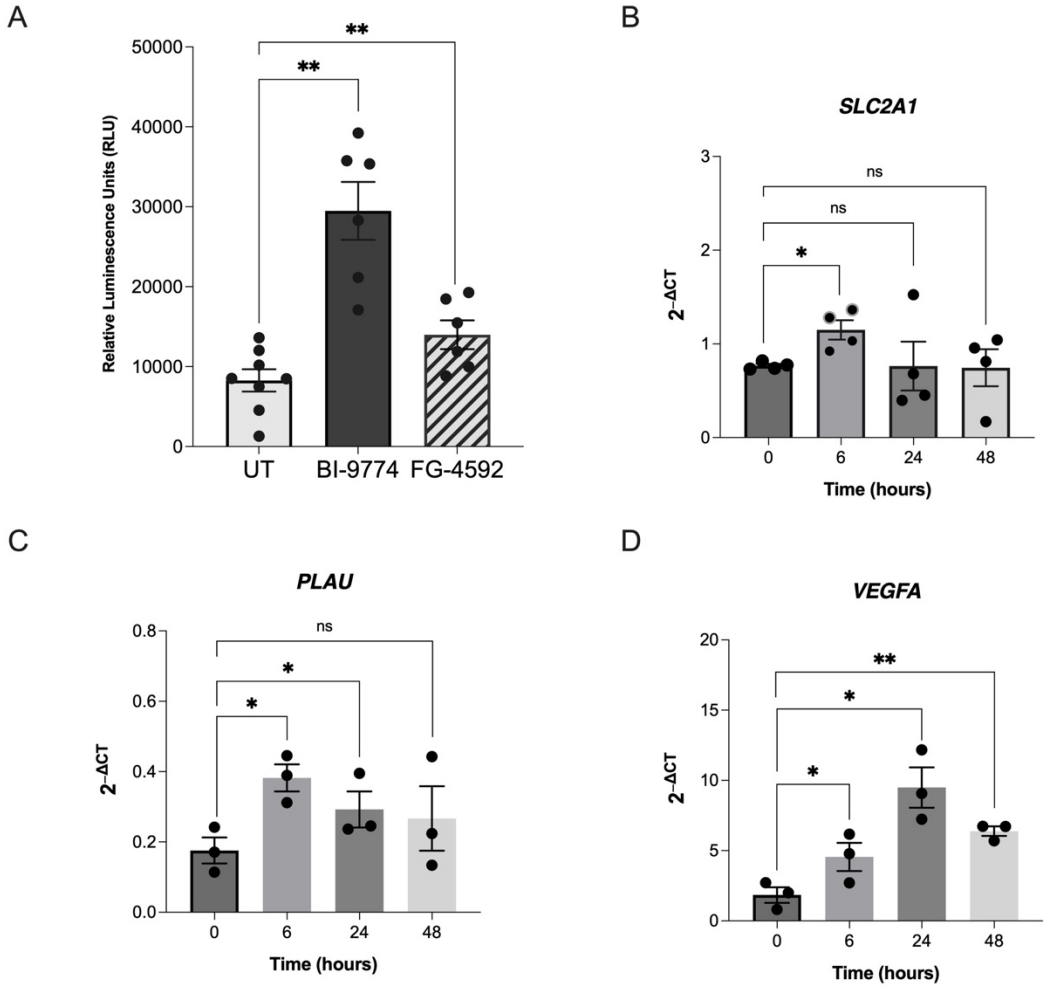


Figure 3.16 *– The effect of BI-9774 treatment on HIF-dependent transcription and target expression in HUVECs.*

(A) HUVECs were transfected with a plasmid expressing firefly luciferase under the control of four HRE repeats (*luc2P/HRE*) and a control plasmid CMV driving the expression of sea pansy luciferase (*Rluc/CMV*) for 24 hours then subsequently treated with BI-9774 (10 μM) or FG-4592 (10 μM) for 16 hours under normoxia (21% O_2). The graph illustrates quantification of luciferase signal compared to *Rluc/CMV* expression. All data is displayed as mean ± SEM with n = 3-4 biological replicates with n = 2 technical replicates. HUVECs were treated with BI-9774 (10 μM) for 6-48 hours prior to RNA extraction and purification with 0 hours being untreated cells. All comparisons were done with baseline (0 hours).
(B) Quantification of mRNA levels of GLUT1 (*SLC2A1*).
(C) Quantification of mRNA levels of urokinase (*PLAU*).
(D) Quantification of mRNA levels of VEGF-A (*VEGFA*).
ΔC_T values were calculated by subtracting raw C_T values from the genes interest from the C_T values of housekeeping gene TATA-binding protein (*TBP)*. Statistical significance was determined using paired t-tests. Ns, not significant, * p-value < 0.05, ** p-value < 0.01, *** p-value < 0.001. Ns, not significant, ** p-value < 0.01.

Next, I examined whether physiological activation of AMPK (i.e., in response to glucose deprivation) has any effect on HIF-1α stability. Previous studies have shown that glucose availability and HIF-1α stabilisation are interlinked as both retinal glial cells and U-937 human monocytic cells enhance HIF-1α levels and induce VEGF mRNA expression under conditions of hypoglycaemia and/or glucose deprivation [345, 346]. HUVECs were subjected to varying concentrations of glucose [0, 0.5 (2.78 mM) and 1 g/L (5.55 mM)] reintroduced in glucose/glutamine/pyruvate-free DMEM under 3 and 21% O_2 for 6 hours prior to lysis. Immunoblotting analysis revealed that HUVECs were able to tolerate a reduction in glucose down to 0.5 g/L without eliciting AMPKα^{T172} and ACC^{S79} phosphorylation. Initial qualitative observations in one HUVEC pool show that glucose deprivation induces stabilisation of HIF-1α under normoxia with augmented expression of HIF-1α in glucose-starved HUVECs compared to their normoglycemic counterparts under 3% O_2 (Figure 3.17). This observation necessitates further experimental repeats to determine if the effect are reproducible and statistically significant in order to draw a conclusion.

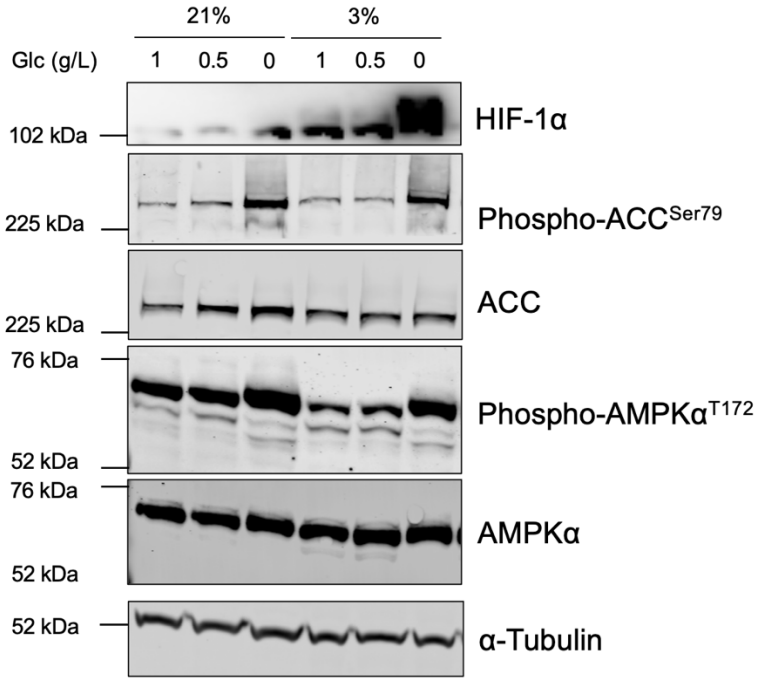


Figure 3.17 *– The effects of glucose deprivation on HIF-1α stability in HUVECs.*

HUVECs were subjected to varying concentrations of glucose (0, 0.5 and 1 g/L) for 6 hours under normoxia (21% O_2) and hypoxia (3% O_2). Levels of HIF-1α, phospho-AMPKα^{T172}, AMPKα, phospho-ACC^{S79} and ACC were analysed with α-Tubulin serving as a loading control (n = 1 biological replicate).

3.4 Discussion and Limitations

3.4.1 AMPK subunit expression and endothelial heterogeneity

The transcriptome of microvascular ECs reflects an organ-specific signature, as ECs adapt their behaviour to fully complement tissue and/or organ function. [347]. Given that AMPK acts as a metabolic gauge the relative expression of $\alpha_{1/2}$, $\beta_{1/2}$ and $\gamma_{1/2}$ and the predominance of distinct AMPK complexes in endothelial cells, may reflect tissue-specific bioenergetic needs. *PRKAA1* is the predominant α subunit expressed in ECs, corroborating previous observations *in vivo* that α_1 is the predominant endothelial catalytic subunit [205]. A consideration to make is that AMPKα_2 KO in mice predisposes to endothelial dysfunction, therefore it is plausible that ECs may express AMPKa_2 *in vivo* and that cultured ECs lose specific expression of *PRKAA2* as they are passaged, a phenomena that has been reported by others in the endothelial biology field [197, 348, 349].

The distinct effects of β and γ subunits are not clear and have not been explored in the endothelium. AMPK γ_1 is the predominant nucleotide sensing regulatory subunit in HAECs and HUVECs whereas γ_1 and γ_2 is expressed at relatively similar amounts only in ECFCs (Figure 3.2). Differential expression of β and γ subunits may be an indication of endothelial heterogeneity, but there is insufficient currently both in this study and in the literature to support this notion [350]. Based on the transcript expression, it could be assumed that at least four complexes of the AMPK holoenzyme exist in ECs, therefore it would be sensible to use pan-AMPK activators at this point in time to examine the effects of AMPK activation on ECs. However, it is important to emphasise that differences in AMPK subunit isoform expression in RNA-seq may not translate to levels of protein, as subunits that fail to form heterotrimers are subsequently degraded. Further work is required to examine protein expression of AMPK subunit isoforms, using isoform specific antibodies for analyses by immunoblotting or *in vitro* kinase assays. A bespoke proteomics approach is required to determine stoichiometry of these isoforms in cell types, but this lies beyond the scope of this thesis.

3.4.2 The effect of hypoxia on basal AMPK phosphorylation status and AMPK activity in ECs

The prevailing theory within the AMPK field is that hypoxia triggers AMPK activation, following impairment of mitochondrial ATP production and subsequent reduction in the [ATP:ADP/AMP] ratio. Given the variability observed in phospho-AMPKα^{T172}, kinase activity assays and the small sample sizes of donors used, it is difficult to ascertain the true effect of hypoxia on both

of these parameters (Figure 3.6 and Figure 3.9). It is perhaps safe to conclude that AMPK is not profoundly affected by hypoxia in ECs. This may not seem surprising as it has been well established that ECs exhibit extraordinary resistance to hypoxia provided that glucose is available, only susceptible to its deleterious effects when nutrients are limiting [351]. Quantitative modelling also reveals that O_2 falls at a faster rate than glucose levels in biological systems [352]. As ECs are heavily reliant on glycolysis, they conserve O_2 for delivery to parenchymal cells when O_2 is limiting. In addition, glycolysis produces ATP with faster kinetics (1.3 Endothelial Metabolism and Control of Whole-Body Energy Balance), allowing ECs to vascularise hypoxic tissues, thereby preserving their function [69]. Therefore, it is not surprising that ECs appear to be relatively resistant to the deleterious effects of hypoxia, at least in O_2 levels between 1-3% based on cell death assays in Figure 3.8. Further work will be required to determine the number of viable cells using the CyQUANT proliferation assay to corroborate this observation.

The idea that hypoxia triggers a fall in the ATP:ADP/AMP ratio fails to consider innate differences in metabolic preferences for ATP production, i.e. OXPHOS-dependent cells activate AMPK in response to hypoxia, whereas AMPK signalling remains unaltered in quiescent/glycolytic cell types (e.g. ECs) as glycolysis does not rely on O_2 consumption. Preliminary observations imply that AMPK is activated under hypoxia in ECs in response to glucose deprivation (Figure 3.17). Further work using kinase assays and assessing which nutrients ECs are highly sensitive to under hypoxia will be required to confirm the role of AMPK primarily serves as a metabolic gauge, rather than an indirect O_2 sensor in ECs as suggested by others. The differences in the observations across these studies could be due to differences in methodologies (e.g., such as the use of hypoxic workstation versus hypoxic incubator) and lysis methods that may impact AMPK signalling. The use of a hypoxic workstation in this study allows equilibration of media and buffers as well as lysis *in situ*, minimising any effects due to reoxygenation.

There were several experiments (e.g., 21% versus 3% O_2 time course and O_2 dose response) where there appeared to be a significant reduction in phospho-AMPKα^{T172} levels and in some instances, a reduction in kinase activity when exposed to longer periods of hypoxia (see Figure 3.6 and Figure 3.9). However, this observation was not consistently seen across all experiments. Levels of phospho-AMPKα^{T172} levels returned to the normoxia baseline after reoxygenation (Figure 3.10). However, this did not correspond to downstream phosphorylation ACC on S79, suggesting that a disconnect exists between phospho-AMPKα^{T172} and downstream phospho-ACC^{S79}. The experiments may require further repeats to show if the trends approach significance and/or aid in the identification of outliers. It is also worth

examining whether the levels of phospho-AMPKα^{T172} correlated with endogenous kinase activity in endothelial cells. Based on these trends, it could be hypothesised that AMPK could be basally active (as indicated by AMPKα^{T172} phosphorylation) but it's downstream signalling is restrained. The disconnect in AMPK activity and downstream target phosphorylation could arise out of a number of reasons including: (i) restrictions on AMPK activity through interactions with inhibitory proteins; (iii) subcellular localisation or (iii) differences in the kinetics of AMPK versus target dephosphorylation. All of these require additional *in vitro* kinase assays and coimmunoprecipitation experiments, which was not investigated in the present study as it lied beyond the scope of the project. Subcellular localisation of AMPK in ECs is also another interesting avenue to explore, particularly in response to activators (991/BI-9774), as it might provide some insight into the functions of AMPK in ECs.

Translational arrest serves as a fundamental homeostatic response to metabolic stress, diverting ATP from energetically demanding processes to processes that facilitate cell survival and metabolic reprogramming [216]. As expected, there is a marked increase in eEF2^{T56} phosphorylation in HUVECs cultured under hypoxia (Figure 3.12). Protein translation is one of the most metabolically demanding processes, consuming approximately ~5 ATP molecules per peptide bond and on average ~2300 ATP molecules per protein [353]. During hypoxia, a reduction in global protein translation could result in elevated intracellular concentrations of ATP. Previous studies have reported that ATP:ADP/AMP ratios are either elevated or remain unaltered following acute exposure to hypoxia [334, 344]. This may explain why there were either no significant changes or a reduction in AMPK activity in certain experiments as a marked reduction in translation will elevate intracellular ATP to allosterically inhibit AMPK. Unfortunately, I was not able to measure ATP, ADP and AMP by liquid chromatography-mass spectrometry (LC-MS) due to technical issues. In the future, it will be possible to quantify levels of adenosine nucleotides cultured for different durations under 3% and 21% O_2 to capture any changes in the ATP:ADP/AMP ratio.

Intracellular ATP levels are sustained within the first hours of hypoxia following inhibition of protein translation attributed in part to suppression of mTORC1 signalling by TSC1/2 and REDD1 [327]. It is unknown whether mTORC2 remains active as there are no studies examining the effect of hypoxia on mTORC2 activity. Hypoxia-dependent proliferation of ECs during angiogenesis requires activation of mTORC1 and mTORC2 activation in endothelial cells [354, 355]. Hence, it would be interesting to see if mTORC1/2 activity remains unaltered, or changes during hypoxia exposure. Due to limited amounts of lysates, I was not able to compare mTORC1/2 signalling across different oxygen tensions. It would be interesting to examine levels of phosphorylated 4E-BP1$^{T37/T46}$ or p70 S6K^{T389} and Akt^{S473} phosphorylation as

hallmarks of mTORC1 and mTORC2 activation, respectively. Future work will require measuring protein translation either by (i) puromycin incorporation [known as surface sensing of translation (SUnSET)] or (ii) stable isotope labelling by amino acids in cell culture (SILAC). The SUnSET approach was attempted but the assay required further optimisation in terms of confluency, puromycin treatment duration and time points.

I examined whether inhibition of phosphatases by NaF alters AMPKα^{T172} phosphorylation under hypoxia (Figure 3.13). It should be emphasised that NaF can also elicit pleiotropic effects, therefore further experiments are required using small molecule phosphatase inhibitors or siRNA knockdown screens as small molecule phosphatase inhibitors can affect multiple phosphatases depending on the concentration. The question of whether phosphatase activity are altered in response to a fall in O_2 tension or whether they interact directly with AMPK remains to be addressed. Only two phosphatases, PP2A and PP2Ca, have been reported to negatively regulate AMPK [99]. Of potential relevance, HIF-1α has been shown to suppress the expression of PP2A activity in SMCs and ventricular cardiomyocytes [356].

Pharmacological inhibition of PHD enzymes using FG-4592 also had no effect on AMPKα^{T172} phosphorylation (Figure 3.11), although it would be useful to perform AMPK kinase assays using these samples to confirm a lack of activity. FG-4592 is only selective for PHDs and does not inhibit FIH-1 activity at the concentration used in this study (IC_{50} > 100 μM for FIH-1), at concentrations that may be cytotoxic to HUVECs [357]. Zhang and colleagues previously reported that mouse embryonic fibroblasts (MEFs) derived from FIH1^{KO} mice have enhanced intracellular ATP levels followed by a resultant reduction in AMPK activity [358]. This necessitates further exploration of how FIH-1 modulates AMPK and whether the asparaginyl hydroxylase indeed contributes to the rapid changes in AMPK activity under different O_2 tensions.

Future studies could also examine whether shear stress impacts AMPK activity under hypoxia. Under normoxic conditions, LSS promotes AMPK/eNOS signalling whereas OSS result in dephosphorylation of AMPK as presented in Table 1.1. Acute hypoxia exposure causes an increase in aortic blood flow and a reduction in peripheral resistance based on murine studies *in vivo* [359]. Disturbed, oscillatory flow enhances HIF-1α expression, tipping the balance towards anaerobic metabolism, resulting in arterial ECs adopting a pseudo-hypoxic, atheroprone phenotype [310]. On the other hand, upregulation of HIF-2α at sites of disturbed flow protected against atherosclerotic lesion formation in murine aortas [360]. The combined effects of hypoxia and shear stress is critical for the formation of collateral vessels in response to ischaemic injury. Therefore, in future studies, it would be interesting to explore the effects

of shear stress on AMPK activation and whether this produces knock-on effects on HIF-1α signalling.

3.4.3 Effect of AMPK activation on HIF-1α stability and HRE-dependent luciferase activity

AMPK small molecule activators such as 991 or BI-9774 had no significant impact on HIF-1α protein stabilisation (Figures 3.14-3.15), although a small increase was noted. However, HRE-dependent luciferase activities and RT-qPCR analysis showed significant increase in transcriptional activity and induction of established target genes with BI-9774 treatment. There were many difficulties with probing for HIF-1α as I had to rely on film exposure for detection, which has a narrow linear range compared to LI-COR. A potential solution could be to increase the amount of protein loaded during gel electrophoresis; however, this may be an issue when lysates are limited or require for other assays (e.g., matched lysates for *in vitro* kinase assays or co-immunoprecipitation experiments). Beyond HIF-1α stabilisation, it is also important to consider interactions with FIH-1, HIF-1β heterodimerisation and nuclear translocation that can affect its transcriptional activity. FIH-1 is resistant to the inhibitory effects of FG-4592 and is often found bound at the C-terminal transactivation domain of HIF-1α [224, 237, 249, 361]. This may also explain as to why induction of HRE-dependent luciferase activity by FG-4592 was lower than BI-9774 (Figure 3.16). A more appropriate control for the luciferase assays would be hypoxia exposure as O_2 tensions below < 6% will inhibit the hydroxylase activities of both PHDs and FIH-1.

In order to address whether BI-9774 affects HIF-1α stability, time course experiments will be performed under both normoxic and physiological O_2 tensions to detect HIF-1α. It may be necessary to perform co-immunoprecipitation experiments using cytosolic versus nuclear fractions to determine:- (i) the amount of HIF-1α present in the nucleus; and (ii) if HIF-1α is bound to any of its co-activators (e.g., HIF-1β and p300) inhibitors (e.g., pVHL, FIH-1). Another caveat is to consider whether PHD enzymes, FIH-1 or pVHL expression or activity could be affected by BI-9774 treatment, which may also explain why BI-9774 increases HRE-dependent luciferase activity in comparison to FG-4592. Further work will be undertaken to fully characterise whether the effects of BI-9774 on HIF-1α stability and transcriptional activity occur through direct and/or indirect mechanisms.

It is also tempting to speculate that glucose deprivation results in HIF-1α stabilisation, in a mechanism that potentially may involve AMPK (Figure 3.17), although further experimental repeats are required before drawing any definitive conclusions. Regulation of HIFα by O_2

availability or TCA metabolites is relatively well defined, but only a handful of studies have considered whether bioenergetic stress impacts HIF-1α. It would be interesting to explore whether deprivation of selective nutrients (e.g. glucose/pyruvate) or inducing mitochondrial dysfunction impacts HIF-1α expression and activity. If indeed HIF-1α is induced under conditions of bioenergetic stress in ECs, the dependency on AMPK activation could be determined by using inhibitors (e.g. BAY-3827) or siRNA knockdown to inhibit the kinase. The O_2 dose-response experiments require repeating using BI-9774 in lieu of 991 to see if the effects of HIF-1α can be reproduced at an earlier time point. The possibility of HIF-1α as a putative target of AMPK phosphorylation is a compelling hypothesis and will be addressed in Chapter 4 – Crosstalk between AMPK and hypoxia in the endothelium.

I identified several limitations and technicalities with many of the experiments in this chapter including small sample sizes (i.e., HUVEC donors), presence of outliers and limitations of certain methods (e.g., using *in vitro* kinase assays to examine basal AMPK activity rather than AMPKα^{T172} phosphorylation). Experimental repeats with HUVEC pools that appear anomalous or increasing the number of pooled HUVEC donors will aid in differentiating. It would also be useful to do power calculations to calculate the minimum replicates required or statistical modelling in R studio to account for donor effects if these variations persist. Certain assays (e.g. luciferase assays) may be more susceptible to variation, therefore it would be useful to increase the number of technical replicates to address these issues. Taking into consideration these limitations and the hypotheses outlined in Section 3.2 Hypotheses and Aims, there is insufficient evidence that AMPK is robustly inactivated under hypoxia, let alone whether this is due to suppressed protein translation. Although, there are some preliminary observation linking BI-9774 treatment with induction of HIF-1α-dependent transcription, further work is required to confirm that this effect is mediated through AMPK.

4. Chapter 4 – Crosstalk between AMPK and hypoxia signalling in the endothelium

4.1 Introduction

The regulation of cell growth and survival is coordinated through the availability of oxygen and key macronutrients, such as glucose, lipids and amino acids. The signalling cascades underlying both O_2 and nutrient sensing pathways intersect in governing bioenergetic homeostasis and other diverse biological processes. However, very little is known about the nature of the relationship between HIFα and critical nutrition/energy kinases like mTOR and AMPK, respectively.

The relationship between AMPK and HIF-1α signalling is even less clear. Deficiency of AMPKα_2 in myeloid cells (AMPKα_2^{MKO}) reduced HIF-1α protein stability as well as induction of its downstream proangiogenic targets (e.g., VEGFA) after hindlimb ischaemia (HLI) [178]. As a result, restoration of blood flow to the ligated area was hindered in the AMPKα_2^{MKO} mice. Another study demonstrated that HIF-1α transiently increased during the G1 cell cycle phase in an AMPK-dependent manner in HCT-116 colon carcinoma cells [362]. However, only a subtle increase of HIF-1α stability at the protein level was noted with AICAR treatment, indicating AMPK is necessary but not sufficient for HIF-1α stabilisation during G1. The authors postulated that AMPK-mediated stabilisation of HIF-1α acts as a surveillance mechanism to ensure cells have adequate nutrients before committing to DNA synthesis and mitosis [362]. ROS-induced AMPK activity was shown to increase HIF-1α activity, protecting it from ubiquitination and inducing its transcriptional activity in the DU145 human prostate cancer cell line [363]. A possibility of phosphorylation has been identified in *C. elegans* where AMPK phosphorylates HIF-1α on S419 *in vitro* resulting in its downregulation, however it should be noted there is no homologous site in humans [364]. Despite preliminary evidence linking both AMPK and HIF-1α, none of these studies identified a molecular mechanism by which AMPK elicits stabilisation of HIF-1α. Therefore, it could be hypothesised that one of mechanisms by which AMPK enhances HIF-1α signalling may be through phosphorylation.

Post-translational modifications (PTMs) of HIFα extend beyond hydroxylation and ubiquitination, with growing appreciation for acetylation, addition of **s**mall **u**biquitin-like **mo**difier proteins i.e. SUMOylation and methylation [244]. Whilst these modifications may play an important role in regulating HIF-1α, phosphorylation provides a rapid and reversible modification that can lead to changes in protein structure (e.g. stability), localisation, protein-protein interactions and function [365]. Therefore, multisite phosphorylation by various kinases

allows for precise control of downstream processes, that can integrate different cellular signalling pathways. Evidence demonstrating HIF-1α phosphorylation was performed by Wang and colleagues, where they subjected hypoxic nuclear extracts to calf intestinal phosphatase treatment. The authors found that phosphatase treatment resulted in the dissociation of HIF-1α:HIF-1β complex and loss of HIF-1α:DNA binding based on electrophoretic mobility shift assays (EMSA) [366]. This suggests that phosphorylation significantly impacts HIF-1α interactions with binding partners and gene transactivation.

At present, a number of phosphorylation sites on HIF-1α have been identified (Figure 4.1), with phosphorylation either enhancing or suppressing its activity. Phosphorylation at S31 was identified by Daly *et al.* and was shown to abrogate transcriptional activity of HIF-1α [367], but the upstream kinase responsible remains unidentified. Casein kinase 1 δ inhibits HIF-1α transcriptional activity through phosphorylation of S247, disrupting its heterodimerisation with HIF-1β without altering its stability or nuclear localisation [368]. HIF-1α phosphorylation at residues within the ODDD and N-TAD domains, T498/S502/S505/T506/S510/S551/T555 and S589, were all reported to be glycogen synthase kinase-3 β (GSK-3β) sites (Figure 4.1) [369, 370]. GSK-3β phosphorylation enhances HIF-1α proteasomal degradation through a non-canonical pathway involving the FBW7-E3 ubiquitin ligase. On the other hand, T63 and S696 were found to be phosphorylated by PKA in HeLa cells, inducing HIF-1α-dependent gene transactivation [371]. Activation of PKA by cyclic AMP in human cardiomyocytes enhanced expression of 5'ecto-nucleotidases CD39 and CD73. Extracellular adenosine signalling proceeds in a two-step enzymatic process where first CD39 converts ATP/ADP to AMP which is subsequently converted into adenosine by CD73. This is thought to contribute to an intrinsic immunosuppressive mechanism in ischaemic and inflammatory conditions to dampen excessive inflammation [265]. All these studies highlight how HIF-1α and its downstream effects can be regulated post-translationally by phosphorylation, independently of O_2 by various kinases. This led me to hypothesise that AMPK may modulate HIF-1α activity by directly phosphorylating the transcription factor and promoting HIF-1α-dependent transcription.

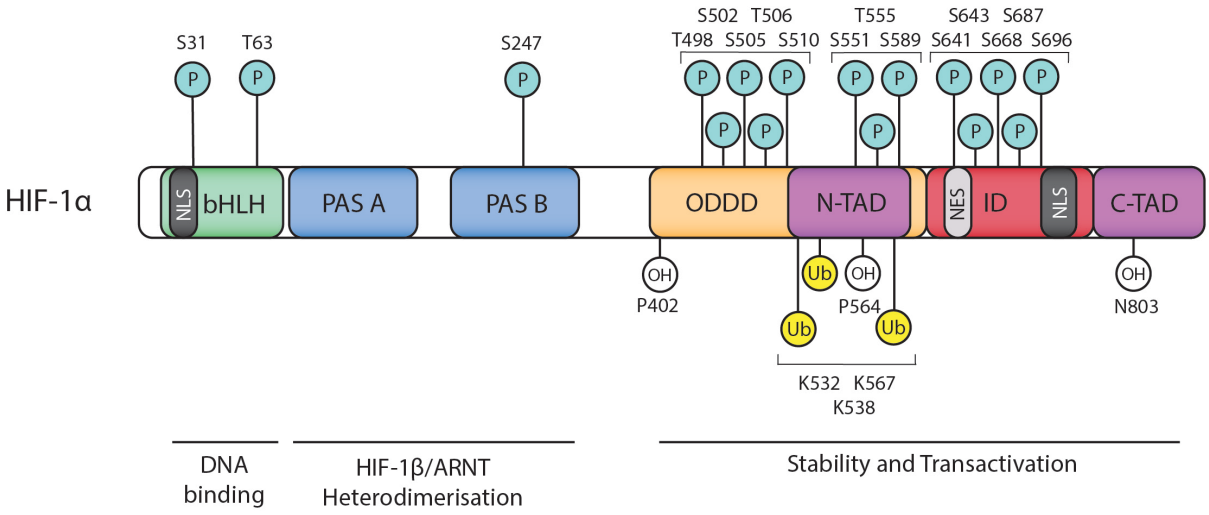


Figure 4.1 *– A schematic representing phosphorylation sites reported in the literature for HIF-1α.*

Schematic was adapted from Albanese *et al.* (2021) [244]. Green circles represent phosphorylation sites, white circles hydroxylation sites and yellow circles lysine ubiquitination sites.
Abbreviations: bHLH: basic helix loop helix; PAS: Per-Arnt-Sim (PAS) domains A (PAS A) and B (PAS B); ODDD: oxygen-dependent degradation domain; N-TAD: N-terminal transactivation domain; C-TAD: C-terminal transactivation domain; ID: inhibitory domain; NES: nuclear export sequence; NLS: nuclear localisation sequence; C-TAD: C-terminal transactivation domain. Figure created in Adobe Illustrator.

4.2 Hypothesis and Aims

Hypothesis: Activation of AMPK using BI-9774 enhances HIF-1α-dependent transcription, potentially by interacting and directly phosphorylating HIF-1α.

Aim 1: Examine the effects of hypoxia and AMPK activation by BI-9774 on the transcriptome in HUVECs by RNA-sequencing.

Aim 2: Compare changes in gene expression in HUVECs response to hypoxia and AMPK activation.

Aim 3: Investigate whether AMPK can phosphorylate HIF-1α *in vitro* and identify putative AMPK phosphorylation sites in HIF-1α by LC-MS^2

Aim 4: Evaluate whether site-directed mutagenesis (SDM) of identified AMPK phospho-sites alter HIF-1α protein stability and transcriptional activity.

4.3 Results

4.3.1 The effect of BI-9774 and/or hypoxia on the endothelial transcriptome

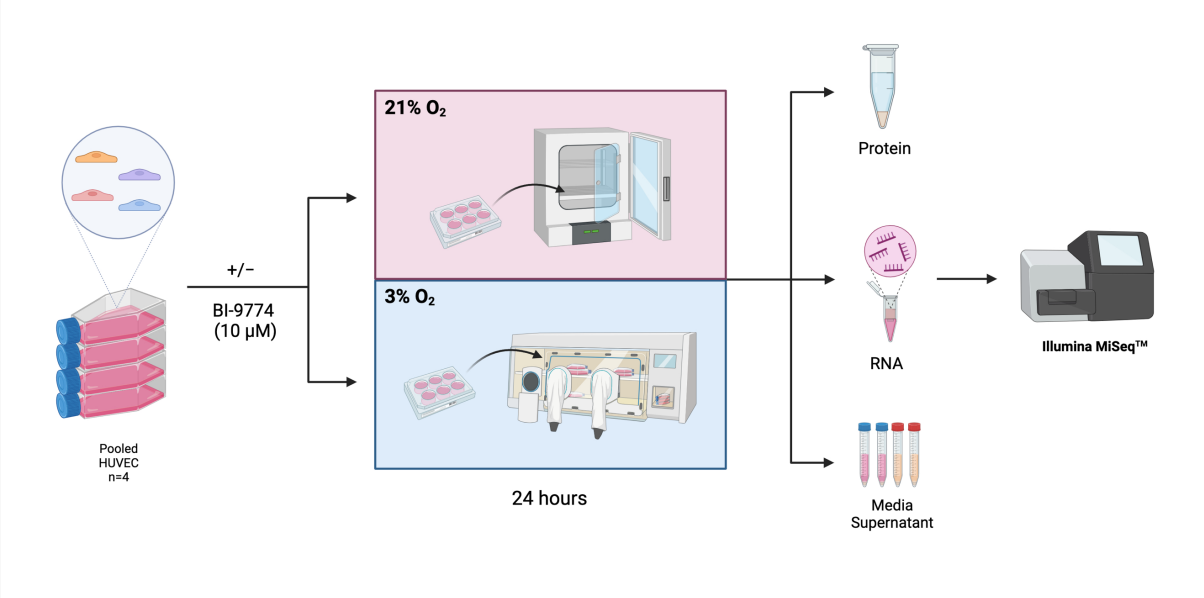


Figure 4.2 *– Schematic describing the experimental design for RNA-sequencing.*

Pooled HUVECs (n=4) were expanded and split into 6-well plates until they reached ~85-90% confluency. HUVECs were subsequently either left untreated (UT) or treated with BI-9774 (10 μM) for 24 hours. Matched plates were seeded to collect protein lysates as well as media supernatant for downstream analysis for target of interest validation. Figure created using BioRender.

Next generation sequencing methods have been used extensively to examine transcriptomics changes in ECs in response to hypoxia, including RNA-seq and ATAC-seq. However, none have used AMPK activators or gain-of-function mutants on ECs to date, especially in response to metabolic stress. Therefore, our knowledge of which pathways and processes are regulated by AMPK and whether AMPK facilitates adaptation under hypoxia remains unknown. HUVECs from four different donor pools were seeded and treated with or without BI-9774 (10 μM) and then placed under 3% O_2 (hypoxia, HX) or 21% O_2 (normoxia, NM) for 24 hours (Figure 4.2) prior to harvesting for RNA. (Figure 4.3). Matched plates were seeded for protein and collection of media supernatant for downstream validation of targets. After RNA purification, poly(A) selection was carried out from all treatment groups. A sample distance heatmap was generated to visualise overall gene expression changes, with factors such as gender of donor, conditions (3% or 21% O_2) and group (defined as combined % O_2 and treatment) taken into consideration (Figure 4.3). The dendrogram shows distinct clustering of the biological replicates according to BI-9774 treatment and/or % O_2. Principal component analysis (PCA) confirmed this observation each set of replicates greatly diverged according to their combined treatment and O_2 tension. Within each group, each biological replicate clustered closely together thus all donors responded similarly to treatment and condition. Principal component

(PC) 1 accounting for 60.74% of the variance whilst PC2 accounts for an additional 30.58% of the variance (Figure 4.3).

Initially, I decided to perform three pairwise comparisons for differentially expressed gene analysis (DEG): 3% (hypoxia) versus 21% O_2 (normoxia) control; BI-9774-treated versus control at normoxia (21% BI-9774) and BI-9774-treated versus control at hypoxia (3% O_2). Only genes that met the criteria of an adjusted p-value < 0.05 and a fold change (FC) of 1.5 were used for DEG analysis (Figure 4.4). Both hypoxia and BI-9774 treatment significantly altered the transcriptome in HUVECs. In HUVECs subjected to 3% O_2, 617 genes were upregulated and 717 downregulated compared to HUVECs maintained at 21% (Figure 4.4A). BI-9774 treatment profoundly altered the HUVEC transcriptome, with 1238 genes upregulated and 1104 genes downregulated compared to non-treated cells maintained at 21% O_2 (Figure 4.4B). Under 3% O_2, BI-9774 promoted the expression of 749 genes whilst suppressing 821 genes compared to untreated HUVECs (Figure 4.4C).

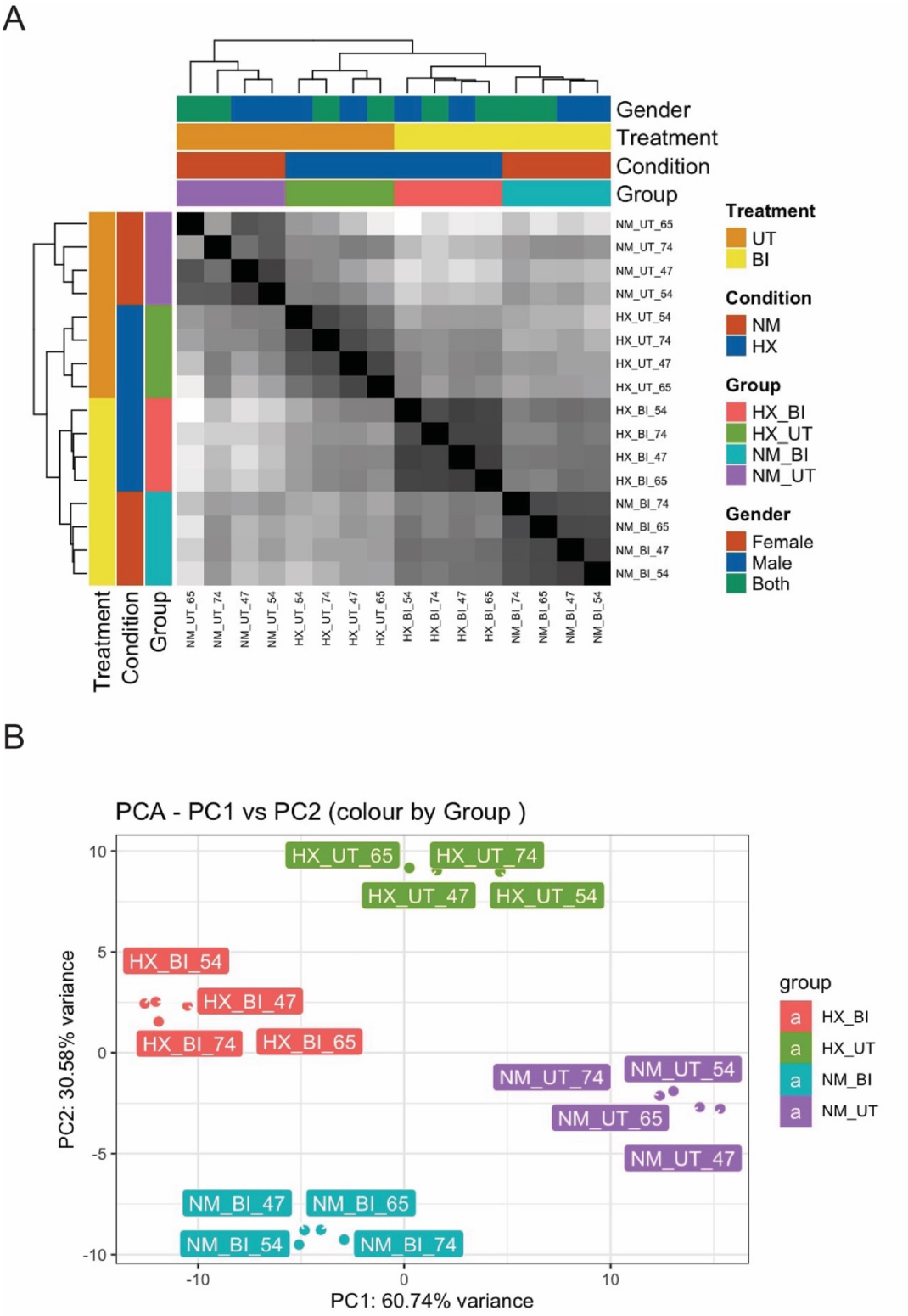


Figure 4.3 *– Cluster analysis of RNA-seq gene expression data.*

Heatmap and principal component analysis (PCA) taking into consideration biological replicates and conditions. The numbers following the oxygen tension (NM/HX) and treatment designation (UT/BI) refers to the lot number of the HUVEC obtained from PromoCell.
(A) Distance heatmap of RNA-seq samples from four different HUVEC donors subjected to 21% O_2 (NM) and 3% O_2 (HX) either untreated (UT) and/or 10 µM BI-9774 (BI).
(B) PCA plot of RNA-seq samples as described for (A).

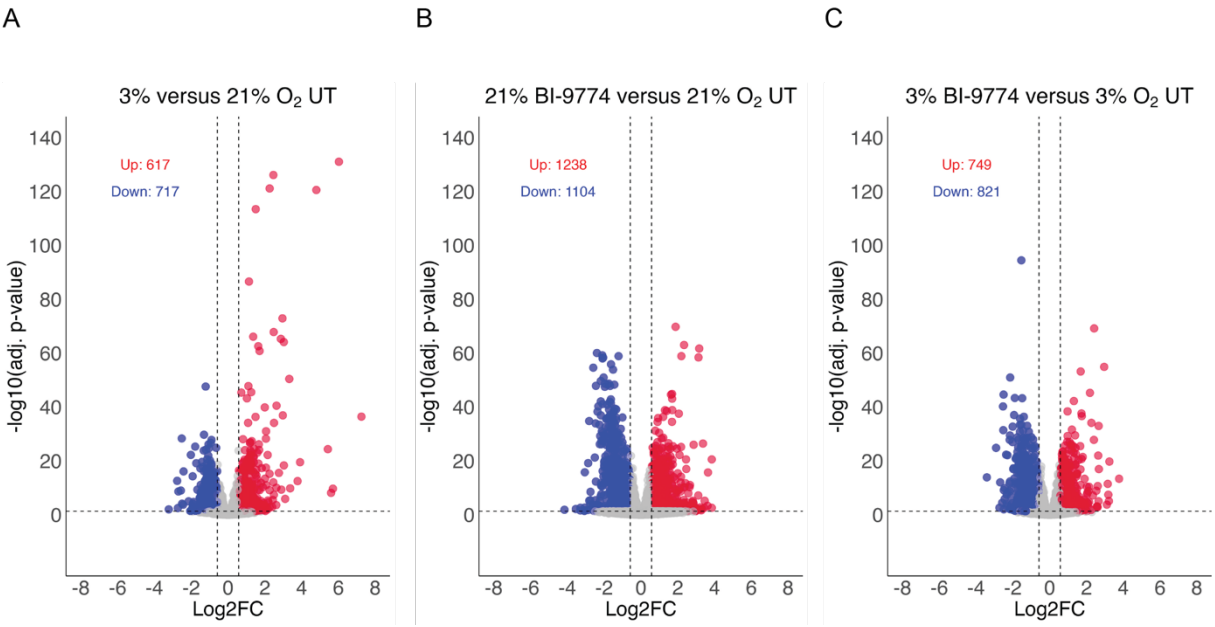


Figure 4.4 *– Volcano plots displaying DEG analysis across all pairwise comparisons.*

(A) Hypoxia (3% O_2) compared to normoxia (21% O_2) UT.
(B) BI-9774 treatment compared to UT at 21% O_2.
(C) BI-9774 treatment compared to UT at 3% O_2.
DEGs were individually plotted on a volcano plot based on log_2FC and the adjusted $-log_{10}$ p-values for each pairwise comparison. Blue dots indicate downregulated genes, red dots indicate upregulated genes, and grey dots indicate non-differentially expressed with the following cut-off criteria of an adjusted p-value < 0.05 and log_2FC > ±1.5.

To characterise the molecular and biological changes that occur in response to hypoxia and/or BI-9774 treatment in HUVECs, Qiagen Ingenuity Pathway Analysis (IPA) was employed to identify overrepresented pathways. IPA provides detailed analysis including upstream analysis along with a disease and function annotation in an endothelial context. The following cut offs of adjusted p-values < 0.05 and FC greater than 1.5. The z-score calculation was also included. The Z-score feature is statistical algorithm developed by Qiagen that can predict activity of a pathway, or a biological function based on DEGs in the experimental dataset. Z-score values close to 0 are not considered significant, whereas positive and negative z value (| z | > 1) indicates upregulation and downregulation, respectively. However, IPA only considers values where | z | > 2 biologically significant. Therefore, pathways/functions with z-scores > 2 or < − 2 are considered activated and deactivated, respectively. All pathways displayed in the bubble plots were filtered based on significance threshold of p-value < 0.05 and | z | > 1.

As expected, robust activation of HIF-1α signalling was observed in the 3% vs 21% O_2 UT dataset (z = 2.646, p-value = 1.023×10^{-3}) (Figure 4.5). HIF-1α is heavily implicated in the tumour microenvironment and wound healing processes, both of which were also upregulated.

NO production and signalling pathways were also upregulated, e.g. eNOS signalling and NO signalling in the cardiovascular system (z = 1.387 and 1.604, respectively, p-values < 0.01). Given its role as a potent vasodilator, ECs may upregulate NO production to increase O_2 perfusion in hypoxic tissues. Glycolysis was also positively enriched due to the switch in anaerobic metabolism, (z =2, p-value = 0.0275). VEGF family ligand-receptor interactions (z = 1.667, p-value < 0.05) suggests increased VEGF paracrine signalling, perhaps to promote angiogenesis in response to low O_2. IPA analysis also revealed a propensity towards pro-inflammatory cytokine signalling, e.g. leukocyte extravasation and other pro-inflammatory cytokines but the activation score was not statistically significant (z-score values < 2). Despite the recurring inflammation related gene signatures, IFN signalling was significantly downregulated under hypoxia (z = -2.236, p-value = 0.0186) (Figure 4.5). Hypoxia greatly alters endothelial senescence and senescence pathway was significantly increased (z = 2.858, p-value = 2.5703957×10^{-4}) whereas sirtuin signalling was suppressed (z = -2.524, p-value = 1.79). Hypoxia induced significant changes in cell cycle related pathways, including significant reduction of the cyclins and cell cycle regulation pathway along with cell cycle: G1/S checkpoint regulation and cell cycle: G1/M DNA damage checkpoint regulation. Moreover, I also observed activation of the growth arrest and DNA damage 45 (GADD45) tumour suppressor proteins signalling (z = 1.51, p-value = 4.57×10^{-5}), suggesting that hypoxia exposure induces growth arrest in HUVECs (Figure 4.5).

No RNA-seq dataset examining the effect of AMPK activators in ECs has been published to date. To get an insight into the potential biological pathways and functions regulated by AMPK, the effect of BI-9774 treatment under standard culture conditions (21% O_2) was analysed. Deactivation of cyclins and cell cycle regulation (z = -3.5 , p-value = 1.34×10^{-5}) and concurrent activation of the G2/M DNA damage cell cycle checkpoint' (z = 2.63 , p-value = 7.94×10^{-7}) was observed. There is also significant activation of senescence signalling (z = 2.8, p-value = 4.07×10^{-5}) (Figure 4.6), suggesting BI-9774 prevents cell cycle progression and triggers growth arrest in HUVECs. Cardiac hypertrophy signalling was positively regulated by BI-9774 treatment (z = 2.722, p-value = 0.0102), which is a striking finding, given pathogenic mutations in AMPKγ_2 promote WPW in humans (Figure 4.6). It can also be inferred that AMPK regulates motility as several pathways related to cell migration (regulation of actin-based motility by Rho/PAK signalling), mechanosensing (paxillin signalling) and bidirectional signalling (ephrin receptor signalling) were enriched, but the z-scores were not significant (z < 2, p-value < 0.05) to conclude their directionality (Figure 4.6).

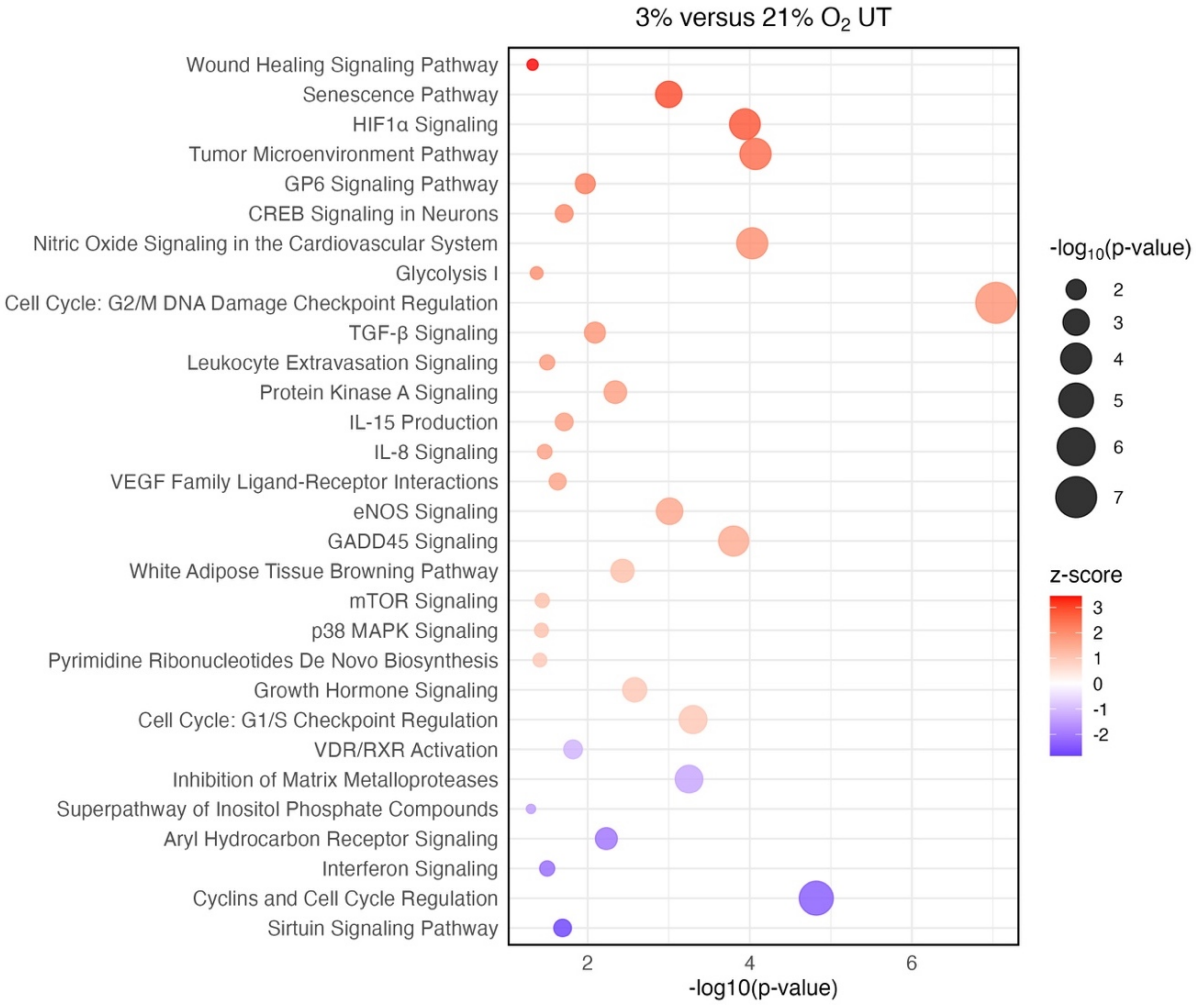


Figure 4.5 *– Canonical Pathways Analysis (CPA) for 3% O_2 (hypoxia) versus 21% O_2 (normoxia).*

Bubble plot displaying the major pathways altered as determined by IPA analysis. The size of the bubbles corresponds to the adjusted $-\log_{10}$(p-values) for each given pathway. Red represents predicted activated pathways whereas blue represents predicted suppressed pathways with the colour intensity indicating the magnitude of z-score. All the pathways in the above plot meet the following thresholds: adjusted p-value < 0.05 and z-scores greater than 1 and less than -1.

Inhibition of inflammatory processes were also observed with downregulation of HMGB1 pro-inflammatory signalling pathways (z-score = -1.29, p-value = 6.46×10^{-3}), presenting a potential mechanism for the reported anti-inflammatory effects of AMPK. Alteration in pathways associated with energy homeostasis and/or lipid metabolism, e.g. PPAR signalling (z-score = 1, p-value = 4.27×10^{-3}) and superpathway of cholesterol biosynthesis (z-score = 2.449, p-value = 2.34×10^{-2}) were altered (Figure 4.6). Significant enhancement of eNOS signalling was observed (z-score = 2.79, p-value = 1.62×10^{-3}), in line with previous observations of AMPK regulating NO production upon drug- and LSS-induced activation. Once again, HIFα transactivation signature in BI-9774 normoxic HUVECs was observed, as demonstrated by significant enrichment of HIF-1α signalling (z-score = 2.611, p-value =

9.55×10^{-5}) along with tumour microenvironment pathway (z-score = 2.449, p-value = 7.59×10^{-3}), suggesting BI-9774 triggers a pseudo-hypoxic response in HUVECs (Figure 4.6).

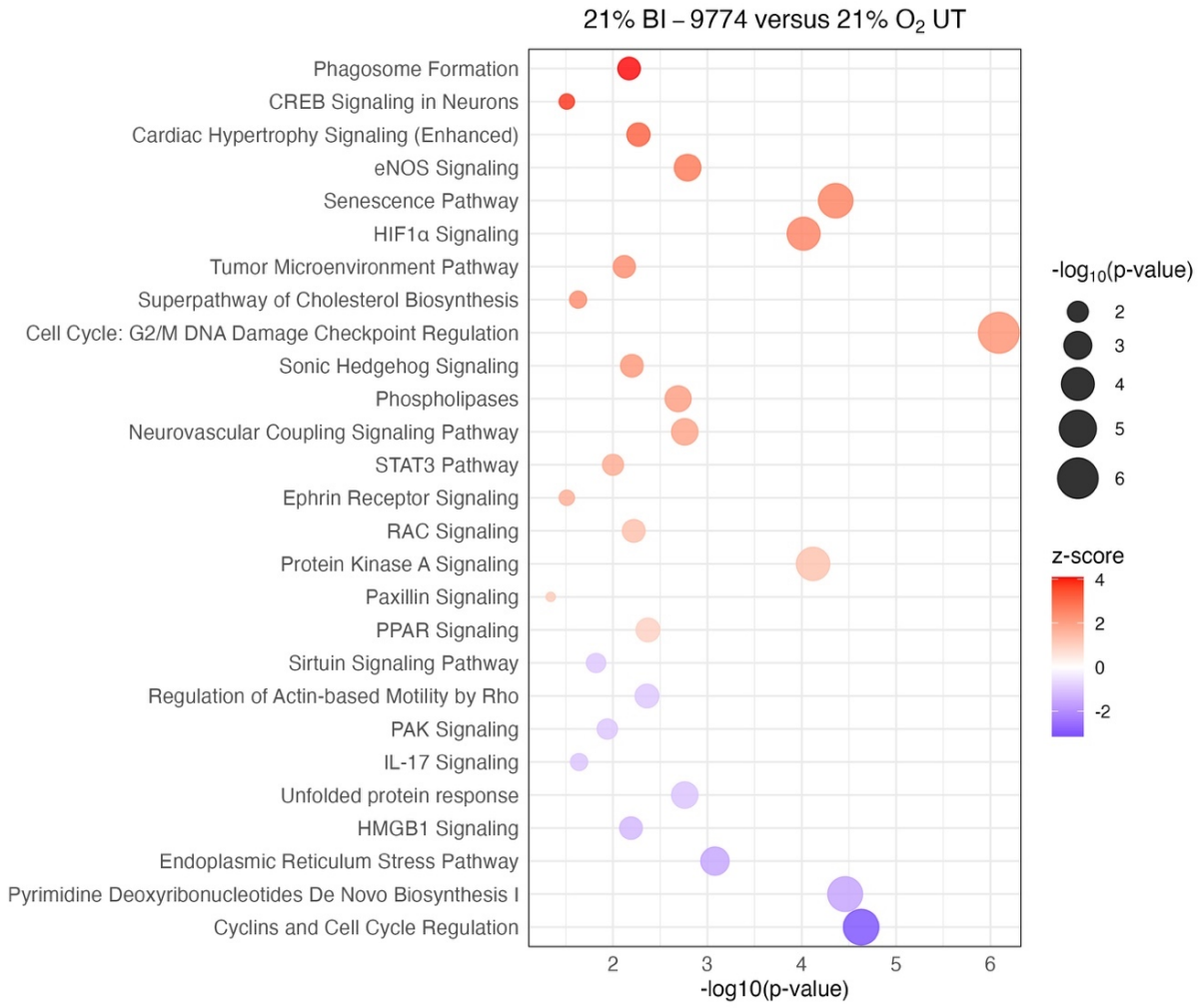


Figure 4.6 *– Canonical Pathways results for BI-9774 treatment versus untreated at 21% O_2.*

Bubble plot displaying the major pathways altered as determined by IPA analysis. The size of the bubbles corresponds to the adjusted $-\log_{10}$(p-values) for each given pathway. Red represents predicted activated pathways whereas blue represents predicted suppressed pathways with the colour intensity indicating the magnitude of z-score. All the pathways in the above plot meet the following thresholds: adjusted p-value < 0.05 and z-scores greater than 1 and less than -1.

Next, I performed pathway analysis on the effects of BI-9774 on HUVECs under 3% O_2 to examine the effect of AMPK activation under hypoxia. There were some similarities in pathways with the normoxic dataset (Figure 4.7). Changes in cell cycle remained a predominant feature as shown by the significant upregulation in the G2/M DNA damage checkpoint regulation pathway (z = 2.496, p-value = 7.24×10^{-8}), senescence (z = 1.569, p-value = 3.39×10^{-4}) and GADD45 signalling (z = 1.155, p-value = 2.75×10^{-5}) with concurrent deactivation of cyclins and cell cycle regulation (z = -2.84, p-value = 5.13×10^{-7}) (Figure 4.7). A shift in inflammation-related pathways was also noted with a significant reduction in the innate immune and inflammatory response pathways e.g., HMGB1 (z = -1.387, p-value = 3.39×10^{-3}) and TREM1 signalling (z = -1.667, p-value = 1.26×10^{-2}). AMPK also appears to influence EC behaviour in proangiogenic processes as there is enrichment in planar cell polarity (PCP) pathway, VEGF and ephrin receptor signalling (Figure 4.7). BI-9774 treatment in hypoxic HUVECs influences the production of vasoactive molecules and lipid signalling mediators, with significant activation of adenosine nucleotides degradation II (z-score = 2, p-value = 6.46×10^{-3}) and eNOS signalling (z-score = 1.069, p-value = 2×10^{-3}). Moreover, AMPK may influence processing of polyunsaturated fatty acids (PUFA) to form eicosanoids (e.g., EPA) as shown by the upregulation of phospholipases and eicosanoid signalling (Figure 4.7). Similar to BI-9774 treatment under normoxia (Figure 4.6), HIF-1α signalling was significantly enriched in the hypoxic BI-9774 data set, but it's z-score fell below 1 (z = 0.928, p-value = 5.91×10^{-5}).



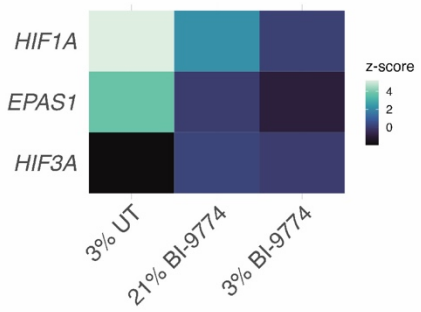
Figure 4.7 *– Canonical Pathways results for BI-9774 treatment versus untreated at 3% O_2.*

Bubble plot displaying the major pathways altered as determined by IPA analysis. The size of the bubbles corresponds to the adjusted $-\log_{10}$(p-values) for each given pathway. Z-scores of ≥ 2 or ≤ -2 are significant in terms of predicted activity. Red represents predicted activated pathways whereas blue represents predicted suppressed pathways with the colour intensity indicating the magnitude of z-score. All the pathways in the above plot meet the following thresholds: adjusted p-value < 0.05 and z-scores greater than 1 and less than -1.

The IPA software contains multiple analysis tools, one of which is the Upstream Function. The Upstream Function analysis tool can predict which transcription factors are responsible for the changes in the Canonical Pathways visualised (Figures 4.5-4.7). I examined all the HIFα isoforms, as the distinction between HIF-1α and HIF-2α signalling has yet to be defined. HIF-3α was also included as it is thought to be a negative regulator of HIFα signalling. As shown in Figure 4.8A, both HIF-1α (*HIF1A*) and HIF-2α (*EPAS1*) are significantly activated under 3% O_2 compared to normoxia (z-scores > 2), whereas HIF-3α activity is downregulated. HIF-1α activation is increased following treatment with BI-9774 at normoxia, whereas HIF-2α remains unchanged, based on their respective z-scores (Figure 4.8B). It should be noted that both HIF-1α and HIF-2α share common targets and that HIF-2α-specific targets are not well elucidated

[311]. There was no difference in the activation state of the HIFα isoforms in the BI-9774 treated group versus untreated at 3% O_2 (Figure 4.8B). Regardless of the z-scores, HIF-1α and HIF-2α are significantly enriched in the BI-9774 conditions (p-value < 0.001) under both O_2 tensions.

A



B

Pairwise Comparison	Isoform	Log_2FC	Activation State	z-score	p-value
3% vs 21% O_2 UT	*HIF1A*	0.142	Activated	5.22	3.99E-23
	EPAS1	-0.406	Activated	3.777	3.43E-18
	HIF3A	0.322		-1.969	0.00368
21% BI-9774 vs 21% O_2 UT	*HIF1A*	0.488	Activated	2.172	1.37E-13
	EPAS1	0.742		0.013	5.92E-16
	HIF3A	0.655		0.243	0.00297
3% BI-9774 vs 3% O_2 UT	*HIF1A*	-0.047		0.118	2.2E-14
	EPAS1	0.393		-0.946	2.25E-13
	HIF3A	0.722		0	0.0351

Figure 4.8 *– IPA Upstream Regulator analysis of HIFα isoforms across all pairwise comparisons.*

(A) Heatmap displaying z-scores of all HIFα isoforms across all datasets.
(B) Table summarising the pairwise comparisons, HIFα isoform, log_2FC, activation state, z-score and the p-value.

4.3.2 Common pathways based on shared DEGs between hypoxia and BI-9774 treatment

To examine the similarity between hypoxia and normoxia-BI gene signatures more closely, I next performed pairwise comparisons of DEGs comparing UT cells under 3% O_2 versus 21% O_2 BI-9774 treated cells, which was visualised using a scatterplot to examine similarities in transcription signature. There were 189 upregulated genes and 361 downregulated genes in common, although no striking correlation was seen overall (Figure 4.9). Next, I sought to assess what pathways the common genes participate in, as it may provide an indication of what pathways AMPK and HIF-1α may be associated with. IPA Canonical Pathway analysis was performed initially on all upregulated and downregulated genes separately. Disease and Functions analysis was also investigated to see which biological processes both AMPK and hypoxia are associated with in an endothelial context.

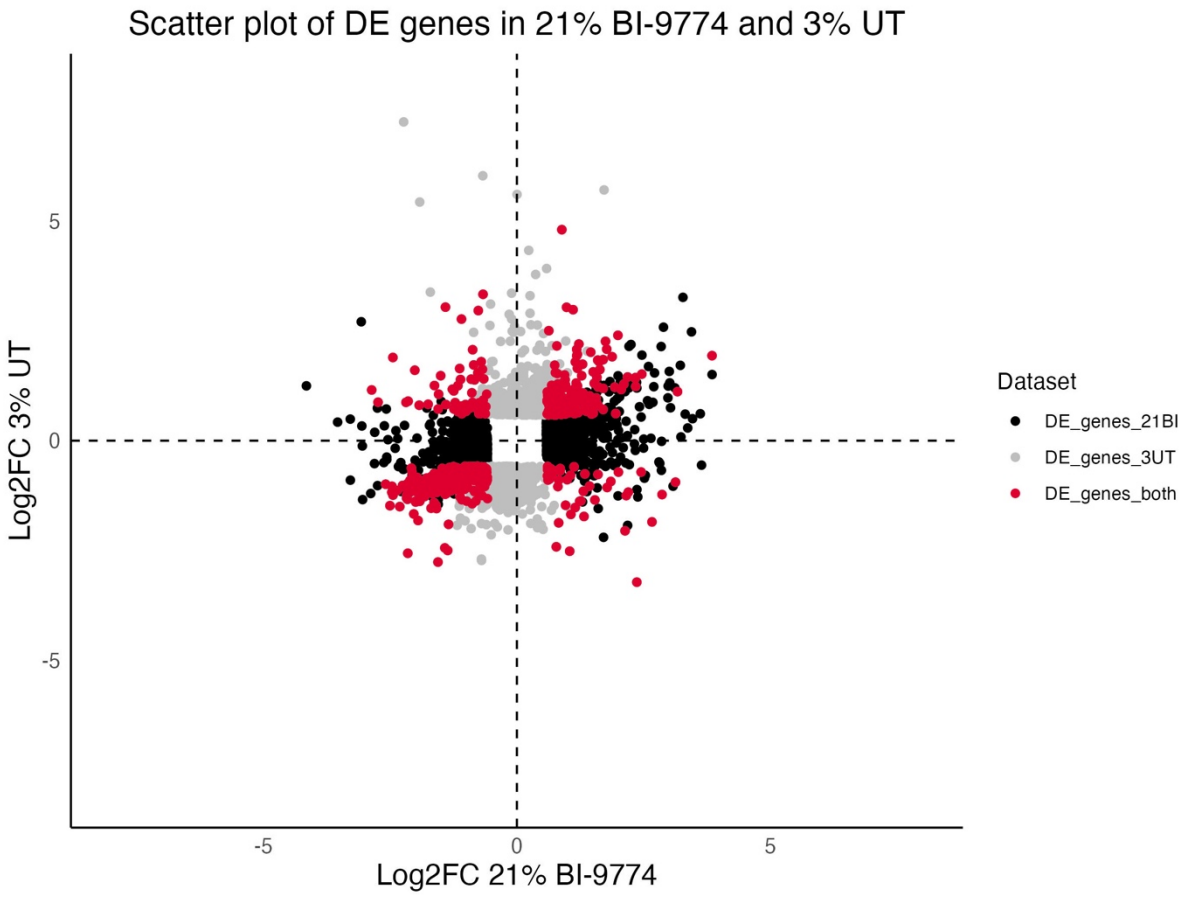


Figure 4.9 *– Pairwise comparison of DEGs between 21% O_2 BI-9774 treated versus 3% O_2 UT.*

A scatterplot displaying DEGs in both 21% O_2 BI-9774 and 3% O_2 UT based on their log_2FC values DEGs altered by 21% O_2 BI-9774 treatment only (black), DEGs altered by 3% O_2 UT only (grey) and DEGs in both (red).

The analysis implicated numerous endothelial processes. HIF-1α signalling was significantly enhanced, suggesting that AMPK may enhance the HIF-1α axis of the hypoxia response. One of the highly enriched processes is ECM remodelling (e.g. ECM organisation and degradation of the ECM), a process that HIF-1α has been implicated in (Table 1.3). Angiogenesis was also implicated with pathways such as VEGF family ligand-receptor Interactions, signalling by VEGF, ephrin receptor signalling and wound healing signalling (Figure 4.10). As mentioned in Section 1.6, in the initial stages of angiogenesis, degradation of ECM occurs in response to proangiogenic factors. Signalling pathways linked to inflammation and/or haemostasis were also altered e.g. HMGB1 signalling and glycoprotein VI (GP6) signalling. A number of these pathways often intersect in physiological processes for example, inflammation, haemostasis, ECM breakdown, angiogenesis and HIF-1α participate in distinct phases of the wound healing response. NO signalling was also enriched in line with previous studies where both AMPK activation and hypoxia alter vascular tone through the NOS isozymes. Both hypoxia and AMPK activation result in a significant upregulation of genes involved in nutrient metabolism [e.g., regulation of insulin-like growth factor (IGF) and uptake by IGFBPs, mTOR signalling] whilst concomitant suppression of mitochondrial-related functions (e.g., mitochondrial protein import and translation) (Figure 4.10). The most significantly downregulated pathways are processes related to cell cycle progression and mitosis, corroborating the individual pairwise comparisons in Figures 4.5 and 4.6.

Given the clear enrichment in growth arrest and inhibition of cell cycle for downregulated genes (Table 8.1), I restricted my analysis to include only upregulated genes common to both hypoxia and BI-9774 for the downstream functions and diseases. The shared DEGs are involved in activation of angiogenesis and vasculogenesis (Figure 4.11), corroborating previous studies showing the importance of hypoxic stimulus and AMPK activation during vascularisation in development (hypoxia) and disease (AMPK). Enrichment in sprouting, formation of cellular protrusions and cell movement of endothelial cells further suggest that both hypoxia and AMPK activation mimic initiation of sprouting in response to nutrient and O_2 deprivation (Section 1.6.1 Sprouting Angiogenesis).

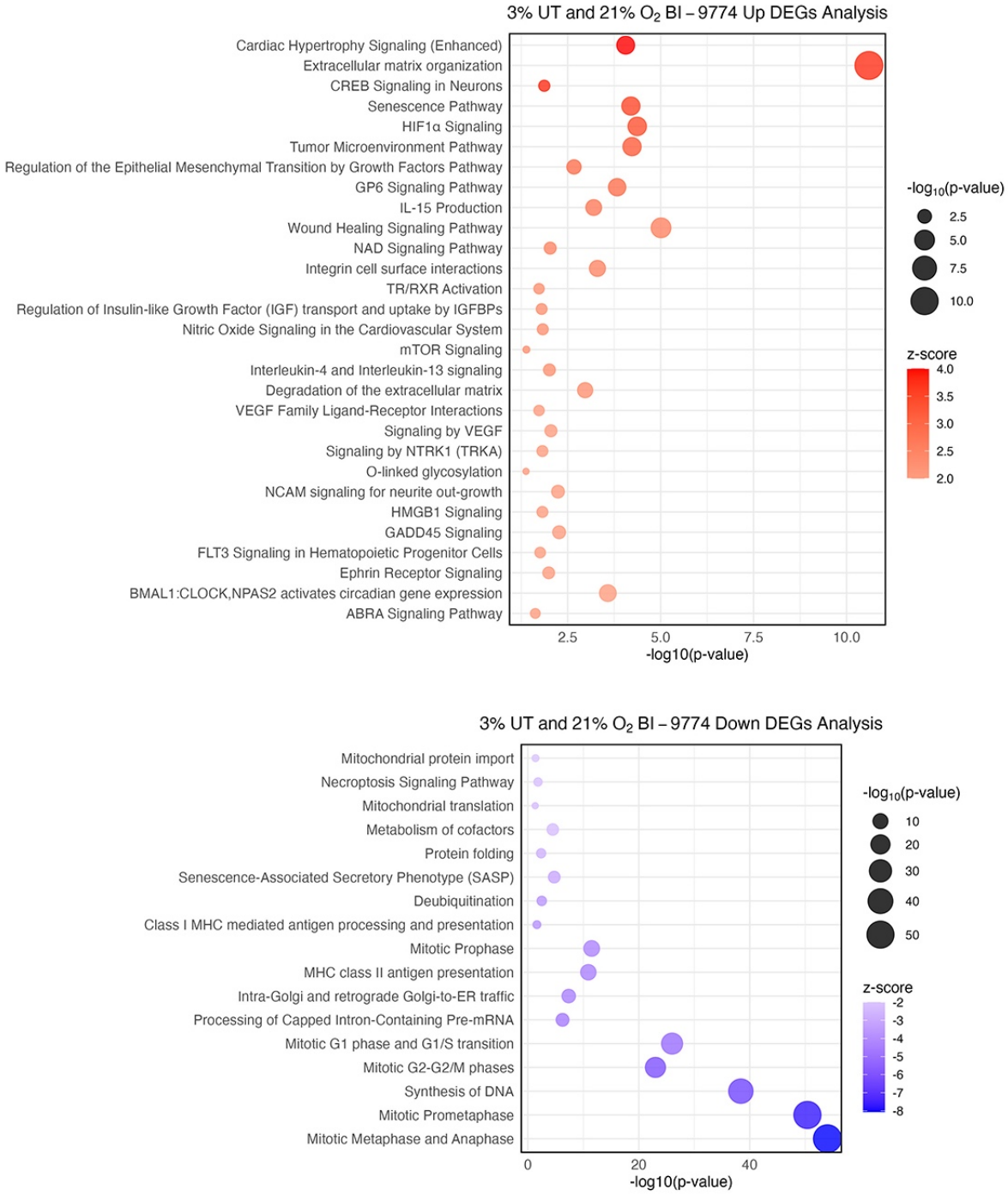


Figure 4.10 *– IPA Canonical Pathways results with common DEGs shared between 3% O_2 UT and 21% O_2 BI-9774.*

Bubble plot displaying results Canonical Pathways as part of Qiagen IPA analysis. The size of the bubbles corresponds to the adjusted $-\log_{10}$(p-values) for each given pathway. Z-scores of ≥ 2 or ≤ -2 are significant in terms of predicted activity. Red represents predicted activated pathways whereas blue represents predicted suppressed pathways with the colour intensity indicating the magnitude of z-score. The following thresholds were applied with adjusted p-value < 0.05 and z-scores greater than 2 and less than -2.

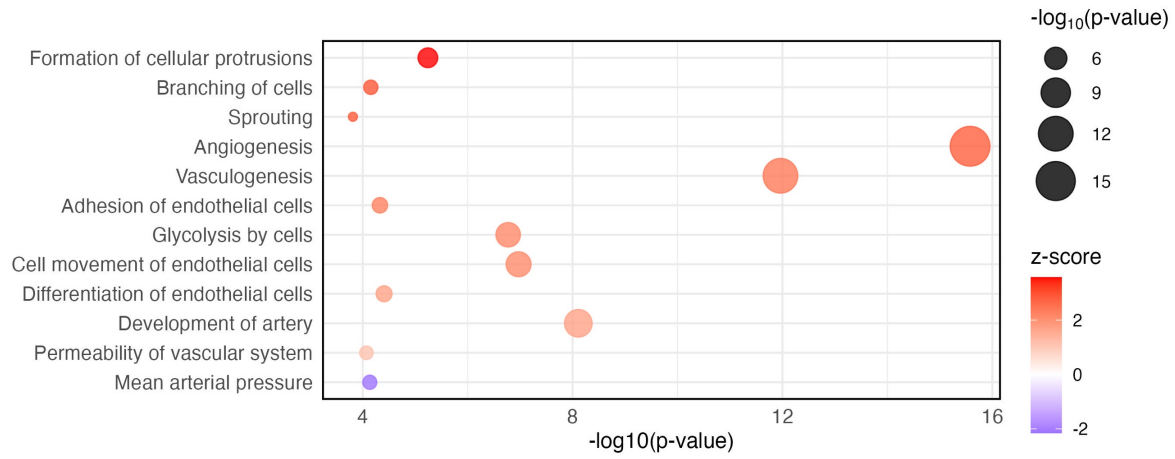


Figure 4.11 *– IPA Functions annotations with common upregulated DEGs shared between 3% O_2 UT and 21% O_2 BI-9774.*

Bubble plots displaying the functions regulated based on the common upregulated DEGs in 3% O_2 UT and 21% O_2 BI-9774 filtered to also include Cardiovascular System Development and Function. The size of the bubbles corresponds to the adjusted $-\log_{10}$(p-values) for each given pathway. Only significantly activated pathways (i.e., z-scores of ≥ 2 or ≤ -2) are displayed. Red represents predicted activated pathways whereas blue represents predicted suppressed pathways with the colour intensity indicating the magnitude of z-score. The following thresholds were applied with adjusted p-value < 0.05.

To gain an understanding which pathways maybe associated with both AMPK and hypoxia signalling, I analysed which disease states are implicated based on the common upregulated DEGs (Figure 4.12). Downregulated DEGs were also examined but the results were heavily enriched in haematological cancers, an area beyond the scope of this project; results are included in the Appendices (Table 8.1). There was a predicted increase in diseases featuring vessel occlusion (e.g. thrombus, stroke/acute myocardial infarction (MI) and atherosclerosis). Pulmonary vascular disease (PVD), including pulmonary hypertension (PH), both had high predicted activation score and -$\log_{10}$(p-value) (Figure 4.12). This was not surprising as hypoxia and/or HIFα play a critical role in. the development of PH. The genes also enriched in conditions featuring endothelial dysfunction such as hypertension, cerebrovascular dysfunction and preeclampsia. Endothelial dysfunction also features in metabolic syndrome and diabetes, both of which were significantly enriched but not deemed significant based on their z-scores (Figure 4.12). Immune-mediated inflammatory disease was significantly downregulated, indicating that AMPK may perhaps mediate anti-inflammatory effects by dampening pro-inflammatory signalling pathways dysregulated in these diseases as shown in Figures 4.6 and 4.7. Unfortunately, the dataset does not delineate between HIF-1α-dependent and -independent responses, therefore it is difficult to establish the shared genes between HIF-1α and AMPK. A limitation of the Qiagen IPA analysis is that it does not determine whether

AMPK and/or HIF-1α directly participates or modulates these processes unless there is independent verification from other studies.

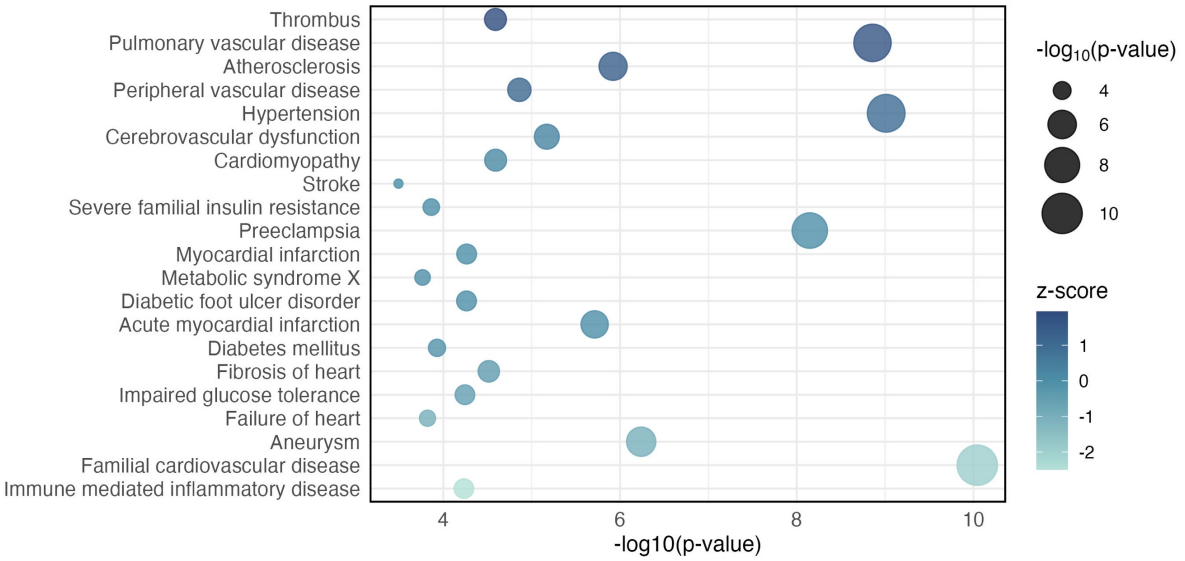


Figure 4.12 *– IPA Diseases annotations on common upregulated DEGs shared between 3% O_2 UT and 21% O_2 BI-9774.*

Bubble plots displaying the functions regulated based on the common upregulated DEGs in 3% UT and 21% BI-9774 filtered to also include Cardiovascular System Development and Function. The size of the bubbles corresponds to the adjusted $-\log_{10}$(p-values) for each given pathway. Only significantly activated pathways (i.e., z-scores of ≥ 2 or ≤ -2) are displayed. Red represents predicted activated pathways whereas blue represents predicted suppressed pathways with the colour intensity indicating the magnitude of z-score. The following thresholds were applied with adjusted p-value < 0.05.

4.3.3 Effect of AMPK-mediated phosphorylation on HIF-1α function

The significant enrichment of HIF-1α transcriptional signature in the BI-9774 treated HUVECs, regardless of O_2 tension led me to hypothesise whether AMPK and HIF-1α interact endogenously in HUVECs. To confirm whether the interaction could be direct, HUVECs were seeded in imaging plates and treated for 16 hours with BI-9774 followed by a 'spike' of MG-132 (10 μM) in the last 1 hour to stabilise HIF-1α to detectable levels. I performed a proximity ligation assay (PLA) assay probed using anti-phospho-AMPKα^{T172} antibodies and anti-HIF-1α antibodies. BI-9774 treatment increased the number of foci in HUVECs (Figure 4.13A), with a mild 1.4-fold increase compared to untreated (Figure 4.13B).

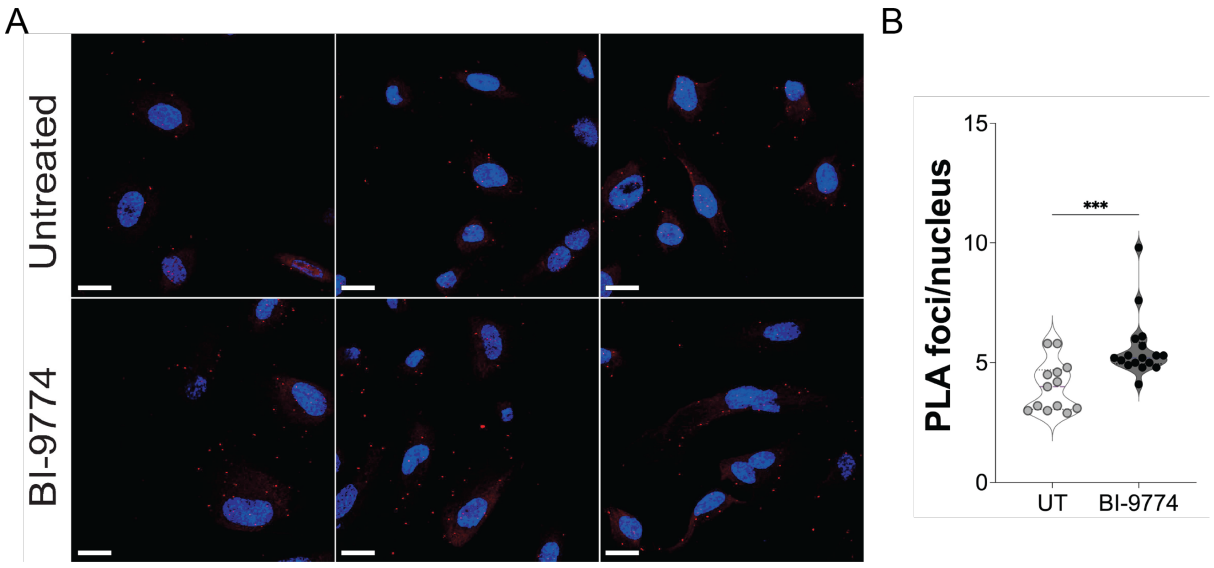


Figure 4.13 *– Proximity Ligation Assay of phospho-AMPKα^{T172} and HIF-1α in HUVECs under 21% O_2.*

(A) Image panel composed of representative confocal images of in situ PLA between phospho-AMPKα^{T172} and HIF-1α in untreated (upper) and BI-9774 (lower) treated HUVEC for 16 hours under 21% O_2, with 10 μM MG-132 1 hour prior to end of treatment. Red dots are foci of AMPK and HIF-1α interactions and blue represent nuclei counter stained with DAPI. Images were obtained on Leica SP8 confocal microscope using 40x oil immersion objective magnification. Scale bar: 25 μm.
(B) Quantification of phospho-AMPKα^{T172} and HIF-1α foci per nucleus. All experiments were conducted on HUVECs (n=3) with 4-6 images obtained per condition for quantification and analysis. QuPath counter tool was used for quantification. Statistical analysis was performed using a paired t-test with *** denoting $p < 0.001$.

Post-translation regulation of HIF-1α has primarily focused on hydroxylation and ubiquitination, although several recent studies have shown phosphorylation may play a role in fine-tuning responses, resulting in either increased or decreased stabilisation. I hypothesised that HIF-1α may be phosphorylated by AMPK to promote its stabilisation. To examine whether AMPK phosphorylates HIF-1α, I performed an *in vitro* kinase assay using recombinant HIF-1α (rHIF-1α) and varying amounts of active recombinant AMPKα$_2$β$_1$γ$_1$ (rAMPK) with [γ-^{32}P]ATP/$MgCl_2$ for 1 hour at 37 ºC, prior to SDS-PAGE and subsequent exposure to film for autoradiography imaging. As shown in Figure 4.14, AMPK was able to robustly phosphorylate

HIF-1α *in vitro*. Moreover, the mobility of HIF-1α on SDS-PAGE decreased following incubation with rAMPK, and this is likely to be due to HIF-1α phosphorylation (see HIF-1α migration in lanes 1 and 3 in the Coomassie gel, Figure 4.14). Migration of HIF-1α is slower following incubation with 1 µg rAMPK compared to 0.1 µg, suggesting the possibility of multiple phosphorylation sites in the presence of the higher amount of rAMPK.

Employing LC/MS-based proteomics approach, I sought to identify putative AMPK phosphorylation sites on HIF-1α. The experiment was repeated with rAMPK and rHIF-1α in the absence and presence of 'cold' ATP/$MgCl_2$. The experiment also included complexes with AMPKα_1 and AMPKα_2 (recombinant AMPK$\alpha_1\beta_1\gamma_1$ and AMPK$\alpha_2\beta_1\gamma_1$, respectively), to see if the catalytic subunits have differential preferences for HIF-1α. Samples were digested by trypsin prior to loading on the column and subsequent detection and analysis by tandem mass spectrometry (LC-MS^2). The spectra were acquired by data-independent acquisition (DIA), enabling the quadrupole to continuously cycle throughout the entire m/z range. *In silico* alignment was performed using Spectronaut software, with searches performed against the UniProt human and *E. Coli* databases, given both rHIF-1α and rAMPK were bacterially produced, and the potential contaminants database. Data acquisition and processing were kindly performed by Dr Pavel Shliaha and Dr Alex Montoya at the MRC LMS Proteomics and Metabolomics facility.

Initially, 24 phosphorylation sites on HIF-1α were identified, with a phospho-multiplicity of 1 for each hit and the localisation probability range lying between 85-100%. The rHIF-1α peptide contained purification tags, therefore, phosphorylation sites spanning the tag sequences were removed. Sites were then further filtered based on the quality of the mass spectrometry data, with phospho-sites lacking 'real features' i.e. peaks with poor intensities, low signal to noise ratio, variable retention times etc., in both conditions were then removed, narrowing it down to 13 potential sites of interest (Figure 4.15). The phospho-sites did not concentrate in one region within HIF-1α, but rather spanned throughout the DNA binding/heterodimerisation and transactivation regions.

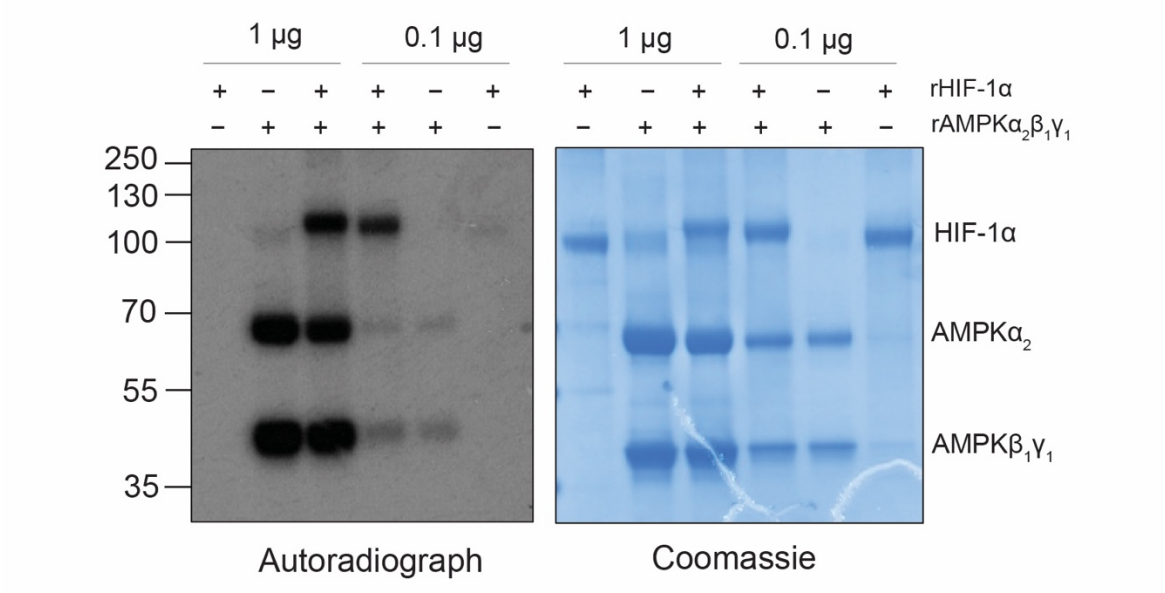
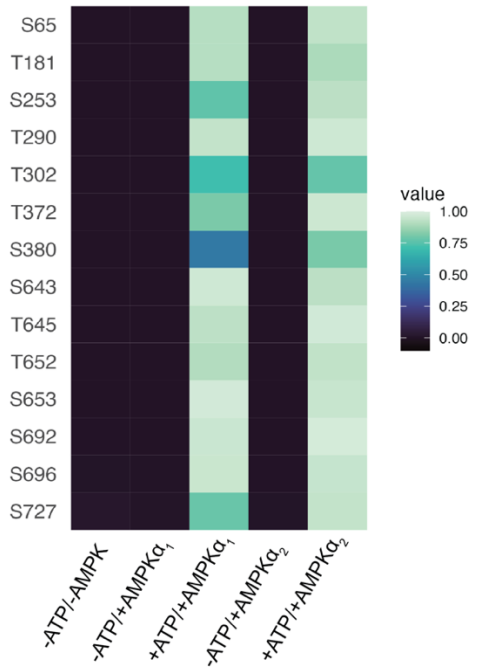


Figure 4.14 *– Phosphorylation of purified HIF-1α by purified active AMPKα$_2$β$_1$γ$_1$ complex in vitro.*

Purified rAMPKα$_2$β$_1$γ$_1$ (1 µg and 0.1 µg as indicated on the Figure) and rHIF-1α (1 µg) were diluted in AMPK kinase buffer in the presence of γ-^{32}P-ATP for 1 h at 37 ºC. The kinase assay mixture resolved using SDS-PAGE. γ-^{32}P-ATP incorporation was detected using X-ray film by autoradiography (left panel). Total protein loading was shown with SimplyBlue™ SafeStain (right panel). rHIF-1α and rAMPKα$_2$β$_1$γ$_1$ only with γ^{32}P-ATP were used as negative controls.

A



B

Site	-5	-4	-3	-2	-1	0	+1	+2	+3	+4
AMPK Motif	Φ	β	β	X β	X β	S T	X	X	X	Φ

Site	-5	-4	-3	-2	-1	0	+1	+2	+3	+4
S65	M	R	L	T	I	**S**	Y	L	R	V
T181	T	S	R	G	R	**T**	M	N	I	K
S253	L	D	M	K	F	**S**	Y	C	D	E
T290	D	H	L	T	K	**T**	H	H	D	M
T302	K	G	Q	V	T	**T**	G	Q	Y	R
T372	S	D	M	K	M	**T**	Q	L	F	T
S380	F	T	K	V	E	**S**	E	D	T	S
S643	L	I	A	S	P	**S**	P	T	H	I
T652	I	H	K	E	T	**T**	S	A	T	S
S653	H	K	E	T	T	**S**	A	T	S	S
S692	P	N	V	V	L	**S**	V	A	L	S
S696	L	S	V	A	L	**S**	Q	R	T	T
S727	M	E	H	D	G	**S**	L	F	Q	A

Figure 4.15 *– Identification of AMPK-mediated HIF-1α phosphorylation sites by LC/MS^2.*

(A) Heatmap displaying mean ratio of FC to maximum site intensity values averaged across all three technical replicates for each phosphorylation site detected by LC/MS^2. Value represents the average site intensity values on a scale between 0-1. Heatmap displays phosphosites whose values were greater than 0.85 in complexes either containing α$_1$ or α$_2$.
(B) Table displaying flanking regions of sites for AMPK motif analysis. Hydrophobic residues (Φ) are highlighted in green, basic residues (β) are highlighted in blue and phosphorylated serine/threonine residues are highlighted in grey.

To aid in the identification of the AMPK sites, the flanking regions of the phospho-sites were compared to the predicted AMPK phosphorylation consensus motif. Based on the motif criteria, I initially assessed S65, T652 and S727 (Figure 4.16). S65 has not been previously identified as a phosphorylation site, but T652 was previously identified in a phospho-proteomics curation set by Cell Signalling Technology although the effect on HIF-1α function has not been defined. S727 has been identified in two independent studies, one where it was shown that the site is phosphorylated by PKA, resulting in protein stability and increased HIF-1α gene transcription in HeLa cells [371, 372]. The output from Spectronaut analysis also revealed that the peptide sequence flanking S65 matches the canonical AMPK motif. However, the peptide sequences for the other two peptides were not identified as possessing an AMPK motif by Spectronaut. T652 appeared to possess the substrate motif for G-protein receptor kinase 1 (GCKR1) whereas S727 was predicted to be phosphorylated by GCKR1, PKA and protein kinase C (PKC) (Supplementary Table 8.3).

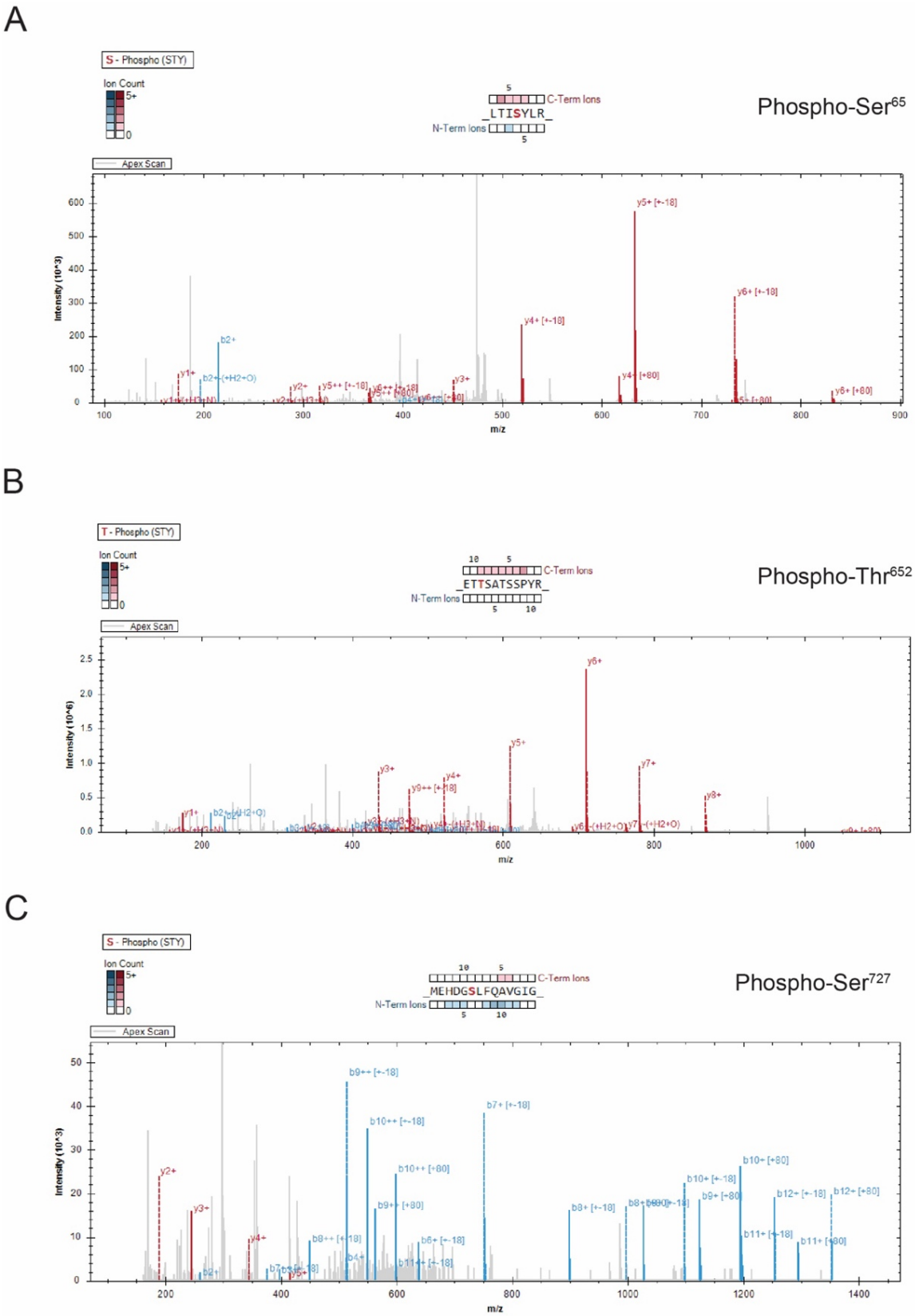


Figure 4.16 – *Mass spectrometry analysis of S65, T652 and S727.*

Mass spectra for all ionised tryptic peptides as detected by LC/MS^2 that contain the phospho-sites of interest.
(A) Identified MS^2 spectrum for S65.
(B) Identified MS^2 spectrum for T652.
(C) Identified MS^2 spectrum for S727.

S65		-5	-4	-3	-2	-1	0	+1	+2	+3	+4
C.elegans	55-64	L	R	V	A	A	T	I	C	R	L
M. musculus	60-69	M	R	L	T	I	**S**	Y	L	R	V
R. norvegicus	61-70	M	R	L	T	I	**S**	Y	L	R	V
B. taurus	60-69	M	R	L	T	I	**S**	Y	L	R	V
M. mulatta	60-69	M	R	L	T	I	**S**	Y	L	R	V
H. sapiens	60-69	M	R	L	T	I	**S**	Y	L	R	V

T652/S653		-5	-4	-3	-2	-1	0	+1	+2	+3	+4
C.elegans	660-662	-	-	-	-	-	-	-	-	-	-
M. musculus	658-669	V	P	Q	E	T	**T**	**T**	-	A	K
R. norvegicus	648-659	V	P	Q	E	M	**T**	**T**	-	A	K
B. taurus	644-655	V	P	K	E	P	P	C	-	A	T
M. mulatta	647-658	I	H	K	E	T	**T**	**S**	-	A	T
H. sapiens	647-658	I	H	K	E	T	**T**	**S**	-	A	T

S727		-5	-4	-3	-2	-1	0	+1	+2	+3	+4
C.elegans	693-697	F	Q	Q	D	E	-	-	-	-	-
M. musculus	732-741	M	E	H	D	G	**S**	L	F	Q	A
R. norvegicus	722-731	M	E	H	D	G	**S**	L	F	Q	A
B. taurus	719-728	I	E	H	D	G	**S**	L	F	Q	A
M. mulatta	722-731	M	E	H	D	G	**S**	L	F	Q	A
H. sapiens	722-731	M	E	H	D	G	**S**	L	F	Q	A

Figure 4.17 *– Evolutionary multiple sequence alignment (MSA) analysis of putative AMPK phosphorylation sites in HIF-1α.*

Peptide sequences flanking the HIF-1α sites S65, T652/S653 and S727 were aligned using EMBL-EBI Clustal Omega MSA tool across the following species: roundworm (*Caenorhabditis elegans*), house mouse (*Mus musculus*), common rat (*Rattus norvegicus*), cattle (*Bos taurus*), rhesus macaque (*Macaca mulatta*) and human (*Homo sapiens*). Hydrophobic residues (Φ) are highlighted in green, basic residues (β) are highlighted in blue and phosphorylated serine/threonine residues are highlighted in grey.

Phosphorylation sites that are functionally relevant are often conserved across different species, and so species conservation of the putative site greatly strengthens the likelihood of it being a physiologically relevant site. Using multiple sequence alignment (MSA), I compared HIF-1α sequences from 6 different species: roundworm (*C. elegans*), house mouse (*M. musculus*), common rat (*R. novergicus*), cattle (*B. taurus*), rhesus macaque (*M. mulatta*) and human (*H. sapiens*) Figure 4.17). For S65, the critical hydrophobic and basic residues are conserved across all species, apart from *C. elegans* where the threonine replaces the characteristic serine residue. Despite reports of AMPK having a strong preference for phosphorylation of serine residues, the presence of a threonine cannot be excluded. A similar observation is seen with S727, except the site does not exist in *C. elegans*, indicating that it

may have emerged later in evolution (Figure 4.17). The analysis for T652 also took into consideration the adjacent S653 which was also detected in by mass spectrometry.

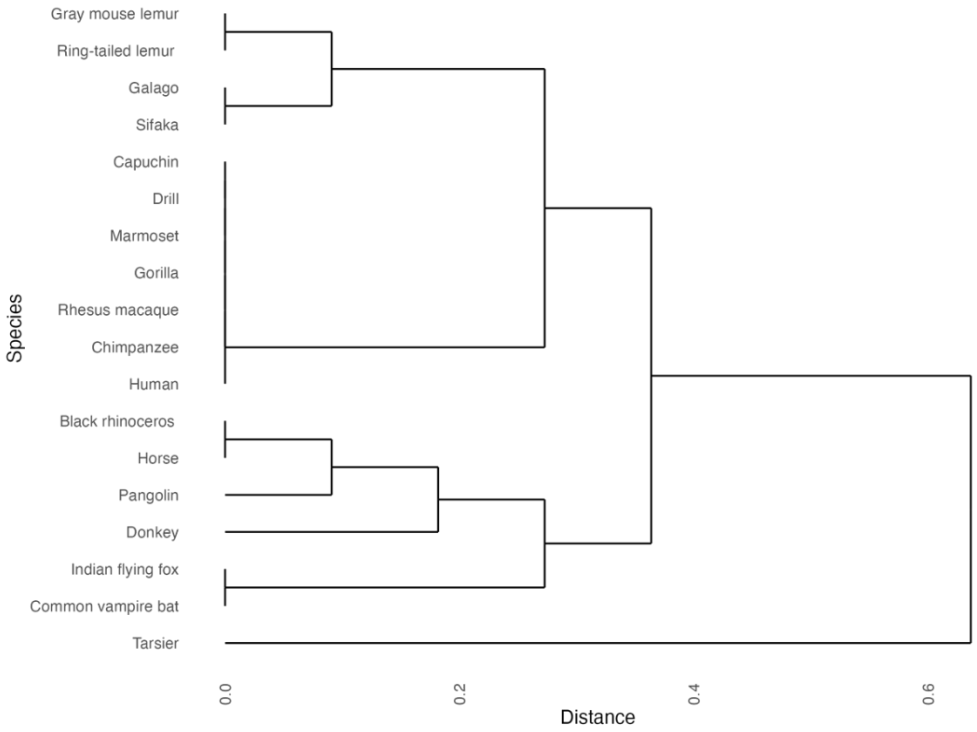


Figure 4.18 *– Dendrogram illustrating the phylogenetic relationship of the T652/S563 flanking peptide sequence across several mammalian species.*

Sequences from species of primates, odd-toed ungulates and bats were chosen for comparisons as these species had both the threonine and serine phosphorylation sites conserved. Diagram created using RStudio using Bioconductor MSA package.

HIFα	Site	-5	-4	-3	-2	-1	0	+1	+2	+3	+4
HIF-1α	S65	M	R	L	T	I	S	Y	L	R	V
HIF-2α	S62	M	R	L	A	I	S	F	L	R	T
HIF-1α	T652	I	H	K	E	T	T	S	A	T	S
HIF-2α	C611	L	P	–	P	C	C	G	Q	A	S
HIF-1α	S727	M	E	H	D	G	S	L	F	Q	A
HIF-2α	Q713	L	E	Y	E	E	Q	A	F	Q	D

Figure 4.19 – Amino acid sequence comparison of phospho-sites between HIF-1α and HIF-2α.

Human HIF-1α and HIF-2α amino acid sequences aligned with S65, T652 and S727. Hydrophobic residues (Φ) are highlighted in green, basic residues (β) are highlighted in blue and phosphorylated serine/threonine residues are highlighted in grey.

The location of PTMs within HIF-1α can determine (i) stability, (ii) heterodimerisation, (ii) localisation and (iv) gene transactivation. All sites were mapped to examine whether they were located near important regulatory residues or in domains critical for transcription factor activity (Figure 4.20). S65 lies within the bHLH domain, therefore phosphorylation may alter its heterodimerisation with HIF-1β and/or its binding to HRE elements in the promoters of target genes. Both T652 and S727 reside in the inhibitory domain, yet T652 lies adjacent to the NES, whereas S727 lies within the NLS (Figure 4.20). Therefore, if these are functionally relevant phosphorylation sites, AMPK-mediated phosphorylation may alter (i) the shuttling of HIF-1α between the nucleus and cytoplasm (T652 and/or S727) and (ii) once in the nucleus, affect its binding to HRE elements (S65).

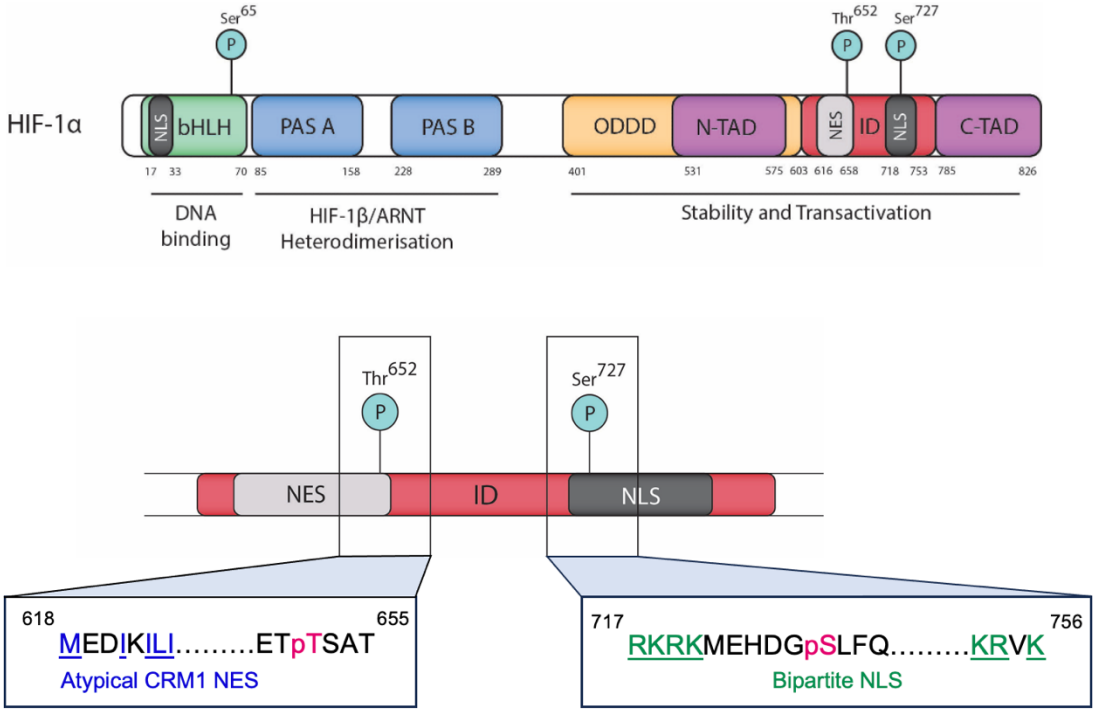


Figure 4.20 *– A schematic mapping the S65, T652 and S727 sites with the sequence of HIF-1α.*

Abbreviations: bHLH: basic helix loop helix; PAS: Per-Arnt-Sim (PAS) domains A (PAS A) and B (PAS B); ODDD: oxygen-dependent degradation domain; N-TAD: N-terminal transactivation domain; C-TAD: C-terminal transactivation domain; ID: inhibitory domain; NES: nuclear export sequence; NLS: nuclear localisation sequence; C-TAD: C-terminal transactivation domain. Figure created in Adobe Illustrator.

To validate whether the sites identified by phosphoproteomics are targeted by AMPK, S→A mutants were generated by site-directed mutagenesis for S65 (S65A), T652 (T652A) and S727 (S727A) along with a double mutant (T652A/S727A, termed DM) and triple mutant (S65A/T652A/S727A, termed TM) each with a C-terminal Myc-tag. Plasmids were overexpressed in HEK293T cells under hypoxia to maximally stabilise HIF-1α and then immunoprecipitated using Myc-Trap® Agarose beads. The beads were then incubated with rAMPK and [γ-^{32}P]-ATP/$MgCl_2$ for 1 hour at 37 ºC followed by SDS-PAGE and autoradiography. If the selected sites were indeed AMPK targets, then HIF-1α phosphorylation will be greatly reduced in the *in vitro* kinase assays. As shown by Figure 4.21, autoradiography revealed that immunoprecipitated individual and TM-HIF-1α mutants were still phosphorylated by rAMPK in comparison to WT-HIF-1α whereas DM-HIF-1α exhibited reduced [γ-^{32}P]-PO_4 incorporation.

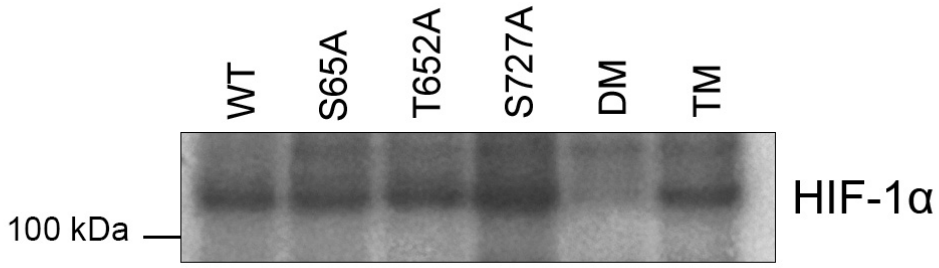


Figure 4.21 *– In vitro phosphorylation of immunoprecipitated WT and mutant HIF-1α.*

Myc-tagged HIF-1α plasmids were transfected into HEK293T cells for 24 hours, followed by immunoprecipitation using Myc-Trap® Agarose beads. The beads were incubated with rAMPK$\alpha_2\beta_1\gamma_1$ [γ^{32}P]-ATP/$MgCl_2$ for 1 h at 37 ºC. The kinase assay mixture resolved using SDS-PAGE. γ-^{32}P-PO_4 incorporation was detected using X-ray film by autoradiography. Coomassie staining is not shown as it was not sensitive enough to detect the amount of protein on the gel. Abbreviations: - DM: T652A/S727A and TM: S65A/T652A/S727A.

To confirm whether the mutations of the selected sites altered HIF-1α protein stability, plasmids encoding WT, S65A and TM HIF-1α mutants were transiently expressed in HUVECs without any treatments to examine baseline stability. As shown in Figure 4.22A, there were no observable differences in the expression of the mutant constructs with follow-up band densitometry quantification revealing no significant differences, despite expression of S65A and TM mutants being lower (Figure 4.22B).

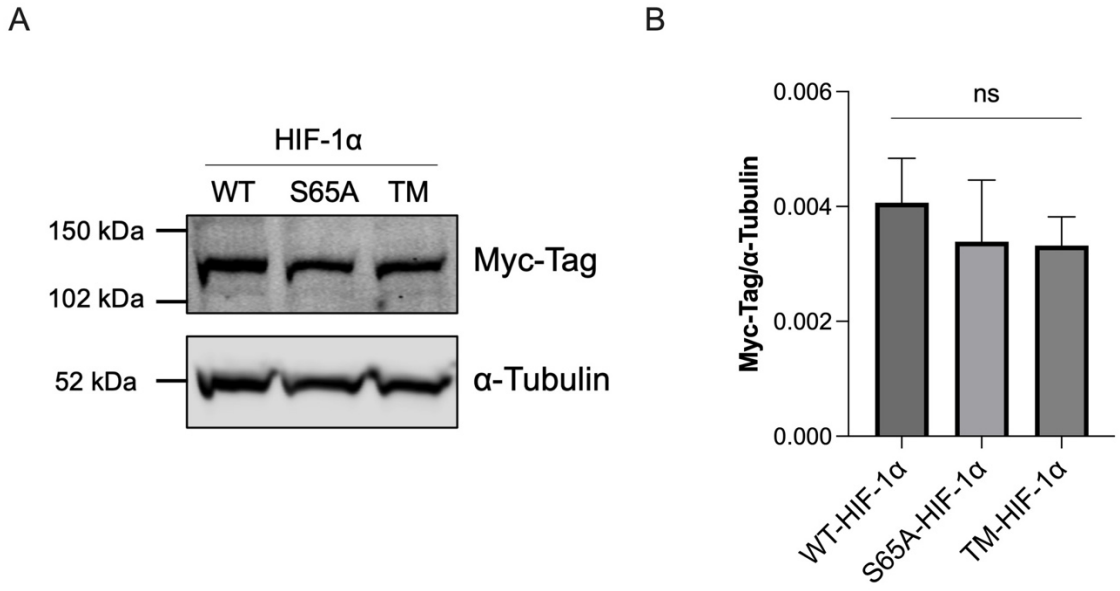


Figure 4.22 *– Transient expression of HIF-1α constructs in HUVECs.*

HUVECs were transfected with the construct plasmids of WT-, S65A- and TM-HIF-1α for 24 hours.
(A) Representative immunoblot showing levels of Myc-Tag and α-Tubulin as the loading control.
(B) Quantification Myc-Tag normalised to α-Tubulin.
Data is displayed as mean ± SEM with n = 3 biological replicates. Data analysis was performed using paired t-tests with ns denoting not significant.

Based on the previous results, it was postulated that mutagenesis of the phospho-sites may impact HIF-1α transactivity, rather than HIF-1α stability as none of the sites lie in the ODDD (Figure 4.20). To address whether the mutants impacted HIF-1α transactivity, HUVECs were transfected with plasmids overexpressing both WT and mutant plasmids, treated with BI-9774 and BAY-3927 (an AMPK inhibitor) prior to performing an HRE-dependent luciferase reporter assay (refer to Figure 4.23A for experimental set up). Transfection of the plasmids significantly increased HIF-1α luciferase activity, approximately between 10-15-fold compared to the activity of endogenous HIFα isoforms (p-value < 0.0007) (Figure 4.23B). There were no significant differences between WT, S65A and TM. BI-9774 significantly increased HRE-dependent luciferase activity in WT (p-value = 0.0412), S65A (p-value = 0.0167) and TM-HIF-1α (p-value = 0.0340) compared to the untreated control. The data also shows that BI-9774 still significantly increased HRE-dependent luciferase activity in the phospho-null mutants. To assess whether the phospho-null mutants rendered HIF-1α more susceptible to AMPK deactivation by BAY-3827, HUVECs were transfected and then subsequently treated with BAY-3827 (5 μM) for 16 hours under normoxia. BAY-3827 had no effect on the HRE-dependent luciferase activities of endogenous HIFα, WT-, S65A or TM-HIF-1α (Figure 4.21D). Altogether, these findings suggest that these mutations are not sufficient to impact HIF-1α stabilisation by AMPK.

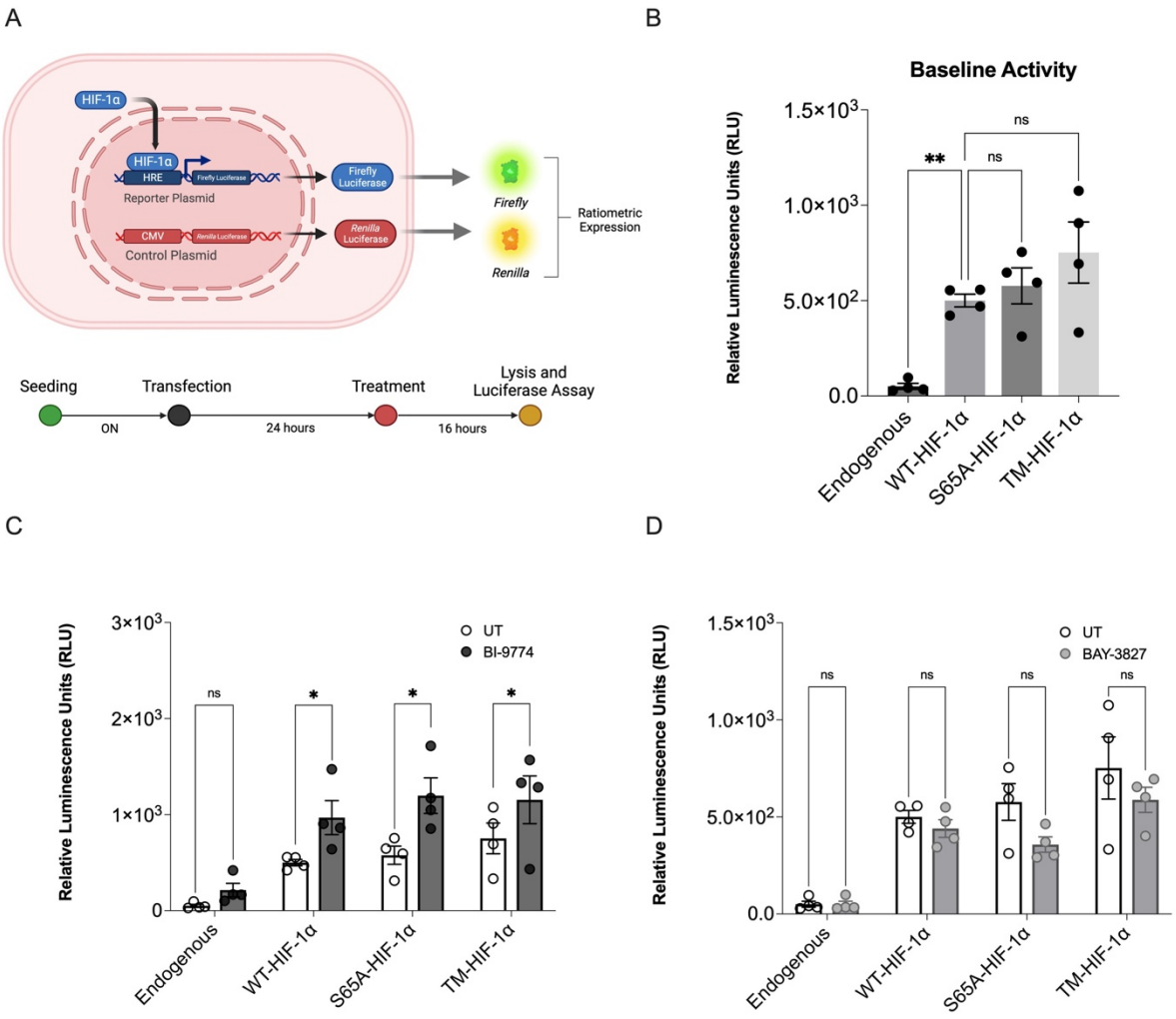


Figure 4.23 *– Transcriptional activity of HIF-1α phospho-mutants using an HRE-dependent luciferase assay.*

(A) Schematic illustrating the basis for a luciferase assay and experimental plan.
(B) Baseline expression comparing endogenous HIFα activity with overexpression of HIF-1α-Myc WT and phospho-mutant constructs at 21% O_2.
(C) Quantification of relative HRE-dependent luciferase activity in HUVECs transfected with WT-, S65A- and TM-HIF-1α constructs ± BI-9774 treatment (10 µM) at 21% O_2.
(D) Quantification of relative HRE-dependent luciferase activity in HUVECs transfected with WT-, S65A- and TM-HIF-1α constructs ± BAY-3827 (5 µM) at 21% O_2.
All experiments were performed with different biological donors of HUVECs (n = 4 pools) with 2 technical replicates for each condition. All data is represented as mean ± SEM and statistical analysis was performed using paired t-tests for all the pairwise comparisons presented on the graph. ns, not significant; * p-value < 0.05, ** p-value < 0.01, *** p-value < 0.001, **** p value < 0.0001. Abbreviations: ON: overnight.

4.4 Discussion and Limitations

The key findings in this chapter reveal (i) a significant enrichment of HIF-1α gene signatures in HUVECs treated with BI-9774; (ii) AMPK and HIF-1α may directly interact in HUVECs *in vitro*; (iii) HIF-1α is likely to be a candidate substrate for AMPK phosphorylation in a cell-free system *in vitro*. HIF-1α stability is induced by pharmacological-induced AMPK activation, corroborating observations of increased endogenous HIF-1α expression in HUVECs even under 21% O_2 as demonstrated in Chapter 3 – Regulation of AMPK under Hypoxia.

4.4.1 The synergistic nature of AMPK and hypoxia signalling

RNA-sequencing data revealed that hypoxia and BI-9774 treatment have common DEGs with the same directionality (Figure 4.9), with significant activation of HIF-1α signalling and transcription factor activity in HUVECs treated with BI-9774 under normoxia (Figure 4.5). Even under hypoxic conditions, IPA analyses showed that BI-9774 treatment still promotes enrichment of HIF-1α signalling, although it doesn't reach the z-score threshold as discussed previously for Figure 4.7. The average log_2FC values of *HIF1A* and *EPAS1* are much higher in normoxic BI-9774-treated HUVECs in comparison to the hypoxia only dataset (Figure 4.8). Furthermore, examination of upstream regulators based on the transcriptomic data showed that HIF-1α transcription factor activity is predicted to be significantly activated in the normoxic BI-9774 dataset (Figure 4.8). There was no significant change in z-scores to ascertain the predicted transcription factor activities of HIF-2α (*EPAS1*) and HIF-3α (*HIF3A*) (Figure 4.8). A potential explanation for this is the dynamics of HIF-1α and HIF-2α changes during hypoxia, with an initial wave of HIF-1α activity (< 24 hours) followed by HIF-2α induction and expression until it reaches steady state levels (> 24 hours). It would be worthwhile to explore whether long-term AMPK activation treatment alters the stabilisation and dynamics of other HIFα isoforms and how this impacts HIFα-dependent transcription under chronic normoxic and hypoxic conditions (> 24 hours). The dependency on HIF-1α and HIF-2α could be determined using siRNA knockdown against *HIF1A* and *EPAS1,* provided that this does not have deleterious consequences on ECs.

It should be prefaced that IPA functional analyses on the input DEGs relies on known interactions between genes and biological functions/diseases derived from other datasets, therefore it does not imply a direct causal relationship nor does it mean that AMPK and HIFα directly participate in the processes. As shown in Figure 4.9-4.10, common enriched pathways are connected to pathways previously associated with HIFα such as nutrient sensing/mTOR signalling, angiogenesis (e.g., signalling by VEGF, degradation of the extracellular matrix) and

blood pressure (e.g. NO signalling in the cardiovascular system) (see Table 1.3 and Figure 4.10). Functional analysis is strongly linked with the results from the canonical pathways, as processes related to angiogenesis (e.g., sprouting, cell motility and endothelial differentiation) are predicted to be significantly activated (Figure 4.11). Intriguingly, artery development was positively enriched for, suggesting that perhaps there is an AMPK connection to a subset of genes that are also involved in arterial specification. Disease analysis strongly implicate diseases characterised by ischaemia (e.g., thrombus, atherosclerosis, stroke, myocardial infarction), metabolic diseases (e.g., metabolic syndrome, diabetes mellitus) and immune-mediated inflammatory conditions (e.g. autoimmune disease) (Figure 4.12). Indeed, hypoxia and/or dysregulated AMPK/HIFα signalling are reportedly linked to the development of numerous metabolic disorders including obesity and NAFLD as reported in other studies [373-376]. The avenues for future research will be touched upon in the Summary and Perspectives chapter.

4.4.2 Potential crosstalk between AMPK and HIF-1α signalling

Initial observations suggest that AMPK and HIF-1α could directly interact at least *in vitro* as shown by PLA in Figure 4.13 where BI-9774 treatment significantly increases interaction between endogenous AMPK and HIF-1α, albeit the effect is modest. PLA is a sensitive method to detect transient protein-protein interactions, for example a kinase phosphorylating its target protein, as opposed to co-immunoprecipitation, which is more appropriate for detection in a multiprotein complex. However, detecting HIF-1α at the protein level under normoxic conditions is difficult due to its rapid degradation and the amount of AMPK present is likely to far exceed its substrate under these conditions. Therefore, MG-132 treatment was required to detect adequate levels of HIF-1α. Unfortunately, MG-132 has been reported to activate AMPK in other studies, which may explain the modest difference between the two conditions and the presence of foci even in the untreated HUVECs [377]. This would require omitting MG-132 treatment and prolonging the amplification step of the PLA to enhance the signal. It is also worth repeating the experiment under physiological normoxia (e.g. 5-10% O_2) to stabilise HIF-1α at detectable levels. Image acquisition could be improved by obtaining z-stacks rather than images on a single plane as done in Figure 4.13, which may have resulted in underestimating the number of positive foci and poor signal at 21% O_2. Z-stacks also allow maximum intensity projection to enhance visualisation of the foci.

Post-translational regulation of HIF-1α is mediated through hydroxylation and subsequent ubiquitination of regulatory resides by PHDs/FIH1 and pVHL, respectively. Hydroxylation and ubiquitination serve to degrade HIF-1α in response to O_2 tension. As mentioned previously,

HIF-1α can also be stabilised in a hypoxia-independent manner in response to a wide repertoire of stimuli including cytokines, metabolites and OSS (Section 1.8.3 Hypoxia-dependent and -independent regulation of HIFα). The work in this chapter did demonstrate for the first time that AMPK is capable of phosphorylating HIF-1α in a cell-free system *in vitro*. Phosphorylation represents a dynamic and reversible approach to regulate HIF-1α function beyond O_2 tension. Based on the most stringent AMPK consensus motif (βϕβXXXpS/TXXXϕ), *in silico* analyses performed by Marin *et al*. (2015) using the ENSEMBL proteome revealed 866 human putative AMPK targets, with less stringent queries revealing up to 4505 human peptides out of 17,000 proteins [378]. Despite a significant proportion of the proteins being involved in transcription, there was no mention of whether HIFα factors were putative substrate of AMPK. Although *in vitro* phosphorylation assays are useful in interrogating potential substrates identified from bioinformatics analysis, successful phosphorylation of a protein by recombinant AMPK *in vitro* does not mean that it is a legitimate AMPK substrate *in vivo*. Furthermore, a strong phosphorylation motif may still prove to be functionally redundant, therefore, site-directed mutagenesis along with functional assays are required in determining whether phosphorylation of these sites are functionally important [379]. Additional work through overexpression of gain-of-function AMPK mutations or BI-9774 treatment is required to see if changes in HIF-1α stabilisation occur at the protein level. Although BI-9774 has been shown to be highly specific towards AMPK based on kinase selectivity screens, shRNA knockdown and/or knockout cell lines need to be performed to prove that the BI-9774 induction of HIF-1α is dependent on AMPK [163].

The adaptive response to bioenergetic stress has been extensively studied solely focusing on nutrient and/or O_2 deprivation, presumed to be acting independently of each other. However, these responses have not been examined in an endothelial context nor whether there is cross regulation between both AMPK and hypoxia/HIFα signalling barring the study by Belapurkar and colleagues [362]. The downstream effects of endothelial AMPK have primarily been inferred from studies utilising non-specific activators and/or cytokines that alter multiple signalling pathways. To my knowledge, this is the first study examining the global effects of AMPK activation using a novel 2nd generation activator, BI-9774, and offers additional novelty by studying endothelial AMPK activation under different O_2 tensions. The dataset confirmed previous observations of AMPK, particularly in regulating cell cycle, NO production and angiogenesis but also revealed novel pathways and functions promoted by AMPK activation under normoxia and hypoxia.

AMPK and HIF-1α have been linked to cell survival and metabolic reprogramming under hypoxia. Both are necessary for revascularisation after ischaemia, therefore AMPK/HIFα could

converge under certain conditions to promote angiogenesis as an adaptive response to increase nutrient and $_{O2}$ perfusion in the long-term [178, 193]. Enrichment in the formation of cellular protrusions and sprouting suggests that the shared subset of upregulated genes could induce the formation of tip cells during the initial stages of angiogenesis (Figure 4.11). Tip cells act as both environmental and guidance sensors, as they protrude filopodia towards tissues secreting proangiogenic molecules. Indeed, tip cells often have restricted access to nutrients and O_2, as often is the case in avascular environments, leading to activation of AMPK and hypoxia signalling, respectively [347, 380]. Tip cells are growth arrested due to elevated levels of p21, in contrast to the proliferative, $Ki67^+$ stalk cells [70, 72]. Therefore, this may explain the paradoxical observation of hypoxia and BI-9774 concomitantly suppressing cell cycle processes whilst upregulating angiogenesis. As tip cells are migratory cells in hypoxic environments, the source of ATP is derived from (i) increased glycolysis and (ii) suppression of anabolic pathways involved in cell growth [69, 70] (Figure 4.11). As AMPK increases both glucose uptake and glycolytic flux whilst concomitantly inhibiting biosynthetic pathways, tip cell induction may also rely on AMPK activation during SA. The role of AMPK in the angiogenic response and regulation of metabolism and energy balance will be further explored in Chapter 5 – Functional characterisation of AMPK activation in the endothelium. Further work is required to determine (i) whether AMPK and HIF-1α actively participates in the aforementioned pathways in Figure 4.10 & Figure 4.11), and (ii) whether HIFα isoforms are necessary for the AMPK-dependent responses.

4.4.3 Identification of putative AMPK sites in HIF-1α

The phospho-proteomics data led to the identification of several putative AMPK sites. My proteomics data has not only detected previously identified uncharacterised sites, T652 and S727, but also identified another novel phospho-site in HIF-1α: S65. These 3 residues were chosen for further analysis because the flanking peptide sequences possessed characteristic features of AMPK consensus motif with the necessary basic and hydrophobic residues. Overexpression of HIF-1α harbouring the S727A mutant had reduced HIF-1α protein stability [371]. PKA has been shown to phosphorylate T63 together with S696 and S727 in HeLa cells to stabilise HIF-1α and enhance its transcriptional activity [371]. Residues neighbouring S65 within the bHLH domain, T63 and Y66, have also been identified to be phosphorylated in HeLa cells, lymphocytes and in human ovarian tumour samples [372, 381]. [381]. Hence, phosphorylation in the bHLH domain region could be a hotspot for competing kinases, with each S/T/Y phosphorylation event exerting a differential effect on HIF-1α heterodimerisation and/or DNA binding.

My data disputes the findings of Bullen *et al.*, as S727A had no impact on HIF-1α stability in HUVECs [371]. However, I wasn't able to investigate the effects of the individual mutants beyond S65A in HUVECs. The S727A construct generated by the authors also harboured additional P402A and P564A mutations to protect the mutant HIF-1α from proteasomal degradation. The hydroxylation-resistant constructs may have facilitated in discriminating the effect of singular sites on HIF-1α stability; therefore, it would be worthwhile to incorporate P402A/P564A when creating constructs in the future. Another caveat is the net contribution of endogenous HIF-1α and HIF-2α, which could have masked the effects of the mutants as both are highly expressed in all ECs [382]. Ideally, HUVECs lacking AMPKα and HIFα isoforms would be useful to reintroduce mutants of both and study the effects. Unfortunately, this could not be done in HUVECs due to the difficulty of transfection and their limited passaging in culture. Future work should utilise HEK293T cells, immortalised endothelial cell lines (HMEC-1) or cord blood ECFCs which have high proliferative capacity and lifespan *in vitro*, for CRISPR/Cas9 manipulation and generation of stable cell lines [383, 384].

Despite my prevailing hypothesis that AMPK directly phosphorylates HIFα and promotes its transcriptional activity, mutagenesis studies of the top 3 sites (S65/T652/S727) had no significant effect on (i) AMPK-mediated phosphorylation in immunoprecipitates (Figure 4.21); (ii) HIF-1α stability (Figure 4.22); or (iii) transactivation at baseline nor did it render them insensitive to the stabilising effects of BI-9774 treatment (Figure 4.23B & C). Single mutants of HIF-1α and TM-HIF-1α remained amenable to phosphorylation by rAMPK (Figure 4.21). However, a discrepancy was observed between DM-HIF-1α, which appeared to have reduced [γ-^{32}P]-ATP incorporation, yet TM-HIF-1α maintained [γ-^{32}P]-ATP incorporation comparable to WT-HIF-1α. A potential explanation may be due to lower input of DM-HIF-1α lysate for the immunoprecipitation, resulting in very low amounts of protein being loaded onto the gel, however, I was not able to confirm this as the levels of protein fell below the detection limit of Coomassie staining.

As demonstrated in Figure 4.21, TM-HIF-1α is still phosphorylated by rAMPK, indicating that mutation of S65, T652 and S727 are not sufficient to impair phosphorylation. Numerous studies have shown that several bHLH family members, including Neurogenin-2 (Ngn2) and OLIG2, harbour multiple serine/threonine sites that are amenable to phosphorylation [385]. Sequential phosphorylation of serine/threonine residues often have an additive effect (e.g., each additional phosphorylation event may increase or decrease the transcription factor's ability to bind DNA). Multisite phosphorylation of transcription factors has been shown to serve as a rheostat mechanism to allow graded transcriptional responses [386, 387]. CDKs phosphorylates Ngn2 on 9 sites, with each phosphorylation event decreasing its affinity for

enhancer box elements in the promoters of neuronal genes, thus limiting its ability to drive neurogenesis *in vivo* [386]. Given that 13 putative phosphorylation sites were identified, a potential explanation is that multisite phosphorylation events are necessary prior to seeing any observable effect on transcription factor activity (Figure 4.15).

S65, T652 and S727 were chosen based on their similarity to the AMPK consensus motif, but consensus sequences only serve as a guide and are not a definitive criteria. A number of other sites identified in the study (T290, T302, T372, S643, S692, and S696), do not match the AMPK consensus motif so they were not prioritised (Figure 4.15). Phosphorylation sites can deviate the consensus motif occasionally due to the tertiary structure of the protein and the local chemical environment. A more likely explanation could be the lack of phospho-peptide enrichment prior to the LC-MS^2 run, resulting in atypical sites being detected. There have been previous reports of AMPK substrates having atypical phosphorylation motifs, but the occurrence is relatively low when taking into consideration the entire repertoire of the targets [102]. Several other candidate phospho-sites appear promising like T181, S253, S380 and S653, but it was not possible to investigate all sites due to limited time. Once I generate plasmids with all sites of interest mutated to alanine, I plan to (i) repeat the *in vitro* kinase assays; (ii) perform EMSA assays to check DNA binding affinity; and (iii) conduct chromatin immunoprecipitation (ChIP) PCR to check promoter occupancy of the mutants.

4.4.4 Evolutionary comparison and analysis of identified phospho-sites in HIFα isoforms

Despite the chosen sites exerting no functional effect on HIF-1α stabilisation and transcriptional activity, all 3 sites were more or less conserved across a vast range of species Figure 4.17. S65 and S727 were highly conserved across all species, except for S727 which did not exist in *C. elegans*. This may be due to their location in critical functional regions in HIF-1α like the bHLH domain (S65) and the NLS (S727). On the other hand, the flanking sequences of T652/S653 exhibited high variability across species as no corresponding threonine or serine site was found in *B. taurus*. The threonine residue exists in mouse and rats, but a threonine residue replaces the adjacent serine. The flanking regions also lack the key basic residues that comprise the AMPK motif. Only *M. mulatta* and *H. sapiens* possess the basic and hydrophobic residues perhaps, indicating once more this phosphorylation site may have emerged relatively recently during evolution (Figure 4.17). Due to only predicted or poor quality FASTA sequences available for a lot of species, it was difficult to derive meaningful phylogenetic data. However, it appears that the AMPK motif for T652/S653 sites is partially conserved in bats, pangolins and odd-toed ungulates, where a histidine residue is replaced by proline at −4 downstream of the threonine residue. The motif is fully conserved in

all primates, except for tarsiers, which has the greatest divergence compared to other species despite being closely related to humans) (Figure 4.18).

I was not able to address whether AMPK interacted with HIF-2α as there was no full-length recombinant protein nor adequate antibodies raised against the latter. HIF-2α is of equal importance as HIF-1α in ECs, given that one cannot fully compensate for the loss of the other [388]. Intriguingly, HIF-2α is expressed at similar levels as HIF-1α at the mRNA level, but the dynamics of protein expression differs depending on the vessel type and vascular bed [382]. Onset of HIF-1α protein stabilisation is rapid in exposure to hypoxia compared to HIF-2α which exhibits delayed stabilisation. However, HIF-2α persists for a longer period of time, illustrating its importance in mediating the long-term adaptational responses [382]. Given that HIF-1α shares 48% primary amino acid sequence homology with HIF-2α, I searched for homologous residues of S65, T652 and S727 residues in HIF-2α. MSA revealed only S65 has a homologous site in HIF-2α. T652 and S727 do not have a corresponding site on HIF-2α, suggesting that these are specific to HIF-1α. This observation raises the possibility of whether AMPK prefers HIF-1α or is capable of differential regulation of both isoforms to elicit a specific downstream response. Future work will address whether (i) AMPK phosphorylates HIF-2α *in vitro*; (ii) the impact of HIF-2α sites on activity; and (iii) if there is preferential phosphorylation and/or stabilisation of one isoform over the other. Based on this, I do not believe I have comprehensively addressed all the aims as outlined in 4.2 Hypothesis and Aims, there is insufficient evidence to prove that the HIF-1α transcriptional activity induced by BI-9774 occurs due to direct phosphorylation of HIF-1α by AMPK.

5. Chapter 5 – Functional characterisation of AMPK activation in the endothelium

5.1 Introduction

The RNA-seq analysis in Chapter 4 revealed the varied effects of AMPK activation in the endothelium. A striking result was the significant enrichment and activation of pathways and functions implicated in metabolism (e.g. glycolysis) and angiogenesis (e.g., sprouting, degradation of ECM and endothelial motility) (Figures 4.10-4.12). ECs generate up to 85% of their intracellular ATP levels from glycolysis whilst also relying on maintaining quiescence by upregulating FAO; both processes are regulated by AMPK [15, 25, 98]. Previous studies have shown that endothelial deletion of AMPKα_1 (*PRKAA1*) results in dysregulation of glycolysis, EC viability and increased formation of atherosclerotic lesions [205]. Moreover, upon treatment with AICAR and metformin in HUVECs, AMPK activation enhances mitochondrial biogenesis by decreasing methylation in the promoters of genes that participate in mitochondrial biogenesis [e.g. *PPARGC1A*, nuclear respiratory factors 1 and 2 (*NRF1*/*NRF2*), *UCP2* and *TFAM*] [389]. AMPK also regulates angiogenesis by crosstalk with PI3K/Akt signalling pathways under hypoxic conditions, as treatment with the AMPK inhibitor compound C impaired HUVEC tube formation *in vitro*, aortic ring sprouting assay *ex vivo* and Matrigel plug *in vivo* [192]. An independent study also showed that AMPK was required for the proangiogenic effects of adiponectin [181]. Endothelial LKB1/AMPK signalling was shown to regulate revascularisation following ischaemic injury in mice [185, 390]. Collectively, these studies demonstrate AMPK's importance in endothelial bioenergetics and angiogenesis. However, the use of non-specific AMPK activators and inhibitors in the studies makes it difficult to determine the precise downstream effects of AMPK as they may exert effects independently of the kinase.

The physiological effects of AMPK have been primarily determined using knockout models as summarised in Table 1.1 and reviewed elsewhere, however, these studies fail to address the physiological effects of AMPK activation *in vivo* [391]. Gain-of-function mutations in the γ_2 and γ_3 subunits cause aberrant glycogen accumulation in the heart or skeletal muscle, respectively, in humans and Hampshire pigs [392, 393]. However, the γ_2 subunit exhibits tissue specific expression patterns, restricting their suitability for investigating global AMPK activation. In collaboration with AstraZeneca, our group generated a mouse model possessing the D316A mutation in the ubiquitously expressed γ_1 subunit, rendering the kinase complex insensitive to dephosphorylation by phosphatases [160, 394]. The global γ_1D316A (γ_1D316A-

Tg) model exhibits hypermetabolism, resistance to diet-induced obesity (DIO) and browning of the scWAT [395, 396]. The widespread effects exerted by global AMPK activation makes it difficult to discern which cell types and/or biological pathways are responsible for the observed phenotype. It was postulated that resistance to DIO may be down to the presence of skeletal muscle-like AMPK reprogrammed thermogenic (SMART) adipocytes [395]. SMART adipocytes are Myf5/6^{+} and Pax7^{+}, perform Ca^{2+} futile cycling with a high energetic phenotype, defined by elevated glycolytic and OXPHOS activity. Investigation of which cell population was responsible for the emergence of these cells were performed by expressing the γ_1D316A-Tg under the following promoters: (i) adiponectin (Adiponectin-Cre), expressed in mature white and brown adipocytes; (ii) platelet-derived growth factor receptor (PdgfRα-Cre) α-promoter, expressed in most preadipocytes present in WAT; and (iii) Mef2c-Cre, expressed in skeletal muscle. Interestingly, no phenotype was observed in either Adiponectin-Cre, PdgfRα-Cre or Mef2c-Cre AMPK activating mice, therefore demonstrating that the skeletal muscle is not responsible for conferring the phenotype and that SMART cells originate from a distinct precursor population of multipotent ADSCs [395]. We also observed a marked increase in mitochondrial biogenesis in metabolically active tissues (e.g., liver, adipose and skeletal muscle) and increase in systemic vascularisation, which may contribute to the beneficial metabolic effects observed. The striking proangiogenic phenotype also implicates that the endothelium may play a critical role, but to date this has not been well-characterised.

5.2 Hypothesis and Aims

Hypothesis: AMPK activation may promote a proangiogenic phenotype with profound effects on endothelial metabolism both *in vitro* and *in vivo*.

I sought to initially characterise the effect of pharmacological and genetic activation of AMPK on endothelial metabolism and angiogenic responses according to the following aims:

Aim 1: Examine the effect of AMPK on endothelial metabolism.
Aim 2: Assess the effect of AMPK on endothelial proliferation and angiogenesis *in vitro* and *in vivo.*
Aim 3: Generation and initial characterisation of the metabolic phenotype of an endothelial-specific AMPK activating (Tie2-Cre AMPKγ_1-D316A-Tg) mouse model.

5.3 Results

5.3.1 The impact of BI-9774-mediated AMPK activation on endothelial glycolytic and mitochondrial metabolism *in vitro*

The functions of AMPK are heavily tied to metabolism and mitochondrial quality control, but there is little evidence to show how these processes are affected by AMPK activation in ECs through the use of specific activators. I employed real time metabolic analysing using the Seahorse XFe96 Flux Analyzer, which measures extracellular acidification rate (ECAR) and oxygen consumption rate (OCR) as readouts of glycolytic and mitochondrial metabolism, respectively (Section 2.18 *In vitro* Seahorse (XFe96) Flux Analyzer Metabolic Phenotyping) under normoxic (21% O_2) and hypoxic (3% O_2) conditions. VEGF-A_{165} treatment was included given its role as a potent inducer of sprouting angiogenesis and has been reported to increase both glycolysis and mitochondrial metabolism in ECs mimicking the canonical functions attributed to AMPK [15, 397, 398]. VEGF also serves as a physiological stimulus to induce AMPK activation in ECs via CAMKK2 [183, 189]. The traces obtained for the XF MitoStress test under different O_2 tensions are displayed in Figure 5.1.

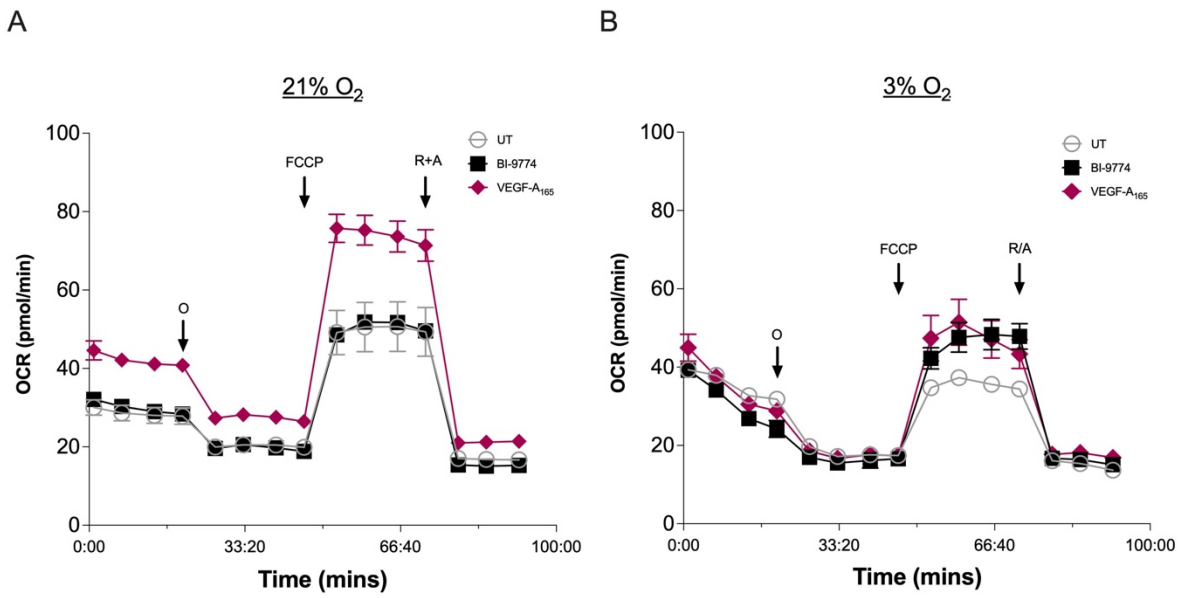


Figure 5.1 *– Representative traces derived from Agilent Seahorse XF MitoStress assay under 3% and 21% O_2.*

Traces obtained for control HUVECs (UT, grey open circle) or treated with BI-9774 (10 μM, black square), VEGF-A_{165} (20 ng/ml, magenta diamond) under normoxia (21% O_2) (A) and hypoxia (3% O_2) (B). The following injections were used to calculate a number of mitochondrial metabolic parameters: (i) O: oligomycin (2.5 μM), ATP synthase (CV) inhibitor; (ii) FCCP: carbonyl cyanide-p-trifluoromethoxyphenylhydrazone (4 μM), an OXPHOS uncoupling agent; and (iii) R+A: rotenone and antimycin A (2 μM for both), inhibitors of CI and CIII, respectively. Data is represented as mean ± SEM with n=3 biological replicates.

Under normoxic conditions, respirometry measurements revealed no differences between UT and BI-9774-treated cells upon examination of the traces obtained from the Seahorse XF Analyzer (Figure 5.1A). Further analysis revealed there were no significant differences were seen in basal and maximal respiration with BI-9774 treatment compared to control (Figure 5.2A-B). Mitochondrial ATP production was also unaffected by BI-9774 treatment under 21% O_2 (Figure 5.2C). As expected, VEGF-A_{165} treatment increased both basal and maximal respiration (1.46-fold-change, p-value < 0.05) which corresponded to increased mitochondrial ATP production (1.42-fold-change, p-value = 0.0491) in normoxic HUVECs (Figure 5.2A-C). There was no effect on maximal respiration by VEGF-A_{165} cells. Under hypoxia, BI-9774 unexpectedly reduced both basal respiration (−49%, p-value = 0.0080) and mitochondrial ATP production (−40%, p-value = 0.0179). No significant differences were noted in maximal respiration under hypoxia with BI-9774 treatment. Hypoxia exposure attenuated the enhanced OXPHOS phenotype (i.e., elevated basal and maximal respiration) induced by VEGF-A_{165} at 21% O_2, as shown by the reduction in basal respiration due to reduce O_2 availability (−35%, p-value = 0.0122). Despite this, combination of VEGF-A_{165} and hypoxia exposure had no significant impact on either maximal respiration or mitochondrial ATP production (Figure 5.2D-F).

Next, I assessed whether O_2 can contribute to the differential effects observed in Figure 5.1. An unanticipated finding was that basal respiration was significantly increased under hypoxia in untreated HUVECs (1.29-fold-change, p-value = 0.0097), corresponding to increased ATP production (1.42-fold change, p-value = 0.0064). However, maximal respiration was significantly impaired under 3% oxygen (−48%, p-value = 0.0010). On the other hand, BI-9774 and VEGF-A_{165} treatment significantly impaired basal respiration under hypoxia (−31% and −42%, respectively, p-value < 0.01). BI-9774 treatment did not impact maximal respiration nor ATP production; however, maximal respiration was significant reduced by VEGF-A_{165} under hypoxia (−38%, p-value = 0.0011) (Figure 5.3). The changes in the mitochondrial parameters were subsequently cross-examined with ECAR readings derived from the same plate. There were no significant differences in basal glycolysis between treatments within the normoxia and hypoxia groups (Figure 5.4A). VEGF-A_{165} treatment significantly enhanced glycolysis under normoxia, with further glycolysis occurring under hypoxic conditions (1.23-fold change, p-value = 0.0466).

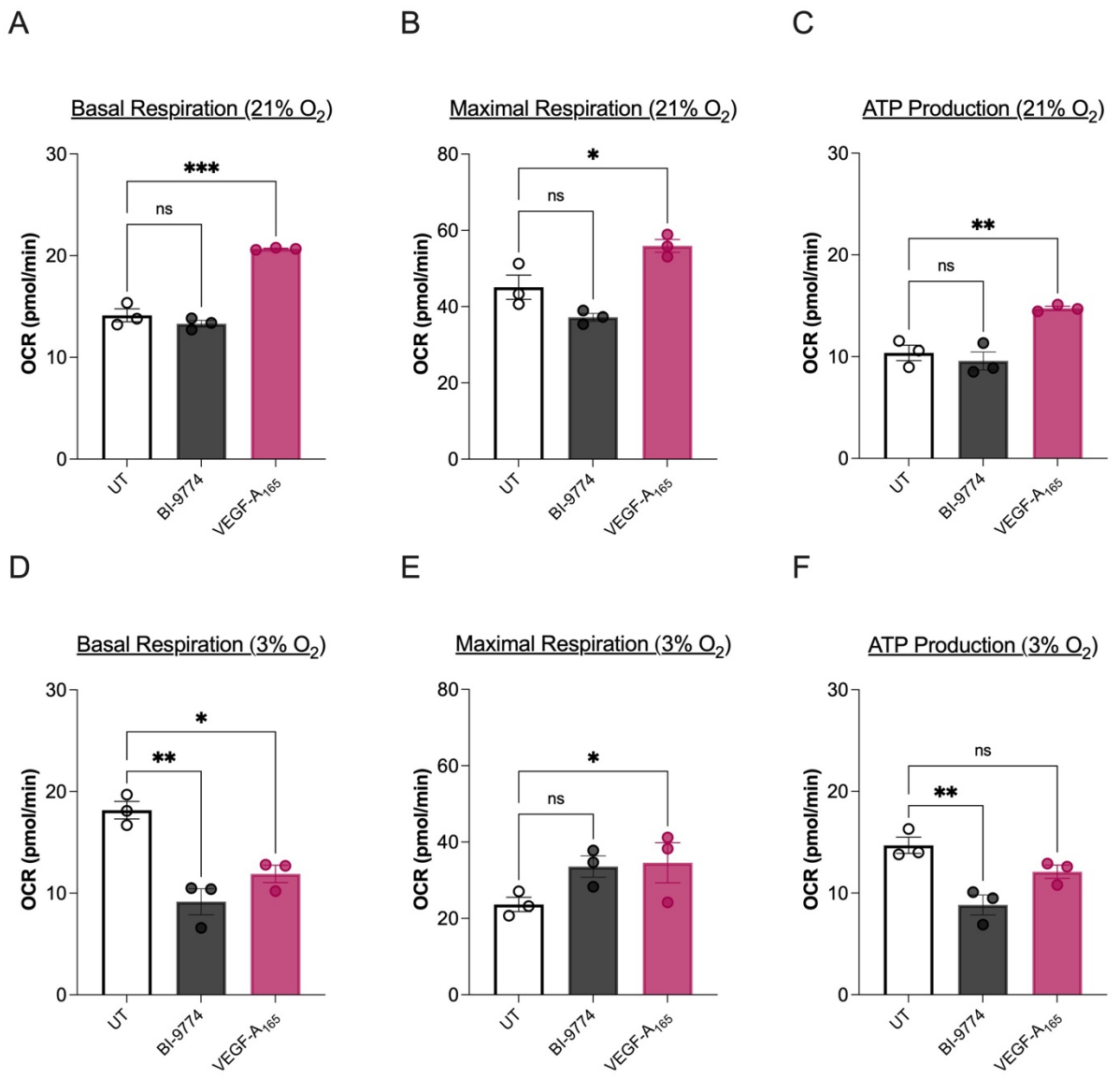


Figure 5.2 *– Comparison of treatments on mitochondrial metabolic parameters as determined by the Agilent Seahorse XF MitoStress assay.*

HUVECs were treated with BI-9774 (10 μM) and VEGF-A_{165} (20 ng/mL) for 24 hours prior to analysis using the Agilent Seahorse XF analyser. The following parameters were determined: basal respiration (A & D), maximal respiration (B & E) and mitochondrial ATP (C & F). Parameters were determined under normoxia (21% O_2, upper panel) and hypoxia (3% O_2, lower panel). Hypoxia data were already normalised to the 'zero O_2' reference as determined by the sodium sulphite injections. Data is represented as mean ± SEM with n=3 biological replicates and averaged across n=4-6 technical replicates on the XF microplate. Data analysis was performed using repeated measures one-way ANOVA followed by Dunnett's multiple comparisons test for comparisons against the control group (UT). ns, not significant; * p-value < 0.05, ** p-value < 0.01.

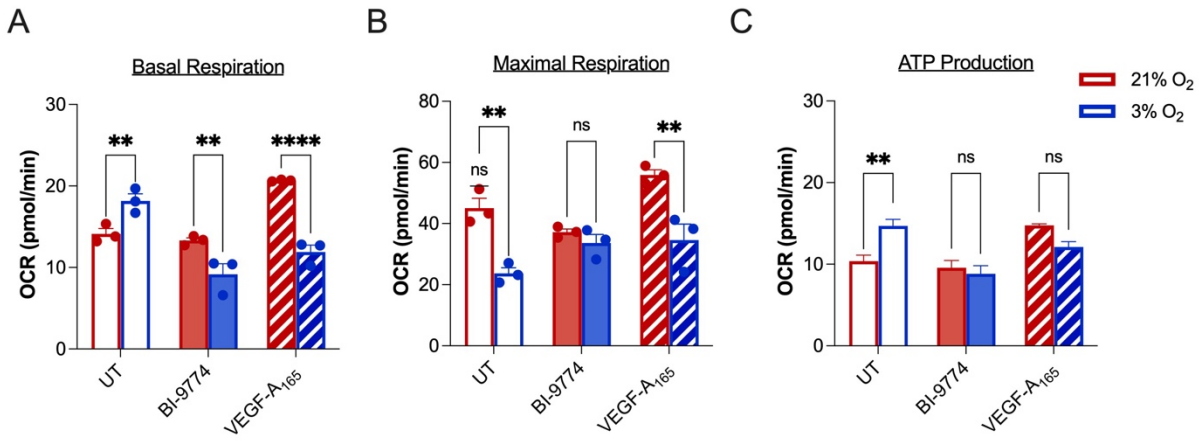


Figure 5.3 *– The effect of treatment responses on OXPHOS parameters under different O_2 tensions in HUVECs.*

HUVECs were treated with BI-9774 (10 nM) and VEGF-A_{165} (20 ng/mL) for 24 hours prior to analysis using the Agilent Seahorse XF analyser. The following mitochondrial respiration parameters, basal respiration (A), maximal respiration (B) and mitochondrial ATP production (C), were measured under normoxia (21% O_2) and hypoxia. Data is represented as mean ± SEM with n=3 biological replicates and averaged across n=4-6 technical replicates on the XF microplate. Data analysis was performed using two-way ANOVA test with Bonferroni multiple comparisons test. ns, not significant; ** p-value < 0.01, **** p-value < 0.0001.

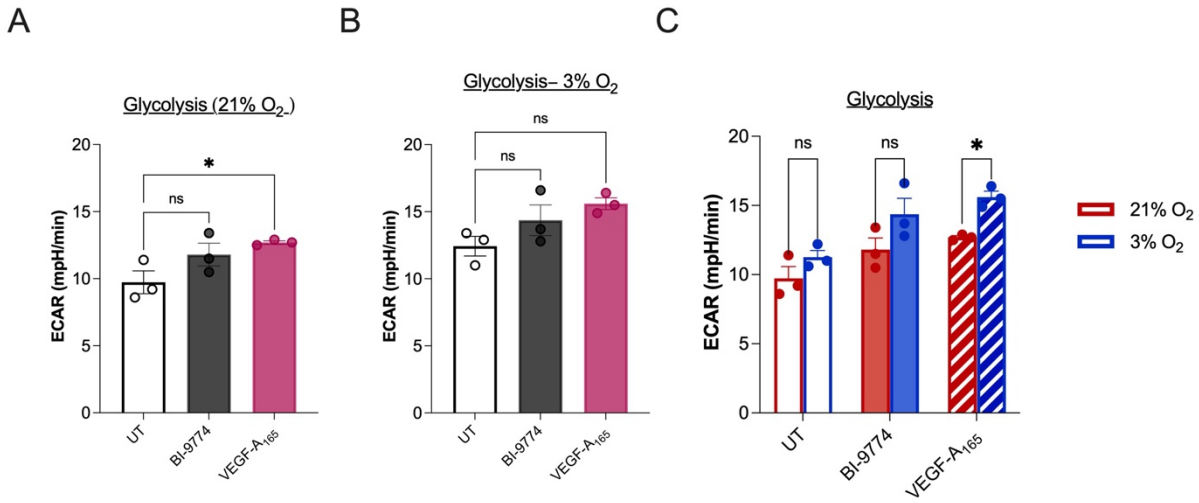


Figure 5.4 *– Comparison of treatments on basal glycolysis between treatment groups and O_2 tension as determined by Agilent Seahorse XF MitoStress assay.*

HUVECs were treated with BI-9774 (10 µM) and VEGF-A_{165} (20 ng/mL) for 24 hours prior to analysis using the Agilent Seahorse XF analyser. Basal glycolysis was measured under normoxia (21% O_2) and hypoxia (3% O_2) (A & B). Differences in glycolysis by treatment depending on O_2 (C). Data is represented as mean ± SEM with n=3 biological replicates and averaged across n=4-6 technical replicates on the XF microplate. Data analysis was performed using repeated measures one-way ANOVA followed by Dunnett's multiple comparisons test for comparisons against the control group (UT) for (A) and (B) and two-way ANOVA followed by Bonferroni correction for multiple comparisons, ns, not significant,* p-value < 0.05.

Mitochondrial membrane potential ($\Delta\Psi_m$) refers to the electrochemical potential across the inner mitochondrial membrane, generated by the proton pumping activities of Complex I, III and IV. Thus, $\Delta\Psi_m$ reflects both mitochondrial electron transport and OXPHOS efficiency. FACS analysis was performed to measure $\Delta\Psi_m$ and mitochondrial content by using TMRM and MitoTracker Green dyes. Normoxic HUVECs were treated with BI-9774 (10 μM) for 24 hours, stained for 30 minutes with the dyes before proceeding with FACS analysis. There was no significant change in TMRM fluorescence, as indicated by mean fluorescence intensity (MFI) values, in BI-9774 treated cells (Figure 5.5A) and a significant reduction in MitoTracker Green fluorescence following BI-9774 treatment (−25%, p-value = 0.0006), indicating that BI-9774 reduced mitochondrial mass (Figure 5.5B). To determine whether the TMRM reduction was due to mitochondrial depolarisation or merely reflected the reduction in mitochondrial content, I calculated the ratio of the MFI of TMRM to MFI MitoTracker Green, thus normalising $\Delta\Psi_m$ to mitochondrial mass. Normalised data via the TMRM:MitoTracker Green ratio revealed that BI-9774 treatment in fact significantly increased TMRM accumulation and suggests enhanced $\Delta\Psi_m$ proportionally in HUVECs (1.15-fold-change, p-value = 0.0116) (Figure 5.5C).

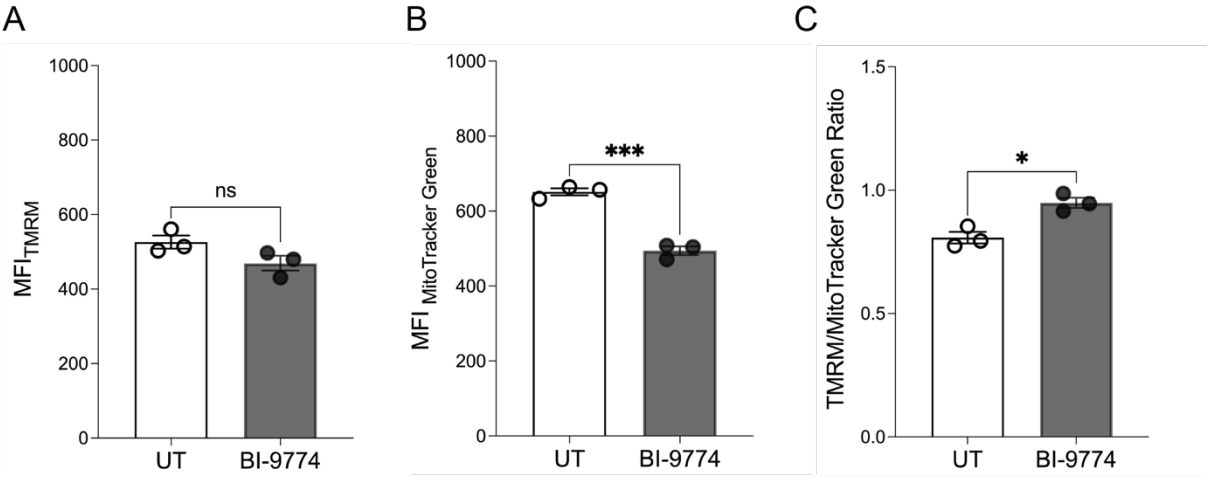


Figure 5.5 *– The effect of acute BI-9774 treatment on mitochondrial membrane potential and mitochondrial mass.*

HUVECs were treated with BI-9774 (10 μM) for 24 hours prior to harvesting for live-cell FACS analysis.
(A) Mean fluorescence index (MFI) of TMRM (25 nM) as an indicator of mitochondrial membrane potential ($\Delta\Psi_m$) by FACS.
(B) Mean fluorescence index (MFI) of MitoTracker Green (20 nM) as an indicator of mitochondrial content by FACS.
(C) Normalisation of TMRM signal to MitoTracker Green as an indicator of TMRM fluorescence per mitochondria.
All data is represented as mean ± SEM with n=3-5 biological replicates. Data analysis was performed using paired t-tests with the following notations: ns, not significant, * p-value < 0.05 and ** p-value < 0.01.

The role of AMPK in increasing mitochondrial content has been well established in metabolically active cell types (e.g., skeletal myocytes, hepatocytes), but this phenomenon also occurs in ECs exposed to LSS. AMPK promotes mitochondrial biogenesis by upregulating PGC-1α, the master regulator of mitochondrial biogenesis, which orchestrates a downstream transcriptional response resulting in increased mitochondrial content. I explored whether long-term pharmacological AMPK activation mirrors the increase in mitochondrial biogenesis seen by AMPK activation in response to physiological stimuli (e.g. in LSS-exposed HUVECs). Chronic activation of AMPK was achieved by daily treatment of BI-9774 under 21% O_2 for 10 days. Relative mtDNA copy number was determined by quantifying copies of mtDNA genes: *MT-ND1* and *MT-CO1*, which encode NADH dehydrogenase 1 (ND1) protein (complex I) and cytochrome c oxidase subunit I (complex IV), respectively. Amplification of mtDNA genes was normalised to the single copy nuclear gene encoding β_2-microglobulin (*B2M*). There was a significant increase in *MT-ND1* (2.1-fold-change, p-value = 0.0019) and *MT-CO1* (2.1-fold-change, p-value = 0.0013) (Figure 5.6A). To further validate that the observations are due to mitochondrial biogenesis, $\Delta\Psi_m$ and mass were quantified by FACS using TMRM and MitoTracker Green, respectively. TMRM fluorescence intensities were significantly higher in chronic BI-9774 treated HUVECs compared to control (1.41-fold-change, p-value = 0.0322) (Figure 5.6B). No significant differences were noted in MitoTracker Green fluorescence when comparing long-term BI-9774 treated HUVECs to its untreated counterpart, although a 1.32-fold change was noted (1.32-fold-change, p-value = 0.0712) (Figure 5.6C). Normalisation of TMRM fluorescence against MitoTracker Green showed no significant differences between untreated and chronically BI-9774-treated HUVECs (Figure 5.6D)

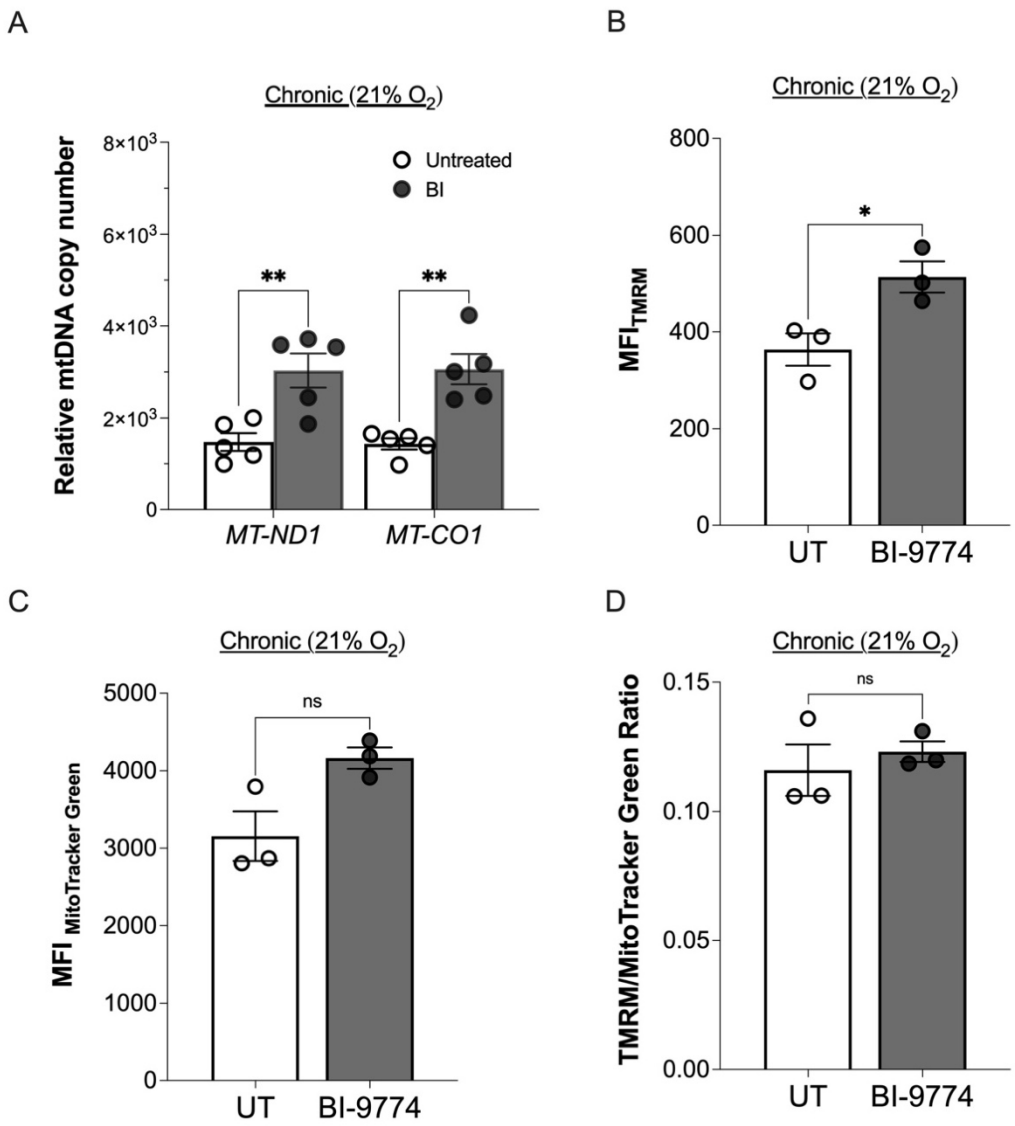


Figure 5.6 *– The effect of chronic BI-9774 treatment on mitochondrial membrane potential, mtDNA content and mitochondrial mass.*

HUVECs were pulsed daily with BI-9774 (10 μM) under normoxia (21% O_2) for 10 days prior to harvesting for DNA extraction.
(A) Relative mtDNA content normalised to single copy nuclear gene encoding β_2 microglobulin (*B2M*).
(B) Mean fluorescence index (MFI) of TMRM as an indicator of mitochondrial membrane potential ($\Delta\Psi_m$) by FACS.
(C) Mean fluorescence index (MFI) of MitoTracker Green as an indicator of mitochondrial content by FACS.
(D) Normalisation of TMRM to MitoTracker Green staining.
All data is represented as mean ± SEM with n=3-5 biological replicates. Data analysis was performed using an paired t-tests with ns denoting not significant, * p-value < 0.05 and ** p-value < 0.01.

5.3.2 The effects of AMPK activation on endothelial proliferation and angiogenesis *in vitro* and *in vivo*.

As shown in Chapter 4, RNA-seq analysis revealed significant deactivation of DNA synthesis, cell cycle progression and mitosis indicative of growth arrest in response to BI-9774 treatment. To evaluate the effects of BI-9774 on endothelial proliferation under normoxia, I assessed (i) EdU incorporation for DNA synthesis and (ii) propidium iodide (PI) for cell cycle analysis. As a nucleoside analogue of thymidine, EdU is incorporated into DNA during the S-phase of the cell cycle. EdU labelling was performed alongside the treatments in HUVECs for 24 hours prior to staining using copper-based click chemistry for FACS analysis. The results show that BI-9774 causes a significant reduction in EdU incorporation in HUVECs (−27%, p-value = 0.0005), demonstrating that AMPK activation reduces DNA replication.

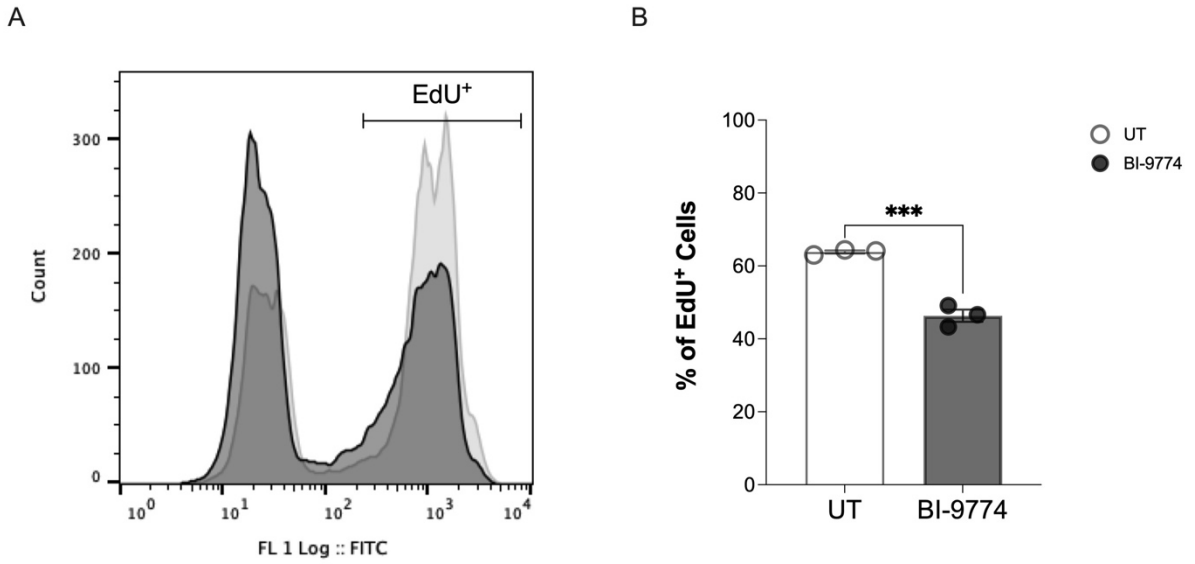


Figure 5.7 *– EdU incorporation as a measurement of DNA synthesis.*

HUVECs were treated with EdU (5 μM) alone or co-treatment with BI-9774 (10 μM) for 24 hours under normoxia (21% O_2) prior to analysis by FACS. Gating for EdU^+ population is also shown, taking into consideration background signal of the Alexa Fluor™ 488 Azide in the absence of EdU and unstained HUVECs.
(A) A representative FACS histogram overlaying UT samples (light grey) BI-9774-treated HUVECs (black).
(B) Quantification of EdU^+ population based off the gating in (A).
All data is represented as mean ± SEM with n=3 biological replicates. Data analysis was performed using paired t-tests with *** denoting p-value < 0.001.

To investigate whether AMPK triggers growth arrest, cell cycle analysis using propidium iodide (PI) staining was performed under normoxic and hypoxic conditions, to detect EC populations at different stages of the cell cycle. VEGF-A_{165} was included as a positive control, given its role in inducing EC proliferation during angiogenesis. Under normoxia and as expected, VEGF-A_{165} treatment promoted cell cycle progression as illustrated by the significantly reduced number of cells in the G_0/G_1 phase (−25%, p-value = 0.0048) but this did not correspond to an increase in the number of cells in the G_2/M phase (Figure 5.8D). No significant changes were noted in the number of cells by the G_0/G_1 phase (Figure 5.8A & B). BI-9774 significantly decreased the number of cells in the G_2/M phase under normoxia (−47.9%, p-value = 0.0108) but no significant differences were observed under hypoxia (p-value = 0.1021) despite a small reduction (Figure 5.8D&E). No significant differences were observed in the percentage of cells in the S-phase in comparison to the control regardless of treatment and O_2 tension. O_2 tension also did not impact cell cycle dynamics at baseline (UT) and following VEGF-A_{165} stimulation. My data therefore suggests that AMPK interferes with proliferation by restricting G2/M phase progression under both oxygen tensions, in agreement with RNA-seq results highlighting cell cycle checkpoint activation.

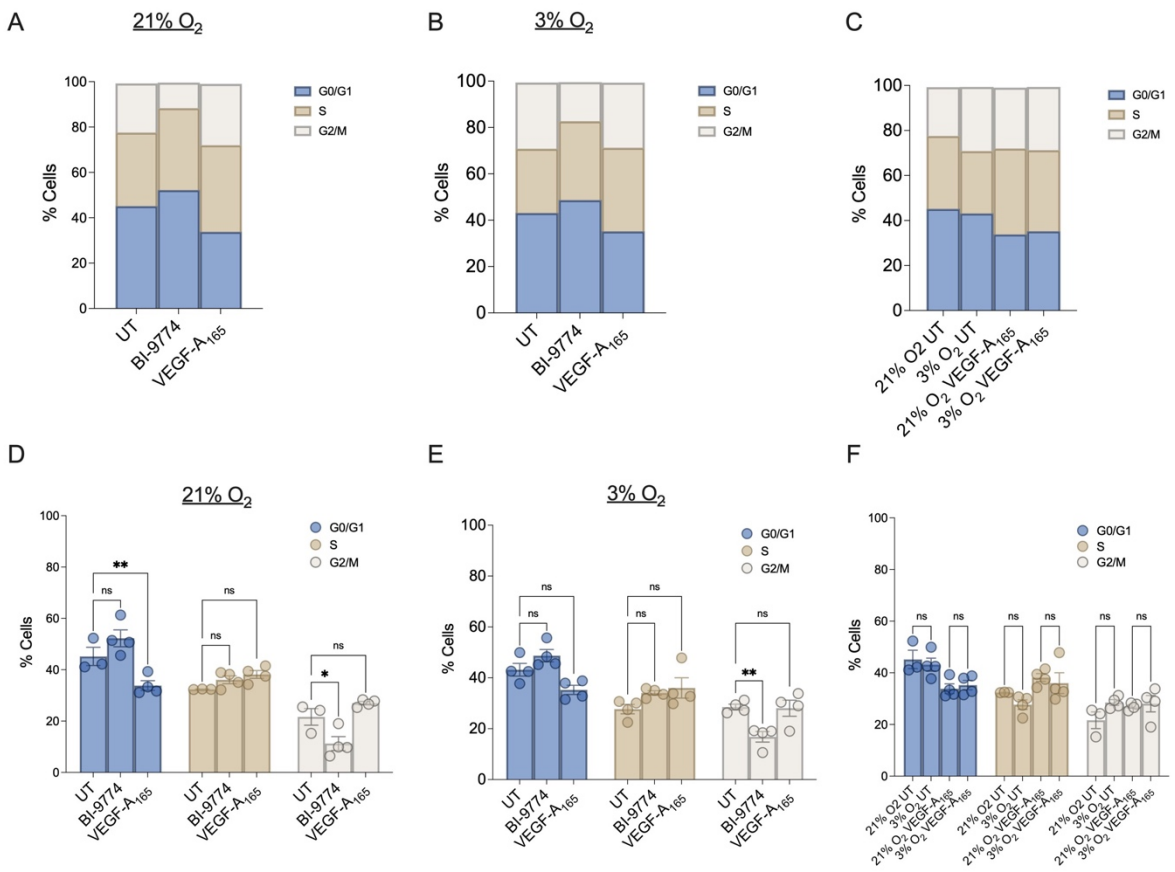


Figure 5.8 *– Propidium iodide (PI) cell cycle analysis of HUVECs.*

HUVECs were initially serum-starved for 24 hours in serum-free EBM2 for synchronisation. The following day, HUVECs were switched to treatment media and cultured either under normoxia (21% O_2) or hypoxia (3% O_2) with the following treatments: BI-9774 (10 μM) and VEGF-A_{165} (20 ng/mL) for 24 hours when they were harvested for downstream analysis. Stacked bar charts showing proportions of cells in G_0/G_1, S and G_2/M phases of the cell cycle under (A) normoxia, (B) hypoxia and (C) both O_2 tensions on cell cycle progression at baseline (UT) or with VEGF-A_{165} stimulation.
(D) A bar chart showing proportions of cells (%) in G_0/G_1, S and G_2/M phases of the cell cycle under normoxia.
(E) A bar chart showing proportions of cells (%) in G_0/G_1, S and G_2/M phases of the cell cycle under hypoxia.
(F) A bar chart comparing the effects of normoxia and hypoxia showing on cell cycle progression at baseline (UT) or with VEGF-A_{165} stimulation.
All data is represented as mean ± SEM with n=3-4 biological replicates. Data analysis was performed using two-way ANOVA with Tukey's multiple comparisons test. N.s, not significant, *p-value < 0.05, ** p-value < 0.01, **** p-value = < 0.0001.

Sprouting angiogenesis produces changes in endothelial morphology, causing them to acquire a polarised phenotype with filopodia and lamellipodia to facilitate their migration. To characterise morphological changes induced by BI-9774 and observed during routine tissue culture practice, HUVECs were stained for phalloidin and cytochrome c, to visualise the cytoskeleton and mitochondria respectively, and analysed by immunofluorescence. As shown in Figure 5.9, HUVECs exhibited profound changes in morphology upon treatment with BI-9774, causing them to adopt an elongated, 'activated' phenotype. Phalloidin staining was

enhanced by BI-9774 as a result of increased formation of stress fibres. BI-9774-treated HUVECs exhibited increased number of membrane extensions, often extended over a great distance (marked by white arrows in Figure 5.9), suggestive of a migratory phenotype.

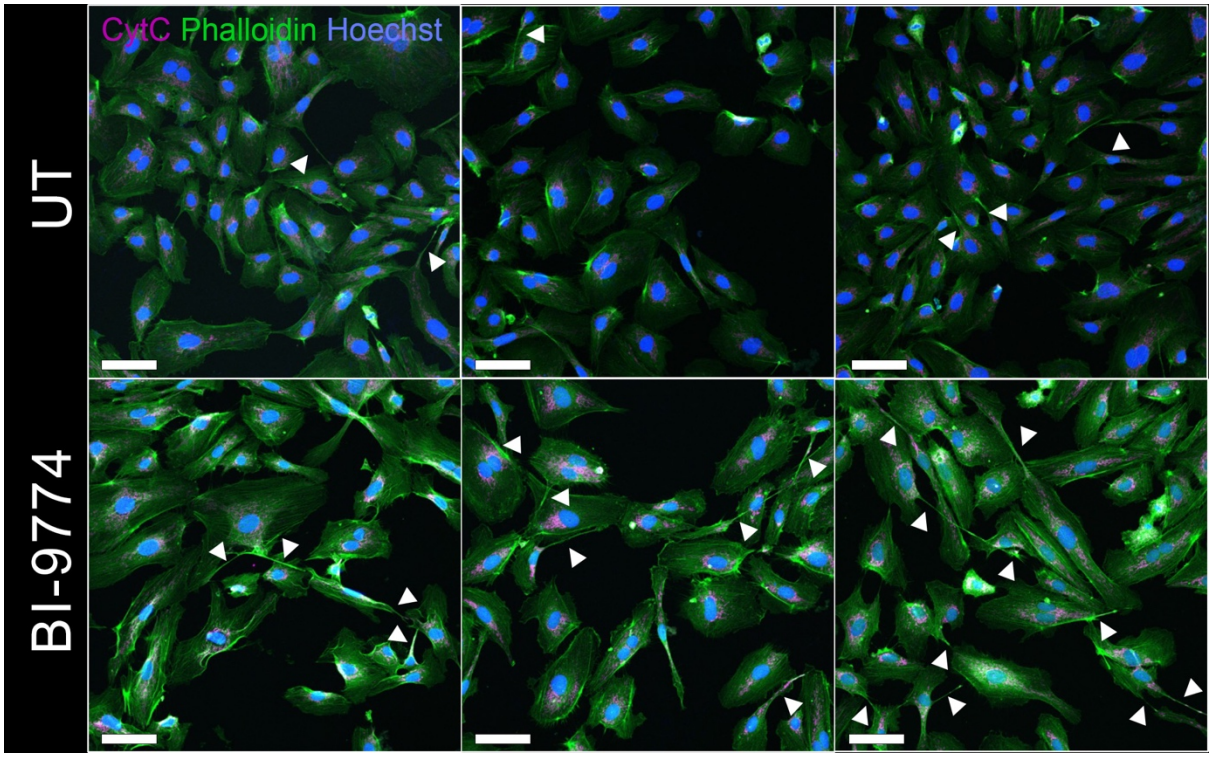


Figure 5.9 *– Morphological changes occurring in HUVEC in response to BI-9774 treatment.*

HUVECs were treated with BI-9774 (10 μM) for 24 hours prior to fixation and staining with phalloidin for visualisation of the cytoskeleton (green), α-cytochrome c to mark the mitochondrial network (magenta) and Hoechst to counter stain the nuclei (blue) obtained using 40× magnification. White arrows indicate the presence of cellular protrusions. Scale bar presents 25 μm.

To assess the effects of AMPK on angiogenesis, I carried out an *in vitro* Matrigel-based endothelial tube formation assay. Matrigel is a solubilised basement membrane extract derived from Engelbreth-Holm-Swarm (EHS) mouse sarcoma, which is rich in ECM constituents such as collagen, laminin and proteoglycans. Synchronised HUVECs were treated with either the AMPK activator BI-9774, AMPK inhibitor BAY-3827 or VEGF-A_{165} (20 ng/mL) for 24 hours in EGM-2 (2%) prior to trypsinisation and reseeding on top of growth factor reduced Matrigel. Images were obtained using both brightfield and fluorescent (Calcein-AM viability staining) microscopy at 4× magnification. Brightfield images were used for analysis using the AngioAnalyzer tool on FIJI to measure the following: (i) junctions (points of contact between three different cells); (ii) segments (number of enclosed areas between junctions); (ii) mean mesh size (area enclosed by segments); and (iii) total mesh area (sum of mesh area in the entire image). HUVECs treated with BI-9774 formed networks within the Matrigel similar to untreated and VEGF-A_{165} treated cells (Figure 5.10A). No significant differences were noted

between these groups according to the number of junctions, segments, mean mesh size and total mesh area, although a great deal of variation was observed across all parameters between these three groups (Figure 5.10B-E). A striking result was observed in HUVECs treated with BAY-3827 where the HUVECs failed to form tubes (Figure 5.10A). There was a noticeable reduction in the number of junctions (−79%, p-value = 0.0004) (Figure 5.10B) and segments (−90%, p-value = 0.0003) (Figure 5.10C), in turn affecting mean mesh size and total mesh area calculations (Figure 5.10D & E). Furthermore, BAY-3827 treatment abolished tube formation upon attempting to rescue the phenotype using VEGF-A_{165}.

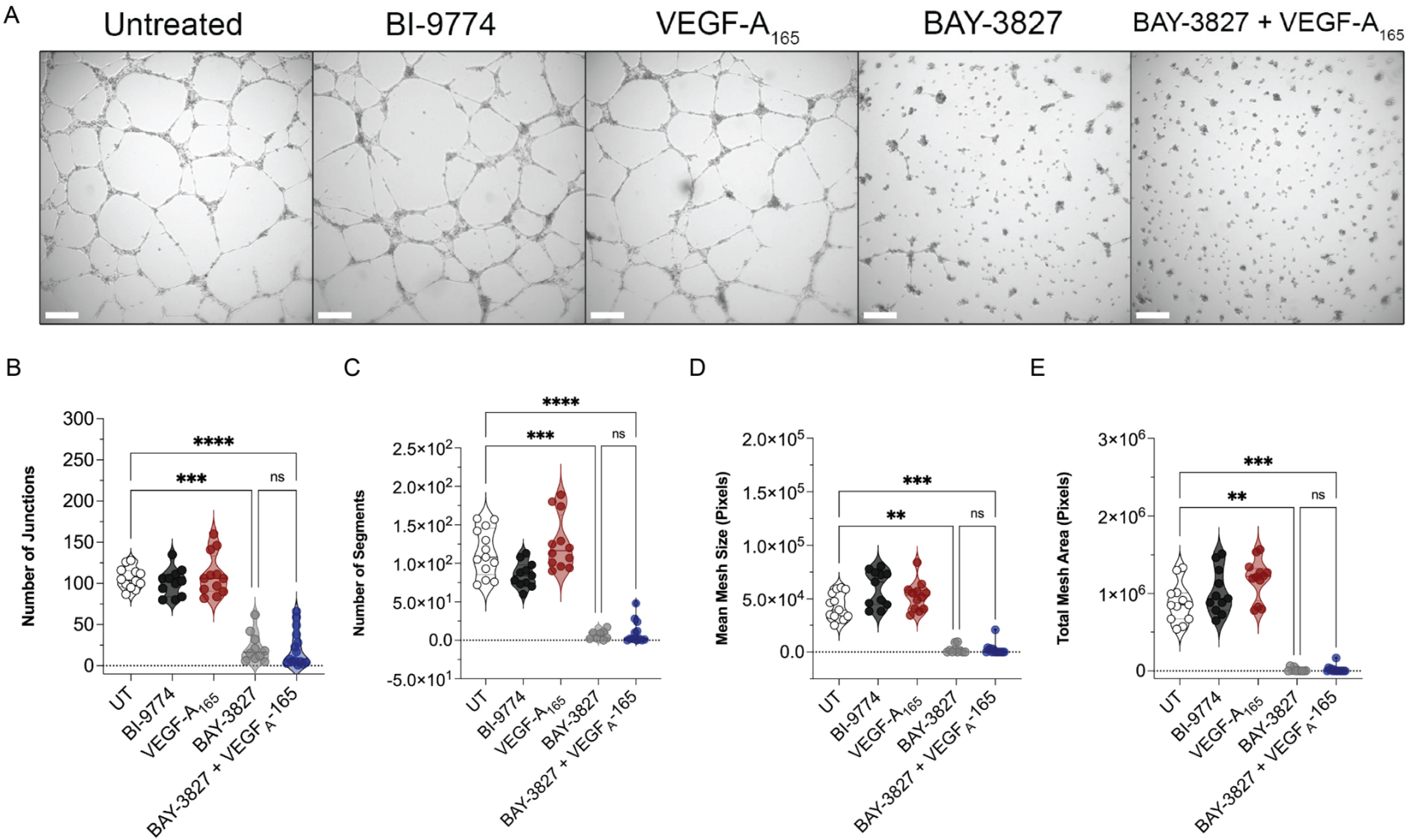


Figure 5.10 *– The effect of AMPK activation and inhibition by BI-9774 and BAY-3827 on Matrigel tube formation in vitro.*

Brightfield images obtained at 4× magnification of HUVECs seeded in Matrigel treated with BI-9774 (10 μM), VEGF-A_{165} (20 ng/mL), BAY-3827 (5 μM) and combined VEGF-A_{165}/BAY-3827 treatment (A), number of junctions formed (B), number of segments (C), mean mesh size (D) and total mesh area (E). Data was analysed using Kruskal-Wallis non-parametric one-way ANOVA test with Dunn's multiple comparisons, ns denoting not significant, ** p-value < 0.01, *** p-value < 0.001 and **** p-value < 0.0001 Scale bar represents 250 μm.

Preliminary data from our group found that chronic activation of AMPK using the global γ_1-D316A mouse model resulted in increased systemic vascularisation, as shown by elevated $CD31^+$ staining in scWAT by immunohistochemistry (unpublished data). To determine whether AMPK promotes hypervascularisation, I chose to focus on the post-natal mouse retina, often utilised as a model to examine angiogenesis *in vivo*. Expansion of the superficial vascular plexus begins at P1, at which point the retina is largely devoid of any vasculature. Radial vessel outgrowth proceeds from the optic, reaching the peripheral edges between P8-9. Beyond this point, the capillaries invaginate the next layers of the retina to form the deep and intermediate vascular plexi [399]. Therefore, to study any changes prior to remodelling and pruning, the retina must be examined within the critical window of P5-7.

Floxed γ_1WT-Tg and γ_1D316A-Tg female mice were crossed with β-actin-Cre male mice to generate mice overexpressing both the WT and D316A γ_1 transgenes. In order to increase numbers of useable mice, I also included Cre negative D316A-Tg mice for analysis and incorporated these into the γ_1WT-Tg data, but for simplicity, I refer to this combined group as γ_1WT-Tg in the text. Mouse pups (P6) were weighed before proceeding with culling and retina harvest, as underdeveloped mice will often have abnormal phenotypes and need to be excluded from analysis.

Analysis of body weights in the pups showed that the γ_1D316A-Tg had a modest, but significant reduction in body weights compared to their γ_1WT-Tg counterparts (−8%, p-value = 0.0101) (Figure 5.11B). For vascular phenotype analysis, two regions were selected: (i) the capillary beds defined as the region between a vein and an artery and (ii) the angiogenic front of the capillary outgrowth at the edges of the retina (Figure 5.11). Visualisation of the retinal vasculature revealed a subtle but a significant increase in increased blood vessel density in the capillary beds of D316A-Tg compared to control mice (Figure 5.11A & C). There also appeared to be increased number of blood vessels at the angiogenic front, however no overt differences in the number of tip cells were observed, at least by isolectin B4 staining [lower two rows, (Figure 5.11A)]. Further analysis is required by using specific markers to differentiate between EC phenotypes to allow a comprehensive characterisation of the cells at the angiogenic front.

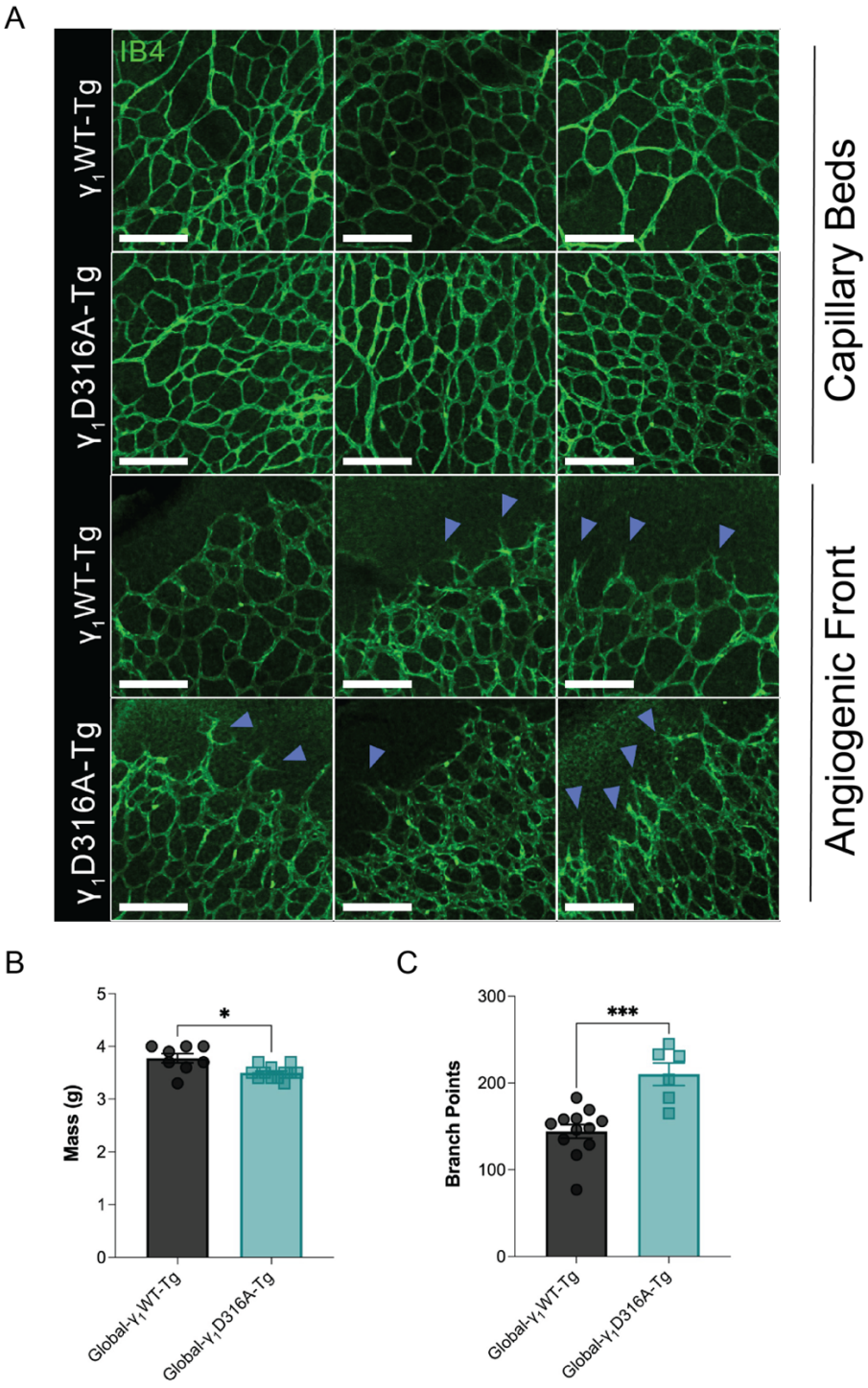


Figure 5.11 *– Wholemount immunostaining of neonatal retinas from global γ1WT-Tg and γ1D316A-Tg mice.*

(A) High magnification confocal images of the retinas derived from global γ1WT-Tg and γ1D316A-Tg post-natal day 6 (P6) mouse retinas, stained with isolectin B4 (green) to visualise the vasculature. Upper two rows of images are derived from the capillary beds and the lower two rows are derived from the angiogenic front (bottom two rows). Blue arrows indicate the presence of tip cells at the angiogenic front.
(B) Body weights of P6 mice from γ1WT-Tg (n = 8) and D316A-Tg (n = 12) mice.
(C) Branch point analysis of the capillary beds of global γ1WT-Tg (n = 6) and D316A-Tg (n = 3) mice with 2 fields per retina used for analysis. Data is represented as mean ± SEM and analysis was performed using unpaired t-test. * p-value < 0.05, *** p-value < 0.001. Scale bar represents 50 μm.

5.3.4 Characterising the metabolic phenotype of the EC-specific AMPK gain-of-function (γ_1D316A-Tg) mouse model *in vivo*

As mentioned in Section 5.1, the global activating AMPK model (β-actin-Cre γ_1D316A-Tg) used by our group exhibits a distinct hypermetabolic phenotype. Extensive characterisation of the model has shown that the adipose and the liver may be responsible for the protective effects observed in response to obesogenic diets [394], [395]. Since we saw an increase in systemic vascularisation in the global model, I sought to investigate the role of the endothelium in conferring the protective effects of global γ_1D316A activation in response to high fat diet (HFD). The noticeable vascular phenotype in the global AMPK activating model led to the generation the EC-specific D316A-Tg strain (referred to from this point onwards as EC-γ_1D316A-Tg) by crossing Tie2-Cre (*Tek-cre*^{12Flv}) males with the floxed females carrying the D316A transgene. Apart from body weight in males (Figure 5.12), the EC-γ_1D316A-Tg did not exhibit the deleterious consequences of chronic global AMPK activation such as cardiac hypertrophy or polycystic kidney as reported elsewhere (Figure 8.1) [396]. To examine whether EC-specific AMPK activation confers a protective phenotype against DIO, I conducted a pilot study to study the metabolic phenotype of EC-γ_1WT-Tg and EC-γ_1D316A-Tg mice fed a HFD (45% kJ from fat) for 16 weeks. Prior to HFD, the initial body weights were recorded. EC-γ_1D316A-Tg males had a significantly lower starting mass (−9.3%, p-value = 0.0128) (Figure 5.12A), however no differences in starting body weight were observed in females between the genotypes (Figure 5.12B).

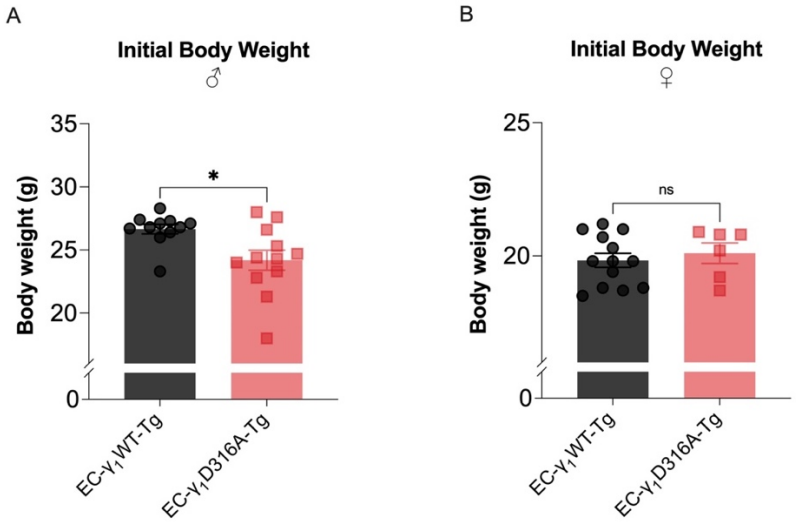


Figure 5.12 *– Initial body weights of EC-γ_1WT-Tg and EC-γ_1D316A-Tg mice prior to DIO.*

Initial body weights of (A) 8-week-old males (♂) and (B) 8-week-old females (♀) for EC-γ_1WT-Tg and EC-γ_1D316A-Tg mice. Data is represented as mean ± SEM (n=6-13 mice) and analysis was performed using an unpaired t-test.
Ns, not significant, * p-value < 0.05.

Following HFD initiation, my results reveal that EC-γ_1D316A-Tg males exhibit a marked resistance to DIO, with reduced weight gain compared to wild-type mice (Figure 5.13A). To account for the lower starting weight in the EC-γ_1D316A-Tg compared to EC-WT-Tg males, I calculated the difference in body weight before and after the HFD study. The weight difference was −30% lower in the EC-γ_1D316A-Tg males (p-value = 0.0038) (Figure 5.13C). Another striking observation is that the female cohort showed no difference throughout the entire duration of HFD and even after accounting for weight differences (Figure 5.13B & D). As this was only the first cohort, the remaining analyses was based on observations on male mice maintained on HFD; exclusion of females will be elaborated further in the discussion. In order to further explore the potential mechanism underlying the difference in bodyweight gain between EC-γ_1WT-Tg and EC-γ_1D316A-Tg males, a small number of mice (n=3 vs n=5-12 per group for all previously described measurements) were housed in a Columbus Instruments Comprehensive Lab Animal Monitoring System (CLAMS), which allows for real time recording of multiple metabolic measurements. I initially examined the respiratory exchange ratio (RER) values, which represents a ratio of volume of CO_2 (VCO_2) produced to volume of O_2 consumed (VO_2). RER (VCO_2/VO_2) values provide insight into substrate utilisation for energy production. For example, predominant carbohydrate utilisation results in RER values of approximately 1.0 whereas the RER values for the predominant utilisation of lipids lies close to 0.7 [400]. Heat production, which provides a readout of metabolic rate and energy expenditure was also measured. As shown by Figure 5.14A, there were no striking differences in the RER values between either genotype, with all values sitting between 0.7-0.8, indicating that mice were utilising predominantly fats. The RER follows a diurnal pattern in chow-fed mice, oscillating between 0.7 and 1 during a 24-hour period which is abrogated upon switching to HFD [401, 402]. As expected, there was very little diurnal change in RER (Figure 5.14A). I also observed no differences between both genotypes with regards to heat production (Figure 5.14B). There were no significant differences in both RER and heat production when averaged over the light and dark periods.

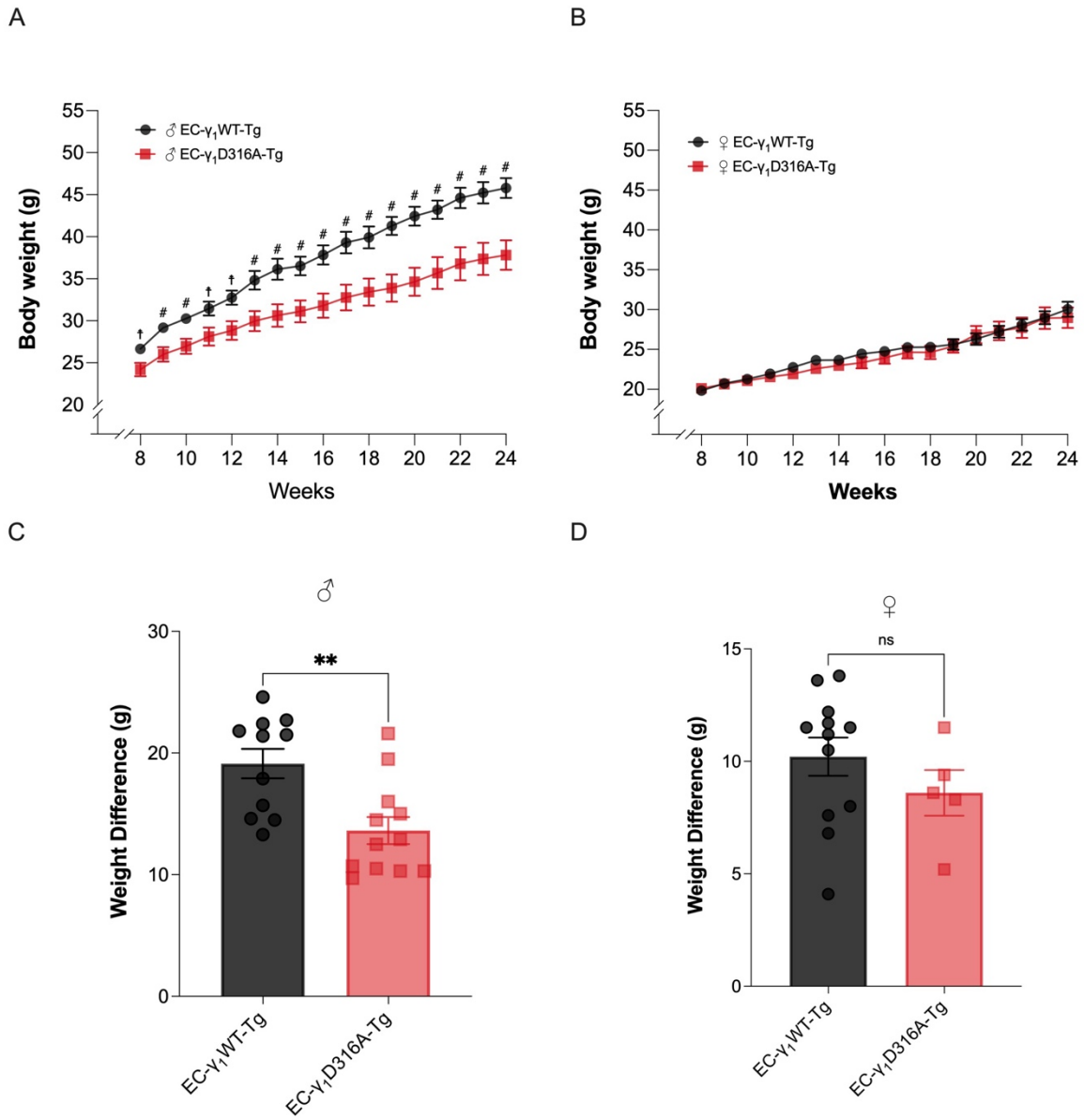


Figure 5.13 *– Body weight throughout the duration of HFD-induced DIO study.*

Body weights of (A) male and (B) female mice throughout the duration on HFD (16-weeks). Difference in body weight from the start and end of the HFD in (C) male and (D) female mice.
Data is represented as mean ± SEM (n=5-12 mice) and analysis was performed using unpaired t-tests. Ns, not significant, * or † p-value < 0.05, ** or # p-value < 0.01.

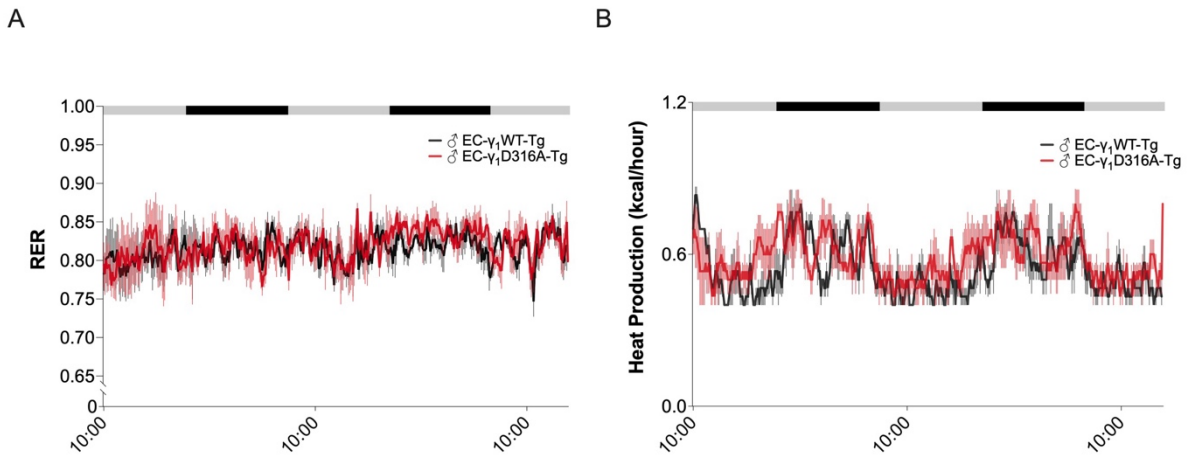


Figure 5.14 *– Metabolic parameters measured by CLAMS of EC-γ1WT-Tg and EC-γ1D316A-Tg mice at 12 weeks of HFD.*

(A) Average respiratory exchange ratio (RER).
(B) Heat production (kcal/hour).
All values were collected over a 2-day period. Data is represented as mean ± SEM for EC-γ1WT-Tg (n=3) and EC-γ1D316A-Tg (n=3) male (♂) mice. Grey bars represent light period (7:00 -19:00) and black bars (19:00-7:00) represent dark periods.

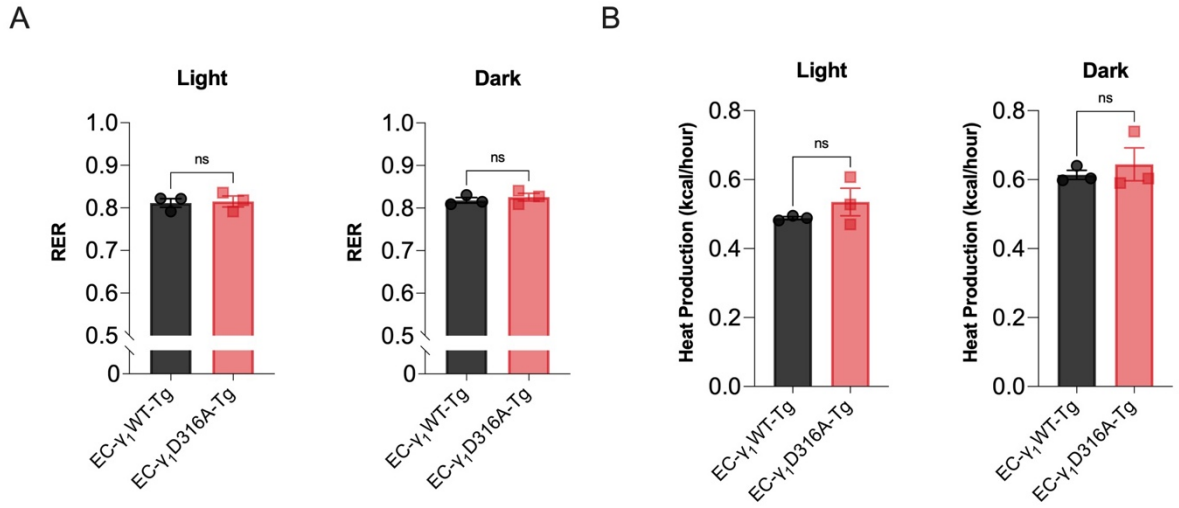


Figure 5.15 *– Quantification of RER and heat production during the light and dark periods.*

(A) Average respiratory exchange ratio (RER) values during light and dark periods, expressed in arbitrary units.
(B) Heat production (kcal/hour) values during light and dark periods.
All values were collected over a 2-day period. Data is represented as mean ± SEM for EC-γ1WT-Tg (n=3) and EC-γ1D316A-Tg (n=3) male (♂) mice. Analysis was performed using an unpaired t-test. Ns, not significant.

At the end of the HFD study, I performed a terminal harvest of male mouse organs for further downstream analysis. I initially examined organs which are disposed to changes on HFD such as the liver and the following adipose depots: intracapsular brown adipose tissue (iBAT), gonadal and inguinal white adipose tissue (gWAT and iWAT, respectively). Measurements in the wet weight of organs revealed no differences in the mass of the gWAT from both genotypes. However, I noted a significant reduction in the mass of iWAT (−38%, p-value = 0.0023), a subcutaneous adipose depot, and the liver (−33%, p-value = 0.0143) (Figure 5.16C

& D). There was no significant difference in the weights of the intracapsular brown adipose tissue (iBAT) depots between the EC-γ_1WT-TG and EC-γ_1D316A-Tg groups, although the weights appeared to be reduced in the latter by approximately ~30% (p-value = 0.1301). There was no significant differences in the weights of the heart, brain and spleen between the genotypes (Figure 5.17).

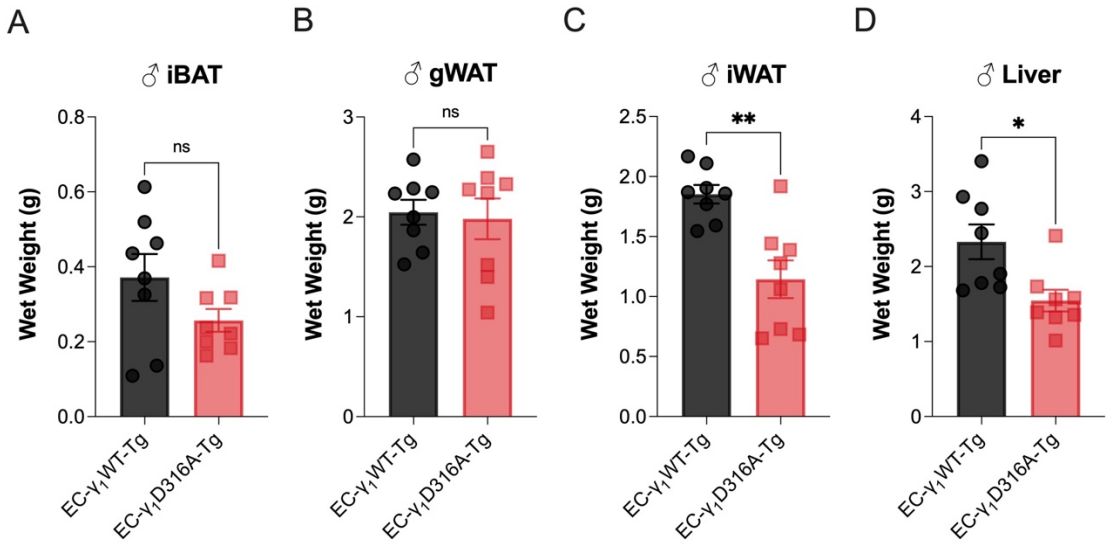


Figure 5.16 *– Wet weights of liver and adipose depots from 16-week HFD-fed male mice.*

Terminal tissue weights from the male EC-γ_1WT-Tg and EC-γ_1D316A-Tg mice at the end of the HFD study.
(A) Intracapsular brown adipose tissue (iBAT)
(B) Gonadal white adipose tissue (gWAT).
(C) Inguinal white adipose tissue (iWAT).
(D) Liver.
Data is represented as mean ± SEM (n=8 mice per genotype) and analysis was performed using an unpaired t-test. Ns, not significant, * p-value < 0.05, ** p-value < 0.01.

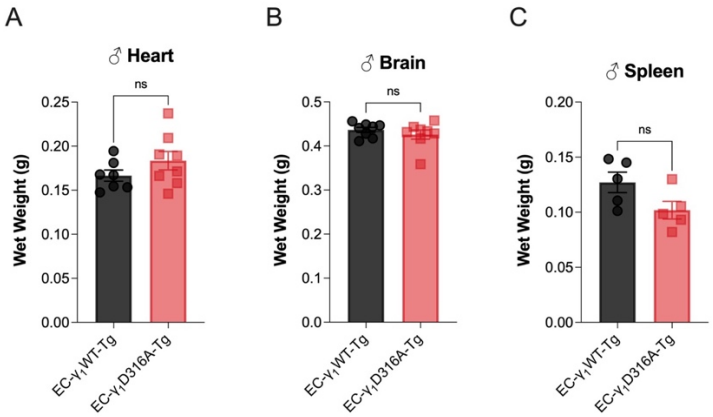


Figure 5.17 *– Wet weights of heart, brain and spleen from 16-week HFD-fed male mice.*

Terminal tissue weights from the male EC-γ_1WT-Tg and EC-γ_1D316A-Tg mice at the end of the HFD study.
(A) Heart.
(B) Brain.
(C) Spleen.
Data is represented as mean ± SEM (n=5-8 mice per genotype) and analysis was performed using an unpaired t-test. Ns, not significant, * p-value < 0.05, ** p-value < 0.01.

Next, I assessed whether there were any changes in the morphological characteristics and lipid accumulation in the iWAT and liver. Sections obtained from paraffin-embedded iWAT and liver were subsequently stained with haematoxylin and eosin (H&E) to identify any changes in morphology. Examination of the iWAT revealed no obvious differences in adipocyte morphology as both genotypes possessed characteristic features typical of white adipocytes: large, unilocular lipid droplets, occupying most of the cell volume (Figure 5.18). Therefore, the phenotype observed in EC-γ_1D316A-Tg mice appears to occur independently of the changes in global γ_1D316A-Tg iWAT, where the adipocytes possessed smaller, multilocular lipid droplets with increased mitochondrial biogenesis, resembling the characteristic features of BAT [178].

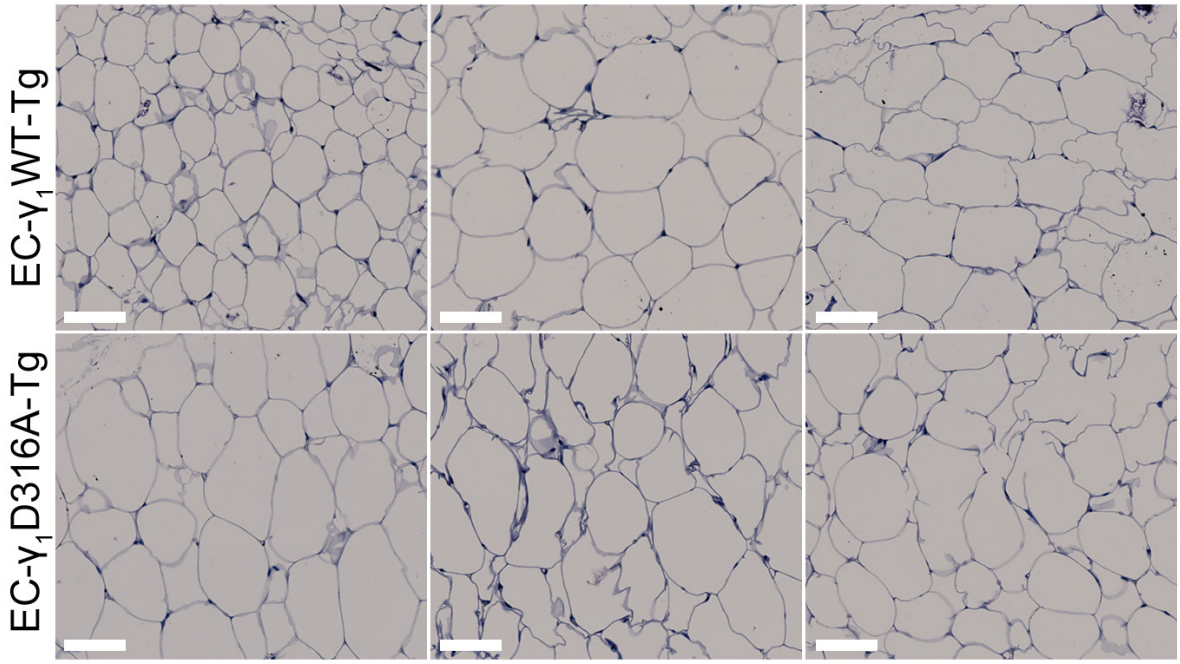


Figure 5.18 *– Histological analysis of haematoxylin-stained iWAT sections from 16-week HFD-fed male mice.*

Sections of iWAT from EC-γ_1WT-Tg and EC-γ_1D316A-Tg (n = 3 mice per genotype) male mice were stained with haematoxylin. Scale bars represent 50 µm.

There were striking differences in the morphology of EC-γ_1WT-Tg and EC-γ_1D316A-Tg livers (Figure 5.19). H&E staining revealed pale colouration of the liver and the presence substantial gaps in the livers of EC-γ_1WT-Tg indicative of the presence of lipid droplets in hepatocytes prior to tissue processing (Figure 5.19). EC-γ_1WT-Tg livers also contained enlarged hepatocytes with an increased number of balloon cells, identified by the presence of wispy cytoplasmic elements by the eosin stain (Figure 5.20). Unlike the macrovesicular steatosis observed in EC-γ_1WT-Tg mice, the livers from EC-γ_1D316A-Tg mice had smaller gaps, with

uniformly sized hepatocytes (Figure 5.20, right), suggesting that chronic AMPK activation in the endothelium protects mice against DIO-induced hepatic steatosis.

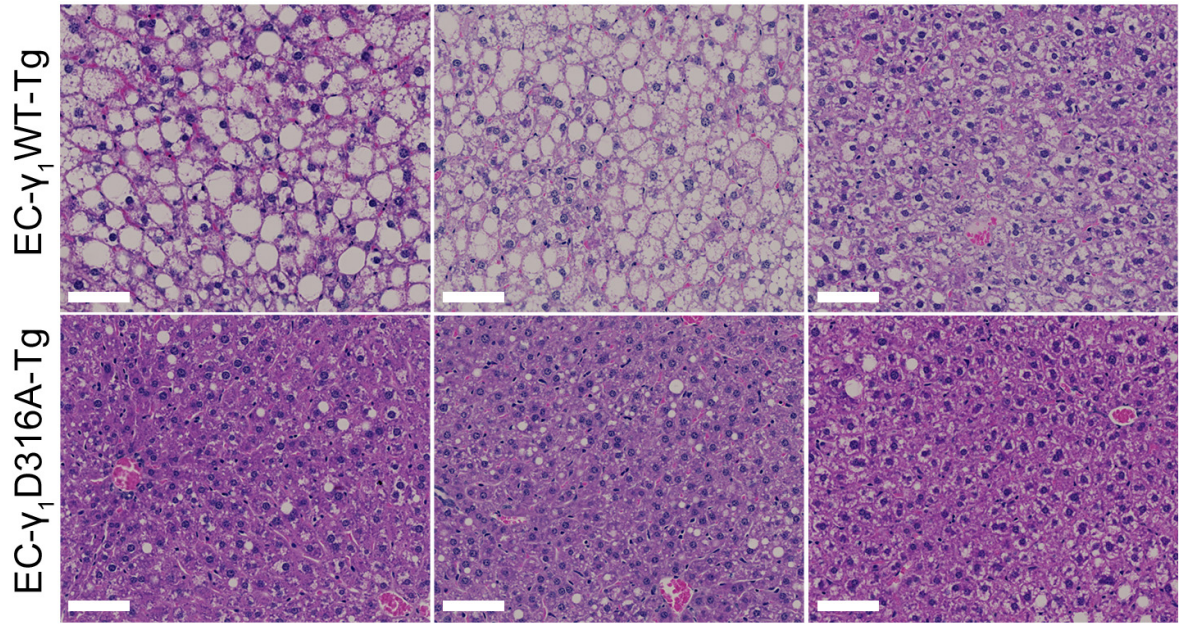


Figure 5.19 *– Histological analysis of haematoxylin and eosin (H&E)-stained liver sections from 16-week HFD-fed male mice.*

Liver sections from EC-γ_1WT-Tg and EC-γ_1D316A-Tg (n = 3 mice per genotype) male mice were stained with H&E. The white-staining areas are indicative of the presence of triglycerides and lipids prior to tissue processing. Scale bars represent 50 µm.

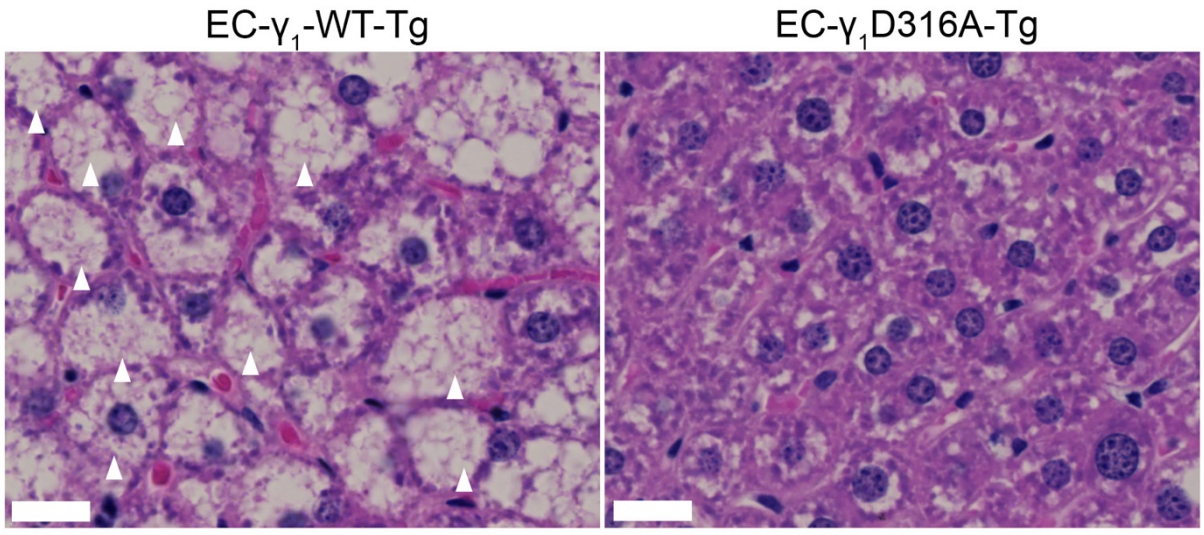


Figure 5.20 *– Magnification 100x of livers from 16-week HFD-fed EC-γ_1WT-Tg and EC-γ_1D316A-Tg male mice.*

Magnified (100×) images obtained from H&E-stained EC-γ_1WT-Tg mice (left) and EC-γ_1D316A-Tg (right) liver sections. White arrows indicate the presence of balloon cells, identified by eosin staining (pink) cells with wispy cytoplasmic elements reminiscent of cobwebs. Scale bar represents 20 µm.

5.4 Discussion and Limitations

Therapeutic activation of AMPK has gained prominence in recent years, due to promising pre-clinical results of novel small molecule activators in the treatment of cardiometabolic diseases. The use of small molecule activators in pre-clinical studies, like BI-9774, have aided in delineating cell-type specific responses without concerns for off-target effects of first-generation AMPK activators. The chapter provides preliminary characterisation of endothelial-specific AMPK functions using pharmacological and genetic models, highlighting its role in angiogenesis and metabolism.

5.4.1 AMPK and endothelial metabolism

As mentioned in Section 1.3 Endothelial Metabolism, ECs heavily rely on aerobic glycolysis for generation of ATP, even when O_2 is abundant. BI-9774 treatment in HUVECs had no significant effect on ECAR. It should be noted that the baseline ECAR measurements were derived from the MitoStress assay, which does not allow calculation of parameters such as basal glycolysis, glycolytic capacity and reserve. Additional assays would be required to examine glycolytic function (e.g., XF Glycolysis Stress assay) and glucose uptake (e.g., fluorescent probes like 2-NBD-glucose) in response to BI-9774 treatment across both O_2 tensions.

As shown by Figure 5.2A, baseline respiration is low in ECs, only increasing modestly with VEGF-A_{165} treatment, corroborating previous findings of other groups [15, 398]. Despite changes in O_2 tension, OCR values of HUVECs were low, residing within the range of 10-20 pmol/min suggesting that ECs exhibit a 'metabolically hypoxic' phenotype (Figure 5.2A & D). Intriguingly, baseline mitochondrial respiration was higher in hypoxic HUVECs (Figure 5.3A). This may be due to increased ROS production under hypoxia, arising out of disruptions in the mitochondrial ETC and redox status as reported elsewhere [338, 403]. Under normoxic conditions, BI-9774-mediated AMPK activation does not alter mitochondrial parameters, only minimally increasing glycolysis (Figure 5.2A-C). However, BI-9774 decreases basal respiration and mitochondria-linked ATP production in HUVECs under hypoxia, suggesting that AMPK activation inhibits mitochondrial respiration when O_2 is limiting.

Restoration of energy balance by AMPK occurs in two distinct phases: the acute phase characterised by enhanced glucose uptake, glycolytic flux and autophagy to normalise the cellular ATP:ADP/AMP rapidly, followed by eliciting mitochondrial biogenesis to enhance metabolic fitness in the long-term. Examination of mitochondrial parameters such as $\Delta\Psi_m$,

mitochondrial content and relative mtDNA copy number revealed distinctions in the temporal effects of AMPK signalling. A biphasic response was observed in normoxic HUVECs subjected to treatment with BI-9774 where acute treatment (≤ 24 hours) resulted in a decrease in mitochondrial content (Figure 5.5), which could explain the reduction in basal OCR observed under hypoxia (Figure 5.3). Mitophagy is regulated by AMPK through (i) phosphorylation of MFF to promote mitochondrial fission and (ii) subsequent engulfment by autophagosomes through activation of ULK1 [404]. Several studies have implicated the mitophagy receptor FUN14 domain containing 1 (FUNDC1) in mediating hypoxia-induced mitophagy [404-406]. FUNDC1 is reported to be a substrate of ULK1, a downstream substrate of AMPK [407, 408].

On the other hand, chronic treatment (≥ 10 days) with BI-9774 significantly enhanced mitochondrial biogenesis as shown by increased mitochondrial content and relative mtDNA copy number (Figure 5.6). The observations with BI-9774 treatment are similar to findings by Marin *et al.* (2017) using non-specific AMPK activators such as AICAR and metformin (Figure 5.6) [389]. A limitation of this study is that I did not examine changes in the mRNA and/or protein expression of *PPARGC1A*, *NRF1*, *NRF2*, *UCP2* and *TFAM*. As it was beyond the scope of this project, I did not examine the roles of chromatin remodellers in altering gene expression as reported in the study. Further studies are required to investigate whether AMPK activation (i) sustains or increases mitochondrial content in ECs under hypoxia and (ii) whether this response is contingent on PGC-1α or occurs through an alternative mechanism. Hypoxia-induced mitochondrial dysfunction characterised by reduced OCR and reduction in mitochondrial content has observed in pulmonary ECs derived from patients with PH [409, 410]. Given that AMPK and mitochondria biogenesis are heavily interlinked, it is intriguing to speculate whether BI-9774 can prevent hypoxia-induced mitochondrial dysfunction and reduction in mitochondrial content in pulmonary arterial ECs derived from PH patients. Recent work by Tilokani and colleagues identified mitochondrial fission regulator 1-like protein (MTFR1L) as a novel substrate of AMPK. As mentioned previously in Section 1.7.2 Metabolic Functions of AMPK, AMPK is critical for mitochondrial quality control. Future work will endeavour to characterise the effects of BI-9774 on mitochondrial dynamics by live-cell imaging and utilising reporters to examine mitophagy (e.g., mtKeima) and mitochondrial biogenesis and ageing (MitoTimer). The use of the aforementioned fluorescent reporters have been used to characterise AMPK function in skeletal myocytes [411, 412].

Acute activation of AMPK promotes $\Delta\Psi_m$ hyperpolarisation, an effect that is lost in HUVECs chronically treated with BI-9774 (Figures 5.5 & 5.6). Hyperpolarisation of $\Delta\Psi_m$ is a hallmark of cells engaged in aerobic glycolysis such as ECs, although how AMPK exerts this effect remains to be determined [413, 414]. One theory is that AMPK may activate the pyruvate

dehydrogenase (PDH) complex, a mitochondrial enzymatic complex that shunts pyruvate derived from glycolysis towards the TCA cycle for oxidation. Several studies in cancer-derived cell lines demonstrate that PDH activation promotes $\Delta\Psi_m$ hyperpolarisation [413, 415]. AMPK was shown phosphorylate the catalytic subunit of PDH on residues of S295/S314 thus enhancing its activity in order to promote cancer cell survival under conditions of metabolic stress.

5.4.2 AMPK and angiogenesis

AMPK is critical in the angiogenic response, demonstrated in studies showing its necessity for (i) VEGF/VEGFR signalling; (ii) revascularisation following ischaemic injury; and (iii) prevention of age-related capillary rarefaction [178, 183, 203, 204]. Treatment with BI-9774 resulted in a significant reduction of proliferating ECs as shown by EdU incorporation (Figure 5.7) and in the proportion of HUVECs in the G2/M phase (Figure 5.8). Regardless low proliferation rates in BI-9774 treated HUVECs, they were successfully able to form tubular structures in Matrigel comparable to untreated or VEGF-A_{165}-treated HUVECs. These findings also corroborate the IPA analysis where despite significant deactivation of proliferation and cell cycle related pathways, angiogenesis is upregulated, which may explain that BI-9774-treated HUVECs are able to form tubes despite being subjected to growth arrest (Figure 4.6). Global AMPK activation also modestly increased branchpoints in the neonatal retina *in vivo,* indicative of increased systemic angiogenesis (Figure 5.11).

Compound C has been used historically to pharmacologically inhibit AMPK, but it has numerous off-target effects, including suppressing *VEGFA* expression. An advantage of this study is that BAY-3827 was used instead of compound C as it is a potent inhibitor of AMPK with higher selectivity compared to its predecessor [416]. BAY-3827-mediated inhibition of AMPK severely impairs tube formation *in vitro*, with HUVECs failing to invade the Matrigel. Cotreatment with VEGF-A_{165} also failed to restore their ability to form tubes. The results from the Matrigel assay imply that AMPK activation is essential for the VEGF-mediated angiogenesis under normoxic conditions. Additional studies to examine AMPK inhibition using siRNA knockdown against *PRKAA1*/*PRKAA2* is required to rule out any off-target effects of BAY-3827.

There are several drawbacks in relying on Matrigel for analysis of angiogenesis *in vitro*, particularly emphasising the assays limitations in sensitivity. Matrigel-based assays can effectively distinguish tube formation under inhibitory conditions but fails to capture subtle changes under pro-angiogenic conditions [324]. HUVECs also have the tendency to form

tubes even under harsh culturing conditions (e.g. in the absence of serum and growth factors) [417]. This may explain as to why no differences were seen between untreated, BI-9774 and VEGF-A_{165} treated HUVECs. An alternative model would be to use the fibrin bead assay, where HUVEC coated beads are resuspended in a fibrin gel and co-cultured with stromal cells (e.g. fibroblasts). The fibrin bead assay creates a 3D culturing system that closely mimics angiogenesis *in vivo* and is a far more superior method in differentiating angiogenic responses. I plan on performing the fibrin bead assay in the future to investigate the effect of BI-9774 in angiogenesis. To study angiogenic responses in the adult mice, it would be useful to examine the vasculature of the ear by tissue staining followed by an *in vivo* Matrigel plug assay for quantitative evaluation of angiogenesis in response to growth factors in the EC-γ_1WT-Tg and EC-γ_1D316A-Tg mice as a cross comparison for the BI-9774 studies *in vitro*.

The ECs that participate in the angiogenic response are a mixed population of both growth-arrested and proliferative cells (Section 1.6.1 Sprouting Angiogenesis). Tube formation primarily relies on cell migration and ECM remodelling. The increased number of extensions and stress fibre formation observed in HUVECs treated with BI-9774 in Figure 5.9 suggest that they have adopted a migratory phenotype. To establish whether AMPK activation enhances cell migration, it would be interesting to assess pathways implicated in regulating cell motility (e.g., FAK signalling), migration assays using timelapse imaging (e.g. scratch-wound and chemotaxis assays) and expression of tip versus stalk cells *in vitro*.

There are two major caveats of the data presented in this chapter such as the lack of: (i) mechanistic studies between endothelial metabolism and function (ii) hypoxia studies conducted in parallel for some of the experiments due to logistical issues and limited time availability. The findings from previous chapters heavily implicates sprouting, angiogenesis and migration based on gene expression changes common to both AMPK and hypoxia signalling. Given that hypoxia is a major stimulus in driving metabolic reprogramming, migration and angiogenesis, future work will aim to repeat these studies under hypoxia (3% O_2) and include glucose deprivation to activate AMPK physiologically.

5.4.3 Endothelial AMPK and regulation of energy homeostasis in vivo

The benefits of AMPK activation on whole-body energy balance are well documented in the muscle, liver, and adipose tissue, using both pharmacological and genetic approaches by our group and others. Improved microvascular perfusion and enhanced cardiac capillarisation was noted in some of these studies, however, they failed to consider the potential contribution role

of the endothelium in alleviating age-associated metabolic decline. As mentioned in Section 1.7.4 AMPK in the Endothelium and the Vasculature, the metabolic effects of endothelial AMPK have primarily relied on global KO models, in contrast to the work presented in this chapter, which utilises novel endothelial-specific expression of constitutive AMPK activation by a mutation in the γ_1 subunit.

The preliminary data suggests that EC-specific AMPK activation may exert profound effects on whole-body energy balance, at least in male mice. EC-γ_1D316A-Tg males are leaner than their EC-γ_1WT-Tg counterparts on chow (Figure 5.12) and exhibit remarkable resistance to HFD-induced weight gain (Figure 5.13) similar to that observed in the β-actin-Cre (global) model [394, 395]. Unlike the global activating model, there appears to be no effect on basal metabolic rate at the end of the study as shown by RER (Figure 5.14) and energy expenditure measurements (Figure 5.15). It should be noted that there appears to be minimal elevation in heat production in the EC-γ_1D316A-Tg males (Figure 5.14B), but a larger cohort will be required to delineate any putative differences. There was no effect on visceral adiposity based on the weights of adipose depots which revealed no discernible change in the gWAT mass (Figure 5.16B). A decrease in BAT mass was noted in the EC-γ_1D316A-Tg males but given the great deal of variation in the EC-γ_1WT-Tg cohort, it was difficult to draw a conclusion. There was a marked reduction in the mass of the iWAT (Figure 5.16C), signifying that EC-specific AMPK activation may regulate subcutaneous adiposity. It would be useful to incorporate further characterisation of the gWAT and BAT in future studies to provide a comparison for the change observed in the iWAT. Despite the decrease in iWAT mass, there was no obvious change in adipocyte size and locularity in the EC-γ_1D316A-Tg compared to EC-γ_1WT-Tg mice (Figure 5.18), although further validation using more quantitative customised macros and scripts in QuPath or FIJI is required to fully validate this conclusion.

Based on the global D316A-Tg model, our group previously hypothesised that the increased vascularisation of the iWAT serves as a stem cell niche for the SMART cell progenitor responsible for the skeletal muscle-like phenotype of the adipose [395]. Despite the reduced mass of the iWAT, no visual changes in adipocyte morphology were observed in the EC-γ_1D316A-Tg depot (Figure 5.18) [395]. As previously mentioned, the EC-γ_1D316A-Tg adipose morphology appears to be indistinguishable from the ECγ_1WT-Tg depot (Figure 5.18). Further validation is required such as measuring mRNA or protein expression of SERCA1 and visualisation of mitochondrial content changes by immunohistochemistry to completely rule out lack of the SMART cell phenotype. If the EC-γ_1D316A-Tg iWAT fails to show differences in terms of SERCA1 expression, myogenic markers, and mitochondrial content, then it is likely

that the SMART cell progenitors may arise from a Tie2/CD202B$^-$ population, potentially due to resident stem cells within the adipose as opposed to the vascular wall.

The liver serves as the primary site for lipid processing, especially in cholesterol and triglyceride metabolism. Accumulation of lipids can occur through increased hepatic *de novo* lipogenesis or absorption of lipids from the plasma (e.g. dietary lipids or adipose lipolysis). Elimination of lipids occur through clearance processes including hepatic lipolysis, lipophagy, secretion of very low-density lipoproteins along with mitochondrial and peroxisomal FAO. Despite AMPK's significant role in lipid metabolism, constitutive liver-specific (Albumin-Cre) AMPK activation only protected against high fructose diet (60% fructose, 10% kJ, HFrD)-induced hepatic steatosis but not against HFD-induced steatosis [394]. In contrast, the EC-γ_1D316A-Tg mice exhibit remarkable resistance against HFD-induced steatosis, with marked reduction of liver mass, hepatic lipid accumulation and reduction in ballooning degeneration (Figure 5.16-5.20), which suggests that the endothelium significantly contributes to hepatocyte function and metabolism.

The liver is a highly vascularised organ, receiving approximately 25% of the cardiac output at rest. The metabolic functions of hepatocyte are supported by the sinusoidal microcirculation, lined by LSECs. These specialised ECs are endowed with numerous fenestrae that permit passage of plasma proteins and lipoproteins into the subendothelial space of Disse [418]. LSECs display high endocytic activity, harbouring an extensive range of scavenging receptors, including Fc fragment of IgG receptor IIb (FcγRIIb2), mannose receptors and stabilins. The cooperative actions of these endocytic receptors facilitate trafficking of lipids and lipoproteins between the blood and liver parenchyma [419]. Very little is currently known about LSEC metabolism and the effects they exert on hepatocyte metabolism. Possible roles of LSECs in metabolic phenotype has been inferred from scRNA-seq data, as LSECs lose their characteristic features within a few days in culture thereby limiting metabolic characterisation. RNA-sequencing analysis in Chapter 4 revealed enrichment in general lipid metabolic process and cholesterol metabolism upon treatment with BI-9774. Therefore, examining markers of lipid and cholesterol metabolism is LSECs and whether genetic AMPK activation in the endothelium may alter LSEC lipid processing and scavenging functions warrants further investigation.

Dysregulation of hepatic lipid metabolism precedes the development of steatosis, arising out of an imbalance between liver *de novo* lipogenesis and lipid absorption and clearance processes. Abnormal liver and plasma triglycerides, non-esterified fatty acids (NEFAs) and ketone bodies have been reported both in NAFLD mouse models and patients, with a

causative link existing between altered plasma metabolite profile and patient mortality [420-424]. Therefore, it is crucial to include hepatic and plasma metabolites profiling in future studies in both chow- and HFD-fed mice. Alterations in mitochondrial dysfunction and bioenergetics are also heavily implicated in the pathogenesis of steatosis. Mitochondrial function can be achieved through combined TMRM and MitoTracker Green staining on isolated LSECs and hepatocytes by FACS. Assessing changes in mitochondrial OXPHOS will rely on using high-resolution respirometry on chow- and HFD-fed liver explants. Future work on $CD146^+$ selected LSECs will assess changes in expression of genes involved in lipid metabolism and processing [425]. From a technical standpoint, the study also lacked quantitative analysis on lipid accumulation. H&E staining, although useful for qualitative purposes, is limited in quantifying the number and size of lipid droplets (Figure 5.19). I attempted quantification of the 'gaps' by QuPath, however, image analysis was not reliable due to (i) increased false positives arising from tissue artefacts; and (ii) failure to distinguish between macrovesicular and microvesicular steatosis (Figure 5.19 & 5.20). Future studies will incorporate Oil Red O and/or BODIPY stains for visualisation and quantification of lipid droplets on frozen tissue sections by microscopy imaging. Quantification of hepatic and plasma lipid content will be achieved either by direct biochemical methods and/or mass-spectrometry lipidomic approaches.

There are several limitations of preliminary *in vivo* data: (i) lack of statistical power; (ii) no comprehensive metabolic phenotyping throughout the HFD study; and (iii) absence of vascular phenotyping. The pilot study was heavily underpowered and therefore the results should be interpreted cautiously, particularly those pertaining to CLAMS metabolic *in vivo* phenotyping, hence a larger sample size must be employed in future cohorts to see if the observations are reproducible, and whether any significant differences in whole body energy metabolism will arise. Whole body composition analysis using EchoMRI was not used to determine whether the reduction in fat mass is responsible for the reduced weight gain observed in males. EchoMRI will be utilised in future cohorts to differentiate between fat and lean mass of mice pre- and post-HFD, so paired analysis can be performed for each individual mouse followed by CLAMs monitoring to observe changes in substrate utilisation over time.

Regardless of genotype, the female mice showed no changes in body weight in response to HFD, with body weight changes following a similar pattern in C57BL/6J mice on chow according to data derived by JAX (Figure 5.21). The confounding result may have been due to issues that arose during the study. I noticed increased barbering in females, which resulted in mice being culled. Alternatively, it could be due to an aversion to HFD or some other cohort-specific phenomenon. Close monitoring of abnormal behaviours, followed by separation if

necessary and food intake (e.g. BioDAQ cages) will be considered if the issues arise again in future cohorts.

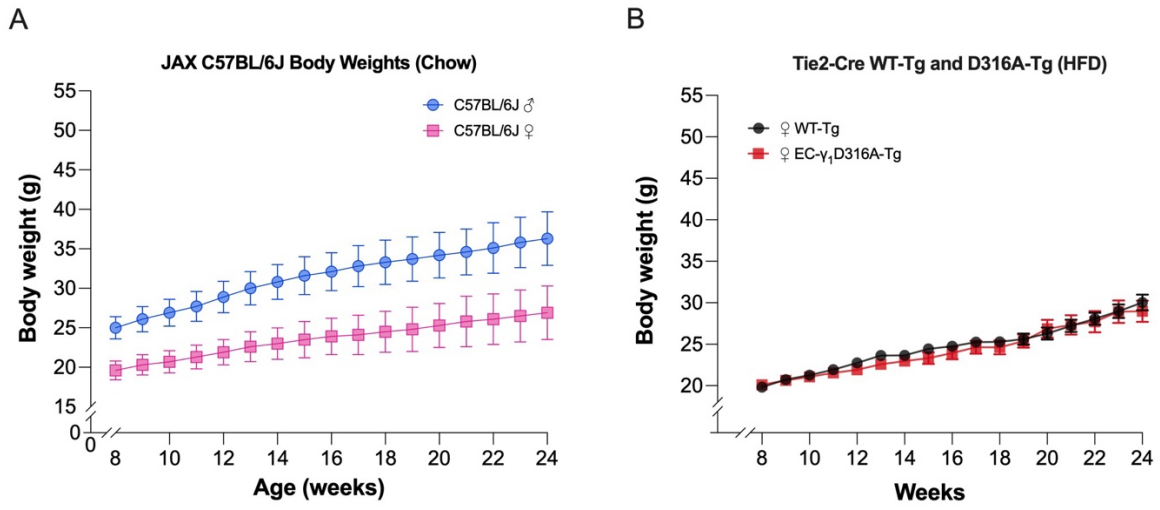


Figure 5.21 *– Comparison of body weights for the C57BL/6J strain on chow versus Tie2-Cre ECγ1WT-Tg and D316A-Tg females on HFD.*

(A) A figure of recorded weight body weight changes for males (♂, blue circle) and females (♀, pink square) on a chow diet. Data is represented as mean ± SEM (n = 40 per sex). Graph adapted from Jackson Laboratory (JAX.org).
(B) Tie2-Cre female mice on HFD for 16-weeks.

Unfortunately, examination of vascular morphology by immunohistochemical staining using endothelial markers [e.g., PECAM-1 (CD31)] was not performed. Immunohistochemical staining would have provided useful information on microvascular density, endothelial proliferation (e.g. EdU labelling *in vivo* or Ki67 staining) and angiogenic markers derived from RNA-seq in Section 4.3.1 The effect of BI-9774 and/or hypoxia on the endothelial transcriptome. However, IHC provides limited information on vessel architecture throughout the tissue, especially those exhibiting zonality like the liver. The use of novel tissue clearing methods [e.g. **i**mmunolabeling-enabled three-**d**imensional **i**maging of **s**olvent-**c**leared **o**rgans, (iDISCO)] will be employed in the future to examine the vasculature in whole tissues and organs.

The Tie2-Cre is the most commonly used for constitutive EC-specific expression in mice, however a limitation is the model's predisposition to non-specific Cre recombinase activity in haematopoietic stem cells (HSCs) [426, 427]. The γ_1 transgenes harbour a C-terminal FLAG-tag therefore it would be useful to examine FLAG expression in FACS-sorted ECs ($CD31^+CD45^-$), monocytes ($CD45^+$) and HSCs [stem cell antigen-1 (Sca-1)] to see if there's ectopic expression in immune cells and HSCs. Employing an endothelial-specific tamoxifen-inducible model (e.g. VE-Cadherin-Cre^{ERT2}) would also confirm if the metabolic benefits can

be recapitulated in the adult endothelium, effectively ruling out non-EC-specific effects. Another caveat is that I was not able to perform hypoxia studies to support the *in vitro* work in this project. There was no *in vivo* hypoxic chamber to house mice available in the animal facility and the project license also lacked the appropriate protocols to allow me to conduct such studies. Therefore, follow up studies are required to thoroughly characterise the effects of hypoxia on the metabolic and vascular phenotype in the global and endothelial γ_1D316A-Tg mice.

Overall, the findings of this chapter show that AMPK activation with BI-9774 has no effect on mitochondrial respiration under 21% O_2 but does reduce basal respiration and mitochondria respiration under 3% O_2. Acute BI-9774 treatment appeared to modestly reduce mitochondrial content whilst promoting mitochondrial hyperpolarisation, whereas chronic treatment with BI-9774 significantly increased mitochondrial copy number with no effect on $\Delta\Psi_m$. Despite BI-9774 reducing EC proliferation, it is necessary for VEGF-A_{165}-dependent tube formation in vitro. An increase in vascularisation was observed in the global gain-of-function AMPK (γ_1D316A-Tg) model, however this phenotype was no investigated in the EC-specific model. Male EC-γ_1D316A-Tg mice were protected from HFD-induced weight gain and hepatic steatosis, in similar vein to the global γ_1D316A-Tg mice. The effects of AMPK activation on endothelial metabolism *in vivo*, and its potential role in endothelial-organ metabolic crosstalk were unfortunately not examined. The findings only partially address the hypothesis outlined in 5.2 Hypothesis and Aims, therefore further work is required to examine if the metabolic findings *in vitro* are recapitulated *in vivo*.

6. Summary and Perspectives

The prevalence of cardiometabolic diseases, an umbrella term for a cluster of conditions that include hypertension, diabetes, NAFLD, cardiovascular disease (CVD) and stroke, has increased as a consequence of the global obesity pandemic [137, 428-430]. The characteristics shared by these conditions include insulin resistance, dyslipidaemia, endothelial dysfunction, systemic inflammation, hypertension and visceral adiposity [137]. Cardiometabolic complications are now the leading causes of morbidity and mortality worldwide, posing a significant burden on quality of life and healthcare systems. Despite significant strides in elucidating how cardiometabolic diseases develop, there is a complex interplay genetic, environmental, and lifestyle factors that influence the development of these diseases. Maladaptive hypoxia responses and dysregulation of AMPK/HIFα signalling have emerged as contributing factors in the development of cardiometabolic diseases.

6.1 The role of AMPK in the hypoxia response

The conservation of cellular ATP is critical for cells facing a fall in O_2 in order to increase their chances of survival. Indeed, AMPK is activated in cardiomyocytes, alveolar epithelial cells and fibroblasts [118, 336, 431]. The findings in Chapter 3 – Regulation of AMPK under hypoxia show that there appears to be either no significant change in AMPK activity or even in some cases, AMPK appears to be rapidly dephosphorylated and deactivated in response to hypoxia. Therefore, it can be inferred that AMPK does not participate in the hypoxia response in ECs, challenging the current paradigm that hypoxia is able to canonically induce AMPK activation. Inhibition of the prolyl hydroxylases also does not appear to impact AMPKα^{T172} phosphorylation status, but further characterisation using *in vitro* kinase assays or longer treatment time points maybe required to validate these findings. As mentioned previously, the differences in the AMPK response could be due to the metabolic dependencies of a given cell type. Therefore, it would be interesting to explore whether AMPK is differentially regulated by hypoxia in either OXPHOS-dependent cell types (e.g. cardiomyocytes) or perivascular cells (e.g. VSMCs) under hypoxia.

The work presented in Chapter 3 lacks *in vivo* studies to examine whether AMPK deactivation occurs. Data from high altitude studies and *in vivo* hypoxia data have revealed results that are inconsistent with the *in vitro* observations presented in this thesis. Several studies have shown elevated AMPKα^{T172} phosphorylation in the placenta of women who resided at moderate (1,700 m) and high altitudes (2,500 m), although total AMPKα was lower in high-altitude residents [432]. AMPK-dependent vasodilation upon treatment with A769662 was increased

in myometrial arteries from high-altitude residents. ACh-dependent vasodilation was blunted myometrial arteries derived from intrauterine growth restriction (IUGR) pregnancies [433] compared to the appropriate for gestational age (AGA) cohort regardless of altitude. Basal AMPK activity was not measured in both appropriate for gestational age (AGA) and IUGR pregnancies [433]. Another study by Skeffington *et al.* (2016) showed increased mRNA expression of LKB1, AMPKα_1 and AMPKα_2 in human placentas at high altitude (3,100 m). Treatment with A769662 greatly reduced phenylephrine-induced vasoconstriction in uterine arteries from hypoxic (10% O_2) pregnant mice by NO-dependent and -independent mechanisms [434]. Collectively, these studies reveal AMPK activation under conditions of high altitude (i.e. hypobaric hypoxia) is important for vasodilatory adaptational responses and subsequent protection against IUGR. Additional *in vivo* work is required to assess the changes basal AMPK activity and its consequence on vasoreactivity in response to hypoxia.

6.2 AMPK and HIFα signalling crosstalk and potential physiological relevance

There have only been a handful of studies either reporting AMPK and HIFα crosstalk or AMPK-mediated regulation of HIFα either under conditions of metabolic stress in cancer or ischaemia *in vivo*. The data in Chapter 4 shows that (i) AMPK is capable of phosphorylating HIF-1α in a cell free system *in vitro* and (ii) AMPK activation enhances HRE-dependent gene transcription and promotes HIF-1α gene signature as shown by RNA-sequencing. The next obvious step to build upon these findings is to identify and validate the functional relevance of the AMPK phospho-sites on HIF-1α if they exist. If hypothetically AMPK phospho-sites do exist within HIF-1α, then generation of phospho-site specific antibodies is required. The study was particularly challenging as there are no available phospho-antibodies against HIF-1α or HIF-2α. It would be useful if the HIFα isoforms were overexpressed in HUVECs, immunoprecipitated and subsequently probed with phospho-AMPK substrate motif [LXRXX(pS/pT)] antibody. In the event that AMPK phosphorylation sites are identified, generation of phospho-antibodies will be required for downstream validation in primary cells or *in vivo* following BI-9774 administration. As mentioned in the introduction, endothelial cells express both HIF-1α and HIF-2α *in vivo*, Another question that remains to be addressed is whether AMPK could phosphorylate HIF-2α was not addressed. If AMPK-mediated phosphorylation does indeed occur in both isoforms, does phosphorylation have differential effects on individual HIFα isoforms?

Variants in AMPK and HIFα signalling components have been detected in native high-altitude populations of the Himalayas and the Andes. The Himalayans, Andeans and Ethiopians

exhibit distinct cardiorespiratory, vascular, metabolic and haematological adaptations, enabling them to thrive in the low O_2 environments at high altitude. The adaptations include increases in haematocrit, plasma NO, arterial O_2 and tissue capillarisation [435-439]. As revealed by RNA-seq analysis, both AMPK and HIF regulate anaerobic metabolism, NO production and proangiogenic signalling pathways (Chapter 4). Genomic analysis revealed selection of both *HIF1A* and *EPAS1* in the Himalayas, with the variants of the latter being highly enriched in Tibetans and Sherpas. Positive selection for variants in genes encoding PHD isoforms (*EGLN1*/*EGLN2*) and AMPKα subunits (*PRKAA1*/*PRKAA2*) have been reported in the Andean populations, suggesting that alterations in AMPK activity could confer beneficial effects at high altitude, perhaps by reducing high-altitude-induced IUGR as discussed above [440]. Further work is required to examine whether the global and endothelial γ_1D316A-Tg model have any differences in their cardiorespiratory, vascular, metabolic and haematological parameters under normoxia and hypoxia. It would also be interesting to see if HIF-1α and HIF-2α temporal signalling is altered by chronic AMPK activation.

Despite the enrichment in HIF-1α signalling following BI-9774 treatment in the RNA-seq data, it is important to consider whether AMPK alters the transcriptional coregulators that interact with HIF-1α to promote a specific response. Further analysis is required by identifying HIF-1α gene targets in available datasets examining whether BI-9774 treatment alters the canonical HIFα transcriptional patterns under hypoxia. As AMPK activation produces a distinct transcriptomic signature different from hypoxia signalling (Chapter 4), it raises a number of questions. Does AMPK activation impact which chromatin remodellers HIFα interacts with? Does this alter which HIF-dependent genes are transcribed? Although this lied beyond the scope of this thesis, it would be informative to perform RIME (**r**apid **i**mmunoprecipitation **m**ass spectrometry of **e**ndogenous proteins), a technique to identify transcriptional co-factors and chromatin associated proteins of HIFα isoforms following hypoxia and BI-9774 treatment.

Epidemiological studies have reported reduced prevalence of diabetes, obesity, CVD and stroke amongst high-altitude residents across multiple continents, even after accounting for classical cardiovascular risk factors [441-446]. On the other hand, low-altitude residents with a history of CVD are at risk of complications due to the low O_2, increased myocardial demand and altered haemodynamics that occur at high altitudes. The vascular adaptations exhibited by native residents at high-altitudes (e.g., increased NO production and muscle capillarisation), is thought to confer a cardiovascular preconditioning effect, similar to that of ischaemic preconditioning (RIPC) [447-450]. Despite the logistical issues in acquiring tissue samples from these populations, it would be useful to assess if differences exist between AMPK activity and HIFα in comparison with their low-altitude counterparts.

Ischemia is a condition characterised by vessel occlusion resulting in reduced oxygen O2 and nutrient deprivation in the affected tissues or organs. Atherosclerosis, embolism, thrombosis, vasoconstriction and systemic inflammation are significant contributors to development of ischemia [451-454]. Treatment options include anticoagulant therapy, thrombolysis/embolectomy and surgical revascularisation depending on the cause and severity of the occlusion [455]. Following an ischaemic event, normalisation of O_2 perfusion is primarily initiated by transient changes in vascular tone to promote angiogenesis and the formation of collateral vessels. Multiple studies have shown an association between the presence of collateral vessels and improved outcome following an ischaemic event [456, 457]. It is no surprise that the therapeutic angiogenesis or arteriogenesis is being extensively studied as a treatment option for patients who are not suited for surgical revascularization options, such as percutaneous coronary interventions (PCI) or coronary artery bypass grafting (CABG) [458, 459].

Therapeutic activation of AMPK and HIFα signalling has been discussed in the context of ischaemic and/or inflammatory diseases elsewhere [374, 376]. RNA-seq analysis has shown that genes common to both hypoxia and BI-9774 are positively associated with both angiogenesis and ischaemic diseases (Chapter 4). Functional data in Chapter 5 demonstrate that genetic activation of AMPK increases vessel density in the mouse retina whereas pharmacological inhibition of AMPK abolishes HUVEC tube formation *in vitro*. A limitation is that I did not examine whether AMPK is required for Matrigel tube formation under hypoxic conditions, something I will aim to address as part of future work.

DEGs common to both hypoxia and BI-9774 treatment are implicated in arterial development; therefore, it is tempting to speculate whether AMPK and HIF-1α could alter endothelial identity (Chapter 4). Hypoxia promotes an arterial phenotype in a HIF-1α-dependent manner through induction of DLL4/NOTCH signalling and the NOTCH target transcription factors: hairy/enhancer-of-split related with YRPW motif protein 1 and 2 (HEY1 and HEY2, respectively) in isolated mouse embryonic mesodermal stem cells [460]. Emerging evidence has revealed that tip cells and arterial specification maybe interconnected, as tip cells and arterial cells show similar transcriptional profiles at the single cell RNA-seq (scRNA-seq) [461]. Multiple lineage tracing studies also revealed that combination of activation of NOTCH signalling and cell cycle arrest in tip cells directs them towards developing arteries [462-465]. In the study by Abdel Malik *et al.* (2017), collateral artery formation was impaired in myeloid-specific AMPKα_2^{KO} mice, providing evidence of AMPK involvement in arteriogenesis [178]. Regardless, whether AMPK activation promotes the transcriptional responses during arterial

fate specification and whether these downstream changes require HIFα has not been examined thus far. Therefore, in-depth characterisation of the vasculature by staining of arteries, veins and lymphatics in tissues from global and endothelial γ_1D316A-Tg models will be necessary.

The work presented in Chapter 5 primarily examined AMPK's role in metabolism and angiogenesis, however it is evident from RNA-seq analysis that AMPK could participate in multiple endothelial processes including regulation of the inflammatory response and thrombosis. To assess whether O_2 tension and BI-9774 alters the inflammatory and thrombotic response of ECs, I will perform further experiments to examine inflammation (e.g. leukocyte adhesion assays) and thrombosis (e.g., thrombin generation assays) following stimulation with pro-inflammatory cytokines. This will provide a better insight into other non-metabolic functions of AMPK in the endothelium and whether BI-9774 could hypothetically treat vascular disorders.

6.3 The metabolic effects of endothelial AMPK

Regulation of whole-body energy metabolism is orchestrated by actions of multiple organs, including the liver, adipose tissue, brain, the gastrointestinal tract, pancreas and muscle. These highly metabolically active tissues and organs are extensively vascularised, resulting in resident ECs within each organ-specific niche tailoring their metabolism to support tissue/organ function. There is now growing appreciation that development of endothelial dysfunction also follows organ-specific metabolic characteristics depending on the disease [466]. These studies underscore the pivotal role that ECs play in regulating systemic energy balance, but the underlying role of endothelial AMPK was never examined. The results presented in this thesis reveal that endothelial activation of AMPK confers resistance against DIO and reduces scWAT fat accumulation. Despite the reduction in the mass of the scWAT, there was no difference in adipocyte size and locularity. The EC-γ_1D316A-Tg model also exhibited remarkable resistance to hepatic steatosis, in contrast to the lack of protection provided by the liver-specific γ_1D316A-Tg model (Chapter 5) [394].

Altered O_2 partial pressures (pO_2) has been observed in tissues from obese patients, who exhibited a reduction in pO_2 in the scWAT depot with a greater reduction observed in insulin-resistant individuals [467, 468]. Goossens and colleagues found that O_2 tension is higher in the WAT of obese individuals, due to impaired expression of adipocyte mitochondrial genes and density lead to low O_2 consumption and increased pO_2 in scWAT [469]. The phenotype is

accompanied by impaired WAT angiogenesis, insulin resistance and increase in pro-inflammatory markers. The authors postulated that obesity-induced scWAT hyperoxia establishes an anti-angiogenic microenvironment which suppresses the hypoxic response and VEGF release. Weight stabilisation after diet-induced weight loss decreased pO_2 in the scWAT of obese individuals and restoring the pro-angiogenic environment, corroborating the observations of previous studies [470, 471]. Interestingly, it appears that the HIFα signalling exerts differential effects in adipose tissue depending on the HIFα isoform and the depot. HIF-1α is pro-angiogenic but can trigger glucose intolerance and mitochondrial uncoupling in adipocytes. Moreover, adipocyte HIF-1α promoted adipose inflammation and fibrosis, whereas adipocyte HIF-2α reduced inflammation and insulin resistance [472].

Variations in O_2 tensions regulates metabolic zonality in the liver, therefore maintenance of the O_2 gradient is critical for the diverse functions of the liver [473]. In NAFLD, increased liver fibrosis and/or intermittent hypoxia as a result of obstructive sleep apnoea (OSA) can exacerbate hepatic steatosis [474]. Although, there is robust experimental data showing that hypoxia promotes lipid accumulation in mouse livers and human hepatocytes, the precise role of HIFα isoforms has not been clarified [475, 476]. Differential effects of HIFα isoforms have also been reported with HIF-1α preventing lipid accumulation [477, 478]. HIF-2α appears to be a major driver in hepatic steatosis by increasing expression of fatty acid translocases [e.g. CD36, adipose differentiation-related protein (ADRP)] increasing hepatocyte lipid uptake [479, 480]. Stabilisation of HIF-2α also led to peroxisome proliferator-activated receptor α (PPARα)-mediated suppression of hepatic FAO [479]. Oxygen supplementation significantly improved hepatic steatosis, decreasing HIF-2α stability and lipogenic genes [481]. In future EC-γ_1WT-Tg and γ_1D316A-Tg HFD cohort studies, immunohistochemistry and immunofluorescence staining will be employed to stain for HIF-1α and HIF-2α. in both the adipose and liver along with the associated vasculature. This will determine if HFD and/or AMPK activation alters HIFα stabilisation in these tissues and may underlie the endothelial-mediated DIO-resistant phenotype that I observed in the EC-γ_1D316A-Tg mice (Chapter 5).

7. Bibliography

1. Fleming, I., B.R. Kwak, and M.J. Meens, *The endothelial cell*, in *The ESC Textbook of Vascular Biology*, R. Krams and M. Bäck, Editors. 2017, Oxford University Press. p. 0.
2. Furchgott, R.F. and J.V. Zawadzki, *The obligatory role of endothelial cells in the relaxation of arterial smooth muscle by acetylcholine.* Nature, 1980. **288**(5789): p. 373-6.
3. Dejana, E., K.K. Hirschi, and M. Simons, *The molecular basis of endothelial cell plasticity.* Nat Commun, 2017. **8**: p. 14361.
4. Yamamizu, K., et al., *Convergence of Notch and beta-catenin signaling induces arterial fate in vascular progenitors.* J Cell Biol, 2010. **189**(2): p. 325-38.
5. Wilkinson, R.N., et al., *Hedgehog signaling via a calcitonin receptor-like receptor can induce arterial differentiation independently of VEGF signaling in zebrafish.* Blood, 2012. **120**(2): p. 477-88.
6. Williams, C., et al., *Hedgehog signaling induces arterial endothelial cell formation by repressing venous cell fate.* Dev Biol, 2010. **341**(1): p. 196-204.
7. You, L.R., et al., *Suppression of Notch signalling by the COUP-TFII transcription factor regulates vein identity.* Nature, 2005. **435**(7038): p. 98-104.
8. Yamazaki, T., et al., *COUP-TFII regulates the functions of Prox1 in lymphatic endothelial cells through direct interaction.* Genes Cells, 2009. **14**(3): p. 425-34.
9. Srinivasan, R.S., et al., *The nuclear hormone receptor Coup-TFII is required for the initiation and early maintenance of Prox1 expression in lymphatic endothelial cells.* Genes Dev, 2010. **24**(7): p. 696-707.
10. Srinivasan, R.S., et al., *Lineage tracing demonstrates the venous origin of the mammalian lymphatic vasculature.* Genes Dev, 2007. **21**(19): p. 2422-32.
11. Aird, W.C., *Phenotypic heterogeneity of the endothelium: I. Structure, function, and mechanisms.* Circ Res, 2007. **100**(2): p. 158-73.
12. Hobson, B. and J. Denekamp, *Endothelial proliferation in tumours and normal tissues: continuous labelling studies.* Br J Cancer, 1984. **49**(4): p. 405-13.
13. Hennigs, J.K., et al., *Vascular Endothelial Cells: Heterogeneity and Targeting Approaches.* Cells, 2021. **10**(10).
14. Geraud, C., et al., *Unique cell type-specific junctional complexes in vascular endothelium of human and rat liver sinusoids.* PLoS One, 2012. **7**(4): p. e34206.
15. De Bock, K., et al., *Role of PFKFB3-driven glycolysis in vessel sprouting.* Cell, 2013. **154**(3): p. 651-63.
16. Helmlinger, G., et al., *Formation of endothelial cell networks.* Nature, 2000. **405**(6783): p. 139-41.
17. Coutelle, O., et al., *Embelin inhibits endothelial mitochondrial respiration and impairs neoangiogenesis during tumor growth and wound healing.* EMBO Mol Med, 2014. **6**(5): p. 624-39.
18. Diebold, L.P., et al., *Mitochondrial complex III is necessary for endothelial cell proliferation during angiogenesis.* Nat Metab, 2019. **1**(1): p. 158-171.
19. Schiffmann, L.M., et al., *Mitochondrial respiration controls neoangiogenesis during wound healing and tumour growth.* Nat Commun, 2020. **11**(1): p. 3653.
20. Ibrahim, A., et al., *Local Mitochondrial ATP Production Regulates Endothelial Fatty Acid Uptake and Transport.* Cell Metab, 2020. **32**(2): p. 309-319 e7.
21. Graupera, M. and M. Claret, *Endothelial Cells: New Players in Obesity and Related Metabolic Disorders.* Trends Endocrinol Metab, 2018. **29**(11): p. 781-794.
22. Schoors, S., et al., *Fatty acid carbon is essential for dNTP synthesis in endothelial cells.* Nature, 2015. **520**(7546): p. 192-197.

23. Wei, X., et al., *De novo lipogenesis maintains vascular homeostasis through endothelial nitric-oxide synthase (eNOS) palmitoylation.* J Biol Chem, 2011. **286**(4): p. 2933-45.
24. Krutzfeldt, A., et al., *Metabolism of exogenous substrates by coronary endothelial cells in culture.* J Mol Cell Cardiol, 1990. **22**(12): p. 1393-404.
25. Kalucka, J., et al., *Quiescent Endothelial Cells Upregulate Fatty Acid beta-Oxidation for Vasculoprotection via Redox Homeostasis.* Cell Metab, 2018. **28**(6): p. 881-894 e13.
26. Banecki, K. and K.A. Dora, *Endothelin-1 in Health and Disease.* Int J Mol Sci, 2023. **24**(14).
27. Sandoo, A., et al., *The endothelium and its role in regulating vascular tone.* Open Cardiovasc Med J, 2010. **4**: p. 302-12.
28. Feng, C., *Mechanism of Nitric Oxide Synthase Regulation: Electron Transfer and Interdomain Interactions.* Coord Chem Rev, 2012. **256**(3-4): p. 393-411.
29. Garcia, V. and W.C. Sessa, *Endothelial NOS: perspective and recent developments.* Br J Pharmacol, 2019. **176**(2): p. 189-196.
30. Nguyen, T.D., et al., *Endothelial Nitric Oxide Synthase (eNOS) S1176 phosphorylation status governs atherosclerotic lesion formation.* bioRxiv, 2023: p. 2022.01.13.476234.
31. Ballermann, B.J., et al., *Shear stress and the endothelium.* Kidney Int Suppl, 1998. **67**: p. S100-8.
32. Chatterjee, S. and A.B. Fisher, *Mechanotransduction in the endothelium: role of membrane proteins and reactive oxygen species in sensing, transduction, and transmission of the signal with altered blood flow.* Antioxid Redox Signal, 2014. **20**(6): p. 899-913.
33. Humphrey, J.D., E.R. Dufresne, and M.A. Schwartz, *Mechanotransduction and extracellular matrix homeostasis.* Nat Rev Mol Cell Biol, 2014. **15**(12): p. 802-12.
34. Tzima, E., et al., *A mechanosensory complex that mediates the endothelial cell response to fluid shear stress.* Nature, 2005. **437**(7057): p. 426-31.
35. Baeyens, N., et al., *Endothelial fluid shear stress sensing in vascular health and disease.* J Clin Invest, 2016. **126**(3): p. 821-8.
36. Nigro, P., J. Abe, and B.C. Berk, *Flow shear stress and atherosclerosis: a matter of site specificity.* Antioxid Redox Signal, 2011. **15**(5): p. 1405-14.
37. Schaper, W., *Collateral circulation: past and present.* Basic Res Cardiol, 2009. **104**(1): p. 5-21.
38. Heuslein, J.L., et al., *Mechanisms of Amplified Arteriogenesis in Collateral Artery Segments Exposed to Reversed Flow Direction.* Arterioscler Thromb Vasc Biol, 2015. **35**(11): p. 2354-65.
39. Schierling, W., et al., *Increased intravascular flow rate triggers cerebral arteriogenesis.* J Cereb Blood Flow Metab, 2009. **29**(4): p. 726-37.
40. Dolan, J.M., et al., *Endothelial cells express a unique transcriptional profile under very high wall shear stress known to induce expansive arterial remodeling.* Am J Physiol Cell Physiol, 2012. **302**(8): p. C1109-18.
41. Chiu, J.J. and S. Chien, *Effects of disturbed flow on vascular endothelium: pathophysiological basis and clinical perspectives.* Physiol Rev, 2011. **91**(1): p. 327-87.
42. Xiao, H., et al., *Sterol regulatory element binding protein 2 activation of NLRP3 inflammasome in endothelium mediates hemodynamic-induced atherosclerosis susceptibility.* Circulation, 2013. **128**(6): p. 632-42.
43. Yao, Y., A. Rabodzey, and C.F. Dewey, Jr., *Glycocalyx modulates the motility and proliferative response of vascular endothelium to fluid shear stress.* Am J Physiol Heart Circ Physiol, 2007. **293**(2): p. H1023-30.
44. Martelli, A., et al., *Spatio-temporal analysis of vascular endothelial growth factor expression and blood vessel remodelling in pig ovarian follicles during the periovulatory period.* J Mol Endocrinol, 2006. **36**(1): p. 107-19.

45. Mai, J., et al., *An evolving new paradigm: endothelial cells--conditional innate immune cells.* J Hematol Oncol, 2013. **6**: p. 61.
46. Amersfoort, J., G. Eelen, and P. Carmeliet, *Immunomodulation by endothelial cells - partnering up with the immune system?* Nat Rev Immunol, 2022. **22**(9): p. 576-588.
47. Kofler, S., T. Nickel, and M. Weis, *Role of cytokines in cardiovascular diseases: a focus on endothelial responses to inflammation.* Clin Sci (Lond), 2005. **108**(3): p. 205-13.
48. Shao, Y., et al., *Vascular Endothelial Cells and Innate Immunity.* Arterioscler Thromb Vasc Biol, 2020. **40**(6): p. e138-e152.
49. Gibot, S., et al., *Triggering Receptor Expressed on Myeloid Cells-1 Inhibitor Targeted to Endothelium Decreases Cell Activation.* Front Immunol, 2019. **10**: p. 2314.
50. Briscoe, D.M., R.S. Cotran, and J.S. Pober, *Effects of tumor necrosis factor, lipopolysaccharide, and IL-4 on the expression of vascular cell adhesion molecule-1 in vivo. Correlation with CD3+ T cell infiltration.* J Immunol, 1992. **149**(9): p. 2954-60.
51. Ley, K., et al., *Getting to the site of inflammation: the leukocyte adhesion cascade updated.* Nat Rev Immunol, 2007. **7**(9): p. 678-89.
52. Fauvarque, M.O. and M.J. Williams, *Drosophila cellular immunity: a story of migration and adhesion.* J Cell Sci, 2011. **124**(Pt 9): p. 1373-82.
53. Uhrig, A., et al., *Development and functional consequences of LPS tolerance in sinusoidal endothelial cells of the liver.* J Leukoc Biol, 2005. **77**(5): p. 626-33.
54. Elvevold, K., et al., *Liver sinusoidal endothelial cells depend on mannose receptor-mediated recruitment of lysosomal enzymes for normal degradation capacity.* Hepatology, 2008. **48**(6): p. 2007-15.
55. Yau, J.W., H. Teoh, and S. Verma, *Endothelial cell control of thrombosis.* BMC Cardiovasc Disord, 2015. **15**: p. 130.
56. Stark, K. and S. Massberg, *Interplay between inflammation and thrombosis in cardiovascular pathology.* Nat Rev Cardiol, 2021. **18**(9): p. 666-682.
57. Wang, M., et al., *Thrombotic Regulation From the Endothelial Cell Perspectives.* Arterioscler Thromb Vasc Biol, 2018. **38**(6): p. e90-e95.
58. Neubauer, K. and B. Zieger, *Endothelial cells and coagulation.* Cell Tissue Res, 2022. **387**(3): p. 391-398.
59. Eelen, G., et al., *Basic and Therapeutic Aspects of Angiogenesis Updated.* Circ Res, 2020. **127**(2): p. 310-329.
60. Potente, M., H. Gerhardt, and P. Carmeliet, *Basic and therapeutic aspects of angiogenesis.* Cell, 2011. **146**(6): p. 873-87.
61. Arroyo, A.G. and M.L. Iruela-Arispe, *Extracellular matrix, inflammation, and the angiogenic response.* Cardiovasc Res, 2010. **86**(2): p. 226-35.
62. Newby, A.C., *Metalloproteinase expression in monocytes and macrophages and its relationship to atherosclerotic plaque instability.* Arterioscler Thromb Vasc Biol, 2008. **28**(12): p. 2108-14.
63. Nyberg, P., L. Xie, and R. Kalluri, *Endogenous inhibitors of angiogenesis.* Cancer Res, 2005. **65**(10): p. 3967-79.
64. Ramjaun, A.R. and K. Hodivala-Dilke, *The role of cell adhesion pathways in angiogenesis.* Int J Biochem Cell Biol, 2009. **41**(3): p. 521-30.
65. Reynolds, A.R., et al., *Stimulation of tumor growth and angiogenesis by low concentrations of RGD-mimetic integrin inhibitors.* Nat Med, 2009. **15**(4): p. 392-400.
66. Davis, G.E., et al., *Regulation of tissue injury responses by the exposure of matricryptic sites within extracellular matrix molecules.* Am J Pathol, 2000. **156**(5): p. 1489-98.
67. Simons, M., E. Gordon, and L. Claesson-Welsh, *Mechanisms and regulation of endothelial VEGF receptor signalling.* Nat Rev Mol Cell Biol, 2016. **17**(10): p. 611-25.
68. Ribatti, D. and E. Crivellato, *"Sprouting angiogenesis", a reappraisal.* Dev Biol, 2012. **372**(2): p. 157-65.
69. Li, X., X. Sun, and P. Carmeliet, *Hallmarks of Endothelial Cell Metabolism in Health and Disease.* Cell Metab, 2019. **30**(3): p. 414-433.

70. Potente, M. and P. Carmeliet, *The Link Between Angiogenesis and Endothelial Metabolism.* Annu Rev Physiol, 2017. **79**: p. 43-66.
71. Yasuda, N., et al., *Tracing behavior of endothelial cells promotes vascular network formation.* Microvasc Res, 2016. **105**: p. 125-31.
72. Muhleder, S., et al., *Endothelial sprouting, proliferation, or senescence: tipping the balance from physiology to pathology.* Cell Mol Life Sci, 2021. **78**(4): p. 1329-1354.
73. Jakobsson, L., et al., *Endothelial cells dynamically compete for the tip cell position during angiogenic sprouting.* Nat Cell Biol, 2010. **12**(10): p. 943-53.
74. Bentley, K., et al., *Tipping the balance: robustness of tip cell selection, migration and fusion in angiogenesis.* PLoS Comput Biol, 2009. **5**(10): p. e1000549.
75. Adams, R.H. and A. Eichmann, *Axon guidance molecules in vascular patterning.* Cold Spring Harb Perspect Biol, 2010. **2**(5): p. a001875.
76. Larrivee, B., et al., *Activation of the UNC5B receptor by Netrin-1 inhibits sprouting angiogenesis.* Genes Dev, 2007. **21**(19): p. 2433-47.
77. Carmeliet, P. and M. Tessier-Lavigne, *Common mechanisms of nerve and blood vessel wiring.* Nature, 2005. **436**(7048): p. 193-200.
78. Kim, J., et al., *Semaphorin 3E-Plexin-D1 signaling regulates VEGF function in developmental angiogenesis via a feedback mechanism.* Genes Dev, 2011. **25**(13): p. 1399-411.
79. Torres-Vazquez, J., et al., *Semaphorin-plexin signaling guides patterning of the developing vasculature.* Dev Cell, 2004. **7**(1): p. 117-23.
80. Kania, A. and R. Klein, *Mechanisms of ephrin-Eph signalling in development, physiology and disease.* Nat Rev Mol Cell Biol, 2016. **17**(4): p. 240-56.
81. Lindskog, H., et al., *Molecular identification of venous progenitors in the dorsal aorta reveals an aortic origin for the cardinal vein in mammals.* Development, 2014. **141**(5): p. 1120-8.
82. Borggrefe, T. and F. Oswald, *The Notch signaling pathway: transcriptional regulation at Notch target genes.* Cell Mol Life Sci, 2009. **66**(10): p. 1631-46.
83. Fang, J.S., et al., *Shear-induced Notch-Cx37-p27 axis arrests endothelial cell cycle to enable arterial specification.* Nat Commun, 2017. **8**(1): p. 2149.
84. Polacheck, W.J., et al., *A non-canonical Notch complex regulates adherens junctions and vascular barrier function.* Nature, 2017. **552**(7684): p. 258-262.
85. Mack, J.J. and M.L. Iruela-Arispe, *NOTCH regulation of the endothelial cell phenotype.* Curr Opin Hematol, 2018. **25**(3): p. 212-218.
86. Caduff, J.H., L.C. Fischer, and P.H. Burri, *Scanning electron microscope study of the developing microvasculature in the postnatal rat lung.* Anat Rec, 1986. **216**(2): p. 154-64.
87. Du Cheyne, C., M. Smeets, and W. De Spiegelaere, *Techniques used to assess intussusceptive angiogenesis: A systematic review.* Dev Dyn, 2021. **250**(12): p. 1704-1716.
88. Mentzer, S.J. and M.A. Konerding, *Intussusceptive angiogenesis: expansion and remodeling of microvascular networks.* Angiogenesis, 2014. **17**(3): p. 499-509.
89. Lee, G.S., et al., *Blood flow shapes intravascular pillar geometry in the chick chorioallantoic membrane.* J Angiogenes Res, 2010. **2**: p. 11.
90. Korshunov, V.S.A., *Arteriogenesis and Collateral Formation*, in *PanVascular Medicine*, P. Lanzer, Editor. 2015, Springer Berlin Heidelberg: Berlin, Heidelberg. p. 167-189.
91. Red-Horse, K. and S. Das, *New Research Is Shining Light on How Collateral Arteries Form in the Heart: a Future Therapeutic Direction?* Curr Cardiol Rep, 2021. **23**(4): p. 30.
92. Heil, M., et al., *Arteriogenesis versus angiogenesis: similarities and differences.* J Cell Mol Med, 2006. **10**(1): p. 45-55.
93. Aghajanian, A., et al., *Decreased inspired oxygen stimulates de novo formation of coronary collaterals in adult heart.* J Mol Cell Cardiol, 2021. **150**: p. 1-11.

94. Takeda, Y., et al., *Macrophage skewing by Phd2 haplodeficiency prevents ischaemia by inducing arteriogenesis.* Nature, 2011. **479**(7371): p. 122-6.
95. Chen, Z., J. Rubin, and E. Tzima, *Role of PECAM-1 in arteriogenesis and specification of preexisting collaterals.* Circ Res, 2010. **107**(11): p. 1355-63.
96. Sweet, D.T., et al., *Endothelial Shc regulates arteriogenesis through dual control of arterial specification and inflammation via the notch and nuclear factor-kappa-light-chain-enhancer of activated B-cell pathways.* Circ Res, 2013. **113**(1): p. 32-39.
97. Meier, P., et al., *Beneficial effect of recruitable collaterals: a 10-year follow-up study in patients with stable coronary artery disease undergoing quantitative collateral measurements.* Circulation, 2007. **116**(9): p. 975-83.
98. Herzig, S. and R.J. Shaw, *AMPK: guardian of metabolism and mitochondrial homeostasis.* Nat Rev Mol Cell Biol, 2018. **19**(2): p. 121-135.
99. Carling, D., *AMPK signalling in health and disease.* Curr Opin Cell Biol, 2017. **45**: p. 31-37.
100. Steinberg, G.R. and D.G. Hardie, *New insights into activation and function of the AMPK.* Nat Rev Mol Cell Biol, 2023. **24**(4): p. 255-272.
101. Steinberg, G.R. and D. Carling, *AMP-activated protein kinase: the current landscape for drug development.* Nat Rev Drug Discov, 2019. **18**(7): p. 527-551.
102. Hardie, D.G., B.E. Schaffer, and A. Brunet, *AMPK: An Energy-Sensing Pathway with Multiple Inputs and Outputs.* Trends Cell Biol, 2016. **26**(3): p. 190-201.
103. Polge, C. and M. Thomas, *SNF1/AMPK/SnRK1 kinases, global regulators at the heart of energy control?* Trends Plant Sci, 2007. **12**(1): p. 20-8.
104. Roustan, V., et al., *An evolutionary perspective of AMPK-TOR signaling in the three domains of life.* J Exp Bot, 2016. **67**(13): p. 3897-907.
105. Gomez-Garcia, I., I. Oyenarte, and L.A. Martinez-Cruz, *The crystal structure of protein MJ1225 from Methanocaldococcus jannaschii shows strong conservation of key structural features seen in the eukaryal gamma-AMPK.* J Mol Biol, 2010. **399**(1): p. 53-70.
106. Mullen, P.J., et al., *The interplay between cell signalling and the mevalonate pathway in cancer.* Nat Rev Cancer, 2016. **16**(11): p. 718-731.
107. Carling, D., V.A. Zammit, and D.G. Hardie, *A common bicyclic protein kinase cascade inactivates the regulatory enzymes of fatty acid and cholesterol biosynthesis.* FEBS Lett, 1987. **223**(2): p. 217-22.
108. Fullerton, M.D., et al., *Single phosphorylation sites in Acc1 and Acc2 regulate lipid homeostasis and the insulin-sensitizing effects of metformin.* Nat Med, 2013. **19**(12): p. 1649-54.
109. Momken, I., et al., *A new leptin-mediated mechanism for stimulating fatty acid oxidation: a pivotal role for sarcolemmal FAT/CD36.* Biochem J, 2017. **474**(1): p. 149-162.
110. Jeppesen, J., et al., *Contraction-induced skeletal muscle FAT/CD36 trafficking and FA uptake is AMPK independent.* J Lipid Res, 2011. **52**(4): p. 699-711.
111. McGarry, J.D. and N.F. Brown, *The mitochondrial carnitine palmitoyltransferase system. From concept to molecular analysis.* Eur J Biochem, 1997. **244**(1): p. 1-14.
112. O'Neill, H.M., et al., *Skeletal muscle ACC2 S212 phosphorylation is not required for the control of fatty acid oxidation during exercise.* Physiol Rep, 2015. **3**(7).
113. Zordoky, B.N., et al., *AMPK-dependent inhibitory phosphorylation of ACC is not essential for maintaining myocardial fatty acid oxidation.* Circ Res, 2014. **115**(5): p. 518-24.
114. Mottillo, E.P., et al., *Lack of Adipocyte AMPK Exacerbates Insulin Resistance and Hepatic Steatosis through Brown and Beige Adipose Tissue Function.* Cell Metab, 2016. **24**(1): p. 118-29.
115. Taylor, E.B., et al., *Discovery of TBC1D1 as an insulin-, AICAR-, and contraction-stimulated signaling nexus in mouse skeletal muscle.* J Biol Chem, 2008. **283**(15): p. 9787-96.

116. Wu, N., et al., *AMPK-dependent degradation of TXNIP upon energy stress leads to enhanced glucose uptake via GLUT1.* Mol Cell, 2013. **49**(6): p. 1167-75.
117. Stoppani, J., et al., *AMP-activated protein kinase activates transcription of the UCP3 and HKII genes in rat skeletal muscle.* Am J Physiol Endocrinol Metab, 2002. **283**(6): p. E1239-48.
118. Marsin, A.S., et al., *Phosphorylation and activation of heart PFK-2 by AMPK has a role in the stimulation of glycolysis during ischaemia.* Curr Biol, 2000. **10**(20): p. 1247-55.
119. Marsin, A.S., et al., *The stimulation of glycolysis by hypoxia in activated monocytes is mediated by AMP-activated protein kinase and inducible 6-phosphofructo-2-kinase.* J Biol Chem, 2002. **277**(34): p. 30778-83.
120. Carling, D. and D.G. Hardie, *The substrate and sequence specificity of the AMP-activated protein kinase. Phosphorylation of glycogen synthase and phosphorylase kinase.* Biochim Biophys Acta, 1989. **1012**(1): p. 81-6.
121. Bultot, L., et al., *AMP-activated protein kinase phosphorylates and inactivates liver glycogen synthase.* Biochem J, 2012. **443**(1): p. 193-203.
122. Johanns, M., et al., *Direct and indirect activation of eukaryotic elongation factor 2 kinase by AMP-activated protein kinase.* Cell Signal, 2017. **36**: p. 212-221.
123. Kazyken, D., et al., *AMPK directly activates mTORC2 to promote cell survival during acute energetic stress.* Sci Signal, 2019. **12**(585).
124. Jacinto, E., et al., *SIN1/MIP1 maintains rictor-mTOR complex integrity and regulates Akt phosphorylation and substrate specificity.* Cell, 2006. **127**(1): p. 125-37.
125. Sarbassov, D.D., et al., *Phosphorylation and regulation of Akt/PKB by the rictor-mTOR complex.* Science, 2005. **307**(5712): p. 1098-101.
126. Gaubitz, C., et al., *TORC2 Structure and Function.* Trends Biochem Sci, 2016. **41**(6): p. 532-545.
127. Albert, V., et al., *mTORC2 sustains thermogenesis via Akt-induced glucose uptake and glycolysis in brown adipose tissue.* EMBO Mol Med, 2016. **8**(3): p. 232-46.
128. Hagiwara, A., et al., *Hepatic mTORC2 activates glycolysis and lipogenesis through Akt, glucokinase, and SREBP1c.* Cell Metab, 2012. **15**(5): p. 725-38.
129. Kleinert, M., et al., *Mammalian target of rapamycin complex 2 regulates muscle glucose uptake during exercise in mice.* J Physiol, 2017. **595**(14): p. 4845-4855.
130. Egan, D.F., et al., *Phosphorylation of ULK1 (hATG1) by AMP-activated protein kinase connects energy sensing to mitophagy.* Science, 2011. **331**(6016): p. 456-61.
131. Kim, J., et al., *Differential regulation of distinct Vps34 complexes by AMPK in nutrient stress and autophagy.* Cell, 2013. **152**(1-2): p. 290-303.
132. Chen, Z., et al., *Global phosphoproteomic analysis reveals ARMC10 as an AMPK substrate that regulates mitochondrial dynamics.* Nat Commun, 2019. **10**(1): p. 104.
133. Toyama, E.Q., et al., *Metabolism. AMP-activated protein kinase mediates mitochondrial fission in response to energy stress.* Science, 2016. **351**(6270): p. 275-281.
134. Laker, R.C., et al., *Ampk phosphorylation of Ulk1 is required for targeting of mitochondria to lysosomes in exercise-induced mitophagy.* Nat Commun, 2017. **8**(1): p. 548.
135. Zong, H., et al., *AMP kinase is required for mitochondrial biogenesis in skeletal muscle in response to chronic energy deprivation.* Proc Natl Acad Sci U S A, 2002. **99**(25): p. 15983-7.
136. Jager, S., et al., *AMP-activated protein kinase (AMPK) action in skeletal muscle via direct phosphorylation of PGC-1alpha.* Proc Natl Acad Sci U S A, 2007. **104**(29): p. 12017-22.
137. Valenzuela, P.L., et al., *Obesity and the risk of cardiometabolic diseases.* Nat Rev Cardiol, 2023. **20**(7): p. 475-494.
138. Corton, J.M., et al., *5-aminoimidazole-4-carboxamide ribonucleoside. A specific method for activating AMP-activated protein kinase in intact cells?* Eur J Biochem, 1995. **229**(2): p. 558-65.

139. Marie, S., et al., *AICA-ribosiduria: a novel, neurologically devastating inborn error of purine biosynthesis caused by mutation of ATIC.* Am J Hum Genet, 2004. **74**(6): p. 1276-81.
140. McGuire, J.J., W.H. Haile, and C.C. Yeh, *5-amino-4-imidazolecarboxamide riboside potentiates both transport of reduced folates and antifolates by the human reduced folate carrier and their subsequent metabolism.* Cancer Res, 2006. **66**(7): p. 3836-44.
141. Beckers, A., et al., *Methotrexate enhances the antianabolic and antiproliferative effects of 5-aminoimidazole-4-carboxamide riboside.* Mol Cancer Ther, 2006. **5**(9): p. 2211-7.
142. Longnus, S.L., et al., *5-Aminoimidazole-4-carboxamide 1-beta -D-ribofuranoside (AICAR) stimulates myocardial glycogenolysis by allosteric mechanisms.* Am J Physiol Regul Integr Comp Physiol, 2003. **284**(4): p. R936-44.
143. Boon, H., et al., *Intravenous AICAR administration reduces hepatic glucose output and inhibits whole body lipolysis in type 2 diabetic patients.* Diabetologia, 2008. **51**(10): p. 1893-900.
144. Iglesias, M.A., et al., *AICAR administration causes an apparent enhancement of muscle and liver insulin action in insulin-resistant high-fat-fed rats.* Diabetes, 2002. **51**(10): p. 2886-94.
145. Cuthbertson, D.J., et al., *5-aminoimidazole-4-carboxamide 1-beta-D-ribofuranoside acutely stimulates skeletal muscle 2-deoxyglucose uptake in healthy men.* Diabetes, 2007. **56**(8): p. 2078-84.
146. Dixon, R., et al., *AICA-riboside: safety, tolerance, and pharmacokinetics of a novel adenosine-regulating agent.* J Clin Pharmacol, 1991. **31**(4): p. 342-7.
147. Jacobson, K.A. and M.L. Reitman, *Adenosine-Related Mechanisms in Non-Adenosine Receptor Drugs.* Cells, 2020. **9**(4).
148. Wiernsperger, N.F. and C.J. Bailey, *The antihyperglycaemic effect of metformin: therapeutic and cellular mechanisms.* Drugs, 1999. **58 Suppl 1**: p. 31-9; discussion 75-82.
149. Zhou, G., et al., *Role of AMP-activated protein kinase in mechanism of metformin action.* J Clin Invest, 2001. **108**(8): p. 1167-74.
150. Wu, M.S., et al., *Effect of metformin on carbohydrate and lipoprotein metabolism in NIDDM patients.* Diabetes Care, 1990. **13**(1): p. 1-8.
151. Stumvoll, M., et al., *Metabolic effects of metformin in non-insulin-dependent diabetes mellitus.* N Engl J Med, 1995. **333**(9): p. 550-4.
152. Schafer, G., *Biguanides. A review of history, pharmacodynamics and therapy.* Diabete Metab, 1983. **9**(2): p. 148-63.
153. Foretz, M., B. Guigas, and B. Viollet, *Metformin: update on mechanisms of action and repurposing potential.* Nat Rev Endocrinol, 2023. **19**(8): p. 460-476.
154. Hawley, S.A., et al., *Use of cells expressing gamma subunit variants to identify diverse mechanisms of AMPK activation.* Cell Metab, 2010. **11**(6): p. 554-65.
155. Foretz, M., et al., *Metformin inhibits hepatic gluconeogenesis in mice independently of the LKB1/AMPK pathway via a decrease in hepatic energy state.* J Clin Invest, 2010. **120**(7): p. 2355-69.
156. Cool, B., et al., *Identification and characterization of a small molecule AMPK activator that treats key components of type 2 diabetes and the metabolic syndrome.* Cell Metab, 2006. **3**(6): p. 403-16.
157. Wu, L., et al., *AMP-Activated Protein Kinase (AMPK) Regulates Energy Metabolism through Modulating Thermogenesis in Adipose Tissue.* Front Physiol, 2018. **9**: p. 122.
158. Goransson, O., et al., *Mechanism of action of A-769662, a valuable tool for activation of AMP-activated protein kinase.* J Biol Chem, 2007. **282**(45): p. 32549-60.
159. Scott, J.W., et al., *Thienopyridone drugs are selective activators of AMP-activated protein kinase beta1-containing complexes.* Chem Biol, 2008. **15**(11): p. 1220-30.
160. Xiao, B., et al., *Structural basis of AMPK regulation by small molecule activators.* Nat Commun, 2013. **4**: p. 3017.

161. Cokorinos, E.C., et al., *Activation of Skeletal Muscle AMPK Promotes Glucose Disposal and Glucose Lowering in Non-human Primates and Mice.* Cell Metab, 2017. **25**(5): p. 1147-1159 e10.
162. Cusi, K., et al., *Efficacy and safety of PXL770, a direct AMP kinase activator, for the treatment of non-alcoholic fatty liver disease (STAMP-NAFLD): a randomised, double-blind, placebo-controlled, phase 2a study.* Lancet Gastroenterol Hepatol, 2021. **6**(11): p. 889-902.
163. Grempler, R., et al., *Discovery and translation of a target engagement marker for AMP-activated protein kinase (AMPK).* PLoS One, 2018. **13**(5): p. e0197849.
164. Myers, R.W., et al., *Systemic pan-AMPK activator MK-8722 improves glucose homeostasis but induces cardiac hypertrophy.* Science, 2017. **357**(6350): p. 507-511.
165. Bernardo, B.C., et al., *Molecular distinction between physiological and pathological cardiac hypertrophy: experimental findings and therapeutic strategies.* Pharmacol Ther, 2010. **128**(1): p. 191-227.
166. Penfold, L., et al., *AMPK activation protects against prostate cancer by inducing a catabolic cellular state.* Cell Rep, 2023. **42**(4): p. 112396.
167. Xiao, W.L., J.;, *Abstract 9817: Krüppel-Like Factor 4 Integrates Immunometabolism of Human Arterial Endothelial Cells.* Circulation, 2021. **144**(A9817).
168. Dunn, J., et al., *Flow-dependent epigenetic DNA methylation regulates endothelial gene expression and atherosclerosis.* J Clin Invest, 2014. **124**(7): p. 3187-99.
169. Palmer, T.M. and I.P. Salt, *Nutrient regulation of inflammatory signalling in obesity and vascular disease.* Clin Sci (Lond), 2021. **135**(13): p. 1563-1590.
170. Bess, E., et al., *Nitric oxide-induced activation of the AMP-activated protein kinase alpha2 subunit attenuates IkappaB kinase activity and inflammatory responses in endothelial cells.* PLoS One, 2011. **6**(6): p. e20848.
171. Spiecker, M., H.B. Peng, and J.K. Liao, *Inhibition of endothelial vascular cell adhesion molecule-1 expression by nitric oxide involves the induction and nuclear translocation of IkappaBalpha.* J Biol Chem, 1997. **272**(49): p. 30969-74.
172. He, C., et al., *AMPK Suppresses Vascular Inflammation In Vivo by Inhibiting Signal Transducer and Activator of Transcription-1.* Diabetes, 2015. **64**(12): p. 4285-97.
173. Rutherford, C., et al., *Phosphorylation of Janus kinase 1 (JAK1) by AMP-activated protein kinase (AMPK) links energy sensing to anti-inflammatory signaling.* Sci Signal, 2016. **9**(453): p. ra109.
174. Oslowski, C.M., et al., *Thioredoxin-interacting protein mediates ER stress-induced beta cell death through initiation of the inflammasome.* Cell Metab, 2012. **16**(2): p. 265-73.
175. Xing, J.H., et al., *NLRP3 inflammasome mediate palmitate-induced endothelial dysfunction.* Life Sci, 2019. **239**: p. 116882.
176. Li, J., et al., *Pharmacological activation of AMPK prevents Drp1-mediated mitochondrial fission and alleviates endoplasmic reticulum stress-associated endothelial dysfunction.* J Mol Cell Cardiol, 2015. **86**: p. 62-74.
177. Venna, V.R., et al., *Chronic metformin treatment improves post-stroke angiogenesis and recovery after experimental stroke.* Eur J Neurosci, 2014. **39**(12): p. 2129-38.
178. Abdel Malik, R., et al., *AMP-Activated Protein Kinase alpha2 in Neutrophils Regulates Vascular Repair via Hypoxia-Inducible Factor-1alpha and a Network of Proteins Affecting Metabolism and Apoptosis.* Circ Res, 2017. **120**(1): p. 99-109.
179. Leick, L., et al., *PGC-1alpha mediates exercise-induced skeletal muscle VEGF expression in mice.* Am J Physiol Endocrinol Metab, 2009. **297**(1): p. E92-103.
180. Zwetsloot, K.A., et al., *AMPK regulates basal skeletal muscle capillarization and VEGF expression, but is not necessary for the angiogenic response to exercise.* J Physiol, 2008. **586**(24): p. 6021-35.
181. Ouchi, N., et al., *Adiponectin stimulates angiogenesis by promoting cross-talk between AMP-activated protein kinase and Akt signaling in endothelial cells.* J Biol Chem, 2004. **279**(2): p. 1304-9.

182. Nagata, D., M. Mogi, and K. Walsh, *AMP-activated protein kinase (AMPK) signaling in endothelial cells is essential for angiogenesis in response to hypoxic stress.* J Biol Chem, 2003. **278**(33): p. 31000-6.
183. Stahmann, N., et al., *Activation of AMP-activated protein kinase by vascular endothelial growth factor mediates endothelial angiogenesis independently of nitric-oxide synthase.* J Biol Chem, 2010. **285**(14): p. 10638-52.
184. Reihill, J.A., M.A. Ewart, and I.P. Salt, *The role of AMP-activated protein kinase in the functional effects of vascular endothelial growth factor-A and -B in human aortic endothelial cells.* Vasc Cell, 2011. **3**: p. 9.
185. Ouchi, N., R. Shibata, and K. Walsh, *AMP-activated protein kinase signaling stimulates VEGF expression and angiogenesis in skeletal muscle.* Circ Res, 2005. **96**(8): p. 838-46.
186. Song, Y., et al., *Transcription factor Kruppel-like factor 2 plays a vital role in endothelial colony forming cells differentiation.* Cardiovasc Res, 2013. **99**(3): p. 514-24.
187. Wang, D., et al., *AMPK-KLF2 signaling pathway mediates the proangiogenic effect of erythropoietin in endothelial colony-forming cells.* Am J Physiol Cell Physiol, 2017. **313**(6): p. C674-C685.
188. Li, X., et al., *AMP-activated protein kinase promotes the differentiation of endothelial progenitor cells.* Arterioscler Thromb Vasc Biol, 2008. **28**(10): p. 1789-95.
189. Spengler, K., et al., *VEGF Triggers Transient Induction of Autophagy in Endothelial Cells via AMPKalpha1.* Cells, 2020. **9**(3).
190. Malik, N., et al., *Induction of lysosomal and mitochondrial biogenesis by AMPK phosphorylation of FNIP1.* Science, 2023. **380**(6642): p. eabj5559.
191. Steingrimsson, E., et al., *The bHLH-Zip transcription factor Tfeb is essential for placental vascularization.* Development, 1998. **125**(23): p. 4607-16.
192. Fan, Y., et al., *Endothelial TFEB (Transcription Factor EB) Positively Regulates Postischemic Angiogenesis.* Circ Res, 2018. **122**(7): p. 945-957.
193. Zhu, H., et al., *AMP-Activated Protein Kinase alpha1 in Macrophages Promotes Collateral Remodeling and Arteriogenesis in Mice In Vivo.* Arterioscler Thromb Vasc Biol, 2016. **36**(9): p. 1868-78.
194. Chen, Z., et al., *Shear stress, SIRT1, and vascular homeostasis.* Proc Natl Acad Sci U S A, 2010. **107**(22): p. 10268-73.
195. Davis, B.J., et al., *Activation of the AMP-activated kinase by antidiabetes drug metformin stimulates nitric oxide synthesis in vivo by promoting the association of heat shock protein 90 and endothelial nitric oxide synthase.* Diabetes, 2006. **55**(2): p. 496-505.
196. Rodriguez, C., et al., *Activation of the AMP-related kinase (AMPK) induces renal vasodilatation and downregulates Nox-derived reactive oxygen species (ROS) generation.* Redox Biol, 2020. **34**: p. 101575.
197. Wang, S., et al., *AMPKalpha2 deletion causes aberrant expression and activation of NAD(P)H oxidase and consequent endothelial dysfunction in vivo: role of 26S proteasomes.* Circ Res, 2010. **106**(6): p. 1117-28.
198. Kroller-Schon, S., et al., *Endothelial alpha1AMPK modulates angiotensin II-mediated vascular inflammation and dysfunction.* Basic Res Cardiol, 2019. **114**(2): p. 8.
199. Zibrova, D., et al., *GFAT1 phosphorylation by AMPK promotes VEGF-induced angiogenesis.* Biochem J, 2017. **474**(6): p. 983-1001.
200. Yu, J.W., et al., *Metformin improves the angiogenic functions of endothelial progenitor cells via activating AMPK/eNOS pathway in diabetic mice.* Cardiovasc Diabetol, 2016. **15**: p. 88.
201. Cayatte, A.J., et al., *S17834, a new inhibitor of cell adhesion and atherosclerosis that targets nadph oxidase.* Arterioscler Thromb Vasc Biol, 2001. **21**(10): p. 1577-84.
202. Li, Y., et al., *AMPK phosphorylates and inhibits SREBP activity to attenuate hepatic steatosis and atherosclerosis in diet-induced insulin-resistant mice.* Cell Metab, 2011. **13**(4): p. 376-388.

203. Steneberg, P., et al., *PAN-AMPK activator O304 improves glucose homeostasis and microvascular perfusion in mice and type 2 diabetes patients.* JCI Insight, 2018. **3**(12).
204. Ericsson, M., et al., *AMPK activator O304 improves metabolic and cardiac function, and exercise capacity in aged mice.* Commun Biol, 2021. **4**(1): p. 1306.
205. Yang, Q., et al., *PRKAA1/AMPKalpha1-driven glycolysis in endothelial cells exposed to disturbed flow protects against atherosclerosis.* Nat Commun, 2018. **9**(1): p. 4667.
206. Erwin, D.H., *Early metazoan life: divergence, environment and ecology.* Philos Trans R Soc Lond B Biol Sci, 2015. **370**(1684).
207. Reinhard, C.T., et al., *Earth's oxygen cycle and the evolution of animal life.* Proc Natl Acad Sci U S A, 2016. **113**(32): p. 8933-8.
208. Lane, N. and W. Martin, *The energetics of genome complexity.* Nature, 2010. **467**(7318): p. 929-34.
209. Booth, A. and W.F. Doolittle, *Reply to Lane and Martin: Being and becoming eukaryotes.* Proc Natl Acad Sci U S A, 2015. **112**(35): p. E4824.
210. Song, B., et al., *The origin and distribution of the main oxygen sensing mechanism across metazoans.* Front Physiol, 2022. **13**: p. 977391.
211. Kaelin, W.G., Jr. and P.J. Ratcliffe, *Oxygen sensing by metazoans: the central role of the HIF hydroxylase pathway.* Mol Cell, 2008. **30**(4): p. 393-402.
212. Hirsila, M., et al., *Characterization of the human prolyl 4-hydroxylases that modify the hypoxia-inducible factor.* J Biol Chem, 2003. **278**(33): p. 30772-80.
213. Carmeliet, P., et al., *Role of HIF-1alpha in hypoxia-mediated apoptosis, cell proliferation and tumour angiogenesis.* Nature, 1998. **394**(6692): p. 485-90.
214. Jiang, B.H., et al., *Dimerization, DNA binding, and transactivation properties of hypoxia-inducible factor 1.* J Biol Chem, 1996. **271**(30): p. 17771-8.
215. Iyer, N.V., et al., *Cellular and developmental control of O2 homeostasis by hypoxia-inducible factor 1 alpha.* Genes Dev, 1998. **12**(2): p. 149-62.
216. Lee, P., N.S. Chandel, and M.C. Simon, *Cellular adaptation to hypoxia through hypoxia inducible factors and beyond.* Nat Rev Mol Cell Biol, 2020. **21**(5): p. 268-283.
217. Poyya, J., et al., *Sequence Analysis and Phylogenetic Studies of Hypoxia-Inducible Factor-1alpha.* Cancer Inform, 2017. **16**: p. 1176935117712242.
218. Tarade, D., J.E. Lee, and M. Ohh, *Evolution of metazoan oxygen-sensing involved a conserved divergence of VHL affinity for HIF1alpha and HIF2alpha.* Nat Commun, 2019. **10**(1): p. 3293.
219. Wang, G., et al., *Molecular characterisation, evolution and expression of hypoxia-inducible factor in Aurelia sp.1.* PLoS One, 2014. **9**(6): p. e100057.
220. Galban, S., et al., *RNA-binding proteins HuR and PTB promote the translation of hypoxia-inducible factor 1alpha.* Mol Cell Biol, 2008. **28**(1): p. 93-107.
221. Hagele, S., et al., *Cytoplasmic polyadenylation-element-binding protein (CPEB)1 and 2 bind to the HIF-1alpha mRNA 3'-UTR and modulate HIF-1alpha protein expression.* Biochem J, 2009. **417**(1): p. 235-46.
222. Sanchez, M., et al., *Iron-regulatory proteins limit hypoxia-inducible factor-2alpha expression in iron deficiency.* Nat Struct Mol Biol, 2007. **14**(5): p. 420-6.
223. Epstein, A.C., et al., *C. elegans EGL-9 and mammalian homologs define a family of dioxygenases that regulate HIF by prolyl hydroxylation.* Cell, 2001. **107**(1): p. 43-54.
224. Mahon, P.C., K. Hirota, and G.L. Semenza, *FIH-1: a novel protein that interacts with HIF-1alpha and VHL to mediate repression of HIF-1 transcriptional activity.* Genes Dev, 2001. **15**(20): p. 2675-86.
225. Rytkonen, K.T. and J.F. Storz, *Evolutionary origins of oxygen sensing in animals.* EMBO Rep, 2011. **12**(1): p. 3-4.
226. Loenarz, C., et al., *The hypoxia-inducible transcription factor pathway regulates oxygen sensing in the simplest animal, Trichoplax adhaerens.* EMBO Rep, 2011. **12**(1): p. 63-70.
227. Davies, B.S. and J. Rine, *A role for sterol levels in oxygen sensing in Saccharomyces cerevisiae.* Genetics, 2006. **174**(1): p. 191-201.

228. Zhang, L. and A. Hach, *Molecular mechanism of heme signaling in yeast: the transcriptional activator Hap1 serves as the key mediator.* Cell Mol Life Sci, 1999. **56**(5-6): p. 415-26.
229. Metzen, E., et al., *Intracellular localisation of human HIF-1 alpha hydroxylases: implications for oxygen sensing.* J Cell Sci, 2003. **116**(Pt 7): p. 1319-26.
230. Appelhoff, R.J., et al., *Differential function of the prolyl hydroxylases PHD1, PHD2, and PHD3 in the regulation of hypoxia-inducible factor.* J Biol Chem, 2004. **279**(37): p. 38458-65.
231. Meneses, A.M. and B. Wielockx, *PHD2: from hypoxia regulation to disease progression.* Hypoxia (Auckl), 2016. **4**: p. 53-67.
232. Ivan, M., et al., *Biochemical purification and pharmacological inhibition of a mammalian prolyl hydroxylase acting on hypoxia-inducible factor.* Proc Natl Acad Sci U S A, 2002. **99**(21): p. 13459-64.
233. Bruick, R.K. and S.L. McKnight, *A conserved family of prolyl-4-hydroxylases that modify HIF.* Science, 2001. **294**(5545): p. 1337-40.
234. Koivunen, P., et al., *Catalytic properties of the asparaginyl hydroxylase (FIH) in the oxygen sensing pathway are distinct from those of its prolyl 4-hydroxylases.* J Biol Chem, 2004. **279**(11): p. 9899-904.
235. Ehrismann, D., et al., *Studies on the activity of the hypoxia-inducible-factor hydroxylases using an oxygen consumption assay.* Biochem J, 2007. **401**(1): p. 227-34.
236. Sang, N., et al., *Carboxyl-terminal transactivation activity of hypoxia-inducible factor 1 alpha is governed by a von Hippel-Lindau protein-independent, hydroxylation-regulated association with p300/CBP.* Mol Cell Biol, 2002. **22**(9): p. 2984-92.
237. Lando, D., et al., *FIH-1 is an asparaginyl hydroxylase enzyme that regulates the transcriptional activity of hypoxia-inducible factor.* Genes Dev, 2002. **16**(12): p. 1466-71.
238. Stroka, D.M., et al., *HIF-1 is expressed in normoxic tissue and displays an organ-specific regulation under systemic hypoxia.* FASEB J, 2001. **15**(13): p. 2445-53.
239. Jewell, U.R., et al., *Induction of HIF-1alpha in response to hypoxia is instantaneous.* FASEB J, 2001. **15**(7): p. 1312-4.
240. Huang, L.E., et al., *Activation of hypoxia-inducible transcription factor depends primarily upon redox-sensitive stabilization of its alpha subunit.* J Biol Chem, 1996. **271**(50): p. 32253-9.
241. Schoenfeld, A., E.J. Davidowitz, and R.D. Burk, *A second major native von Hippel-Lindau gene product, initiated from an internal translation start site, functions as a tumor suppressor.* Proc Natl Acad Sci U S A, 1998. **95**(15): p. 8817-22.
242. Min, J.H., et al., *Structure of an HIF-1alpha -pVHL complex: hydroxyproline recognition in signaling.* Science, 2002. **296**(5574): p. 1886-9.
243. Kamura, T., et al., *Rbx1, a component of the VHL tumor suppressor complex and SCF ubiquitin ligase.* Science, 1999. **284**(5414): p. 657-61.
244. Albanese, A., et al., *The Role of Hypoxia-Inducible Factor Post-Translational Modifications in Regulating Its Localisation, Stability, and Activity.* Int J Mol Sci, 2020. **22**(1).
245. Tanimoto, K., et al., *Mechanism of regulation of the hypoxia-inducible factor-1 alpha by the von Hippel-Lindau tumor suppressor protein.* EMBO J, 2000. **19**(16): p. 4298-309.
246. Paltoglou, S. and B.J. Roberts, *HIF-1alpha and EPAS ubiquitination mediated by the VHL tumour suppressor involves flexibility in the ubiquitination mechanism, similar to other RING E3 ligases.* Oncogene, 2007. **26**(4): p. 604-9.
247. Groulx, I. and S. Lee, *Oxygen-dependent ubiquitination and degradation of hypoxia-inducible factor requires nuclear-cytoplasmic trafficking of the von Hippel-Lindau tumor suppressor protein.* Mol Cell Biol, 2002. **22**(15): p. 5319-36.
248. Ortmann, B., J. Druker, and S. Rocha, *Cell cycle progression in response to oxygen levels.* Cell Mol Life Sci, 2014. **71**(18): p. 3569-82.

249. Lando, D., et al., *Asparagine hydroxylation of the HIF transactivation domain a hypoxic switch.* Science, 2002. **295**(5556): p. 858-61.
250. Horak, P., et al., *Negative feedback control of HIF-1 through REDD1-regulated ROS suppresses tumorigenesis.* Proc Natl Acad Sci U S A, 2010. **107**(10): p. 4675-80.
251. Chen, N., et al., *BCL-xL is a target gene regulated by hypoxia-inducible factor-1alpha.* J Biol Chem, 2009. **284**(15): p. 10004-12.
252. Shirole, N.H., et al., *Abstract PR011: Downregulation of the HIF2a target cyclin D1 underlies the efficacy of the HIF2a inhibitor belzutifan in kidney cancer.* Cancer Research, 2023. **83**(16_Supplement): p. PR011-PR011.
253. Raval, R.R., et al., *Contrasting properties of hypoxia-inducible factor 1 (HIF-1) and HIF-2 in von Hippel-Lindau-associated renal cell carcinoma.* Mol Cell Biol, 2005. **25**(13): p. 5675-86.
254. Oktay, Y., et al., *Hypoxia-inducible factor 2alpha regulates expression of the mitochondrial aconitase chaperone protein frataxin.* J Biol Chem, 2007. **282**(16): p. 11750-6.
255. Scortegagna, M., et al., *Multiple organ pathology, metabolic abnormalities and impaired homeostasis of reactive oxygen species in Epas1-/- mice.* Nat Genet, 2003. **35**(4): p. 331-40.
256. Gruber, M., et al., *Acute postnatal ablation of Hif-2alpha results in anemia.* Proc Natl Acad Sci U S A, 2007. **104**(7): p. 2301-6.
257. Qing, G. and M.C. Simon, *Hypoxia inducible factor-2alpha: a critical mediator of aggressive tumor phenotypes.* Curr Opin Genet Dev, 2009. **19**(1): p. 60-6.
258. Karshovska, E., et al., *Expression of HIF-1alpha in injured arteries controls SDF-1alpha mediated neointima formation in apolipoprotein E deficient mice.* Arterioscler Thromb Vasc Biol, 2007. **27**(12): p. 2540-7.
259. Yang, S., et al., *Hypoxia-inducible factor-2alpha is a catabolic regulator of osteoarthritic cartilage destruction.* Nat Med, 2010. **16**(6): p. 687-93.
260. Chen, C., et al., *Regulation of glut1 mRNA by hypoxia-inducible factor-1. Interaction between H-ras and hypoxia.* J Biol Chem, 2001. **276**(12): p. 9519-25.
261. Besse-Patin, A., et al., *PGC1A regulates the IRS1:IRS2 ratio during fasting to influence hepatic metabolism downstream of insulin.* Proc Natl Acad Sci U S A, 2019. **116**(10): p. 4285-4290.
262. Mirtschink, P., et al., *HIF-driven SF3B1 induces KHK-C to enforce fructolysis and heart disease.* Nature, 2015. **522**(7557): p. 444-449.
263. Tannahill, G.M., et al., *Succinate is an inflammatory signal that induces IL-1beta through HIF-1alpha.* Nature, 2013. **496**(7444): p. 238-42.
264. Dang, E.V., et al., *Control of T(H)17/T(reg) balance by hypoxia-inducible factor 1.* Cell, 2011. **146**(5): p. 772-84.
265. Poth, J.M., et al., *Transcriptional control of adenosine signaling by hypoxia-inducible transcription factors during ischemic or inflammatory disease.* J Mol Med (Berl), 2013. **91**(2): p. 183-93.
266. Jung, F., et al., *Hypoxic regulation of inducible nitric oxide synthase via hypoxia inducible factor-1 in cardiac myocytes.* Circ Res, 2000. **86**(3): p. 319-25.
267. Cowburn, A.S., et al., *HIF2alpha-arginase axis is essential for the development of pulmonary hypertension.* Proc Natl Acad Sci U S A, 2016. **113**(31): p. 8801-6.
268. Qiu, B., et al., *HIF2alpha-Dependent Lipid Storage Promotes Endoplasmic Reticulum Homeostasis in Clear-Cell Renal Cell Carcinoma.* Cancer Discov, 2015. **5**(6): p. 652-67.
269. Sowter, H.M., et al., *HIF-1-dependent regulation of hypoxic induction of the cell death factors BNIP3 and NIX in human tumors.* Cancer Res, 2001. **61**(18): p. 6669-73.
270. Covello, K.L., et al., *HIF-2alpha regulates Oct-4: effects of hypoxia on stem cell function, embryonic development, and tumor growth.* Genes Dev, 2006. **20**(5): p. 557-70.
271. Mazumdar, J., et al., *O2 regulates stem cells through Wnt/beta-catenin signalling.* Nat Cell Biol, 2010. **12**(10): p. 1007-13.

272. Kappler, M., H. Taubert, and A.W. Eckert, *Oxygen sensing, homeostasis, and disease.* N Engl J Med, 2011. **365**(19): p. 1845-6; author reply 1846.
273. De Bels, D., F. Corazza, and C. Balestra, *Oxygen sensing, homeostasis, and disease.* N Engl J Med, 2011. **365**(19): p. 1845; author reply 1846.
274. Hernansanz-Agustin, P., et al., *Acute hypoxia produces a superoxide burst in cells.* Free Radic Biol Med, 2014. **71**: p. 146-156.
275. Chandel, N.S., et al., *Reactive oxygen species generated at mitochondrial complex III stabilize hypoxia-inducible factor-1alpha during hypoxia: a mechanism of O2 sensing.* J Biol Chem, 2000. **275**(33): p. 25130-8.
276. Willson, J.A., et al., *Neutrophil HIF-1alpha stabilization is augmented by mitochondrial ROS produced via the glycerol 3-phosphate shuttle.* Blood, 2022. **139**(2): p. 281-286.
277. Guzy, R.D., et al., *Loss of the SdhB, but Not the SdhA, subunit of complex II triggers reactive oxygen species-dependent hypoxia-inducible factor activation and tumorigenesis.* Mol Cell Biol, 2008. **28**(2): p. 718-31.
278. Fuhrmann, D.C. and B. Brune, *Mitochondrial composition and function under the control of hypoxia.* Redox Biol, 2017. **12**: p. 208-215.
279. Kumar, A., et al., *HIF1alpha stabilization in hypoxia is not oxidant-initiated.* Elife, 2021. **10**.
280. Chua, Y.L., et al., *Stabilization of hypoxia-inducible factor-1alpha protein in hypoxia occurs independently of mitochondrial reactive oxygen species production.* J Biol Chem, 2010. **285**(41): p. 31277-84.
281. Isaacs, J.S., et al., *HIF overexpression correlates with biallelic loss of fumarate hydratase in renal cancer: novel role of fumarate in regulation of HIF stability.* Cancer Cell, 2005. **8**(2): p. 143-53.
282. Selak, M.A., et al., *Succinate links TCA cycle dysfunction to oncogenesis by inhibiting HIF-alpha prolyl hydroxylase.* Cancer Cell, 2005. **7**(1): p. 77-85.
283. Zhang, H., et al., *Hypoxia-inducible factor directs POMC gene to mediate hypothalamic glucose sensing and energy balance regulation.* PLoS Biol, 2011. **9**(7): p. e1001112.
284. Ryan, H.E., J. Lo, and R.S. Johnson, *HIF-1 alpha is required for solid tumor formation and embryonic vascularization.* EMBO J, 1998. **17**(11): p. 3005-15.
285. Peng, J., et al., *The transcription factor EPAS-1/hypoxia-inducible factor 2alpha plays an important role in vascular remodeling.* Proc Natl Acad Sci U S A, 2000. **97**(15): p. 8386-91.
286. Scortegagna, M., et al., *The HIF family member EPAS1/HIF-2alpha is required for normal hematopoiesis in mice.* Blood, 2003. **102**(5): p. 1634-40.
287. Skuli, N., et al., *Endothelial deletion of hypoxia-inducible factor-2alpha (HIF-2alpha) alters vascular function and tumor angiogenesis.* Blood, 2009. **114**(2): p. 469-77.
288. Yamashita, T., et al., *Hypoxia-inducible transcription factor-2alpha in endothelial cells regulates tumor neovascularization through activation of ephrin A1.* J Biol Chem, 2008. **283**(27): p. 18926-36.
289. Ben-Yosef, Y., et al., *Hypoxia of endothelial cells leads to MMP-2-dependent survival and death.* Am J Physiol Cell Physiol, 2005. **289**(5): p. C1321-31.
290. Elvert, G., et al., *Cooperative interaction of hypoxia-inducible factor-2alpha (HIF-2alpha) and Ets-1 in the transcriptional activation of vascular endothelial growth factor receptor-2 (Flk-1).* J Biol Chem, 2003. **278**(9): p. 7520-30.
291. Liu, Y., et al., *Hypoxia regulates vascular endothelial growth factor gene expression in endothelial cells. Identification of a 5' enhancer.* Circ Res, 1995. **77**(3): p. 638-43.
292. Tang, N., et al., *Loss of HIF-1alpha in endothelial cells disrupts a hypoxia-driven VEGF autocrine loop necessary for tumorigenesis.* Cancer Cell, 2004. **6**(5): p. 485-95.
293. Krock, B.L., N. Skuli, and M.C. Simon, *Hypoxia-induced angiogenesis: good and evil.* Genes Cancer, 2011. **2**(12): p. 1117-33.

294. Patel, N.S., et al., *Up-regulation of delta-like 4 ligand in human tumor vasculature and the role of basal expression in endothelial cell function.* Cancer Res, 2005. **65**(19): p. 8690-7.
295. Cui, X., et al., *Venous Endothelial Marker COUP-TFII Regulates the Distinct Pathologic Potentials of Adult Arteries and Veins.* Sci Rep, 2015. **5**: p. 16193.
296. Tsang, K.M., et al., *Embryonic Stem Cell Differentiation to Functional Arterial Endothelial Cells through Sequential Activation of ETV2 and NOTCH1 Signaling by HIF1alpha.* Stem Cell Reports, 2017. **9**(3): p. 796-806.
297. Zhu, Y., et al., *Roxadustat promotes angiogenesis through HIF-1alpha/VEGF/VEGFR2 signaling and accelerates cutaneous wound healing in diabetic rats.* Wound Repair Regen, 2019. **27**(4): p. 324-334.
298. Takeda, N., et al., *Differential activation and antagonistic function of HIF-alpha isoforms in macrophages are essential for NO homeostasis.* Genes Dev, 2010. **24**(5): p. 491-501.
299. Cowburn, A.S., et al., *HIF isoforms in the skin differentially regulate systemic arterial pressure.* Proc Natl Acad Sci U S A, 2013. **110**(43): p. 17570-5.
300. Lambden, S., et al., *Endothelial cell regulation of systemic haemodynamics and metabolism acts through the HIF transcription factors.* Intensive Care Med Exp, 2021. **9**(1): p. 28.
301. Sankaran, V.G. and M.J. Weiss, *Anemia: progress in molecular mechanisms and therapies.* Nat Med, 2015. **21**(3): p. 221-30.
302. Borawski, B., et al., *Current Status of Renal Anemia Pharmacotherapy-What Can We Offer Today.* J Clin Med, 2021. **10**(18).
303. Kooistra, M.P., et al., *Low-dose aspirin does not prevent thrombovascular accidents in low-risk haemodialysis patients during treatment with recombinant human erythropoietin.* Nephrol Dial Transplant, 1994. **9**(8): p. 1115-20.
304. Flamme, I., et al., *Mimicking hypoxia to treat anemia: HIF-stabilizer BAY 85-3934 (Molidustat) stimulates erythropoietin production without hypertensive effects.* PLoS One, 2014. **9**(11): p. e111838.
305. Luo, R., et al., *Elevated Endothelial Hypoxia-Inducible Factor-1alpha Contributes to Glomerular Injury and Promotes Hypertensive Chronic Kidney Disease.* Hypertension, 2015. **66**(1): p. 75-84.
306. Dai, Z., et al., *Therapeutic Targeting of Vascular Remodeling and Right Heart Failure in Pulmonary Arterial Hypertension with a HIF-2alpha Inhibitor.* Am J Respir Crit Care Med, 2018. **198**(11): p. 1423-1434.
307. Bryant, A.J., et al., *Endothelial HIF signaling regulates pulmonary fibrosis-associated pulmonary hypertension.* Am J Physiol Lung Cell Mol Physiol, 2016. **310**(3): p. L249-62.
308. Tang, H., et al., *Endothelial HIF-2alpha contributes to severe pulmonary hypertension due to endothelial-to-mesenchymal transition.* Am J Physiol Lung Cell Mol Physiol, 2018. **314**(2): p. L256-L275.
309. Xiao, W., et al., *Immunometabolic Endothelial Phenotypes: Integrating Inflammation and Glucose Metabolism.* Circ Res, 2021. **129**(1): p. 9-29.
310. Wu, D., et al., *HIF-1alpha is required for disturbed flow-induced metabolic reprogramming in human and porcine vascular endothelium.* Elife, 2017. **6**.
311. Downes, N.L., et al., *Differential but Complementary HIF1alpha and HIF2alpha Transcriptional Regulation.* Mol Ther, 2018. **26**(7): p. 1735-1745.
312. Wong, B.W., et al., *Endothelial cell metabolism in health and disease: impact of hypoxia.* EMBO J, 2017. **36**(15): p. 2187-2203.
313. Bellot, G., et al., *Hypoxia-induced autophagy is mediated through hypoxia-inducible factor induction of BNIP3 and BNIP3L via their BH3 domains.* Mol Cell Biol, 2009. **29**(10): p. 2570-81.
314. Rodriguez, J.C., et al., *Peroxisome proliferator-activated receptor mediates induction of the mitochondrial 3-hydroxy-3-methylglutaryl-CoA synthase gene by fatty acids.* J Biol Chem, 1994. **269**(29): p. 18767-72.

315. Djouadi, F., et al., *A gender-related defect in lipid metabolism and glucose homeostasis in peroxisome proliferator- activated receptor alpha- deficient mice.* J Clin Invest, 1998. **102**(6): p. 1083-91.
316. Chinetti, G., et al., *PPAR-alpha and PPAR-gamma activators induce cholesterol removal from human macrophage foam cells through stimulation of the ABCA1 pathway.* Nat Med, 2001. **7**(1): p. 53-8.
317. Chawla, A., et al., *A PPAR gamma-LXR-ABCA1 pathway in macrophages is involved in cholesterol efflux and atherogenesis.* Mol Cell, 2001. **7**(1): p. 161-71.
318. Huang, B., et al., *Regulation of pyruvate dehydrogenase kinase expression by peroxisome proliferator-activated receptor-alpha ligands, glucocorticoids, and insulin.* Diabetes, 2002. **51**(2): p. 276-83.
319. Batth, T.S., et al., *Protein Aggregation Capture on Microparticles Enables Multipurpose Proteomics Sample Preparation.* Mol Cell Proteomics, 2019. **18**(5): p. 1027-1035.
320. Bruderer, R., et al., *Extending the limits of quantitative proteome profiling with data-independent acquisition and application to acetaminophen-treated three-dimensional liver microtissues.* Mol Cell Proteomics, 2015. **14**(5): p. 1400-10.
321. Frankenfield, A.M., et al., *Protein Contaminants Matter: Building Universal Protein Contaminant Libraries for DDA and DIA Proteomics.* J Proteome Res, 2022. **21**(9): p. 2104-2113.
322. Cox, J., et al., *Accurate proteome-wide label-free quantification by delayed normalization and maximal peptide ratio extraction, termed MaxLFQ.* Mol Cell Proteomics, 2014. **13**(9): p. 2513-26.
323. Perry, S.W., et al., *Mitochondrial membrane potential probes and the proton gradient: a practical usage guide.* Biotechniques, 2011. **50**(2): p. 98-115.
324. Carpentier, G., et al., *Angiogenesis Analyzer for ImageJ - A comparative morphometric analysis of "Endothelial Tube Formation Assay" and "Fibrin Bead Assay".* Sci Rep, 2020. **10**(1): p. 11568.
325. Pitulescu, M.E., et al., *Inducible gene targeting in the neonatal vasculature and analysis of retinal angiogenesis in mice.* Nat Protoc, 2010. **5**(9): p. 1518-34.
326. Mina, A.I., et al., *CalR: A Web-Based Analysis Tool for Indirect Calorimetry Experiments.* Cell Metab, 2018. **28**(4): p. 656-666 e1.
327. DeYoung, M.P., et al., *Hypoxia regulates TSC1/2-mTOR signaling and tumor suppression through REDD1-mediated 14-3-3 shuttling.* Genes Dev, 2008. **22**(2): p. 239-51.
328. Kaul, G., G. Pattan, and T. Rafeequi, *Eukaryotic elongation factor-2 (eEF2): its regulation and peptide chain elongation.* Cell Biochem Funct, 2011. **29**(3): p. 227-34.
329. Proud, C.G., *Regulation and roles of elongation factor 2 kinase.* Biochem Soc Trans, 2015. **43**(3): p. 328-32.
330. Chen, Z., et al., *Hypoxia-regulated microRNA-210 modulates mitochondrial function and decreases ISCU and COX10 expression.* Oncogene, 2010. **29**(30): p. 4362-8.
331. Wilson, D.F., et al., *The oxygen dependence of mitochondrial oxidative phosphorylation measured by a new optical method for measuring oxygen concentration.* J Biol Chem, 1988. **263**(6): p. 2712-8.
332. Cooper, C.E., *The steady-state kinetics of cytochrome c oxidation by cytochrome oxidase.* Biochim Biophys Acta, 1990. **1017**(3): p. 187-203.
333. Emerling, B.M., et al., *Hypoxic activation of AMPK is dependent on mitochondrial ROS but independent of an increase in AMP/ATP ratio.* Free Radic Biol Med, 2009. **46**(10): p. 1386-91.
334. Liu, L., et al., *Hypoxia-induced energy stress regulates mRNA translation and cell growth.* Mol Cell, 2006. **21**(4): p. 521-31.
335. Barnes, B.R., et al., *The 5'-AMP-activated protein kinase gamma3 isoform has a key role in carbohydrate and lipid metabolism in glycolytic skeletal muscle.* J Biol Chem, 2004. **279**(37): p. 38441-7.

336. Gusarova, G.A., et al., *Hypoxia leads to Na,K-ATPase downregulation via Ca(2+) release-activated Ca(2+) channels and AMPK activation.* Mol Cell Biol, 2011. **31**(17): p. 3546-56.
337. Aley, P.K., et al., *Hypoxic modulation of Ca2+ signaling in human venous endothelial cells. Multiple roles for reactive oxygen species.* J Biol Chem, 2005. **280**(14): p. 13349-54.
338. Quintero, M., et al., *Mitochondria as signaling organelles in the vascular endothelium.* Proc Natl Acad Sci U S A, 2006. **103**(14): p. 5379-84.
339. Keeley, T.P., et al., *A PP2A-mediated feedback mechanism controls Ca(2+)-dependent NO synthesis under physiological oxygen.* FASEB J, 2017. **31**(12): p. 5172-5183.
340. de Boer, S., et al., *Endothelial characteristics in healthy endothelial colony forming cells; generating a robust and valid ex vivo model for vascular disease.* J Thromb Haemost, 2020. **18**(10): p. 2721-2731.
341. Paschalaki, K.E. and A.M. Randi, *Recent Advances in Endothelial Colony Forming Cells Toward Their Use in Clinical Translation.* Front Med (Lausanne), 2018. **5**: p. 295.
342. Kutikhin, A.G., et al., *Human Peripheral Blood-Derived Endothelial Colony-Forming Cells Are Highly Similar to Mature Vascular Endothelial Cells yet Demonstrate a Transitional Transcriptomic Signature.* Cells, 2020. **9**(4).
343. Romero-Ruiz, A., et al., *Prolyl hydroxylase-dependent modulation of eukaryotic elongation factor 2 activity and protein translation under acute hypoxia.* J Biol Chem, 2012. **287**(12): p. 9651-8.
344. Lefebvre, V.H., et al., *Adenine nucleotides and inhibition of protein synthesis in isolated hepatocytes incubated under different pO2 levels.* Arch Biochem Biophys, 1993. **304**(2): p. 322-31.
345. Satake, S., et al., *Up-regulation of vascular endothelial growth factor in response to glucose deprivation.* Biol Cell, 1998. **90**(2): p. 161-8.
346. Guo, C., et al., *HIF-1alpha accumulation in response to transient hypoglycemia may worsen diabetic eye disease.* Cell Rep, 2023. **42**(1): p. 111976.
347. Dumas, S.J., M. Garcia-Caballero, and P. Carmeliet, *Metabolic Signatures of Distinct Endothelial Phenotypes.* Trends Endocrinol Metab, 2020. **31**(8): p. 580-595.
348. Dong, Y., et al., *Reduction of AMP-activated protein kinase alpha2 increases endoplasmic reticulum stress and atherosclerosis in vivo.* Circulation, 2010. **121**(6): p. 792-803.
349. Aranguren, X.L., et al., *Unraveling a novel transcription factor code determining the human arterial-specific endothelial cell signature.* Blood, 2013. **122**(24): p. 3982-92.
350. Ng, C.J., et al., *Single-cell transcriptional analysis of human endothelial colony-forming cells from patients with low VWF levels.* Blood, 2022. **139**(14): p. 2240-2251.
351. Mertens, S., et al., *Energetic response of coronary endothelial cells to hypoxia.* Am J Physiol, 1990. **258**(3 Pt 2): p. H689-94.
352. Buchwald, P., *A local glucose-and oxygen concentration-based insulin secretion model for pancreatic islets.* Theor Biol Med Model, 2011. **8**: p. 20.
353. Princiotta, M.F., et al., *Quantitating protein synthesis, degradation, and endogenous antigen processing.* Immunity, 2003. **18**(3): p. 343-54.
354. Li, W., et al., *Hypoxia-induced endothelial proliferation requires both mTORC1 and mTORC2.* Circ Res, 2007. **100**(1): p. 79-87.
355. Humar, R., et al., *Hypoxia enhances vascular cell proliferation and angiogenesis in vitro via rapamycin (mTOR)-dependent signaling.* FASEB J, 2002. **16**(8): p. 771-80.
356. Elgenaidi, I.S. and J.P. Spiers, *Hypoxia modulates protein phosphatase 2A through HIF-1alpha dependent and independent mechanisms in human aortic smooth muscle cells and ventricular cardiomyocytes.* Br J Pharmacol, 2019. **176**(11): p. 1745-1763.
357. Yeh, T.L., et al., *Molecular and cellular mechanisms of HIF prolyl hydroxylase inhibitors in clinical trials.* Chem Sci, 2017. **8**(11): p. 7651-7668.

358. Zhang, N., et al., *The asparaginyl hydroxylase factor inhibiting HIF-1alpha is an essential regulator of metabolism.* Cell Metab, 2010. **11**(5): p. 364-78.
359. Kuwahira, I., et al., *Effect of chronic hypoxia on hemodynamics, organ blood flow and O2 supply in rats.* Respir Physiol, 1993. **92**(2): p. 227-38.
360. Pirri, D., et al., *EPAS1 Attenuates Atherosclerosis Initiation at Disturbed Flow Sites through Endothelial Fatty Acid Uptake.* bioRxiv, 2023: p. 2023.12.05.570309.
361. Wang, E., et al., *The role of factor inhibiting HIF (FIH-1) in inhibiting HIF-1 transcriptional activity in glioblastoma multiforme.* PLoS One, 2014. **9**(1): p. e86102.
362. Belapurkar, R., et al., *A transient increase of HIF-1alpha during the G1 phase (G1-HIF) ensures cell survival under nutritional stress.* Cell Death Dis, 2023. **14**(7): p. 477.
363. Jung, S.N., et al., *Reactive oxygen species stabilize hypoxia-inducible factor-1 alpha protein and stimulate transcriptional activity via AMP-activated protein kinase in DU145 human prostate cancer cells.* Carcinogenesis, 2008. **29**(4): p. 713-21.
364. Hwang, A.B., et al., *Feedback regulation via AMPK and HIF-1 mediates ROS-dependent longevity in Caenorhabditis elegans.* Proc Natl Acad Sci U S A, 2014. **111**(42): p. E4458-67.
365. Ardito, F., et al., *The crucial role of protein phosphorylation in cell signaling and its use as targeted therapy (Review).* Int J Mol Med, 2017. **40**(2): p. 271-280.
366. Wang, G.L., B.H. Jiang, and G.L. Semenza, *Effect of protein kinase and phosphatase inhibitors on expression of hypoxia-inducible factor 1.* Biochem Biophys Res Commun, 1995. **216**(2): p. 669-75.
367. Daly, L.A., et al., *Oxygen-dependent changes in binding partners and post-translational modifications regulate the abundance and activity of HIF-1alpha/2alpha.* Sci Signal, 2021. **14**(692).
368. Kalousi, A., et al., *Casein kinase 1 regulates human hypoxia-inducible factor HIF-1.* J Cell Sci, 2010. **123**(Pt 17): p. 2976-86.
369. Cassavaugh, J.M., et al., *Negative regulation of HIF-1alpha by an FBW7-mediated degradation pathway during hypoxia.* J Cell Biochem, 2011. **112**(12): p. 3882-90.
370. Flugel, D., et al., *Glycogen synthase kinase 3 phosphorylates hypoxia-inducible factor 1alpha and mediates its destabilization in a VHL-independent manner.* Mol Cell Biol, 2007. **27**(9): p. 3253-65.
371. Bullen, J.W., et al., *Protein kinase A-dependent phosphorylation stimulates the transcriptional activity of hypoxia-inducible factor 1.* Sci Signal, 2016. **9**(430): p. ra56.
372. So, L., et al., *The 4E-BP-eIF4E axis promotes rapamycin-sensitive growth and proliferation in lymphocytes.* Sci Signal, 2016. **9**(430): p. ra57.
373. Gonzalez, F.J., C. Xie, and C. Jiang, *The role of hypoxia-inducible factors in metabolic diseases.* Nat Rev Endocrinol, 2018. **15**(1): p. 21-32.
374. Liang, Y., et al., *Interplay of hypoxia-inducible factors and oxygen therapy in cardiovascular medicine.* Nat Rev Cardiol, 2023. **20**(11): p. 723-737.
375. Day, E.A., R.J. Ford, and G.R. Steinberg, *AMPK as a Therapeutic Target for Treating Metabolic Diseases.* Trends Endocrinol Metab, 2017. **28**(8): p. 545-560.
376. Qi, D. and L.H. Young, *AMPK: energy sensor and survival mechanism in the ischemic heart.* Trends Endocrinol Metab, 2015. **26**(8): p. 422-9.
377. Jiang, S., et al., *Participation of proteasome-ubiquitin protein degradation in autophagy and the activation of AMP-activated protein kinase.* Cell Signal, 2015. **27**(6): p. 1186-97.
378. Marin, T.L., et al., *Identification of AMP-activated protein kinase targets by a consensus sequence search of the proteome.* BMC Syst Biol, 2015. **9**: p. 13.
379. Dephoure, N., et al., *Mapping and analysis of phosphorylation sites: a quick guide for cell biologists.* Mol Biol Cell, 2013. **24**(5): p. 535-42.
380. Weidemann, A., et al., *Astrocyte hypoxic response is essential for pathological but not developmental angiogenesis of the retina.* Glia, 2010. **58**(10): p. 1177-85.

381. Mertins, P., et al., *Ischemia in tumors induces early and sustained phosphorylation changes in stress kinase pathways but does not affect global protein levels.* Mol Cell Proteomics, 2014. **13**(7): p. 1690-704.
382. Bartoszewski, R., et al., *Primary endothelial cell-specific regulation of hypoxia-inducible factor (HIF)-1 and HIF-2 and their target gene expression profiles during hypoxia.* FASEB J, 2019. **33**(7): p. 7929-7941.
383. Wiesener, M.S., et al., *Induction of endothelial PAS domain protein-1 by hypoxia: characterization and comparison with hypoxia-inducible factor-1alpha.* Blood, 1998. **92**(7): p. 2260-8.
384. Smadja, D.M., et al., *Standardization of methods to quantify and culture endothelial colony-forming cells derived from peripheral blood: Position paper from the International Society on Thrombosis and Haemostasis SSC.* J Thromb Haemost, 2019. **17**(7): p. 1190-1194.
385. Dennis, D.J., S. Han, and C. Schuurmans, *bHLH transcription factors in neural development, disease, and reprogramming.* Brain Res, 2019. **1705**: p. 48-65.
386. Ali, F., et al., *Cell cycle-regulated multi-site phosphorylation of Neurogenin 2 coordinates cell cycling with differentiation during neurogenesis.* Development, 2011. **138**(19): p. 4267-77.
387. Hardwick, L.J. and A. Philpott, *Multi-site phosphorylation regulates NeuroD4 activity during primary neurogenesis: a conserved mechanism amongst proneural proteins.* Neural Dev, 2015. **10**: p. 15.
388. Koh, M.Y. and G. Powis, *Passing the baton: the HIF switch.* Trends Biochem Sci, 2012. **37**(9): p. 364-72.
389. Marin, T.L., et al., *AMPK promotes mitochondrial biogenesis and function by phosphorylating the epigenetic factors DNMT1, RBBP7, and HAT1.* Sci Signal, 2017. **10**(464).
390. Ohashi, K., et al., *LKB1 deficiency in Tie2-Cre-expressing cells impairs ischemia-induced angiogenesis.* J Biol Chem, 2010. **285**(29): p. 22291-8.
391. Viollet, B., et al., *AMPK: Lessons from transgenic and knockout animals.* Front Biosci (Landmark Ed), 2009. **14**(1): p. 19-44.
392. Milan, D., et al., *A mutation in PRKAG3 associated with excess glycogen content in pig skeletal muscle.* Science, 2000. **288**(5469): p. 1248-51.
393. Arad, M., C.E. Seidman, and J.G. Seidman, *AMP-activated protein kinase in the heart: role during health and disease.* Circ Res, 2007. **100**(4): p. 474-88.
394. Woods, A., et al., *Liver-Specific Activation of AMPK Prevents Steatosis on a High-Fructose Diet.* Cell Rep, 2017. **18**(13): p. 3043-3051.
395. Pollard, A.E., et al., *AMPK activation protects against diet induced obesity through Ucp1-independent thermogenesis in subcutaneous white adipose tissue.* Nat Metab, 2019. **1**(3): p. 340-349.
396. Wilson, L., et al., *Chronic activation of AMP-activated protein kinase leads to early-onset polycystic kidney phenotype.* Clin Sci (Lond), 2021. **135**(20): p. 2393-2408.
397. Wright, G.L., et al., *VEGF stimulation of mitochondrial biogenesis: requirement of AKT3 kinase.* FASEB J, 2008. **22**(9): p. 3264-75.
398. Domigan, C.K., et al., *Autocrine VEGF maintains endothelial survival through regulation of metabolism and autophagy.* J Cell Sci, 2015. **128**(12): p. 2236-48.
399. Stahl, A., et al., *The mouse retina as an angiogenesis model.* Invest Ophthalmol Vis Sci, 2010. **51**(6): p. 2813-26.
400. Compher, C., et al., *Best practice methods to apply to measurement of resting metabolic rate in adults: a systematic review.* J Am Diet Assoc, 2006. **106**(6): p. 881-903.
401. Casimiro, I., et al., *Phenotypic sexual dimorphism in response to dietary fat manipulation in C57BL/6J mice.* J Diabetes Complications, 2021. **35**(2): p. 107795.
402. Fromme, T., et al., *Bile acid supplementation decreases body mass gain in C57BL/6J but not 129S6/SvEvTac mice without increasing energy expenditure.* Sci Rep, 2019. **9**(1): p. 131.

403. Kondoh, M., et al., *Hypoxia-induced reactive oxygen species cause chromosomal abnormalities in endothelial cells in the tumor microenvironment.* PLoS One, 2013. **8**(11): p. e80349.
404. Zhang, W., et al., *Hypoxic mitophagy regulates mitochondrial quality and platelet activation and determines severity of I/R heart injury.* Elife, 2016. **5**.
405. Liu, L., et al., *Mitochondrial outer-membrane protein FUNDC1 mediates hypoxia-induced mitophagy in mammalian cells.* Nat Cell Biol, 2012. **14**(2): p. 177-85.
406. Nanayakkara, G., et al., *Cardioprotective HIF-1alpha-frataxin signaling against ischemia-reperfusion injury.* Am J Physiol Heart Circ Physiol, 2015. **309**(5): p. H867-79.
407. Zhu, Y., et al., *Vaspin Attenuates Atrial Abnormalities by Promoting ULK1/FUNDC1-Mediated Mitophagy.* Oxid Med Cell Longev, 2022. **2022**: p. 3187463.
408. Wu, W., et al., *ULK1 translocates to mitochondria and phosphorylates FUNDC1 to regulate mitophagy.* EMBO Rep, 2014. **15**(5): p. 566-75.
409. Xu, W., et al., *Alterations of cellular bioenergetics in pulmonary artery endothelial cells.* Proc Natl Acad Sci U S A, 2007. **104**(4): p. 1342-7.
410. Fijalkowska, I., et al., *Hypoxia inducible-factor1alpha regulates the metabolic shift of pulmonary hypertensive endothelial cells.* Am J Pathol, 2010. **176**(3): p. 1130-8.
411. Drake, J.C., et al., *Mitochondria-localized AMPK responds to local energetics and contributes to exercise and energetic stress-induced mitophagy.* Proc Natl Acad Sci U S A, 2021. **118**(37).
412. Tilokani, L., et al., *AMPK-dependent phosphorylation of MTFR1L regulates mitochondrial morphology.* Sci Adv, 2022. **8**(45): p. eabo7956.
413. Luengo, A., et al., *Increased demand for NAD(+) relative to ATP drives aerobic glycolysis.* Mol Cell, 2021. **81**(4): p. 691-707 e6.
414. Bhat, T.A., et al., *Restoration of mitochondria function as a target for cancer therapy.* Drug Discov Today, 2015. **20**(5): p. 635-43.
415. Cai, Z., et al., *Phosphorylation of PDHA by AMPK Drives TCA Cycle to Promote Cancer Metastasis.* Mol Cell, 2020. **80**(2): p. 263-278 e7.
416. Lemos, C., et al., *The potent AMPK inhibitor BAY-3827 shows strong efficacy in androgen-dependent prostate cancer models.* Cell Oncol (Dordr), 2021. **44**(3): p. 581-594.
417. Francescone, R.A., 3rd, M. Faibish, and R. Shao, *A Matrigel-based tube formation assay to assess the vasculogenic activity of tumor cells.* J Vis Exp, 2011(55).
418. Abdel-Misih, S.R. and M. Bloomston, *Liver anatomy.* Surg Clin North Am, 2010. **90**(4): p. 643-53.
419. McMahan, R.H., et al., *Free Fatty Acids Differentially Downregulate Chemokines in Liver Sinusoidal Endothelial Cells: Insights into Non-Alcoholic Fatty Liver Disease.* PLoS One, 2016. **11**(7): p. e0159217.
420. Donnelly, K.L., et al., *Sources of fatty acids stored in liver and secreted via lipoproteins in patients with nonalcoholic fatty liver disease.* J Clin Invest, 2005. **115**(5): p. 1343-51.
421. Luukkonen, P.K., et al., *Distinct contributions of metabolic dysfunction and genetic risk factors in the pathogenesis of non-alcoholic fatty liver disease.* J Hepatol, 2022. **76**(3): p. 526-535.
422. Mannisto, V.T., et al., *Ketone body production is differentially altered in steatosis and non-alcoholic steatohepatitis in obese humans.* Liver Int, 2015. **35**(7): p. 1853-61.
423. Post, A., et al., *Nonalcoholic fatty liver disease, circulating ketone bodies and all-cause mortality in a general population-based cohort.* Eur J Clin Invest, 2021. **51**(12): p. e13627.
424. Anstee, Q.M. and R.D. Goldin, *Mouse models in non-alcoholic fatty liver disease and steatohepatitis research.* Int J Exp Pathol, 2006. **87**(1): p. 1-16.
425. Guo, Q., et al., *Isolation and Characterization of Mouse Primary Liver Sinusoidal Endothelial Cells.* J Vis Exp, 2021(178).

426. Heffner, C.S., et al., *Supporting conditional mouse mutagenesis with a comprehensive cre characterization resource.* Nat Commun, 2012. **3**: p. 1218.
427. Payne, S., S. De Val, and A. Neal, *Endothelial-Specific Cre Mouse Models.* Arterioscler Thromb Vasc Biol, 2018. **38**(11): p. 2550-2561.
428. Guo, F., D.R. Moellering, and W.T. Garvey, *The progression of cardiometabolic disease: validation of a new cardiometabolic disease staging system applicable to obesity.* Obesity (Silver Spring), 2014. **22**(1): p. 110-8.
429. Vincent, G.E., et al., *Improving Cardiometabolic Health with Diet, Physical Activity, and Breaking Up Sitting: What about Sleep?* Front Physiol, 2017. **8**: p. 865.
430. Tahir, U.A. and R.E. Gerszten, *Omics and Cardiometabolic Disease Risk Prediction.* Annu Rev Med, 2020. **71**: p. 163-175.
431. Hashimoto, T., et al., *Severe hypoxia increases expression of ATM and DNA-PKcs and it increases their activities through Src and AMPK signaling pathways.* Biochem Biophys Res Commun, 2018. **505**(1): p. 13-19.
432. Lorca, R.A., et al., *High altitude regulates the expression of AMPK pathways in human placenta.* Placenta, 2021. **104**: p. 267-276.
433. Lorca, R.A., et al., *AMPK activation in pregnant human myometrial arteries from high-altitude and intrauterine growth-restricted pregnancies.* Am J Physiol Heart Circ Physiol, 2020. **319**(1): p. H203-H212.
434. Skeffington, K.L., et al., *Hypoxia, AMPK activation and uterine artery vasoreactivity.* J Physiol, 2016. **594**(5): p. 1357-69.
435. Beall, C.M., D. Laskowski, and S.C. Erzurum, *Nitric oxide in adaptation to altitude.* Free Radic Biol Med, 2012. **52**(7): p. 1123-34.
436. Beall, C.M., et al., *Variation in hemoglobin concentration among samples of high-altitude natives in the Andes and the Himalayas.* Am J Hum Biol, 1990. **2**(6): p. 639-651.
437. Droma, Y., et al., *The blunted vascular endothelial growth factor-A (VEGF-A) response to high-altitude hypoxia and genetic variants in the promoter region of the VEGFA gene in Sherpa highlanders.* PeerJ, 2022. **10**: p. e13893.
438. Weitz, C.A. and R.M. Garruto, *A comparative analysis of arterial oxygen saturation among Tibetans and Han born and raised at high altitude.* High Alt Med Biol, 2007. **8**(1): p. 13-26.
439. Lahiri, S. and J.S. Milledge, *Sherpa physiology.* Nature, 1965. **207**(997): p. 610-2.
440. Bigham, A.W., et al., *Maternal PRKAA1 and EDNRA genotypes are associated with birth weight, and PRKAA1 with uterine artery diameter and metabolic homeostasis at high altitude.* Physiol Genomics, 2014. **46**(18): p. 687-97.
441. del Pilar Valle, M., et al., *Improvement of myocardial perfusion in coronary patients after intermittent hypobaric hypoxia.* J Nucl Cardiol, 2006. **13**(1): p. 69-74.
442. Woolcott, O.O., M. Ader, and R.N. Bergman, *Glucose homeostasis during short-term and prolonged exposure to high altitudes.* Endocr Rev, 2015. **36**(2): p. 149-73.
443. Woolcott, O.O., et al., *Inverse association between diabetes and altitude: a cross-sectional study in the adult population of the United States.* Obesity (Silver Spring), 2014. **22**(9): p. 2080-90.
444. Sherpa, L.Y., et al., *Obesity in Tibetans aged 30-70 living at different altitudes under the north and south faces of Mt. Everest.* Int J Environ Res Public Health, 2010. **7**(4): p. 1670-80.
445. Matsubayashi, K., et al., *Comprehensive geriatric assessment of elderly highlanders in Qinghai, China I: activities of daily living, quality of life and metabolic syndrome.* Geriatr Gerontol Int, 2009. **9**(4): p. 333-41.
446. Faeh, D., et al., *Lower mortality from coronary heart disease and stroke at higher altitudes in Switzerland.* Circulation, 2009. **120**(6): p. 495-501.
447. Lang, J.A. and J. Kim, *Remote ischaemic preconditioning - translating cardiovascular benefits to humans.* J Physiol, 2022. **600**(13): p. 3053-3067.
448. Donato, M., et al., *Myocardial remote ischemic preconditioning: from cell biology to clinical application.* Mol Cell Biochem, 2021. **476**(10): p. 3857-3867.

449. Hummitzsch, L., et al., *Effects of remote ischemic preconditioning (RIPC) and chronic remote ischemic preconditioning (cRIPC) on levels of plasma cytokines, cell surface characteristics of monocytes and in-vitro angiogenesis: a pilot study.* Basic Res Cardiol, 2021. **116**(1): p. 60.
450. Hyngstrom, A.S., et al., *Two weeks of remote ischemic conditioning improves brachial artery flow mediated dilation in chronic stroke survivors.* J Appl Physiol (1985), 2020. **129**(6): p. 1348-1354.
451. Pugh, D., et al., *Large-vessel vasculitis.* Nat Rev Dis Primers, 2022. **7**(1): p. 93.
452. Campbell, B.C.V., et al., *Ischaemic stroke.* Nat Rev Dis Primers, 2019. **5**(1): p. 70.
453. Wolberg, A.S., et al., *Venous thrombosis.* Nat Rev Dis Primers, 2015. **1**: p. 15006.
454. Libby, P., et al., *Atherosclerosis.* Nat Rev Dis Primers, 2019. **5**(1): p. 56.
455. Hachamovitch, R., et al., *Impact of ischaemia and scar on the therapeutic benefit derived from myocardial revascularization vs. medical therapy among patients undergoing stress-rest myocardial perfusion scintigraphy.* Eur Heart J, 2011. **32**(8): p. 1012-24.
456. Habib, G.B., et al., *Influence of coronary collateral vessels on myocardial infarct size in humans. Results of phase I thrombolysis in myocardial infarction (TIMI) trial. The TIMI Investigators.* Circulation, 1991. **83**(3): p. 739-46.
457. Sabia, P.J., et al., *An association between collateral blood flow and myocardial viability in patients with recent myocardial infarction.* N Engl J Med, 1992. **327**(26): p. 1825-31.
458. Annex, B.H. and J.P. Cooke, *New Directions in Therapeutic Angiogenesis and Arteriogenesis in Peripheral Arterial Disease.* Circ Res, 2021. **128**(12): p. 1944-1957.
459. Robich, M.P., et al., *Myocardial therapeutic angiogenesis: a review of the state of development and future obstacles.* Expert Rev Cardiovasc Ther, 2011. **9**(11): p. 1469-79.
460. Diez, H., et al., *Hypoxia-mediated activation of Dll4-Notch-Hey2 signaling in endothelial progenitor cells and adoption of arterial cell fate.* Exp Cell Res, 2007. **313**(1): p. 1-9.
461. Sabbagh, M.F., et al., *Transcriptional and epigenomic landscapes of CNS and non-CNS vascular endothelial cells.* Elife, 2018. **7**.
462. Quillien, A., et al., *Distinct Notch signaling outputs pattern the developing arterial system.* Development, 2014. **141**(7): p. 1544-52.
463. Hasan, S.S., et al., *Endothelial Notch signalling limits angiogenesis via control of artery formation.* Nat Cell Biol, 2017. **19**(8): p. 928-940.
464. Pitulescu, M.E., et al., *Dll4 and Notch signalling couples sprouting angiogenesis and artery formation.* Nat Cell Biol, 2017. **19**(8): p. 915-927.
465. Xu, C., et al., *Arteries are formed by vein-derived endothelial tip cells.* Nat Commun, 2014. **5**: p. 5758.
466. Hildreth, A.D., et al., *Single-cell sequencing of human white adipose tissue identifies new cell states in health and obesity.* Nat Immunol, 2021. **22**(5): p. 639-653.
467. Pasarica, M., et al., *Reduced adipose tissue oxygenation in human obesity: evidence for rarefaction, macrophage chemotaxis, and inflammation without an angiogenic response.* Diabetes, 2009. **58**(3): p. 718-25.
468. Lawler, H.M., et al., *Adipose Tissue Hypoxia, Inflammation, and Fibrosis in Obese Insulin-Sensitive and Obese Insulin-Resistant Subjects.* J Clin Endocrinol Metab, 2016. **101**(4): p. 1422-8.
469. Goossens, G.H., et al., *Increased adipose tissue oxygen tension in obese compared with lean men is accompanied by insulin resistance, impaired adipose tissue capillarization, and inflammation.* Circulation, 2011. **124**(1): p. 67-76.
470. Vink, R.G., et al., *Diet-induced weight loss decreases adipose tissue oxygen tension with parallel changes in adipose tissue phenotype and insulin sensitivity in overweight humans.* Int J Obes (Lond), 2017. **41**(5): p. 722-728.
471. Gealekman, O., et al., *Depot-specific differences and insufficient subcutaneous adipose tissue angiogenesis in human obesity.* Circulation, 2011. **123**(2): p. 186-94.

472. Lee, Y.S., et al., *Increased adipocyte O2 consumption triggers HIF-1alpha, causing inflammation and insulin resistance in obesity.* Cell, 2014. **157**(6): p. 1339-1352.
473. Jungermann, K. and T. Kietzmann, *Oxygen: modulator of metabolic zonation and disease of the liver.* Hepatology, 2000. **31**(2): p. 255-60.
474. Mesarwi, O.A., R. Loomba, and A. Malhotra, *Obstructive Sleep Apnea, Hypoxia, and Nonalcoholic Fatty Liver Disease.* Am J Respir Crit Care Med, 2019. **199**(7): p. 830-841.
475. Mattijssen, F., et al., *Hypoxia-inducible lipid droplet-associated (HILPDA) is a novel peroxisome proliferator-activated receptor (PPAR) target involved in hepatic triglyceride secretion.* J Biol Chem, 2014. **289**(28): p. 19279-93.
476. Mylonis, I., et al., *Hypoxia causes triglyceride accumulation by HIF-1-mediated stimulation of lipin 1 expression.* J Cell Sci, 2012. **125**(Pt 14): p. 3485-93.
477. Arai, T., M. Tanaka, and N. Goda, *HIF-1-dependent lipin1 induction prevents excessive lipid accumulation in choline-deficient diet-induced fatty liver.* Sci Rep, 2018. **8**(1): p. 14230.
478. Nishiyama, Y., et al., *HIF-1alpha induction suppresses excessive lipid accumulation in alcoholic fatty liver in mice.* J Hepatol, 2012. **56**(2): p. 441-7.
479. Chen, J., et al., *Hypoxia exacerbates nonalcoholic fatty liver disease via the HIF-2alpha/PPARalpha pathway.* Am J Physiol Endocrinol Metab, 2019. **317**(4): p. E710-E722.
480. Rey, E., et al., *Hypoxia-inducible factor 2alpha drives hepatosteatosis through the fatty acid translocase CD36.* Liver Int, 2020. **40**(10): p. 2553-2567.
481. Yu, L., et al., *Oxygen therapy alleviates hepatic steatosis by inhibiting hypoxia-inducible factor-2alpha.* J Endocrinol, 2020. **246**(1): p. 57-67.

8. Appendices

Functions Annotation	p-value	Predicted Activation State	Activation z-score	# Molecules
Segregation of chromosomes	1.23E-56	Decreased	-2.372	58
Cell cycle progression	1.05E-52	Decreased	-2.887	149
DNA replication	6.59E-38	Decreased	-2.674	61
Metabolism of DNA	4.66E-34	Decreased	-3.52	70
M phase	1.58E-27	Decreased	-2.521	49
Checkpoint control	1.44E-26	Decreased	-2.541	29
Alignment of chromosomes	1.74E-23	Decreased	-2.876	19
Metabolism of macromolecule	2.25E-21	Decreased	-3.854	118
Chromosomal congression of chromosomes	1.78E-17	Decreased	-2.345	11
Cell viability of tumor cell lines	3.74E-17	Decreased	-7.282	95
Cell survival	8.67E-17	Decreased	-7.544	126
Cell viability	1.5E-16	Decreased	-7.107	122
Cycling of centrosome	1.58E-16	Decreased	-2.305	25
Cell cycle progression of tumor cell lines	2.34E-16	Decreased	-2.452	42
Homologous recombination	5.5E-16	Decreased	-2.896	27
Cytokinesis	2.78E-15	Decreased	-3.156	30
G1 phase	2.93E-15	Decreased	-2.067	53
Cell proliferation of adenocarcinoma cell lines	1.64E-13	Decreased	-4.099	31
Colony formation	1.72E-12	Decreased	-4.276	65
Recombination of cells	1.96E-12	Decreased	-2.451	21
Cell proliferation of breast cancer cell lines	1.32E-11	Decreased	-3.944	55
Homologous recombination of cells	2.83E-11	Decreased	-2.89	19
Chromosome separation	7.86E-11	Decreased	-2.121	8
Chromosome condensation	1.65E-10	Decreased	-2.433	8
Colony formation of cells	1.15E-09	Decreased	-2.773	51
G1/S phase transition	1.01E-08	Decreased	-2.368	25
Ploidy of cells	2.5E-24	Increased	2.143	35
Necrosis	1.04E-22	Increased	6.166	197
Apoptosis	1.66E-21	Increased	6.577	190
Quantity of mitotic spindle	1.94E-14	Increased	2.084	12
Breakage of chromosomes	2.5E-13	Increased	3.211	16
Cell death of carcinoma cell lines	2.65E-12	Increased	3.843	50
Senescence of cells	9.54E-12	Increased	3.324	40

Table 8.1 *– IPA Functions annotations for common downregulated DEGs.*

Diseases Annotation	p-value	Predicted Activation State	Activation z-score	# Molecules
Digestive system cancer	8.57E-18	Decreased	-2.092	422
Lymphoma	6.84E-34	Increased	2.81	154
Development of lung tumor	1.41E-27	Increased	2.601	158
Non-squamous non-small cell lung carcinoma	1.9E-27	Increased	2.198	157
Lung adenocarcinoma	3.87E-27	Increased	2.198	156
Tumorigenesis of lymphocytes	2.58E-26	Increased	2.769	182
Lymphocytic cancer	1.09E-22	Increased	2.769	200
Malignant lymphocytic neoplasm	1.09E-22	Increased	2.769	200
Hematologic cancer of cells	1.36E-22	Increased	2.81	184
Neoplasia of leukocytes	4.1E-22	Increased	2.877	190
Hematologic cancer	2.02E-20	Increased	2.602	231
Myeloid or lymphoid neoplasm	5.35E-20	Increased	2.761	231
Hematopoietic neoplasm	7.31E-20	Increased	2.254	232
Neoplasia of blood cells	5.45E-19	Increased	2.889	221
Development of hematological system tumor	3.12E-15	Increased	3.634	30
Incidence of lymphoma	8.19E-15	Increased	3.715	29
Renal tumor	2.22E-13	Increased	2	113
Non-Hodgkin lymphoma	8.74E-11	Increased	2.345	93

Table 8.2 *– IPA Disease functions for common downregulated DEGs.*

HIF-1α site	Known site	Origin	PhosphoSitePlus kinase	PhosphoSiteP lus window	Motifs
S696	+	HTP;LTP	ATM	NVLsVALsQRTtVPE	ATM kinase substrate motif;Casein kinase II substrate motif;DNA dependent Protein kinase substrate motif;G protein-coupled receptor kinase 1 substrate motif;MAPKAPK2 kinase substrate motif;PKA kinase substrate motif;PKC kinase substrate motif
T652	+	CST		THIHkEttsATssPY	Calmodulin-dependent protein kinase II substrate motif;Chk1 kinase substrate motif;G protein-coupled receptor kinase 1 substrate motif;PKA kinase substrate motif;PKC kinase substrate motif
S727	+	HTP;LTP	PKACA	RkMEHDGsLFQAVGI	G protein-coupled receptor kinase 1 substrate motif
T372					G protein-coupled receptor kinase 1 substrate motif;PKA kinase substrate motif;PKC kinase substrate motif
T290					Casein kinase II substrate motif
S692	+	HTP;LTP	PKACA	PRsPNVLsVALsQRT	G protein-coupled receptor kinase 1 substrate motif;GSK3 kinase substrate motif
T645					DNA dependent Protein kinase substrate motif;MAPKAPK2 kinase substrate motif
S653	+	CST;HTP		HIHkEttsATssPYR	Casein kinase I substrate motif;Casein kinase II substrate motif;G protein-coupled receptor kinase 1 substrate motif;GSK3 kinase substrate motif;PKA kinase substrate motif
S65					AMP-activated protein kinase substrate motif
S380					b-Adrenergic Receptor kinase substrate motif;Calmodulin-dependent protein kinase II substrate motif;Casein kinase II substrate motif;G protein-coupled receptor kinase 1 substrate motif;GSK3 kinase substrate motif;PKA

					kinase substrate motif;PKC kinase substrate motif
T458	+	HTP		sPLPtAEtPkPLRSs	b-Adrenergic Receptor kinase substrate motif;Growth associated histone HI kinase substrate motif;GSK-3, ERK1, ERK2, CDK5 substrate motif;PKA kinase substrate motif;PKC kinase substrate motif;WW domain binding motif
S643	+	HTP;LTP	ERK2	kILIAsPsPTHIHkE	Casein kinase II substrate motif;DNA dependent Protein kinase substrate motif;ERK1,2 kinase substrate motif;GSK-3, ERK1, ERK2, CDK5 substrate motif;WW domain binding motif
T455	+	HTP;LTP	PKACA	LAMsPLPtAEtPkPL	DNA dependent Protein kinase substrate motif;G protein-coupled receptor kinase 1 substrate motif;MAPKAPK2 kinase substrate motif
T383					b-Adrenergic Receptor kinase substrate motif
T181					Calmodulin-dependent protein kinase II substrate motif;MAPKAPK2 kinase substrate motif;PKC kinase substrate motif
S253					Casein kinase II substrate motif;PKA kinase substrate motif;PKC kinase substrate motif;Pyruvate dehydrogenase kinase substrate motif
S700	+	HTP;LTP	PKACA	VALsQRTtVPEEELN	Casein kinase II substrate motif;MAPKAPK2 kinase substrate motif;PKA kinase substrate motif;PKC kinase substrate motif
T302					Casein kinase II substrate motif
S464					Casein kinase II substrate motif;G protein-coupled receptor kinase 1 substrate motif;PKA kinase substrate motif;Pyruvate dehydrogenase kinase substrate motif
S683	+	HTP		VIEQTEksHPRsPNV	G protein-coupled receptor kinase 1 substrate motif;GSK3 kinase substrate motif

Table 8.3 *– Spectronaut analysis on putative kinases for the identified HIF-1α phosphosites.*

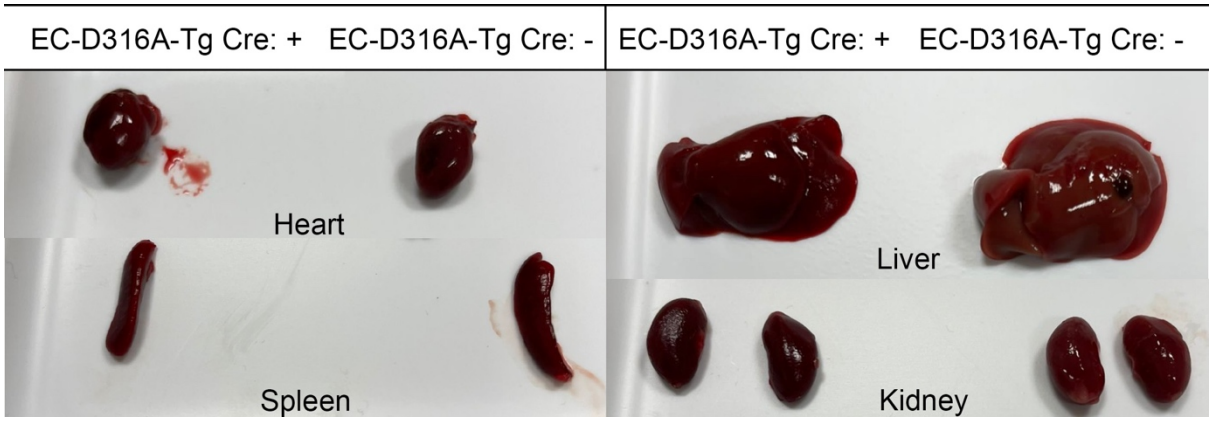


Figure 8.1 *– Images of organs from EC-γ_1WT-Tg and EC-γ_1D316A-Tg 3-month-old male mice.*

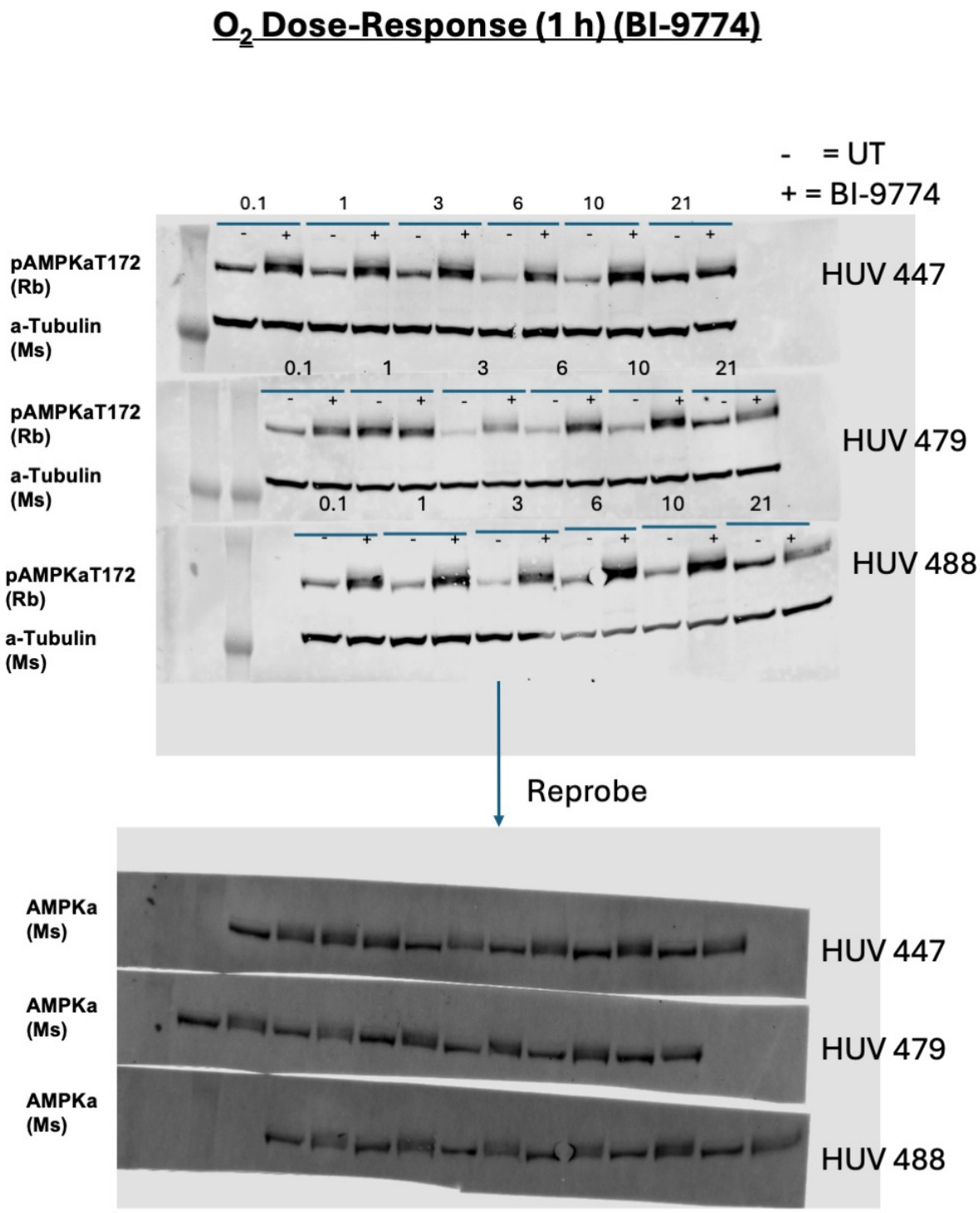


Figure 8.2 *- O_2 Dose Response (1 hour) with BI-9774 Raw Images*

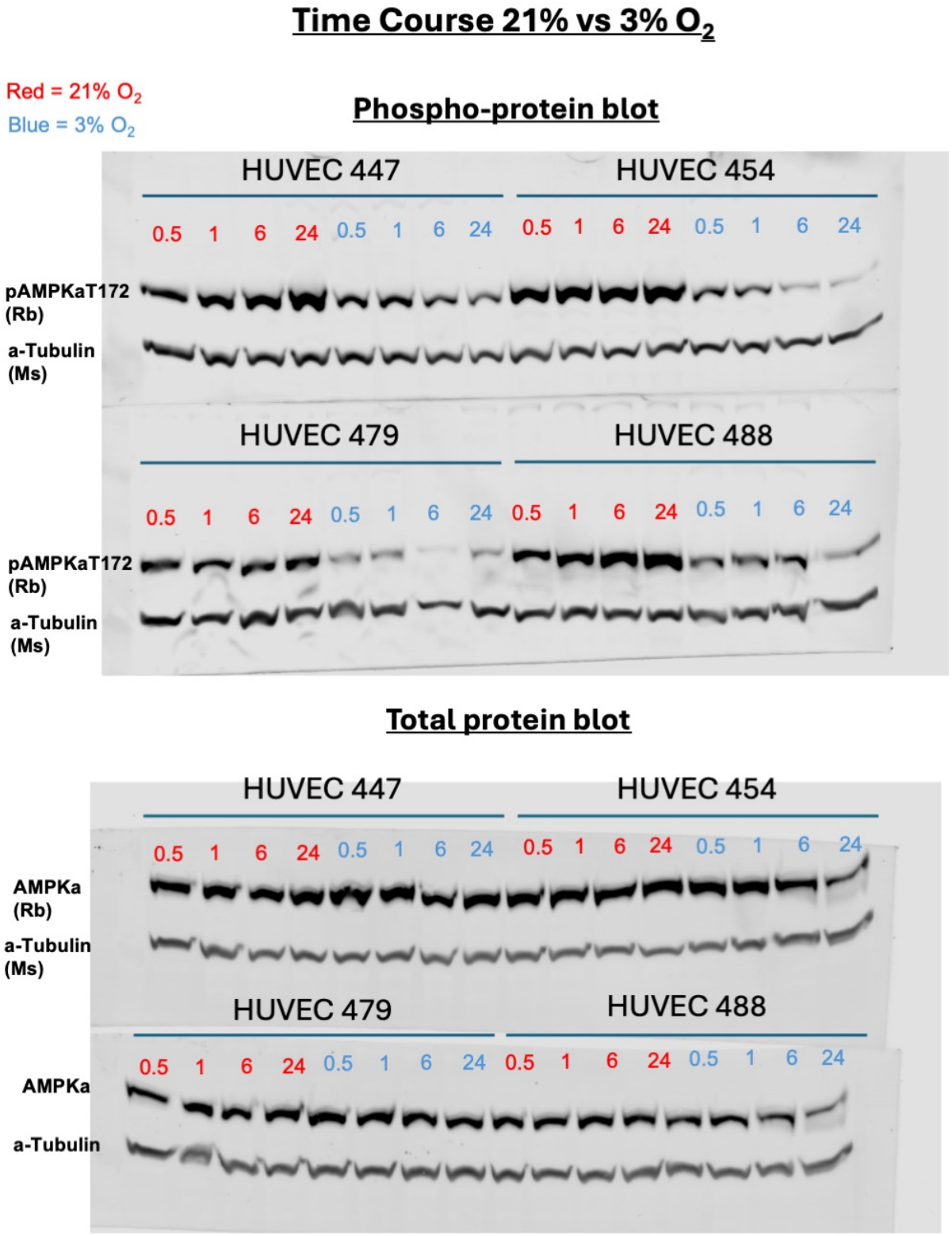


Figure 8.3 *– Time Course (21% versus 3% O_2) Raw Images with phospho-AMPKα^{T172}, AMPKα and α-Tubulin.*

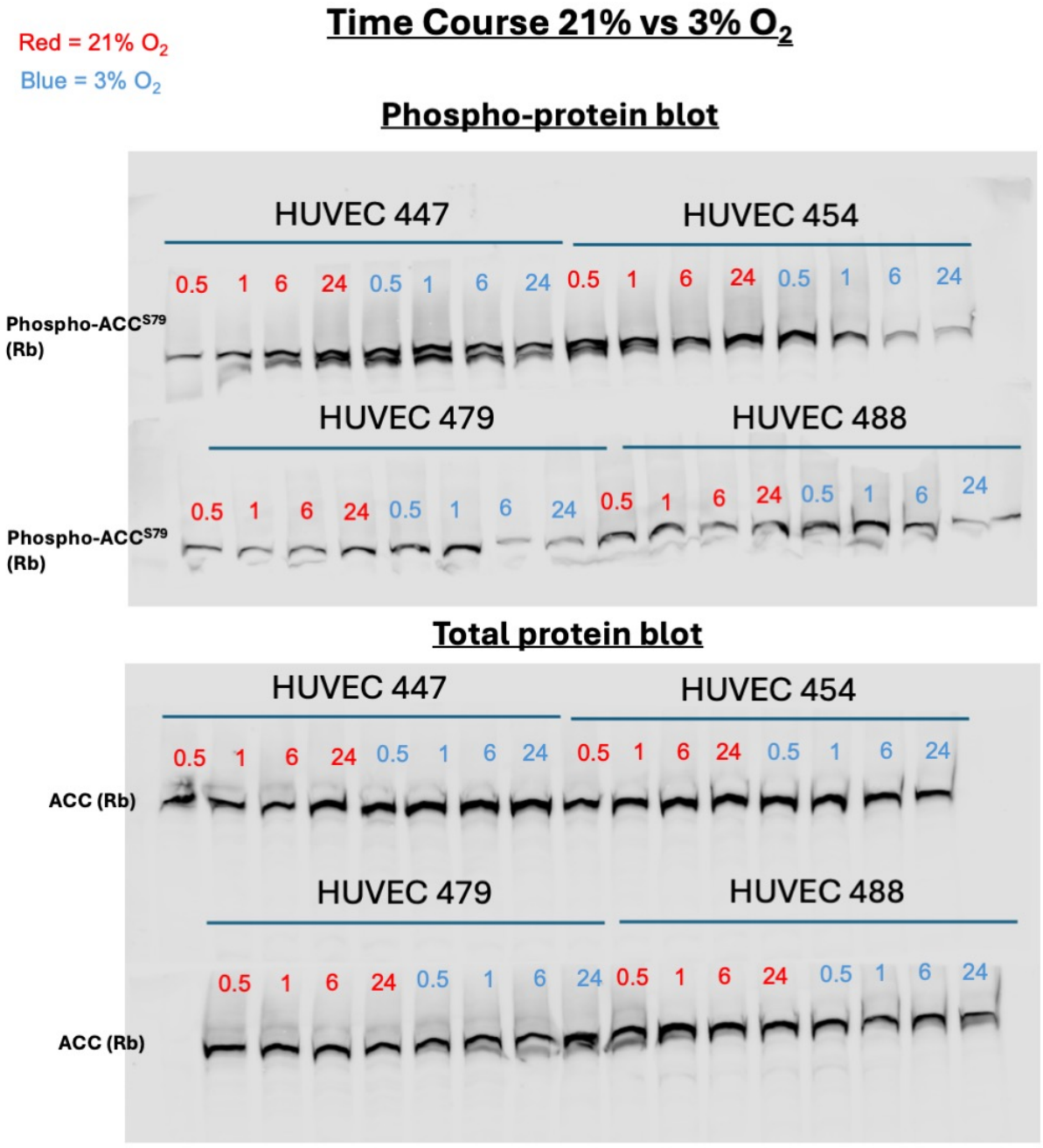


Figure 8.4 *– Time Course (21% versus 3% O_2) Raw Images with phospho-ACCS^{79} and ACC.*

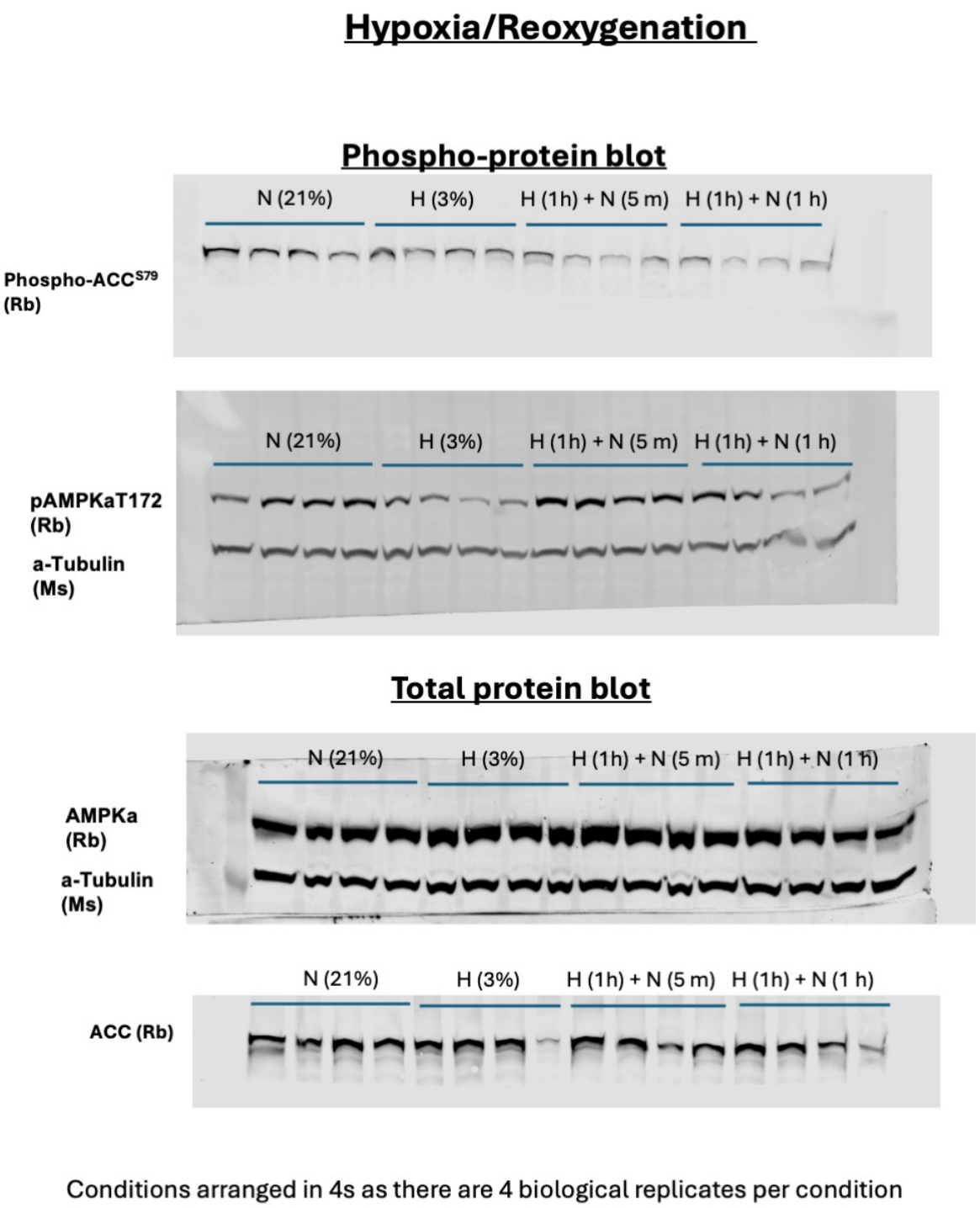


Figure 8.5 *– Hypoxia/Reoxygenation Experiment Raw Images*

NaF Treatment

Gel (1)

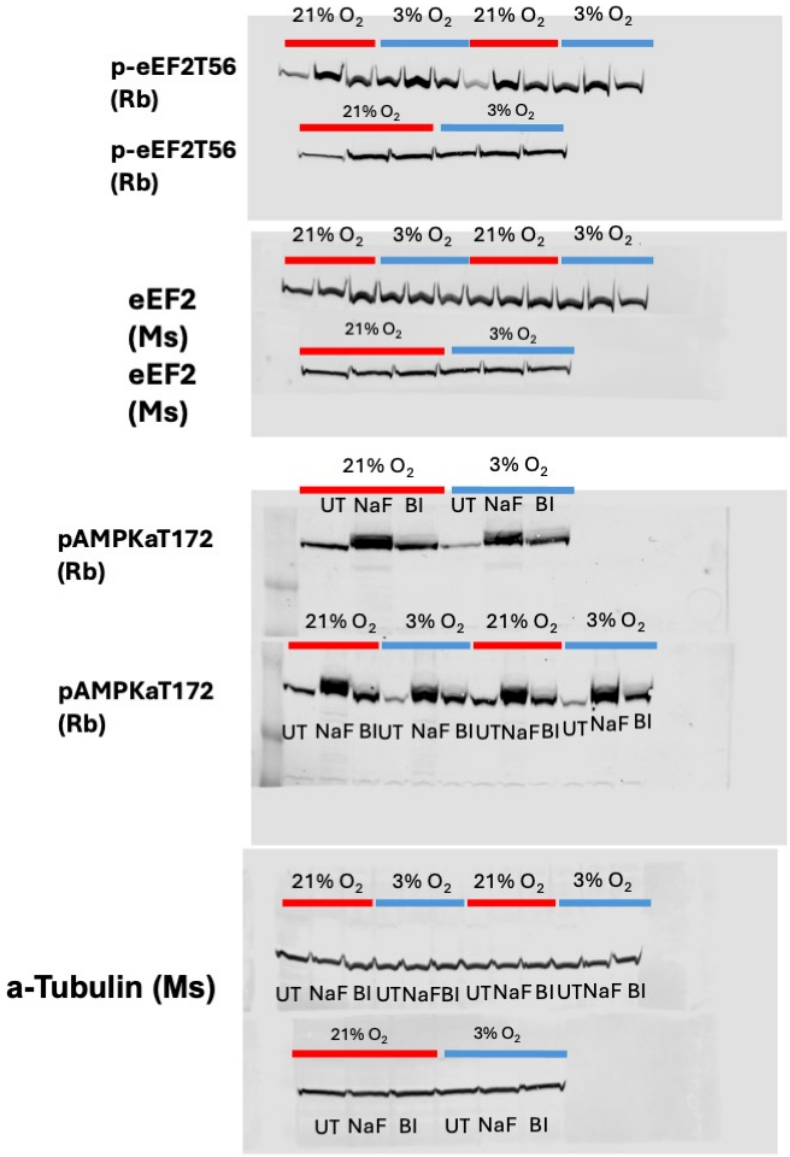


Figure 8.6 *– NaF and BI-9774 treatment under normoxia (21% O_2) and hypoxia (3% O_2) Raw Images.*

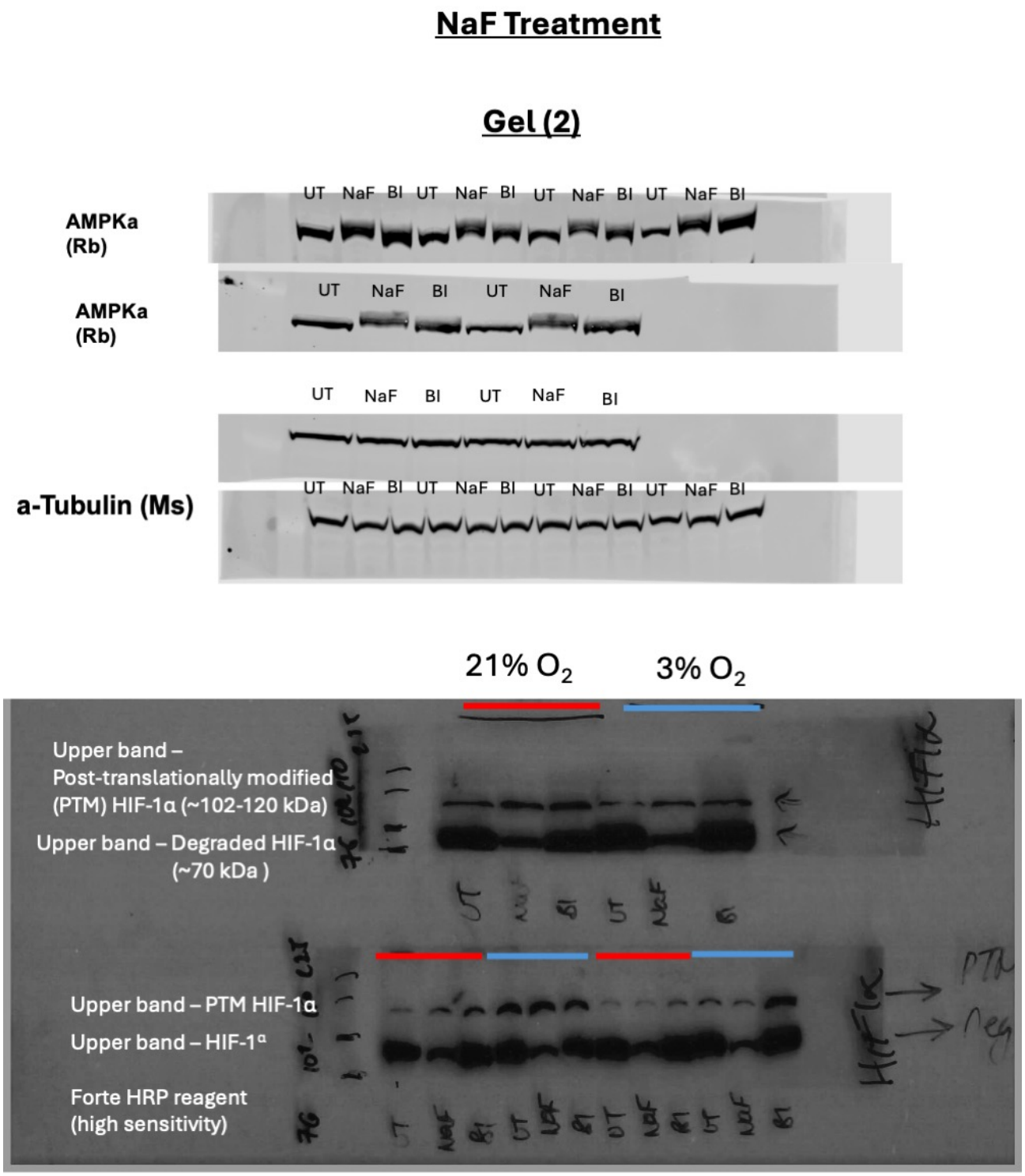


Figure 8.7 *– NaF and BI-9774 treatment under normoxia (21% O_2) and hypoxia (3% O_2) Raw Images.*